Echoes of Correlations

Quantum-Optical High-Order Harmonic Generation From Strongly Correlated Systems

PhD thesis

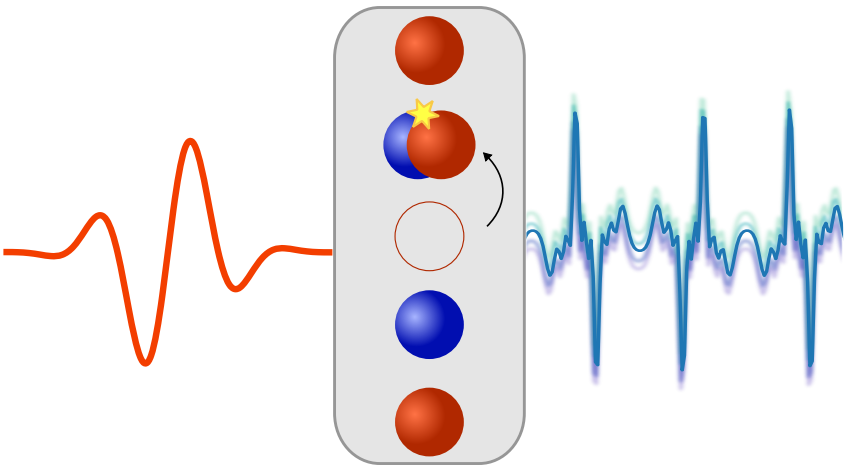

Christian Saugbjerg Lange

Department of Physics and Astronomy
Aarhus University, Denmark

Christian Saugbjerg Lange
Department of Physics and Astronomy
Aarhus University
Ny Munkegade 120, Building 1520
8000 Aarhus C
Denmark

Cover image:
Visualization of the quantum-optical process
of high-order harmonic generation
from a strongly correlated material.
Made with Inkscape.

Echoes of Correlations

Quantum-Optical High-Order Harmonic Generation From Strongly Correlated Systems

Christian Saugbjerg Lange

Department of Physics and Astronomy
Aarhus University, Denmark

PhD thesis
August 2025

Op, al den ting, som Gud har gjort,
hans herlighed at prise!
Det *mindste*, han har skabt, er stort
og kan hans magt bevise.

—H.A. Brorson, 1734

This thesis has been submitted to the Graduate School of Natural Sciences at Aarhus University to fulfill the requirements for obtaining a PhD degree in physics.

Supervisor

Lars Bojer Madsen, Professor, PhD, Dr.Scient.
Department of Physics and Astronomy,
Aarhus University

Assessment Committee

Mikhail Ivanov, Professor, PhD
Max Born Institute, Berlin

Oren Cohen, Professor, PhD
Technion Israel Institute of Technology, Haifa

Head of Committee

Jill Miwa, Associate Professor, PhD
Department of Physics and Astronomy,
Aarhus University

Funding Information

Danish National Research Foundation through the Center of Excellence "CCQ" (DNRF152)
Graduate School of Natural Sciences

Copyright Information

This document was compiled and typeset in LaTeX.

Printing: Fællestrykkeriet - AUTRYK, Aarhus University, Denmark

Abstract

Electrons are fundamental components of matter and are essential to our understanding of natural phenomena across all scientific disciplines, such as in molecular reactions, biochemical processes, and modern technological electronic devices. Additionally, light, both visible and nonvisible, also originates from electron motion. Electrons are therefore of immense importance and interest. One way to study electrons is to subject them to an intense laser field, which induces nonlinear electron dynamics resulting in the emission of light in the strong-field process of high-order harmonic generation (HHG). Not only is HHG a useful spectroscopic tool to investigate electron dynamics within a system, but it is also used as a method to generate ultrashort bursts of light, which again can be used to study electron dynamics in matter.

The thesis aims to investigate the quantum optical nature of the light emitted by HHG. The motivation for this quantum optical approach to HHG is twofold: First, it may widen and improve on HHG as a spectroscopic method, allowing a deeper and more fundamental understanding of the induced electron dynamics. Secondly, the quantum optical study of HHG may reveal how ultrashort pulses of light with desirable quantum properties are generated, which has its own potential applications in spectroscopy, quantum sensing, and quantum information science. To investigate the quantum optical nature of HHG, the Fermi-Hubbard model is considered, which includes electron-electron correlations in order to study both uncorrelated and strongly correlated electrons. First, using a semiclassical treatment of HHG from the model, the appearance of noninteger harmonics in the HHG spectrum is investigated and is explained by the population of multiple Floquet states. Using a quantum optical treatment, it is found that electron-electron correlations induce nonclassical states of light when driven by an intense laser. In particular, it is found that a Mott exciton in the extended Hubbard model is dominant in the nonclassical response. Further, it is found that the quantum nature of the emitted radiation is due to nonvanishing time correlations of the induced current. Finally, an uncorrelated electron model is driven by nonclassical states of light, where it is found that different types of light yield drastically different harmonic spectra, showing how the quantum optical nature of HHG provides new insights into fundamental physics.

Dansk resumé

Elektroner er fundamentale bestanddele af stof og er afgørende for vores forståelse af naturlige fænomener på tværs af alle videnskabelige discipliner, såsom molekylære reaktioner, biokemiske processer og moderne elektroniske teknologier. Derudover stammer lys – både synligt og usynligt – også fra elektroners bevægelse. Elektroner er derfor af enorm betydning og interesse. En måde at studere elektroner på er ved at udsætte dem for et intenst laserfelt, som inducerer ikke-lineær elektrondynamik, hvilket resulterer i lysudsendelse gennem den stærkfeltproces, der kaldes højordens harmonisk generering (HHG). HHG er ikke blot et nyttigt spektroskopisk værktøj til at undersøge elektrondynamik i et system, men kan også bruges som en metode til at generere ultrakorte lyspulser, som igen kan anvendes til at studere elektrondynamik i stof.

Afhandlingen har til formål at undersøge den kvanteoptiske natur af det lys, der udsendes ved HHG. Motivation for denne kvanteoptiske beskrivelse af HHG er todelt: For det første kan den udvide og forbedre HHG som en spektroskopisk metode og muliggøre en dybere og mere fundamental forståelse af den inducerede elektrondynamik. For det andet kan den kvanteoptiske undersøgelse af HHG afsløre, hvordan ultrakorte lyspulser med særlige kvanteegenskaber genereres, hvilket har potentielle anvendelser inden for spektroskopi, kvantesensensing og kvanteinformation. For at undersøge den kvanteoptiske natur af HHG anvendes Fermi-Hubbard-modellen, som inkluderer elektron-elektron-korrelationer, til at studere både ukorrelerede og stærkt korrelerede elektroner. Først undersøges fremkomsten af ikke-heltallige harmoniske i HHG-spektret ved hjælp af en semiklassisk beskrivelse af HHG, hvilket skyldes population af flere Floquet-tilstande. Ved hjælp af en kvanteoptisk behandling findes det, at elektron-elektron-korrelationer inducerer ikke-klassiske tilstande af lys, når de drives af en intens laser. I særdeleshed er det vist, at en Mott-exciton i den udvidede Hubbard-model er dominerende i den ikke-klassiske respons. Ydermere konkluderes det, at den kvanteoptiske natur af den udsendte stråling skyldes ikkeforsvindende tidskorrelationer i den inducerede strøm. Endelig drives en ukorreleret elektronmodel af ikke-klassiske lystilstande, hvor det ses, at forskellige typer lys giver markant forskellige harmoniske spektre, hvilket viser, hvordan den kvanteoptiske natur af HHG giver ny indsigt i fundamental fysik.

Preface

The thesis consists of research conducted during my PhD studies in the period of June 2023 to August 2025 under the supervision of Prof. Lars Bojer Madsen at the Department of Physics and Astronomy, Aarhus University, Denmark. I spent the first part of my PhD (September 2021 to May 2023) under the supervision of Prof. Thomas Pohl within the Center for Complex Quantum Systems (CCQ) at Aarhus University. The change of supervisor was due to Prof. Thomas Pohl leaving Aarhus University. Unfortunately, the research carried out under his supervision did not lead to any publications. In order to present a single and coherent thesis, none of the research carried out under the supervision of Prof. Thomas Pohl is included.

The Graduate School of Natural Sciences (GSNS) allows the thesis to be formatted in either of two ways. The first way is as a single cohesive monograph, and the second way is as a collection of manuscripts and papers that relate to the PhD topic. The thesis will be formatted according to the latter, and will therefore consist of two parts. The first part is a review that derives, highlights, and discusses the central results of the research papers. The second part includes all peer-reviewed and published research papers with a declaration of the author contribution to each of these. The thesis uses the collective pronoun "we" for clarity, which also signifies that most of this work was done in collaboration with colleagues.

Units

Unless stated otherwise, the thesis as well as the research papers use atomic units (a.u.) which satisfy $\hbar = m_e = e = 4\pi\epsilon_0 = 1$, where $\hbar$ is the reduced Planck's constant, m_e is the electron mass, e is the electron charge, and ϵ_0 is the vacuum permittivity. This set of units is often used in the research field, and as is tradition within the research field, timescales can be given in femto- or attoseconds where 1 a.u. ≈ 24.19 as.

Acknowledgments

I would like to dedicate this thesis to my parents. Your unfailing love and constant support have been the greatest gift and my greatest advantage in life. I love you both dearly. Thank you.

Throughout my PhD journey, I have been fortunate to be surrounded by people who have brought me joy, offered support, and shared meaningful experiences. First and foremost, I would like to thank my supervisor, Lars Bojer Madsen. Your ability to act with kindness, empathy, and humor—both professionally and personally—is a great inspiration to me. You rekindled my love for physics, made me enjoy doing research, and helped me believe in myself. Having you as my supervisor was the single best thing that happened during my PhD. Thank you.

I have also had the pleasure of being part of Lars' research group. I am grateful to all the members over the past few years for their camaraderie and insightful discussions: Asbjørn Thornøe Andersen, Asger Weeth, Pieter Hessel Harkema, Simon Vendelbo Bylling Jensen, and Mads Brøndum Carlsen. Extended thanks to Thomas Hansen and Rasmus Vesterager Gothelf for fruitful collaborations. My thanks also go to Thomas Pohl for providing me with the opportunity to pursue a PhD, and to the wonderful people at CCQ for creating a friendly and stimulating scientific atmosphere. I wish to give special thanks to Jan Kumlin for his guidance and stimulating conversations, and to Victor Rueskov Christiansen for good times and discussions in our office. I am also grateful to Niels Carl W. Hansen and Brigitte Henderson for their help and support during my PhD, and to Thomas Hansen, Simon Vendelbo Bylling Jensen, Rasmus Vesterager Gothelf, and Anton Lauenborg Andersen for proofreading the thesis and providing valuable feedback.

Studying physics alongside Daniel Holleufer, Magnus Linnet Madsen, and Martin Mikkelsen has been a real pleasure—I believe we made each other better physicists. Thanks to everyone in K3 for making it feel like home, and to the cycling community in Aarhus, cykelgutterne, and Sport X for great memories. A special thanks to Viktor Eriksen for your friendship—both on and off the bike—your honesty, support, and mindset ("Det kan vi godt, det bliver pisse fedt!") have meant a great deal to me. Additionally, I would like to express my gratitude to "gutterne," my friends through many years. Even though our lives have evolved in different ways, our persistent friendship is very dear to me. In particular, I want to thank Signe and Krag (and Birk!) for your deep and honest friendship. Thank you for always taking the time to listen to me and for your sincere and caring input. Your friendship and support have been invaluable to me. Finally, to my girlfriend, Ida—you are my ray of sunshine and constant reminder of the beauty in life.

Aarhus, August 2025
Christian Saugbjerg Lange

List of publications

The thesis is composed of the following papers, which will be referenced in the text by their respective Roman numerals and are also cited as references (Refs.) [1–5] in captions or in conjunction with others.

I **C.S. Lange**, T. Hansen and L. B. Madsen, *Noninteger high-order harmonic generation from extended correlated systems*, Phys. Rev. A **109**, 063103 (2024) [1]

II **C.S. Lange**, T. Hansen and L. B. Madsen, *Electron-correlation-induced nonclassicality of light from high-order harmonic generation*, Phys. Rev. A **109**, 033110 (2024) [2]

III **C.S. Lange**, T. Hansen and L. B. Madsen, *Excitonic Enhancement of Squeezed Light in Quantum-Optical High-Harmonic Generation from a Mott Insulator*, Phys. Rev. Lett. **135**, 043603 (2025) [3]

IV **C.S. Lange** and L. B. Madsen, *Hierarchy of approximations for describing quantum light from high-harmonic generation: A Fermi-Hubbard-model study*, Phys. Rev. A **111**, 013113 (2025) [4]

V R. V. Gothelf, **C.S. Lange**, and L. B. Madsen, *High-order harmonic generation in a crystal driven by quantum light*, Phys. Rev. A **111**, 063105 (2025) [5]

All publications are reproduced with permission from the respective publishers.

Abbreviations

In the thesis and research papers, the following abbreviations are used both in the main text and in captions.

App.	Appendix
APP	Approximative Positive P
ATI	Above-Threshold Ionization
a.u.	Atomic Units
BSV	Bright Squeezed Vacuum
CB	Conduction Band
Ch.	Chapter
Chs.	Chapters
Eq.	Equation
Eqs.	Equations
Fig.	Figure
Figs.	Figures
GS	Glauber-Sudarshan
HHG	High-order Harmonic Generation
IR	Infrared
LG	Length Gauge
MSA	Markov-State Approximation
QED	Quantum Electrodynamics
Ref.	Reference
Refs.	References
SBE	Semiconductor Bloch Equations
Sec.	Section
TDSE	Time-Dependent Schrödinger Equation
UV	Ultraviolet
VB	Valence Band
VG	Velocity Gauge
XUV	Extreme Ultraviolet

Contents

Review

CHAPTER 1

Introduction

The most prominent and distinguished role of science is to understand and clarify the fundamentals of the physical world. This investigation covers a vast range of length scales: from the size of the entire universe down to the fundamental building blocks of matter, the structure and dynamics of atoms, and biological processes on the microscopic scale. Similarly, natural processes unfold across vastly different timescales, from the age of the universe ($\sim 4 \cdot 10^{17}$s) all the way down to the shortest intervals observed in nature: the attosecond and even shorter. The attosecond (10^{-18}s) is an incredibly short unit of time. To put it in perspective, there are more attoseconds in one second than there are seconds in the age of the universe. Nonetheless, it is on the attosecond timescale that electrons move. The electron, being one of the fundamental particles of matter, is vital in many aspects of our world. On the fundamental level, electrons are central in all of chemistry, as they bind atoms together and appear as the main ingredient in chemical reactions. This also extends to the biochemical processes in the human body and all other organic material. Electrons are also central to the emission of light across a broad range of frequencies. From a more technological perspective, electrons are also the main constituent in electronics, central to modern life and infrastructure. Scientists are interested in studying such systems - both to advance fundamental science and to consider potential technological applications - and it is thus central to examine and control the electron dynamics, as the electron is the vital ingredient across all of these platforms. In order to study the electron, one must be able to

interact with it. Fortunately, as the electron is much lighter than the nucleus to which it is bound, it can be steered using electric and magnetic fields. To study the electron on its natural timescale—the attosecond—one needs probe fields capable of interacting with it on this scale, which is far shorter than the nanosecond timescales accessible with modern electronics. Fortunately, many years of both theoretical and experimental development have made it possible to generate short and rapidly oscillating electromagnetic fields, ultrashort pulses of light, by illuminating electrons with intense laser fields. Such ultrashort pulses of light are short enough to be able to interrogate electrons on their natural timescale, giving access to a whole new time domain in nature. Interestingly, this pulse-generating strong-field process might generate pulses with quantum properties. An ultrashort pulse with nonclassical properties will, due to the fact that more observables can be considered, have improved spectroscopic and technological applications while at the same time providing new insights about the fundamental electron dynamics in the generating medium.

1.1 A brief history of electron-light interactions

For more than a century, light has been used to interrogate matter. The nature of light itself, however, has been disputed. In 1801, Thomas Young presented his double-slit experiment showing the wave-like nature of light. These results could not be explained by the corpuscular theory of light, presented by Sir Isaac Newton, which claimed that light consisted of smaller particles. A century later, however, Max Planck, in an attempt to explain blackbody radiation, suggested that the light-matter interactions must involve not continuous but discrete chunks of energy, which favors a more particle-like nature of light [6]. This idea of quantized light was further used by Einstein to explain the photoelectric effect, for which he was awarded the Nobel Prize in 1921 [7], and the term *photon*, coined by Gilbert Lewis, later arose to describe this particle-like nature of light [8]. Niels Bohr, inspired by the quantized nature of light-matter interactions, presented his model of the atom in 1913 and was able to predict spectral lines from atoms [9]. The photoelectric effect was central in the foundation of much of modern physics as it introduced a quantized nature of light and matter, giving birth to the paradigm of quantum mechanics, later developed with Heisenberg, Schrödinger, and Dirac as central figures. With the photoelectric effect, scientists could now study material properties, such as the binding energies, by measuring the energy of the emitted photoelectrons. Kai Siegbahn later developed these techniques of photoelectron spectroscopy to study the nature of the inner electrons in atoms for which he was awarded the Nobel prize in 1981 [10].

In 1960, the study of matter using light took a big leap forward with the invention of the laser [11]. With this rapidly growing technology, the optical properties of both atoms, solids, and molecules could be studied in much greater

detail. However, a single laser is in itself not always completely adequate to study the dynamics of a quantum system, as the interrogation of electrons sometimes needs to occur at specific times in order to study how the electron evolves. In other words, a time-dependent laser field — a laser pulse — is required to pump the system and initiate its dynamics, followed by a second pulse at a later time to probe the system and image how the electrons have evolved. By varying the delay between the two pulses, one can then study the dynamics of the electrons. However, in order to be able to image the electron, the laser pulse should be of adequate duration and only briefly interact with the electrons. If the duration is too long, the electrons will have too much time to move, such that the electrons will be in a different position at the end of the pulse than they were at the beginning. This will make the captured image blurred, just in the same way that a too-long exposure time for a modern camera makes the photo blurred if one tries to capture a moving object. However, if the pulse is adequately short, one can capture the system dynamics by combining multiples of such images.

With the development of Q-switching [12] and mode locking [13], a 6 femtosecond laser pulse was achieved in 1987 [14]. This would allow phenomena in biological systems, such as photosynthesis, to be studied at the nanoscale and on their natural timescales, as the motion of molecular nuclei could now be resolved [15]. This gave rise to the field of femtochemistry for which Ahmed Zewail was awarded the Nobel Prize in Chemistry in 1999. However, even though the motion of nuclei could now be resolved, chemical reactions are governed by electron dynamics, and a new breakthrough in laser technology was needed in order to go into the required attosecond regime. Curiously, it would actually be an ultrafast electron mechanism that would enable the generation of attosecond light pulses. In this way, ultrafast dynamics would be a key ingredient in the generation of light that would enable the study of ultrafast dynamics. This ultrafast electron dynamics was probed by driving atoms with an intense laser field, leading to nonlinear electron-light dynamics and the different processes of strong-field physics.

1.1.1 Strong-field physics

Alongside the development of short laser pulses, more intense laser pulses were also sought after. Significant contributions to generate intense laser pulses, achieved by *chirped pulse amplification*, were made by Donna Strickland and Gérard Mourou, for which they were awarded the Nobel Prize in Physics in 2018 [16].

While not immediately understood by researchers at the time, it was clear that by illuminating atoms with these novel, intense short pulses of light, new nonlinear phenomena were accessed. Similar to the photoelectric effect, where electrons were ionized by the absorption of a single photon, the strong laser

fields also ionized the electrons. This strong-field ionization of electrons has been understood in two different pictures. For driving fields with higher frequencies, this ionization of electrons has been understood from a quantum optical perspective, with the absorption of one or many photons exciting the electron above the ionization threshold. In the low-frequency regime, the perspective has been semiclassical, where the electric driving field has strongly perturbed the atomic binding potential, allowing for tunneling ionization [17–20]. Further, in 1979, experiments for the first time showed how photoelectrons ionized by an intense laser field had a kinetic energy way larger than their ionization potential [21]. This was the first observation of above-threshold ionization (ATI), a central phenomenon in strong-field physics, that also later led to strong-field double ionization [22]. It was clear that with the advent of novel intense laser pulses, electrons could undergo new nonlinear processes, which allowed for new spectroscopic methods and ways of steering electrons. Following these findings, it was natural to ask if these nonlinear processes involving electrons could be utilized to generate new types of light inheriting characteristics from the ultrafast electron dynamics.

The first experiment regarding light generation from strong-field processes was conducted in 1987. Here, an intense ultraviolet (UV) laser pulse drove nonlinear dynamics in various rare gases, which in turn generated light at much higher frequencies [23]. Curiously, the generated light only had frequency components which was an odd integer multiple of the laser frequency. In the following year, a similar experiment was performed using an intense infrared (IR) driving field which generated light consisting of harmonics extending all the way up to the 33'rd harmonic with a frequency component in the extreme ultraviolet (XUV) spectral regime [24]. With these findings, the concept of high-order harmonic generation (HHG) was born, which has been subject to both experimental and theoretical investigations for decades. It is the process of HHG that was later utilized to generate the long-sought-after attosecond pulses of light. The experimental demonstration of these attosecond light pulses was the motivation for the 2023 Nobel Prize in Physics awarded to Pierre Agostini, Ferenc Krausz, and Anne L'Hullier.

The spectra obtained from HHG have been subject to theoretical considerations with explanations for their characteristics, such as the plateau and harmonic cutoff. To gain intuition, the HHG process is often described by the semiclassical three-step model [25] shown in Figure (Fig.) 1.1, which also shows other strong-field phenomena. The steps of this semiclassical three-step model will now be explained.

Ionization: When an intense laser pulse is applied, there is a significant probability that an electron will ionize and escape the atom. This probability is larger for larger field amplitudes and is thus most likely at the extrema of the oscillating field. Depending on the frequency of the laser,

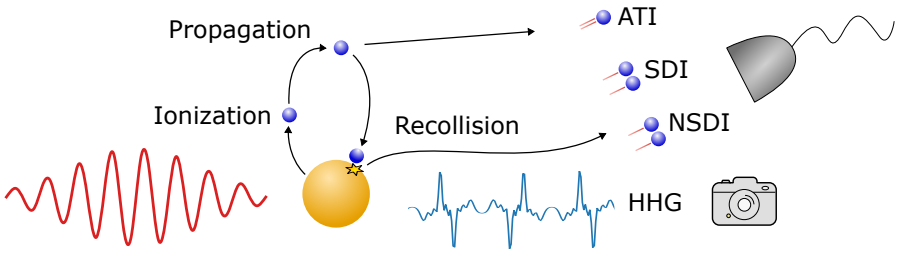

Figure 1.1: Illustration of the semiclassical three-step model for atoms. The three steps involved are ionization, propagation, and recollision, or recombination for HHG. Other strong-field processes are also included: above-threshold ionization (ATI), sequential double ionization (SDI), and nonsequential double ionization (NSDI). Figure inspired from Ref. [26].

this ionization process can be understood as single-photon absorption, multi-photon absorption, or tunneling ionization [17–20]. If the electrons completely escape the atomic potential, they can absorb more photons and be detected as ATI electrons. More electrons in the parent ion can also be ionized. This is known as sequential double ionization.

Propagation: After the electron is ionized, it is in the continuum where it is dressed by the driving field from which it will gain kinetic energy. In a quantum mechanical description, this is known as a Volkov state [27]. As the driving field is intense, it will dominate the electron dynamics to such an extent that the Coulomb potential from the parent ion can be neglected in the strong-field approximation (SFA) [17, 18, 20].

Recollision: If the ionization step occurs at certain times during the laser pulse cycle, the electron will return to the vicinity of its ion and recollide. Several processes can take place in this recollision step. One of the processes is the inelastic scattering with the ion, resulting in the ionization of an additional electron, a process known as nonsequential double ionization [28]. The electron can also elastically rescatter off of its parent ion, gaining even more energy, and be emitted as high-order ATI. Finally, if the electron recombines with its parent ion, the excess energy will be emitted as a burst of light in HHG.

Using the semiclassical three-step model, various phenomena and observations in strong-field physics can be explained. The model gives a clear physical interpretation of the results and can explain, e.g., the spectral structure from HHG in atoms. Building on the intuition of the semiclassical three-step model, a quantum mechanical treatment was presented using the time-dependent Schrödinger equation (TDSE) with the electric dipole approximation and the

single-active electron approximation [29]. From this work, it became apparent that electrons could become ionized at different points in time during the laser cycle. Some electrons will be ionized during the peak of the electric field with a high probability and gain a lot of kinetic energy, resulting in a long trajectory in space before the recollision step. During these long trajectories, the electron will be subject to more quantum diffusion, making recombination less likely. Conversely, with a smaller probability, electrons will be ionized at times with a weaker field and gain less kinetic energy. They will hence have a short trajectory in space with less quantum diffusion, making the recombination more likely to occur. By utilizing the knowledge of these electron trajectories, the experimental parameters such as laser polarization, laser intensity, wavelength, focus area, and atomic gas pressure can be tuned to balance the contributions of the different trajectories such that the harmonic generation from each of these can be phase matched to generate attosecond pulses of light. Currently, at the time of writing, the shortest pulse of light ever created from HHG is 43 as [30], allowing researchers to enter the natural time domain of electrons.

1.1.2 High-order harmonic generation in condensed matter

For many years, atomic gases were the main medium for HHG studies. High-harmonic generation from solid state targets was also investigated; however, only in a reflection geometry [31–34] or only perturbative harmonics were found [35]. In 2011, the interest in HHG from condensed matter systems was rekindled, as nonperturbative harmonics were observed from a bulk crystal of ZnO [36]. It was found that the harmonic cutoff scales linearly with the driving field intensity in solids, different from the quadratic scaling in atomic spectra. Consequently, the underlying physical mechanisms generating HHG must be qualitatively different in solids from those in atoms, and new physical models and theoretical frameworks would have to be developed. In addition to the fundamental interest in solid state HHG, potential applications to create, e.g., ultrafast electronics, are conceived, due to the ultrafast manipulation of electrons in compact condensed matter targets. However, before such applications can be achieved, a deeper understanding of how to coherently drive and control electrons in various condensed matter targets is crucial. Already, many different condensed matter targets have been utilized as HHG medium in experiments. This ranges from semiconductors [36], insulators [37], metals [38], Weyl semimetals [39], nanostructures and monolayers [40, 41], doped semiconductors [42], liquids [43], amorphous solids [44], Dirac semimetals [45], rare noble-gas solids [46], topological insulators [47], liquid crystals [48], and particular relevant for the thesis and research papers, also Mott insulators [49, 50]. When compared to atomic gases, HHG from such condensed matter systems reveals that the

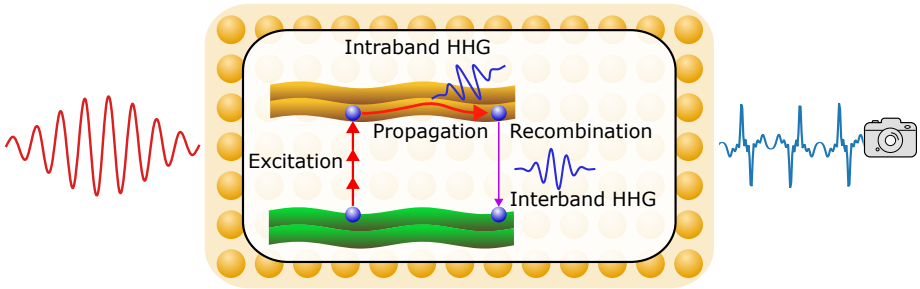

Figure 1.2: Illustration of the three-step model in condensed matter systems. The steps involved in the model are excitation, propagation, and recombination as outlined in the main text. Figure inspired by Ref. [26].

underlying generating mechanism is more complex. However, as for atomic gases, HHG from condensed matter systems can also be understood from a semiclassical three-step model. This model is formulated in the picture of semiconductor Bloch equations (SBE) in momentum space, where electrons propagate along or in between energy bands of the material. This model is shown in Fig. 1.2 and outlined in detail below.

Excitation: An electron in the valence band (VB) can absorb photons and be excited into the conduction band (CB). This excitation is most likely to occur at the point in momentum space where the energy difference between the two bands is minimal, i.e., at the minimal band gap. The excited electron in the CB leaves a hole in the VB.

Propagation: Once excited to the CB, the electron propagates within the CB with a time-dependent crystal momentum which follows the electromagnetic vector potential. The same holds for the hole in the VB. During this propagation step, current is generated, called intraband current, which will result in the emission of harmonics, called intraband harmonics.

Recombination: During the propagation step, there is a considerable likelihood that an electron-hole pair will recombine in real space. Note that this does not need to be between the same electron-hole pair generated in the excitation step. This recombination generates a current called the interband current as it occurs from electron dynamics across different bands. Consequently, the HHG emitted from interband current has an energy larger than the minimum band gap energy and is referred to as interband harmonics.

Different from the atomic three-step model, the solid-state three-step model contains two steps that emit harmonic radiation. The last step, the recombination

step, where an electron-hole pair recombines, generating interband current, is similar to the recombination of an electron with its parent ion in the atomic three-step model. Additionally, in the condensed matter three-step model, the intraband current in the propagation step will also emit harmonic radiation. This is due to the generally nonquadratic dispersion relation in the system, a property inherent to condensed matter systems and not found in atoms. The two contributions, intra- and interband currents, are inherently coupled. Generally, in a HHG spectrum, the signal at frequencies below the minimum band gap is typically dominated by contributions from the intraband mechanism, while the interband mechanism is dominant at energies above the minimum band gap energy [51, 52].

The three-step model for condensed matter systems assumes that all electrons can be treated independently without any other contributions to their dynamics. However, this simplified picture is not always adequate. In recent years, several works have considered more specialized or complicated mechanisms that are not captured in the simple three-step model. For instance, theoretical works have considered the effect of topology [53, 54], finite-size effects [55], doping [56], lattice imperfections [57], light propagation [58], phonons [59], spin-orbit coupling [60, 61], beyond-mean-field interactions [62], and strongly correlated interactions [63]. Recently, works have also considered combinations of these, e.g., strongly correlated interactions with finite-size effects [64], doping [65], or lattice imperfections [66].

Further, in recent years, a new perspective on HHG, both in atomic gases and condensed matter systems, has been of great interest, namely, the study of the quantum optical properties of HHG. This avenue of strong-field physics, called strong-field quantum optics, will be explored in further detail below in Section (Sec) 1.2.

1.1.3 Quantum optics

Building on Planck's idea of quantized light, the discovery of the photoelectric effect, and the subsequent development of quantum mechanics, light came to be understood as a fundamentally quantum phenomenon. The study of quantum optics is a merge between classical optics and quantum mechanics, where light is described in a quantized manner. The field of quantum optics is in itself too broad to be covered in all detail here, but central developments and contributions will be highlighted.

The first contributions to a quantized light-matter description were given by Paul Dirac. Using field theory, he developed quantum electrodynamics (QED), which, among other achievements, quantized the electromagnetic field as particles, *photons*, successfully describing the quantized nature of light-matter interactions [67–69]. In the 1950s, Robert Hanbury Brown and Richard Twiss

studied the coherence of light from interstellar objects. Their results showed how photons from thermal sources were bunched [70–72]. These considerations also led to the next major theoretical contribution, which came in 1963 with the formalized description of optical coherence in quantum optics published in a seminal paper by Roy Glauber [73]. In particular, the correlation functions as presented by Glauber laid the theoretical foundations for the possibility of nonclassical states of light, which is a central concept in many modern studies of quantum optics. The study of optical coherence was also developed further by Emil Wolf, George Sudarshan, Leonard Mandel, John Klauder, and many others [74]. Glauber received the Nobel Prize in Physics in 2005 for his contributions.

In the following decades, the field of quantum optics flourished with both theoretical and experimental discoveries. On the theory side, Dan Walls and Howard Carmichael studied open quantum systems and showed how the interaction between a quantum system with its environment could lead to antibunched light, a clear nonclassical feature [75, 76]. Also, a measurement-based trajectory theory to describe open quantum systems was developed by Klaus Mølmer, Jean Dalibard, and Yvan Castin, now known as Monte Carlo wavefunctions [77, 78], giving insights into the continuous nature of decay rates with the quantized nature of atoms. Among the experimental contributions is the methods developed by Serge Haroche and David Wineland to study and manipulate individual photons and their interactions with matter by trapping single atoms in cavities, today known as cavity-QED [79–84]. Both Haroche and Wineland received the Nobel Prize in 2012 for their work. Experimental works also tested the quantum nature of light as predicted by theory. In 1972, John Clauser used a clever scheme of optical equipment to demonstrate how photons violated Bell's inequalities, showing that photons could be entangled beyond classical correlations [85, 86], confirming the predictions of quantum theory. This experiment was later refined and improved by Alain Aspect in 1982, confirming the results of Clauser with greater statistical confidence. Crucially, Aspect's experiment used a setup that closed some loopholes with regard to locality that remained after Clauser's experiment [87]. Later, in 1997, Anton Zeilinger used quantum optics to entangle photons in order to teleport a quantum state [88]. For their experiments with entangled photons, Clauser, Aspect, and Zeilinger were awarded the Nobel Prize in physics in 2022. Another experimental discovery worth highlighting is the Hong-Ou-Mandel effect. Here, two identical photons are sent into a symmetric beam splitter, and if the temporal overlap of the photons is tuned in a specific way, the photons will exit the beam splitter in the same output mode, meaning they will always be observed together and never separately [89]. In addition to being a measurement setup to test the indistinguishability of photons, the Hong-Ou-Mandel effect also has applications as a logic gate in linear quantum computing [90]. In fact, much of research in quantum optics have focused on both testing and in particular utilizing the quantum nature of light for purposes

in, e.g., quantum metrology [91, 92], spectroscopy [93, 94], quantum information processing [95], quantum information science [96, 97], and photonic quantum technology [98]. All of these applications rely not only on the deeper understanding of quantized light but also on reliable ways of generating light with specific nonclassical properties. In recent years, a new way of generating nonclassical light has gained interest, where the intense driving lasers and induced nonlinear phenomena of strong-field physics are merged with the theoretical framework of quantum optics in the new emerging field of strong-field quantum optics.

1.2 Strong-field quantum optics

Strong-field quantum optics is the intersection of strong-field physics and quantum optics, aiming to describe strong-field phenomena within the framework of quantum optical theory. For decades, strong-field physics has been treated semiclassically, that is, with a quantum description of the electronic system but with a classical description of both the applied and emitted electromagnetic fields. This description has been highly successful in many of its predictions of experimental results. Until recent years, a quantum optical description of strong-field phenomena was never fully pursued, because the strong laser fields involved have negligible quantum fluctuations, which justifies the semiclassical approach in many regards. In some way, strong-field physics and quantum optics are an unlikely match: In strong-field physics, one typically considers both a macroscopic number of photons as well as many electronic states, including the continuum of free electron states. In contrast, only a few photons and a few electronic states are typically involved in quantum optics. Merging quantum optics with strong-field physics thus requires one to handle the unusually large number of photons in the quantum optical description, and hence new techniques are needed.

In the preceding sections, a broad overview of the history of the relevant research fields was given with emphasis on both experimental and theoretical breakthroughs. In this section, we provide an overview of the emerging research field of strong-field quantum optics and discuss central works in greater detail to set the scene for the present state of the research field.

It is not only the strong laser fields that are subject to quantum optical considerations. Another field with ultrafast perspectives is the study of free electrons, where early works considered free electrons interacting with a quantized monochromatic electromagnetic field [99–102]. More recent studies has found, for instance, that free electrons interacting with a quantized electromagnetic field can transfer optical coherence [103], probe the photon statistics of the driving field [104, 105], manipulate the driving field to generate quantum light [106–108], be used as a quantum sensor for light-matter systems [109] and photonic state tomography [110], and have applications in quantum information science [111].

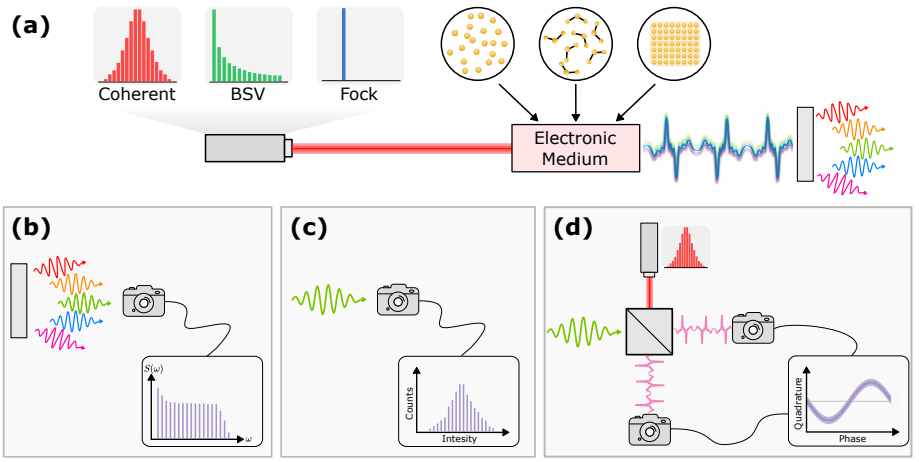

Figure 1.3: Quantum optical HHG. In (a), an overview of the HHG process is given. The applied strong field with a given photon distribution is driving the HHG process in the electronic medium (gas of atoms, molecules, or a condensed matter system), with quantum-optical harmonic radiation being emitted from the generating process. (b)-(d) illustrates the different observables of interest: (b) the spectrum, (c) photon counting to calculate photon statistics, and (d) homodyne detection to calculate the degree of squeezing.

In strong-field physics, works have, for instance, considered driving strong-field processes with quantum light, that is, light that is not a Glauber coherent state. These processes include, e.g., strong-field ionization with quantum light of atoms [112] as well as high-order ATI [113], double ionization [114], and free electrons [115]. In these works, it is found that both the ionization probability and the momentum distribution of the free electrons strongly depend on the photon statistics of the driving field, showing how the quantum nature of the driving field is principal in the light-induced electron dynamics. In this direction, experiments have already studied photoelectron emission with nonclassical light from needle tips [116, 117] that confirm the effect of the photon statistics of the driving field.

The strong-field process that has been subjected to quantum optical considerations the most, however, is HHG. Different from ATI, HHG also involves an emitted field, which can be considered quantum optically. This opens a whole new avenue of research questions: Does the light generated from HHG have nonclassical features? If so, under what conditions is the light quantum? Can both light fields and electronic systems be engineered to generate light with specific properties, with, e.g., technological applications? Can the quantum nature of HHG be used as a spectroscopic measure to study the generating

medium and yield information not present in the semiclassical spectrum? Due to the great interest both in fundamental science and in the prospect of potential technological applications, HHG has in recent years been subject to various quantum optical considerations and questions in a wide range of electronic systems. Overall, there are two main avenues within quantum optical HHG. The first one is to use a classical (coherent) driving field to drive the HHG process. Due to different processes and mechanisms in the generating medium, the emitted light can potentially be nonclassical. A more detailed overview of this avenue is given in section (Sec.) 1.2.1 below. The other avenue within quantum optical HHG is to use a nonclassical driving field with the expectation that the emitted harmonics will inherit its nonclassical nature. An overview of this avenue of quantum optical HHG is given in Sec. 1.2.2 below. The common goal of both avenues of quantum HHG is to create ultrashort pulses of light with quantum properties at frequencies not previously considered in quantum optics. In addition to testing quantum optics at new frequencies, these studies also enable applications like spectroscopy by exploiting the quantum degrees of freedom previously ignored in semiclassical approaches. Further, by utilizing the quantum nature of these ultrashort pulses of light, technological and experimental applications in quantum information science might be considered [118]. Figure 1.3 provides an overview of the quantum optical HHG. In Fig. 1.3(a), a schematic overview of the generating process is given. The applied strong field in a given state, e.g., a coherent, BSV, or Fock state, is driving the HHG dynamics in an electronic medium (atoms, molecules, or condensed matter system), and harmonic radiation is emitted. In Fig. 1.3(b)-(c), different observables are measured. Measurement of the spectrum is illustrated in Fig. 1.3(b), photon counting used to calculate photon statistics is illustrated in Fig. 1.3(c), and the degree of squeezing via homodyne detection is illustrated in Fig. 1.3(d).

1.2.1 High-order harmonic generation with a classical driver

The inclusion of quantum optics in the description of HHG goes back to the early 1990s, where pioneering work included a quantized description of the emitted field while keeping the driving field classical [119–123]. In these works, both the Heisenberg equations of motion and the Schrödinger equation were used. Of particular interest in these works were the generation of incoherent and coherent emission from an atomic ensemble and their relation to experiments. Here, it was found that only the coherent part of the emitted radiation (proportional to the number of independent emitters squared) was measured in experiments with HHG from atomic gases. In more recent work, a quantum formalism describing HHG as spontaneous emission from time-dependent dressed states

with a classical dressing field was developed [124–126]. Later experimental and theoretical works also used a quantized description of the driving field mode [127, 128] with signatures of the nonclassical light due to the interaction with the generating medium [129–131]. Though there were indications of nonclassical signatures in the emitted HHG, the quantum optical nature of HHG had not been treated in full detail by including a quantized description of both the driving and emitted fields. Further, observables to probe the nonclassical nature of HHG, such as squeezing or photon statistics, were not considered.

This was until the pioneering work of Ref. [132], which considered both the driving and emitted fields quantum mechanically and computed both the degree of squeezing and photon statistics of the entire emitted spectrum. Here, it was found that an atomic ensemble of helium atoms generates squeezed light as well as nontrivial photon statistics for certain harmonics. Following this work, several works appeared which consider various electronic systems, develop theoretical approximations and methods, and investigate observables not accessible from a semiclassical perspective. A central finding in this field is the generation of coherent state superposition of light, a so-called Schrödinger cat state, not generated via the electronic response itself, but by performing subsequent condition measurements. This optical cat state showed to have higher photon numbers than previously achieved by other schemes [133, 134] with experimental observation already in 2021 [135], a pioneering work and central result for quantum optical HHG. The theoretical considerations relied on a negligible depletion of the ground state population, which allows for an exact analytical treatment that can be utilized to study entanglement [136] in the light-matter system or for quantum state engineering purposes by performing condition measurements on the emitted harmonics [137]. Going beyond this approximation and including nonnegligible ground state depletion, a perturbative treatment of the light-matter coupling has yielded analytical solutions of the quantum state of the field for, e.g., atomic gases [138], atoms initially in the first excited state [139], and molecules [140]. Notably, in Ref. [138], a novel approach is presented by considering transitions between two laser-dressed states induced by one of the generated harmonics. It is shown that this process entangles the light-matter system, which can generate quantum states of light in the emitted harmonics without any subsequent condition measurements. The only requirement of the electronic medium is its ability to generate a given harmonic with sufficient intensity to induce such a transition between laser-dressed states. Other works using atomic gases includes the use of HHG to entangle XUV photons [141], considerations on the role of long and short electron trajectories [142], parametric models [143] or how photon statistics and correlations evolve in time during the interaction with the driving field [144]. Further, it has been shown that by preparing an ensemble of atoms in a highly correlated state, a so-called Dicke state, the emitted radiation from HHG inherits this quantum

nature as shown by the nonclassical features in the Wigner functions [145].

Solids have been considered as the generating medium for quantum optical HHG as well. This includes intraband models [2, 146] and a two-band model [147] for uncorrelated electrons. Interestingly, the results in Refs. [2] and [146] disagree on the nature of the emitted radiation from a single band. In Ref. [2], it is found analytically that intraband harmonics are classical coherent states independent of the nature of the band structure, while in Ref. [146] it is found, under certain approximations, that the quantum state of the fundamental mode is slightly modified. Other condensed matter systems have been considered, including strongly-correlated materials such as Mott-insulators [2]. Here it is found that, due to the strong electron-electron interactions that correlate the electrons, the emitted harmonics show nonclassical features such as squeezing, especially above the so-called Mott gap. Recent works have also included a quasiparticle, a Mott-exciton, which has been shown to be dominant in the system dynamics as both the spectrum and squeezing show clear peaks in their signal exactly at the exciton energy [3]. These results will be elaborated on later in the thesis. On the experimental side, experiments have already considered the photon statistics of the emitted HHG radiation from band gap materials. However, the nature of the emitted harmonics remains inconclusive as it is found in Ref. [148] that the harmonics are superbunched, while it in Ref. [149] is found that the harmonics (from coherent driving only) yield close to Poissonian statistics. Both experiments considered ZnO, which is a typical band gap material used in solid state HHG. It should be noted that the laser intensity used in the experiments differs by an order of magnitude, and as indicated in Ref. [148], the photon statistics approaches that of a coherent field for increasing intensity, which might be the explanation for the discrepancy.

In parallel to the works that investigate the nonclassical response from various electronic systems, other works have attempted to clarify and improve the various approximations employed. The theoretical description of quantum optical HHG requires the handling of the quantum degrees of freedom of *both* the electrons and photons, and it is thus more complicated than semiclassical descriptions. So far, in fact, the equations that describe the quantum nature of the emitted HHG have not been solved in an exact manner, and all works have consequently relied on approximations. The approximations employed include, e.g., neglecting correlations of dipole moments, sometimes referred to as *negligible ground state depletion* [133–137], which results in the harmonics being coherent states. Other kinds of approximations include decoupling of harmonic modes [3, 4, 132] which neglects correlations between the harmonics, or inclusion of only two quantum optical states [138–140, 147] which renders a perturbative solution. To gain more insights and intuition into the mechanism that generates the nonclassical features in the emitted HHG, works have considered a Markov-type approximation, which assumes that the cumulative influence of past interactions

can be expressed by an instantaneous operator at a given point in time [139, 150]. This approximation was first introduced in Ref. [150], where a closed form expression for the photonic state was found which was later coined the Markov-state approximation (MSA) in Ref. [4]. Using the MSA, it was found that the quantum nature of HHG arises from nonvanishing time correlations (or quantum fluctuations) of the time-dependent dipole (or current for condensed matter systems). This is specified further in Ch. 4. The validity of MSA was later verified in Ref. [4] for a strongly correlated material, and not only does the MSA yield analytical insights due to its closed-form expression, but it also drastically eases the required numerical efforts compared to more exact calculations. These findings will be elaborated on later in the thesis. Other theoretical efforts have considered different approaches by using a trajectory-based simulation [151], and recently the Heisenberg equations of motion have been revisited, now with quantum optical perspectives in HHG, considering also the photon statistics of the emitted radiation [152]. Some of the findings presented above will be elaborated on later in the thesis and are the contributions of the author of the thesis.

1.2.2 High-order harmonic generation with a nonclassical driver

The other approach to generate nonclassical harmonics is to use a nonclassical driving field. By driving HHG with light sources with a quantum state different from a coherent state, new electron dynamics might be probed and potentially generate harmonic radiation with a different quantum nature. The motivation to consider other types of driving fields comes from decades of improvements in laser technology, in particular the development of beams of so-called bright squeezed vacuum (BSV) light [153–159]. Recently, such beams have proved to be sufficiently intense to drive nonlinear dynamics such as HHG [149, 160] and multiphoton electron emission [117], which opens a whole new perspective on strong-field physics. BSV is a special type of light: It has a vanishing mean electric field, yet it has squeezed electric field variance below that of vacuum on and consists of a macroscopic number of photons in a superposition of even-number Fock states [159–161]. BSV is generated by high-gain parametric down-conversion, where a strong driving laser is directed into a nonlinear crystal, which produces entangled photon pairs. This is thought of as an amplification of vacuum fluctuations [161].

Thus far, a few experiments have used BSV in HHG. In Ref. [160], HHG from a crystal driven by BSV was observed. Here, harmonics both above and below the minimal band-gap energy were recorded. In particular, it was found, by studying the power scaling of the harmonics, that BSV could be used at higher intensities than coherent light before the optical damage of the crystal

was reached. In Ref. [149], HHG from ZnO was driven by a strong coherent field perturbed by a weaker BSV beam with twice the frequency. It was seen that when the BSV beam was turned off, only odd harmonics with classical Poissonian photon statistics were observed. In contrast, with the additional perturbation from the BSV, sidebands at even harmonics appeared with photon statistics similar to that of the BSV beam. Interestingly, only a perturbation of BSV was required to generate nonclassical light even though the electron dynamics was dominated by the strong coherent field. In Ref. [161], BSV is also used as a perturbation to a strong coherent driving field, here from an atomic ensemble. Different from Ref. [149], the frequency of the BSV beam is at half the frequency of the driving field in Ref. [161]. Due to this two-color setup, four different half-cycles appear, resulting in four 'types' of harmonics: even, odd, and half-integer harmonics. Interestingly, the different harmonic types show different photon statistics. The odd harmonics yielded Poissonian photon statistics, while the half-integer and even harmonics show superbunching similar to the BSV field. Further, as the electron dynamics is mapped onto the quantum properties of the emitted HHG radiation, the two-color setup can act as a sub-cycle interferometer [162], showing ultrafast correlations of the electrons and enabling access to phase information. By this interferometric setup, a scheme similar to homodyne detection is used, enabling quantum state tomography of the emitted XUV light. In another recent experiment, a cat state generated via HHG was used to act as the nonclassical driver in second harmonic generation [163].

Theoretically, it is challenging to model a nonclassical driving field. In order to employ knowledge and methods from semiclassical studies, the nonclassical driving fields have been expressed in terms of coherent driving fields of different phase and amplitude, weighted by an adequate probability distribution depending on the nature of the driving field. In the theoretical works, both coherent, Fock, thermal, and BSV fields are considered as driving fields. Due to the fluctuations of the driving field, it was found that an effective photon-statistics force modifies the electron trajectories in addition to the coherent dynamics [164]. In Ref. [165], HHG spectra from atomic ensembles were calculated for various types of driving fields. Central in this work is the fact that the HHG spectrum from both a BSV and a thermal driving field yields an extended cutoff when compared to driving with a coherent state. This is attributed to the long-tailed photon number distribution of BSV and thermal light. This was further understood by the obtained analytical expressions of the cutoff energy for different driving fields. The quantum state of the emitted harmonics from atomic gases was calculated in Ref. [166] via the nonlinear response function of the system and its Jacobian, showing that the harmonics inherit the quantum nature of the driving field. Crystals have also been considered with a nonclassical driving field. In Ref. [5], an intraband model is employed, which yields harmonic spectra

with the same features as those from atoms. Of particular interest in this work is the fact that the harmonic cutoff could be understood analytically as the overlap between the probability distribution representing the driving field and Bessel functions originating from an analytical expression of the induced current. Again, the long-tailed distribution of BSV was shown to be the reason for the extended cutoff in the spectra from HHG driven by BSV.

Common to these theoretical works is the formalism used. This formalism makes approximations that are difficult to verify but are needed in order to account for a nonclassical driving, which is more complicated to handle analytically than a coherent driving field. Unfortunately, this means that so far, no works have considered the quantum back action on the generated light, i.e., included the quantum nature of the generated light from the electronic medium as discussed in Sec. 1.2.1. Recent work has employed a lattice method in an attempt to overcome some of these approximations [167], but still open questions remain with regard to the validity and consequences of the employed approximations.

1.3 Scope of this work

With the recent studies on the quantum optical nature of HHG with both classical and nonclassical driving fields, many strong-field research questions are revisited with a quantum optical perspective, ranging from, e.g., the photon statistics of the emitted light to analytical expressions for the harmonic cutoff for nonclassical driving fields. In other words, the quantum optical treatment of HHG raises many fundamental research questions while also alluding to potential applications in other related research fields or technology.

Pioneering works in the field of quantum optical HHG were published a few years prior to the PhD study, and with them, as mentioned above, many new research questions were raised. In this respect, the PhD study aspires to aid in the development of the quantum optical description of HHG and the study of the quantum properties of the emitted radiation. The research papers of the thesis have specifically contributed to this by bringing quantum optical HHG to the condensed matter phase with a focus on strongly correlated systems. This has illuminated the dependency of the light on the nature of the electronic system. These insights contribute both to the application of designing ultrashort light pulses with desirable quantum properties as well as using the quantum degrees of freedom as spectroscopic measures that reveal characteristics of the electronic system. Further, the research papers have brought nonclassical driving fields to condensed matter systems. Additionally, they have aided in the development and numerical verification of approximations that both ease the required numerical efforts in simulations while also providing

a better understanding of the requirements for generating nonclassical light from HHG.

1.4 Outline

The thesis consists of two parts. The first part contains several Chapters (Chaps.) and forms a review of the research study.

In the preceding Ch. 1, an introduction is given to the research field, including a historical overview and a highlight of central results. A detailed overview of the works within strong-field quantum optics is provided to contextualize and motivate the research of the thesis. Furthermore, terminologies and concepts relevant to the thesis are given to serve as a basis for the concepts presented in the thesis.

Then, Ch. 2 provides a review of both semiclassical and quantum optical light-matter interactions. Additionally, relevant quantum optical states relevant for the thesis are reviewed. The theory and formalism presented in this chapter serve as a basis for the methods used in the thesis.

In Chaps. 3 - 5, the theoretical analysis and corresponding results of the research papers are presented and discussed.

First, in Ch. 3 introduces the condensed matter model, the Fermi-Hubbard model, which will serve as the generating medium for HHG in the thesis. Further, the chapter also presents the main results of Paper I and considers HHG semiclassically generated from different phases of the model. The findings are discussed with the use of symmetry-based selection rules and Floquet theory.

Then, in Ch. 4, a full quantum optical description of HHG is reviewed with a calculation of relevant quantum optical observables. The main results of Papers II & III are presented, showing how electron-electron correlations induce nonclassical light from HHG. Further, an investigation and numerical verification of additional approximations is presented to shed light on the electronic mechanism responsible for generating nonclassical harmonic radiation, highlighting the findings of Paper IV.

This is followed by Ch. 5, where nonclassical driving of a crystal is investigated, presenting the main results of Paper V. It is shown how the harmonic spectrum drastically depends on the quantum nature of the driving field. Additionally, the harmonic cutoff, power law scaling of the harmonics, and the generated electric field are studied. The chapter concludes with a discussion of the involved theoretical approximations.

Chapter 6 summarizes the main findings of the review part of the thesis and provides an outlook with new research questions motivated by the thesis work. This is followed by a bibliography and appendices that conclude the review part of the thesis. Reprints of the research papers, along with author contribution statements, are provided in the second part of the thesis.

CHAPTER 2

Interactions between light and matter

As outlined in Ch. 1, electrons are vital for many purposes, ranging from fundamental understanding in physics and chemistry to applications in technology. The main tool to manipulate and study electron dynamics is an applied time-dependent electromagnetic field, and consequently, the theoretical modeling of this interaction is central. In this chapter, the description of interactions between electrons and light is reviewed. Most of the equations and concepts in this chapter can be found in textbooks (see, e.g., Refs. [18, 74, 168–175]) and, as such, only equations relevant for later use in the thesis are in focus.

This chapter follows a natural progression starting with a review of semi-classical light-matter interactions in Sec. 2.1, followed by an introduction to quantum optics in Sec. 2.2 with a review of relevant observables and quantum states, including a phase-space representation. Finally, a quantum-optical light-matter description is introduced. As the quantum-optical description of light-matter coupling is the main focus of the thesis, more emphasis is given to quantum optics in this chapter. A similar structure can also be found elsewhere, e.g., in Ref. [176].

2.1 Semiclassical perspective

In early development of theory, the semiclassical treatment of light-matter interactions was highly successful in its predictions of observables in strong-field physics [25, 29]. By *semiclassical*, we mean that both the applied and emitted electromagnetic fields are described as classical electromagnetic waves while the electron system is treated quantum mechanically. Here, the central equations for semiclassical interactions are presented. As many of these equations are derived in textbooks (see, e.g., Refs. [168, 174]), we will not provide a full derivation here.

2.1.1 Classical electromagnetic waves in vacuum

The most central equations in classical electromagnetism are arguably Maxwell's equations and the equation for the Lorentz force. These describe the nature of electric fields, $\boldsymbol{E}(\boldsymbol{r},t)$, magnetic fields $\boldsymbol{B}(\boldsymbol{r},t)$, and how charges move in such fields. To describe and study electromagnetic phenomena, it is often suitable to introduce a scalar potential, $\varphi(\boldsymbol{r},t)$, and a vector potential, $\boldsymbol{A}(\boldsymbol{r},t)$. They are related to the electric and magnetic fields via

$$\boldsymbol{E}(\boldsymbol{r},t) = -\boldsymbol{\nabla}\varphi(\boldsymbol{r},t) - \frac{\partial \boldsymbol{A}(\boldsymbol{r},t)}{\partial t}, \tag{2.1}$$

$$\boldsymbol{B}(\boldsymbol{r},t) = \boldsymbol{\nabla} \times \boldsymbol{A}(\boldsymbol{r},t). \tag{2.2}$$

It is important to emphasize that these potentials cannot be measured directly themselves, but serve as a convenient theoretical description of the physical fields. This can also be seen from the fact that they are gauge-dependent. For example, given a scalar function $\alpha(\boldsymbol{r},t)$, one can make the gauge transformation $\boldsymbol{A}'(\boldsymbol{r},t) = \boldsymbol{A}(\boldsymbol{r},t) + \boldsymbol{\nabla}\alpha(\boldsymbol{r},t)$ and $\varphi'(\boldsymbol{r},t) = \varphi(\boldsymbol{r},t) - \frac{\partial\alpha(\boldsymbol{r},t)}{\partial t}$ and still preserve the same physical fields. In this thesis, we will use this *gauge freedom* and employ the *Coulomb gauge*, which is particularly useful when describing electromagnetic waves. In the Coulomb gauge, one takes $\boldsymbol{\nabla}\cdot\boldsymbol{A}(\boldsymbol{r},t) = 0$ and $\varphi(\boldsymbol{r},t) = 0$. The plane-wave solution to Maxwell's equations in the Coulomb gauge is given as

$$\boldsymbol{A}(\boldsymbol{r},t) = \sum_{\boldsymbol{k},\sigma} \boldsymbol{e}_\sigma A_{\boldsymbol{k},\sigma} e^{i(\boldsymbol{k}\cdot\boldsymbol{r}-\omega_k t)} + \text{c.c.}, \tag{2.3}$$

where the summation is over wavevectors $\boldsymbol{k}$ and two orthogonal polarizations σ. The polarization unit vector is denoted $\boldsymbol{e}_\sigma$, $\omega_k = c|\boldsymbol{k}|$ is the angular frequency for a given mode with the complex amplitude $A_{\boldsymbol{k},\sigma}$. From Eq. (2.3), the electric and magnetic fields can be found via Eqs. (2.1) and (2.2)

$$\boldsymbol{E}(\boldsymbol{r},t) = \sum_{\boldsymbol{k},\sigma} \boldsymbol{e}_\sigma A_{\boldsymbol{k},\sigma}(i\omega_k) e^{i(\boldsymbol{k}\cdot\boldsymbol{r}-\omega_k t)} + \text{c.c.}, \tag{2.4}$$

$$\boldsymbol{B}(\boldsymbol{r},t) = \sum_{\boldsymbol{k},\sigma} i(\boldsymbol{k}\times\boldsymbol{e}_\sigma) A_{\boldsymbol{k},\sigma} e^{i(\boldsymbol{k}\cdot\boldsymbol{r}-\omega_k t)} + \text{c.c.}. \tag{2.5}$$

With the solutions in Eqs. (2.3)-(2.5), we can now continue to express how these fields affect charged particles such as electrons.

2.1.2 Semiclassical light-matter coupling

The force governing charge dynamics in the presence of electric and magnetic fields is the Lorentz force. For a free particle with mass m and charge Q traveling with velocity $\boldsymbol{v}$, the Lorentz force is calculated as [168]

$$\boldsymbol{F}(\boldsymbol{r},t) = Q[\boldsymbol{E}(\boldsymbol{r},t) + \boldsymbol{v}\times\boldsymbol{B}(\boldsymbol{r},t)]. \tag{2.6}$$

The corresponding classical Hamiltonian, which yields the same equations of motion, is [174]

$$H(t) = \frac{1}{2m}\big[\boldsymbol{p} - Q\boldsymbol{A}(\boldsymbol{r},t)\big]^2. \tag{2.7}$$

Equation (2.7) is called the *minimal coupling* Hamiltonian as it only involves charge distributions and not higher multipole moments.

So far, all quantities have been treated classically. We now wish to treat this problem quantum mechanically. To this end, we promote the canonical variables $(\boldsymbol{r},\boldsymbol{p})$ to quantum operators $(\hat{\boldsymbol{r}},\hat{\boldsymbol{p}})$, where we introduced the hat to denote quantum operators. These operators satisfy the canonical commutation relations $[\hat{r}_i,\hat{p}_j] = i\delta_{i,j}$, where $\delta_{i,j}$ is the Kronecker delta. Promoting Eq. (2.7) to a quantum operator and adding a potential, $\hat{U}$, for generality yields the so-called velocity gauge (VG) Hamiltonian

$$\hat{H}_{\text{VG}}(t) = \frac{1}{2m}\big[\hat{\boldsymbol{p}} - Q\boldsymbol{A}(\hat{\boldsymbol{r}},t)\big]^2 + \hat{U}(\hat{\boldsymbol{r}}), \tag{2.8}$$

which describes a charged particle in the presence of both a potential (from, e.g., other charges) and a *classical* electromagnetic field. The dynamics is then, in the quantum description, determined by the TDSE

$$i\partial_t|\psi(t)\rangle_{\text{VG}} = \hat{H}_{\text{VG}}(t)|\psi(t)\rangle_{\text{VG}}, \tag{2.9}$$

where $|\psi(t)\rangle_{\text{VG}}$ is the quantum state of the charged particle.

2.1.3 The dipole approximation and the length gauge

It is often difficult to treat the spatial dependency of the applied electromagnetic field in the calculation of the dynamics due to nonvanishing commutation relations involving $\hat{\boldsymbol{r}}$ and $\hat{\boldsymbol{p}}$. To overcome this, in many situations, the *dipole approximation* is applied. This approximation treats the applied electric field as constant over the interaction region, which is a good approximation when the wavelength of the applied field is much larger than the length of the interaction region. Fortunately, this scenario is often the case in strong-field physics where a low-frequency field is applied to a small quantum system, e.g., a 800 nm laser field applied to atoms which are of size on the order of 1 Å. The dipole approximation has been applied to both atomic gases, molecules, and solid-state systems, and will also be relevant later in this thesis. Mathematically, the exponential function in Eq. (2.3) is approximated as $\exp(i\boldsymbol{k}\cdot\boldsymbol{r}) \simeq 1$, such that the vector potential is given as

$$\boldsymbol{A}(\boldsymbol{r},t) \simeq \boldsymbol{A}^{\mathrm{dip}}(t) = \sum_{\boldsymbol{k},\sigma} \boldsymbol{e}_\sigma \alpha_{\boldsymbol{k},\sigma} e^{-i\omega_k t} + \text{c.c.}, \tag{2.10}$$

where $\boldsymbol{A}^{\mathrm{dip}}(t)$ denotes the vector potential in the dipole approximation. From now on, we write $\boldsymbol{A}^{\mathrm{dip}}(t) = \boldsymbol{A}(t)$ for simplicity. Using the dipole approximation, the minimal coupling Hamiltonian in Eq. (2.8) can be transformed into an alternative length-gauge (LG) description of the light-matter interaction. This is done by applying the unitary operator

$$|\psi(t)\rangle_{\mathrm{LG}} = e^{iQ\boldsymbol{A}(t)\cdot\hat{\boldsymbol{r}}}|\psi(t)\rangle_{\mathrm{VG}}. \tag{2.11}$$

By inserting Eq. (2.11) into the TDSE and using the Baker-Campbell-Hausdorff Lemma [173], we obtain the LG Hamiltonian

$$\hat{H}_{\mathrm{LG}}(t) = \frac{\hat{\boldsymbol{p}}^2}{2m} + \hat{U}(\hat{\boldsymbol{r}}) - Q\boldsymbol{E}(t)\cdot\hat{\boldsymbol{r}}, \tag{2.12}$$

where the term proportional to $\boldsymbol{A}^2(t)$ has been discarded as it only contributes with a global phase. The TDSE in the LG is then given as

$$i\partial_t|\psi(t)\rangle_{\mathrm{LG}} = \hat{H}_{\mathrm{LG}}(t)|\psi(t)\rangle_{\mathrm{LG}}. \tag{2.13}$$

Note that in the VG in Eq. (2.7), the interaction between the charged particle and the electromagnetic field is treated as $\boldsymbol{A}\cdot\hat{\boldsymbol{p}}$, while in the LG in Eq. (2.12), it is treated as $-\boldsymbol{E}\cdot\hat{\boldsymbol{r}}$. Within the dipole approximation, these formulations are equivalent and have both been widely used in strong-field physics. Note that both gauges consider a single particle. Later in the thesis, we will extend this to multiple particles.

2.2 Quantum-optical perspective

Of course, it is not only matter that is governed by the laws of quantum mechanics. Light is of a quantum nature as well, with more degrees of freedom than what a classical description reveals. As the thesis to a great extent deals with a quantum optical description of strong-field physics, this chapter introduces quantum optics to provide an introduction to central concepts and equations that can also be found in textbooks, see, e.g., Refs. [18, 74, 169–172, 175]. Using the language of quantum optics, we can define the notion of nonclassical states of light.

2.2.1 Quantization of the electromagnetic field

As a starting point, the electromagnetic field has to be treated quantum mechanically. The procedure to quantize the electromagnetic field is found in textbooks [18, 74, 169–173], which expresses the electromagnetic field as a set of uncoupled harmonic oscillators for each frequency mode and polarization. Essentially, this shows how light can be treated as bosonic particles, called photons, in a harmonic oscillator undergoing periodic motion. The quantization is performed by calculating the energy density of the electromagnetic field, defining two canonical variables in terms of field amplitude, promoting these variables to quantum operators, and finally transforming back to field amplitudes. The field amplitudes are now also promoted to operators, given by

$$\hat{a}_{\boldsymbol{k},\sigma} = \frac{1}{\sqrt{2\omega_k}}(\omega_k \hat{q}_{\boldsymbol{k},\sigma} + i\hat{p}_{\boldsymbol{k},\sigma}), \tag{2.14}$$

which will be called the photonic annihilation operator with its hermitian conjugate, denoted $\hat{a}^\dagger_{\boldsymbol{k},\sigma}$, being the photonic creation operator. In Eq. (2.14), the two canonical operators, $q_{\boldsymbol{k},\sigma}$, and $p_{\boldsymbol{k},\sigma}$, satisfy the canonical commutation relations

$$[\hat{q}_{\boldsymbol{k},\sigma}, \hat{p}_{\boldsymbol{k}',\sigma'}] = i\delta_{\boldsymbol{k},\boldsymbol{k}'}\delta_{\sigma,\sigma'}, \qquad [\hat{q}_{\boldsymbol{k},\sigma}, \hat{q}_{\boldsymbol{k}',\sigma'}] = [\hat{p}_{\boldsymbol{k},\sigma}, \hat{p}_{\boldsymbol{k}',\sigma'}] = 0. \tag{2.15}$$

Using the canonical commutation relations in Eq. (2.15), we can derive the bosonic commutation relations for the photonic operators

$$[\hat{a}_{\boldsymbol{k},\sigma}, \hat{a}^\dagger_{\boldsymbol{k}',\sigma'}] = \delta_{\boldsymbol{k},\boldsymbol{k}'}\delta_{\sigma,\sigma'}, \qquad [\hat{a}_{\boldsymbol{k},\sigma}, \hat{a}_{\boldsymbol{k},\sigma}] = [\hat{a}^\dagger_{\boldsymbol{k},\sigma}, \hat{a}^\dagger_{\boldsymbol{k},\sigma}] = 0. \tag{2.16}$$

The energy in the free electromagnetic field is also promoted to an operator and is given as

$$\hat{H}_F = \sum_{\boldsymbol{k},\sigma} \omega_k \hat{a}^\dagger_{\boldsymbol{k},\sigma}\hat{a}_{\boldsymbol{k},\sigma}, \tag{2.17}$$

where the vacuum energy has been neglected. Following the same quantization procedure leading to the expression for the fields in Eqs. (2.3)-(2.5), we can

express the now quantized fields in terms of the photonic operators in Eq. (2.14) as

$$\hat{\boldsymbol{A}}(\hat{\boldsymbol{r}}) = \sum_{\boldsymbol{k},\sigma} \frac{g_0}{\sqrt{\omega_k}} \left[\boldsymbol{e}_\sigma \hat{a}_{\boldsymbol{k},\sigma} e^{i\boldsymbol{k}\cdot\hat{\boldsymbol{r}}} + \text{h.c.}\right], \tag{2.18}$$

$$\hat{\boldsymbol{E}}(\hat{\boldsymbol{r}}) = \sum_{\boldsymbol{k},\sigma} g_0 \sqrt{\omega_k} \left[i\boldsymbol{e}_\sigma \hat{a}_{\boldsymbol{k},\sigma} e^{i\boldsymbol{k}\cdot\hat{\boldsymbol{r}}} + \text{h.c.}\right], \tag{2.19}$$

$$\hat{\boldsymbol{B}}(\hat{\boldsymbol{r}}) = \sum_{\boldsymbol{k},\sigma} \frac{g_0}{\sqrt{\omega_k}} \left[i(\boldsymbol{k} \times \boldsymbol{e}_\sigma) \hat{a}_{\boldsymbol{k},\sigma} e^{i\boldsymbol{k}\cdot\hat{\boldsymbol{r}}} + \text{h.c.}\right], \tag{2.20}$$

where we have defined the coupling strength $g_0 = \sqrt{2\pi/V}$ for convenience with V being the quantization volume. Note that there is no time dependence in Eqs. (2.18)-(2.20). This is due to the fact that the time dependence of the free fields is determined via the free-field Hamiltonian in Eq. (2.17). Going into a rotating frame with respect to Eq. (2.17) will reproduce the time dependence similar to the classical fields. Equations (2.18) - (2.20) will be of use later when discussing quantum-optical light-matter interactions.

Going back to the free-field Hamiltonian in Eq. (2.17), we note that it is the Hamiltonian for the well-known quantum harmonic oscillator. Its eigenstates for a given mode are defined via

$$\hat{H}_F^{(\boldsymbol{k},\sigma)} |n\rangle_{\boldsymbol{k},\sigma} = n\omega_k |n\rangle_{\boldsymbol{k},\sigma}, \tag{2.21}$$

where $\hat{H}_F^{(\boldsymbol{k},\sigma)} = \omega_k \hat{a}^\dagger_{\boldsymbol{k},\sigma} \hat{a}_{\boldsymbol{k},\sigma}$ and $|n\rangle_{\boldsymbol{k},\sigma}$ is a Fock state in mode $(\boldsymbol{k},\sigma)$. A Fock state is also often referred to as a number state, denoting a well-defined number of excitations or, as often used in quantum optics, a well-defined number of photons. In this way, photons can be thought of as excitations of the electromagnetic field. It is also worth noting that the effect of the photon operators on a number state is

$$\hat{a}_{\boldsymbol{k},\sigma} |n\rangle_{\boldsymbol{k},\sigma} = \sqrt{n} |n-1\rangle_{\boldsymbol{k},\sigma} \tag{2.22}$$

$$\hat{a}^\dagger_{\boldsymbol{k},\sigma} |n\rangle_{\boldsymbol{k},\sigma} = \sqrt{n+1} |n+1\rangle_{\boldsymbol{k},\sigma}. \tag{2.23}$$

Such a number state is an example of a nonclassical state of light. Before discussing what we mean by a nonclassical state of light, we first need to introduce quantum optical observables, which are also relevant for the rest of the thesis.

2.2.2 Observables and nonclassical light

Historically, the main observable of interest in HHG has been the spectrum. The spectrum reveals the amplitude of a given harmonic in the emitted light.

However, a quantum optical description of the emitted light allows one to calculate other observables such as photon statistics and the degree of squeezing of the light.

2.2.2.1 Spectrum

The harmonic spectrum, as stated, is a central observable in HHG, as it can be used for spectroscopic purposes and has applications in the generation of ultrashort pulses as well. Semiclassically, the spectrum is calculated via the acceleration of charges. The induced current in a solid-state system is given by

$$\boldsymbol{j}(t) = -\boldsymbol{v}(t) = -\frac{d}{dt}\boldsymbol{r}(t) \tag{2.24}$$

The generated field is proportional to the time derivative of the induced current

$$\boldsymbol{E}_{\text{gen}}(t) \propto -\frac{d}{dt}\boldsymbol{j}(t) = \frac{d^2}{dt^2}\boldsymbol{r}(t) = \boldsymbol{a}(t). \tag{2.25}$$

By Fourier transformation of Eq. (2.25), the generated field as a function of frequency, ω, can be obtained

$$\boldsymbol{E}_{\text{gen}}(\omega) \propto -\frac{1}{\sqrt{2\pi}}\int_{-\infty}^{\infty} dt e^{-i\omega t}\frac{d}{dt}\boldsymbol{j}(t). \tag{2.26}$$

By performing partial integration on the right-hand side of Eq. (2.26), and taking the norm square, we obtain the total signal

$$S_{\text{sc}}(\omega) \propto \omega^2\left|\tilde{\boldsymbol{j}}(\omega)\right|^2, \tag{2.27}$$

where $\tilde{\boldsymbol{j}}(\omega) = (2\pi)^{-1/2}\int_{-\infty}^{\infty} dt \exp(-i\omega t)\boldsymbol{j}(t)$ is the Fourier transformed current and $S_{\text{sc}}(\omega)$ is the semiclassical spectrum. Equation (2.27) is also known as Larmor's formula [168, 177], and relates the experimentally observed signal to the induced current on the microscopic level. However, as Eq. (2.27) is obtained from classical considerations, it does not reveal anything about the quantum nature of the emitted field.

In a quantum-optical description, the spectrum is calculated via the photonic operators. The total energy in the emitted radiation is given by

$$\mathcal{E} = \sum_{\boldsymbol{k},\sigma}\omega_k\langle\hat{n}_{\boldsymbol{k},\sigma}\rangle, \tag{2.28}$$

where

$$\hat{n}_{\boldsymbol{k},\sigma} = \hat{a}^\dagger_{\boldsymbol{k},\sigma}\hat{a}_{\boldsymbol{k},\sigma} \tag{2.29}$$

is the photonic *number operator*. By taking the continuum limit in Eq. (2.28)

$$\sum_{\boldsymbol{k}} \rightarrow \frac{V}{8c^3\pi^3}\int d\Omega d\omega \omega^2, \tag{2.30}$$

we can calculate the energy per frequency per solid angle as

$$S(\omega_{\boldsymbol{k}}) = \frac{d\mathcal{E}}{d\Omega d\omega_k} = \frac{\omega^3}{g_0^2(2\pi)^2c^3}\sum_{\sigma}\langle \hat{n}_{\boldsymbol{k},\sigma}\rangle. \tag{2.31}$$

The quantum optical expression for the spectrum in Eq. (2.31) only involves the first moment of the photon number, and it is hence not a measure that reveals anything about the photon statistics in the emission. For this purpose, other quantum optical observables need to be considered.

2.2.2.2 Photon statistics

With the quantum optical description, one can ask what the photon number probability distribution of light is. In other words, if you were to measure the number of photons in a specific mode, what would be the probability of observing a different number of photons. As a simple measure, which can capture nonclassical features of light, we will in this thesis and in the research papers use the Mandel-Q parameter. For a single mode $(\boldsymbol{k},\sigma)$, it is given as [74]

$$\begin{aligned} Q_{\boldsymbol{k},\sigma} &= \frac{\langle(\Delta\hat{n}_{\boldsymbol{k},\sigma})^2\rangle - \langle\hat{n}_{\boldsymbol{k},\sigma}\rangle}{\langle\hat{n}_{\boldsymbol{k},\sigma}\rangle} \\ &= \frac{\langle\hat{n}^2_{\boldsymbol{k},\sigma}\rangle - \langle\hat{n}_{\boldsymbol{k},\sigma}\rangle^2}{\langle\hat{n}_{\boldsymbol{k},\sigma}\rangle} - 1 \\ &= \frac{\langle\hat{a}^\dagger_{\boldsymbol{k},\sigma}\hat{a}^\dagger_{\boldsymbol{k},\sigma}\hat{a}_{\boldsymbol{k},\sigma}\hat{a}_{\boldsymbol{k},\sigma}\rangle - \langle\hat{a}^\dagger_{\boldsymbol{k},\sigma}\hat{a}_{\boldsymbol{k},\sigma}\rangle^2}{\langle\hat{a}^\dagger_{\boldsymbol{k},\sigma}\hat{a}_{\boldsymbol{k},\sigma}\rangle}, \end{aligned} \tag{2.32}$$

where $\langle(\Delta\hat{n}_{\boldsymbol{k},\sigma})^2\rangle = \langle\hat{n}^2_{\boldsymbol{k},\sigma}\rangle - \langle\hat{n}_{\boldsymbol{k},\sigma}\rangle^2$ is the variance of the counting operator, $\hat{n}_{\boldsymbol{k},\sigma}$, and where the commutation relations in Eq. (2.16) have been used in the last line. If the photons in a given mode obey Poissonian statistics where the variance is equal to the mean, we see that $Q_{\boldsymbol{k},\sigma} = 0$. Consequently, if one calculates $Q_{\boldsymbol{k},\sigma} > 0$, the distribution is said to be *super*-Poissonian, while $Q_{\boldsymbol{k},\sigma} < 0$ is called *sub*-Poissonian. While super-Poissonian statistics can be found from classical light sources, sub-Poissonian is a nonclassical effect [74], also referred to as number squeezing.

We note that in the literature, the second-order correlation function, $g^{(2)}_{\boldsymbol{k},\sigma}(\tau)$ is also used as a measure of the photon statistics. It is given by

$$g^{(2)}_{\boldsymbol{k},\sigma}(\tau) = \frac{\langle\hat{a}^\dagger_{\boldsymbol{k},\sigma}(0)\hat{a}^\dagger_{\boldsymbol{k},\sigma}(\tau)\hat{a}_{\boldsymbol{k},\sigma}(\tau)\hat{a}_{\boldsymbol{k},\sigma}(0)\rangle}{\langle\hat{a}^\dagger_{\boldsymbol{k},\sigma}(0)\hat{a}_{\boldsymbol{k},\sigma}(0)\rangle\langle\hat{a}^\dagger_{\boldsymbol{k},\sigma}(\tau)\hat{a}_{\boldsymbol{k},\sigma}(\tau)\rangle}, \tag{2.33}$$

which is a measure of how likely it is to detect a second photon at time $t = \tau$ after detecting a photon at time $t = 0$. If $g^{(2)}_{\boldsymbol{k},\sigma}(\tau) = 1$, the light is independently distributed. For $g^{(2)}_{\boldsymbol{k},\sigma}(0) > g^{(2)}_{\boldsymbol{k},\sigma}(\tau)$, we see that the probability of detecting a second photon after time τ decreases, leading to the notion of photon *bunching*. On the other hand, for $g^{(2)}_{\boldsymbol{k},\sigma}(0) < g^{(2)}_{\boldsymbol{k},\sigma}(\tau)$ the probability for detecting a second photon increases leading to the notion of antibunching of photons. The Mandel-Q parameter is related to the second-order correlation function via

$$Q_{\boldsymbol{k},\sigma} = \langle \hat{n}_{\boldsymbol{k},\sigma} \rangle [g^{(2)}_{\boldsymbol{k},\sigma}(0) - 1]. \tag{2.34}$$

Note that while $Q_{\boldsymbol{k},\sigma} < 0$ shows sub-Poissonian statistics, this is not the same as photon antibunching. The condition for antibunching is, as stated above, $g^{(2)}_{\boldsymbol{k},\sigma}(0) < g^{(2)}_{\boldsymbol{k},\sigma}(\tau)$, while the condition for sub-Poissonian statistics is $g^{(2)}_{\boldsymbol{k},\sigma}(0) < 1$ as seen in Eq. (2.34). Consequently, anti-bunching does *not* imply sub-Poissonian statistics [74]. Experimentally, the photon statistics of a light field is obtained by photon counting measurements or by intensity correlation measurements as sketched in Fig. 1.3.

In the remainder of the thesis and in the research papers, only the Mandel-Q parameter will be considered.

2.2.2.3 Squeezing

A clear nonclassical property of light is quadrature squeezing. The quadrature operator for a given mode $(\boldsymbol{k}, \sigma)$ is given as

$$\hat{X}_{\boldsymbol{k},\sigma}(\vartheta_{\boldsymbol{k},\sigma}) = \frac{1}{2}\big(\hat{a}_{\boldsymbol{k},\sigma} e^{-i\vartheta_{\boldsymbol{k},\sigma}} + \hat{a}^\dagger_{\boldsymbol{k},\sigma} e^{i\vartheta_{\boldsymbol{k},\sigma}}\big), \tag{2.35}$$

where the angle $\vartheta_{\boldsymbol{k},\sigma}$ determines the direction of the quadrature in phase space. In literature, often $\hat{X}_{\boldsymbol{k},\sigma}(0) = \hat{X}_{\boldsymbol{k},\sigma}$ and $\hat{X}_{\boldsymbol{k},\sigma}(\pi/2) = \hat{P}_{\boldsymbol{k},\sigma}$ indicating the correspondence to canonical operators in quantum mechanics as seen from Eq. (2.15). From the commutation relations [Eq. (2.16)], it can be shown that $[\hat{X}_{\boldsymbol{k},\sigma}(\vartheta_{\boldsymbol{k},\sigma}), \hat{X}_{\boldsymbol{k},\sigma}(\vartheta_{\boldsymbol{k},\sigma} + \pi/2)] = i/2$. It then follows from the Heisenberg uncertainty principle that [173]

$$\langle [\Delta \hat{X}_{\boldsymbol{k},\sigma}(\vartheta_{\boldsymbol{k},\sigma})]^2 \rangle \langle [\Delta \hat{X}_{\boldsymbol{k},\sigma}(\vartheta_{\boldsymbol{k},\sigma} + \pi/2)]^2 \rangle \geq \frac{1}{16}, \tag{2.36}$$

where

$$\begin{aligned}
\langle [\Delta \hat{X}_{\boldsymbol{k},\sigma}(\vartheta_{\boldsymbol{k},\sigma})]^2 \rangle =& \langle \hat{X}_{\boldsymbol{k},\sigma}(\vartheta_{\boldsymbol{k},\sigma})^2 \rangle - \langle \hat{X}_{\boldsymbol{k},\sigma}(\vartheta_{\boldsymbol{k},\sigma}) \rangle^2 \\
=& \frac{1}{4}\Big[e^{-2i\vartheta_{\boldsymbol{k},\sigma}} \big(\langle \hat{a}^2_{\boldsymbol{k},\sigma} \rangle - \langle \hat{a}_{\boldsymbol{k},\sigma} \rangle^2 \big) + e^{2i\vartheta_{\boldsymbol{k},\sigma}} \big(\langle \hat{a}^{\dagger 2}_{\boldsymbol{k},\sigma} \rangle - \langle \hat{a}^\dagger_{\boldsymbol{k},\sigma} \rangle^2 \big) \\
& + 2\big(\langle \hat{a}^\dagger_{\boldsymbol{k},\sigma} \hat{a}_{\boldsymbol{k},\sigma} \rangle - \langle \hat{a}^\dagger_{\boldsymbol{k},\sigma} \rangle \langle \hat{a}_{\boldsymbol{k},\sigma} \rangle \big) + 1 \Big]
\end{aligned} \tag{2.37}$$

is the variance of the quadrature operator. If the uncertainty inequality in Eq. (2.36) is saturated, the state is referred to as a minimum uncertainty state. One such state is the vacuum state, for which we have $\langle[\Delta\hat{X}_{\boldsymbol{k},\sigma}(0)]^2\rangle = \langle[\Delta\hat{X}_{\boldsymbol{k},\sigma}(\pi/2)]^2\rangle = 1/4$.

A state is quadrature squeezed if for some angle $\vartheta_{\boldsymbol{k},\sigma}$, the variance of the quadrature operator satisfy

$$\langle[\Delta\hat{X}_{\boldsymbol{k},\sigma}(\vartheta_{\boldsymbol{k},\sigma})]^2\rangle < \frac{1}{4}, \tag{2.38}$$

that is, the variance of the quadrature is below that of the vacuum. This can only be true if the conjugate quadrature is anti-squeezed, i.e., it satisfies $[\Delta\hat{X}_{\boldsymbol{k},\sigma}(\vartheta_{\boldsymbol{k},\sigma} + \pi/2)]^2 > 1/4$ for the uncertainty relation in Eq. (2.36) to be satisfied. To quantify the degree of squeezing, we use the following squeezing measure [95, 169]

$$\eta_{\boldsymbol{k},\sigma} = -10\log_{10}\{4 \min_{\vartheta_{\boldsymbol{k},\sigma}\in[0,\pi)]}[\Delta\hat{X}_{\boldsymbol{k},\sigma}(\vartheta_{\boldsymbol{k},\sigma})]^2\}, \tag{2.39}$$

where $\eta_{\boldsymbol{k},\sigma}$ is the degree of squeezing in units of dB. In words, Eq. (2.39) computes the minimum quadrature variance minimized over all directions in phase space determined by the angle $\vartheta_{\boldsymbol{k},\sigma}$. It is easily seen from Eq. (2.39), that if the minimum variance is $[\Delta\hat{X}_{\boldsymbol{k},\sigma}(\vartheta^{\min}_{\boldsymbol{k},\sigma})]^2 = \frac{1}{4}$, then $\eta_{\boldsymbol{k},\sigma} = 0$. Thus, if a state is squeezed, it follows that $\eta_{\boldsymbol{k},\sigma} > 0$, and it is hence a clear observable for detecting nonclassical light. Squeezing can be observed by measuring the quadrature, which is done with a homodyne detection scheme where the signal is interfered with a strong coherent field in a beam splitter as sketched in Fig. 1.3.

2.2.2.4 Electric field and its fluctuations

The last observable of interest to us is the electric field. This is easily calculated using Eq. (2.19). For convenience, we define the electric field of a single mode

$$\hat{\boldsymbol{E}}_{\boldsymbol{k},\sigma}(\hat{\boldsymbol{r}}) = g_0\sqrt{\omega_k}\big[i\boldsymbol{e}_\sigma\hat{a}_{\boldsymbol{k},\sigma}e^{i\boldsymbol{k}\cdot\hat{\boldsymbol{r}}} + \text{h.c}\big], \tag{2.40}$$

from where it follows that $\hat{\boldsymbol{E}}(\hat{\boldsymbol{r}}) = \sum_{\boldsymbol{k},\sigma}\hat{\boldsymbol{E}}_{\boldsymbol{k},\sigma}(\hat{\boldsymbol{r}})$ by comparison with Eq. (2.19). Additionally, as will become apparent later in the thesis, the fluctuations of the electric field are also of interest. The fluctuations (variance) are calculated via $\left\langle[\Delta\hat{\boldsymbol{E}}(\hat{\boldsymbol{r}})]^2\right\rangle = \langle\hat{\boldsymbol{E}}^2(\hat{\boldsymbol{r}})\rangle - \langle\hat{\boldsymbol{E}}(\hat{\boldsymbol{r}})\rangle^2$. Inserting Eq. (2.19) and noting that all terms with $\boldsymbol{k} \neq \boldsymbol{k}'$ cancels, we obtain for a single mode

$$\langle[\Delta\hat{\boldsymbol{E}}_{\boldsymbol{k},\sigma}(\hat{\boldsymbol{r}})]^2\rangle = g_0^2\omega_k\Big[- e^{2i\boldsymbol{k}\cdot\boldsymbol{r}}\big(\langle\hat{a}_{\boldsymbol{k},\sigma}^2\rangle - \langle\hat{a}_{\boldsymbol{k},\sigma}\rangle^2\big) \\ - e^{-2i\boldsymbol{k}\cdot\boldsymbol{r}}\big(\langle(\hat{a}_{\boldsymbol{k},\sigma}^\dagger)^2\rangle - \langle\hat{a}_{\boldsymbol{k},\sigma}^\dagger\rangle^2\big) \\ + 2\big(\langle\hat{a}_{\boldsymbol{k},\sigma}^\dagger\hat{a}_{\boldsymbol{k},\sigma}\rangle - \langle\hat{a}_{\boldsymbol{k},\sigma}^\dagger\rangle\langle\hat{a}_{\boldsymbol{k},\sigma}\rangle\big) + 1\Big], \tag{2.41}$$

with the fluctuations for the entire field given by

$$\langle[\Delta\hat{\boldsymbol{E}}(\hat{\boldsymbol{r}})]^2\rangle = \sum_{\boldsymbol{k},\sigma}\langle[\Delta\hat{\boldsymbol{E}}_{\boldsymbol{k},\sigma}(\hat{\boldsymbol{r}})]^2\rangle. \tag{2.42}$$

As we shall see below, some quantum states of light can have a vanishing mean electric field with nonvanishing uncertainty.

2.2.3 Review of quantum states of light

In this thesis and in general quantum optical HHG, different quantum states are relevant to describe both the generated and the nonclassical driving fields. These will now be reviewed with a highlight of relevant properties and calculation of observables introduced in Sec. 2.2.2 above. For clarity, the dipole approximation is employed in the following for calculations of expectation values involving the electric field operator. It is, however, trivial to include the spatial dependence in the expressions.

2.2.3.1 Coherent state

One of the most used quantum optical states is a coherent state. It can be shown that a coherent state is emitted from a classical time-dependent current [74, 169]. In this sense, a coherent state is often seen as a quantum optical description of a classical state of light, as it is generated from classical processes. Mathematically, a coherent state is described by applying the displacement operator

$$|\alpha_{\boldsymbol{k},\sigma}\rangle = \hat{\mathcal{D}}(\alpha_{\boldsymbol{k},\sigma})|0\rangle_{\boldsymbol{k},\sigma}, \tag{2.43}$$

where $|\alpha_{\boldsymbol{k},\sigma}\rangle$ is a coherent state in the mode $(\boldsymbol{k},\sigma)$ with complex amplitude $\alpha_{\boldsymbol{k},\sigma} = |\alpha_{\boldsymbol{k},\sigma}|e^{i\phi_{\boldsymbol{k},\sigma}}$ and the displacement operator for a given mode is

$$\hat{\mathcal{D}}(\alpha_{\boldsymbol{k},\sigma}) = e^{\alpha_{\boldsymbol{k},\sigma}\hat{a}_{\boldsymbol{k},\sigma}^\dagger - \alpha_{\boldsymbol{k},\sigma}^*\hat{a}_{\boldsymbol{k},\sigma}}. \tag{2.44}$$

Note that $\alpha_{\boldsymbol{k},\sigma}$ can be time dependent, which will be used later in the thesis. The displacement operator is unitary and has the following useful properties

$$\hat{\mathcal{D}}(\alpha_{\boldsymbol{k},\sigma})\hat{\mathcal{D}}^{\dagger}(\alpha_{\boldsymbol{k},\sigma}) = \hat{\mathcal{D}}^{\dagger}(\alpha_{\boldsymbol{k},\sigma})\hat{\mathcal{D}}(\alpha_{\boldsymbol{k},\sigma}) = \mathbb{I} \tag{2.45}$$

$$\hat{\mathcal{D}}(-\alpha_{\boldsymbol{k},\sigma}) = \hat{\mathcal{D}}^{\dagger}(\alpha_{\boldsymbol{k},\sigma}) \tag{2.46}$$

$$\hat{\mathcal{D}}(\alpha_{\boldsymbol{k},\sigma})\hat{\mathcal{D}}(\beta_{\boldsymbol{k},\sigma}) = e^{\alpha_{\boldsymbol{k},\sigma}\beta^{*}_{\boldsymbol{k},\sigma} - \alpha^{*}_{\boldsymbol{k},\sigma}\beta_{\boldsymbol{k},\sigma}}\ \hat{\mathcal{D}}(\alpha_{\boldsymbol{k},\sigma} + \beta_{\boldsymbol{k},\sigma}) \tag{2.47}$$

$$\hat{\mathcal{D}}^{\dagger}(\alpha_{\boldsymbol{k},\sigma})\hat{a}_{\boldsymbol{k},\sigma}\hat{\mathcal{D}}(\alpha_{\boldsymbol{k},\sigma}) = \hat{a}_{\boldsymbol{k},\sigma} + \alpha_{\boldsymbol{k},\sigma} \tag{2.48}$$

$$\hat{\mathcal{D}}(\alpha_{\boldsymbol{k},\sigma})\hat{a}_{\boldsymbol{k},\sigma}\hat{\mathcal{D}}^{\dagger}(\alpha_{\boldsymbol{k},\sigma}) = \hat{a}_{\boldsymbol{k},\sigma} - \alpha_{\boldsymbol{k},\sigma}, \tag{2.49}$$

where $\mathbb{I}$ is the identity operator. For analytical considerations, it can be beneficial to express the displacement operator in Eq. (2.44) as

$$\hat{\mathcal{D}}(\alpha_{\boldsymbol{k},\sigma}) = e^{-\frac{1}{2}|\alpha_{\boldsymbol{k},\sigma}|^2} e^{\alpha_{\boldsymbol{k},\sigma}\hat{a}^{\dagger}_{\boldsymbol{k},\sigma}} e^{-\alpha^{*}_{\boldsymbol{k},\sigma}\hat{a}_{\boldsymbol{k},\sigma}}. \tag{2.50}$$

A key property of a coherent state is the fact that it is an eigenstate for the photonic annihilation operator

$$\hat{a}_{\boldsymbol{k},\sigma}|\alpha_{\boldsymbol{k},\sigma}\rangle = \alpha_{\boldsymbol{k},\sigma}|\alpha_{\boldsymbol{k},\sigma}\rangle, \tag{2.51}$$

which can be used to show that the coherent state can be expanded in a Fock basis as

$$|\alpha_{\boldsymbol{k},\sigma}\rangle = e^{-\frac{1}{2}|\alpha_{\boldsymbol{k},\sigma}|^2} \sum_{n=0}^{\infty} \frac{\alpha^{n}_{\boldsymbol{k},\sigma}}{\sqrt{n!}} |n_{\boldsymbol{k},\sigma}\rangle, \tag{2.52}$$

from which it can easily be calculated that a coherent state yields Poissonian photon number statistics

$$P^{\mathrm{Coh}}_{\boldsymbol{k},\sigma}(m) = |\langle m_{\boldsymbol{k},\sigma}|\alpha_{\boldsymbol{k},\sigma}\rangle|^2 = e^{-|\alpha_{\boldsymbol{k},\sigma}|^2} \frac{|\alpha_{\boldsymbol{k},\sigma}|^{2m}}{m!}, \tag{2.53}$$

where

$$\langle \hat{n}_{\boldsymbol{k},\sigma}\rangle = |\alpha_{\boldsymbol{k},\sigma}|^2 \tag{2.54}$$

is the mean number of photons, and the superscript refers to a coherent state. Note that coherent states are non-orthogonal as

$$\langle \beta_{\boldsymbol{k},\sigma}|\alpha_{\boldsymbol{k},\sigma}\rangle = e^{-\frac{1}{2}(|\beta_{\boldsymbol{k},\sigma}|^2 + |\alpha_{\boldsymbol{k},\sigma}|^2 - 2\beta^{*}_{\boldsymbol{k},\sigma}\alpha_{\boldsymbol{k},\sigma})} \neq \delta(\alpha_{\boldsymbol{k},\sigma} - \beta_{\boldsymbol{k},\sigma}). \tag{2.55}$$

From Eq. (2.51), it can easily be calculated that $Q^{\mathrm{Coh}}_{\boldsymbol{k},\sigma} = \eta^{\mathrm{Coh}}_{\boldsymbol{k},\sigma} = 0$ for a coherent state, i.e., it has classical photons statistics and no squeezing. This is also seen from calculating the variance of the quadrature operator in Eq. (2.35)

$$\left\langle [\Delta \hat{X}^{\mathrm{Coh}}_{\boldsymbol{k},\sigma}(\vartheta_{\boldsymbol{k},\sigma})]^2 \right\rangle = 1/4, \tag{2.56}$$

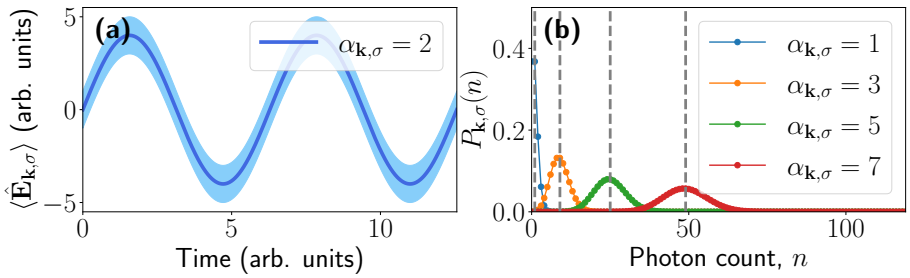

Figure 2.1: Characteristics of a coherent state. (a) The mean electric field [Eq. (2.57)] with its fluctuations, which we note are equal to those of the vacuum are hence constant in time. (b) The photon number probability distribution [Eq. (2.53)] for different values of $\alpha_{\boldsymbol{k},\sigma}$. The vertical dashed lines indicate the mean photon number [Eq. (2.54)].

which is independent of $\alpha_{\boldsymbol{k},\sigma}$ and $\vartheta_{\boldsymbol{k},\sigma}$ and is identical to the quadrature variance of the vacuum. Additionally, it can be found that the mean electric field [under the evolution of $\hat{H}_F$, Eq. (2.17)] is

$$\begin{aligned}\langle \hat{\boldsymbol{E}}^{\mathrm{Coh}}_{\boldsymbol{k},\sigma} \rangle &= g_0 \sqrt{\omega_k} [i \boldsymbol{e}_\sigma \alpha_{\boldsymbol{k},\sigma} e^{-i(\omega_k t - \boldsymbol{k}\cdot\boldsymbol{r})} + \mathrm{h.c}] \\ &= 2 g_0 |\alpha_{\boldsymbol{k},\sigma}| \sqrt{\omega_k} \boldsymbol{e}_\sigma \sin(\omega_k t - \boldsymbol{k}\cdot\boldsymbol{r} - \phi) \\ &= F_0 \sin(\omega_k t - \boldsymbol{k}\cdot\boldsymbol{r} - \phi) \boldsymbol{e}_\sigma, \end{aligned} \tag{2.57}$$

where we have defined the field amplitude $F_0 = 2 g_0 \sqrt{\omega_k} \alpha_{\boldsymbol{k},\sigma}$ and assumed linear polarization. Note further that the phase of $\alpha_{\boldsymbol{k},\sigma}$ enters as the phase of the electric field and that we have assumed an evaluation in the real space basis, i.e., the eigenbasis of $\hat{\boldsymbol{r}}$. Additionally, by using Eq. (2.51), it is readily seen that from Eq. (2.41) that $\left\langle [\Delta \hat{\boldsymbol{E}}^{\mathrm{Coh}}_{\boldsymbol{k},\sigma}]^2 \right\rangle = g_0^2 \omega_k$ which is the variance of the vacuum. Note that we have neglected the variance of the vacuum in all the unpopulated modes, $(\boldsymbol{k}', \sigma') \neq (\boldsymbol{k}, \sigma)$, when calculating the variance of the electric field. This will also be the case in the rest of the thesis. The light emitted by lasers is often well approximated by coherent states, and these are hence used to model the classical driving field in HHG. The characteristics of a coherent state are illustrated in Fig. 2.1.

2.2.3.2 Displaced squeezed state

A more general state is the displaced squeezed state or, equivalently, a squeezed coherent state[1]. The two names will be used interchangeably in the thesis.

[1] Mathematically, they are not the same as the displacement and squeezing operators do not commute. However, as $\hat{\mathcal{D}}(\alpha_{\boldsymbol{k},\sigma})\hat{S}(\xi_{\boldsymbol{k},\sigma}) = \hat{S}(\xi_{\boldsymbol{k},\sigma})\hat{\mathcal{D}}(\gamma_{\boldsymbol{k},\sigma})$ with

Squeezing can occur in nonlinear optical devices with second-order nonlinear susceptibility, where one photon is converted into two photons of half the frequency, known as degenerate parametric down conversion [74]. A displaced squeezed state is given by

$$|\alpha_{\boldsymbol{k},\sigma}, \xi_{\boldsymbol{k},\sigma}\rangle = \hat{\mathcal{D}}(\alpha_{\boldsymbol{k},\sigma})\hat{S}(\xi_{\boldsymbol{k},\sigma})|0\rangle, \tag{2.58}$$

where $\hat{\mathcal{D}}(\alpha_{\boldsymbol{k},\sigma})$ is the displacement operator in Eq. (2.44) and

$$\hat{S}(\xi_{\boldsymbol{k},\sigma}) = e^{\frac{1}{2}(\xi^*_{\boldsymbol{k},\sigma}\hat{a}^2_{\boldsymbol{k},\sigma} - \xi_{\boldsymbol{k},\sigma}\hat{a}^{\dagger 2}_{\boldsymbol{k},\sigma})}, \tag{2.59}$$

is the squeezing operator with complex squeezing parameter

$$\xi_{\boldsymbol{k},\sigma} = r_{\boldsymbol{k},\sigma}e^{i\theta_{\boldsymbol{k},\sigma}}, \tag{2.60}$$

where $r_{\boldsymbol{k},\sigma}$ and $\theta_{\boldsymbol{k},\sigma}$ are real. Note that $\theta_{\boldsymbol{k},\sigma}$ determines the squeezing angle, whereas $\vartheta_{\boldsymbol{k},\sigma}$ in Eq. (2.35) describes the direction for the quadrature operator. Similarly to the displacement operator, the squeezing operator in Eq. (2.59) is unitary and satisfies the following

$$\hat{S}(\xi_{\boldsymbol{k},\sigma})\hat{S}^\dagger(\xi_{\boldsymbol{k},\sigma}) = \hat{S}^\dagger(\xi_{\boldsymbol{k},\sigma})\hat{S}(\xi_{\boldsymbol{k},\sigma}) = \mathbb{I} \tag{2.61}$$

$$\hat{S}(-\xi_{\boldsymbol{k},\sigma}) = \hat{S}^\dagger(\xi_{\boldsymbol{k},\sigma}) \tag{2.62}$$

$$\hat{S}^\dagger(\xi_{\boldsymbol{k},\sigma})\hat{a}_{\boldsymbol{k},\sigma}\hat{S}(\xi_{\boldsymbol{k},\sigma}) = \hat{a}_{\boldsymbol{k},\sigma}\cosh(r_{\boldsymbol{k},\sigma}) - e^{i\theta_{\boldsymbol{k},\sigma}}\hat{a}^\dagger_{\boldsymbol{k},\sigma}\sinh(r_{\boldsymbol{k},\sigma}). \tag{2.63}$$

The mean photon number of a displaced squeezed state is

$$\langle\hat{n}_{\boldsymbol{k},\sigma}\rangle = |\alpha_{\boldsymbol{k},\sigma}|^2 + \sinh^2(r_{\boldsymbol{k},\sigma}) \tag{2.64}$$

which shows the separate contributions from the displacement and the squeezing operator, respectively. Analytically calculating the Mandel-Q parameter in Eq. (2.32) for a displaced squeezed state yields

$$\begin{aligned} Q^{\mathrm{SC}}_{\boldsymbol{k},\sigma} =& \frac{1}{|\alpha_{\boldsymbol{k},\sigma}|^2 + \sinh^2(r_{\boldsymbol{k},\sigma})}\Big[2\sinh^4(r_{\boldsymbol{k},\sigma}) + \sinh^2(r_{\boldsymbol{k},\sigma})(1+2|\alpha_{\boldsymbol{k},\sigma}|^2) \\ & - 2|\alpha_{\boldsymbol{k},\sigma}|^2\cosh(r_{\boldsymbol{k},\sigma})\sinh(r_{\boldsymbol{k},\sigma})\cos(2\phi_{\boldsymbol{k},\sigma} - \theta_{\boldsymbol{k},\sigma})\Big], \end{aligned} \tag{2.65}$$

where the superscript refers to a squeezed coherent state and where we note the dependency of the phases of both $\alpha_{\boldsymbol{k},\sigma}$ and $\xi_{\boldsymbol{k},\sigma}$. For certain values of $|\alpha_{\boldsymbol{k},\sigma}|$ and $r_{\boldsymbol{k},\sigma}$, specific choices of this phase can yield both sub- and super-Poissonian

$\gamma_{\boldsymbol{k},\sigma} = \alpha_{\boldsymbol{k},\sigma}\cosh(r_{\boldsymbol{k},\sigma}) + \alpha^*_{\boldsymbol{k},\sigma}e^{i\theta_{\boldsymbol{k},\sigma}}\sinh(r_{\boldsymbol{k},\sigma})$, the two states are identical up to a modified coherent state amplitude.

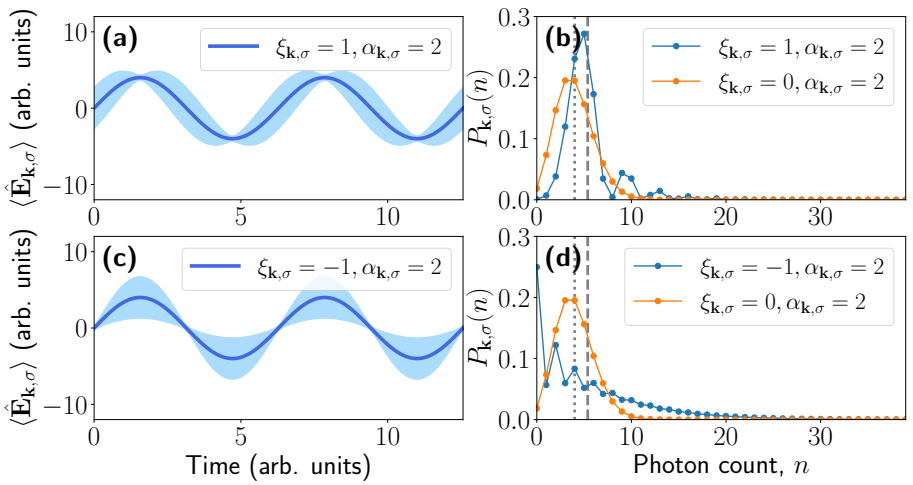

Figure 2.2: Characteristics of a displaced squeezed state with squeezing parameter defined in Eq. (2.60). The mean electric field [Eq. (2.57)] with its fluctuations [Eq. (2.70)] is shown for an amplitude squeezed (a) and phase squeezed (c) state. The probability distribution [Eq. (2.66)] (blue) is shown for an amplitude squeezed (b) and phase squeezed state (d), along with the corresponding distribution for a coherent state without squeezing (orange). The dashed vertical lines indicate the mean photon number [Eq. (2.64)] for the displaced squeezed state, while the vertical dotted line shows the mean photon number for the corresponding coherent state [Eq. (2.54)]. Note in (b), the photon distribution is narrower than its corresponding coherent state, meaning that the photon statistics is sub-Poissonian.

statistics. This is also seen in the expression for the probability to measure m photons [74]

$$
\begin{aligned}
P^{\mathrm{SC}}_{\boldsymbol{k},\sigma}(m) &= |\langle m_{\boldsymbol{k},\sigma} | \alpha_{\boldsymbol{k},\sigma}, \xi_{\boldsymbol{k},\sigma} \rangle|^2 \\
&= \frac{[\frac{1}{2}\tanh(r_{\boldsymbol{k},\sigma})]^m}{m!\cosh(r_{\boldsymbol{k},\sigma})} \\
&\quad \times \exp\left[-|\alpha_{\boldsymbol{k},\sigma}|^2 - |\alpha_{\boldsymbol{k},\sigma}|^2 \cos(2\phi_{\boldsymbol{k},\sigma} - \theta_{\boldsymbol{k},\sigma}) \tanh(r_{\boldsymbol{k},\sigma}) \right] \\
&\quad \times \left| H_m\left\{ \frac{\alpha_{\boldsymbol{k},\sigma}\cosh(r_{\boldsymbol{k},\sigma}) + \alpha^*_{\boldsymbol{k},\sigma} e^{i\theta_{\boldsymbol{k},\sigma}} \sinh(r_{\boldsymbol{k},\sigma})}{\sqrt{e^{i\theta_{\boldsymbol{k},\sigma}} \sinh(2r_{\boldsymbol{k},\sigma})}} \right\} \right|^2 ,
\end{aligned}
\tag{2.66}
$$

where the phase difference enters multiple places. As seen in Fig. 2.2, for $2\phi_{\boldsymbol{k},\sigma}-\theta_{\boldsymbol{k},\sigma}=0$ the state yields sub-Poissonian statistics, while for $2\phi_{\boldsymbol{k},\sigma}-\theta_{\boldsymbol{k},\sigma}=\pm\pi$ the statistics is super-Poissonian. In other words, the phase difference between the coherent and squeezing part determines if the photon statistics is considered nonclassical (for certain values of $|\alpha_{\boldsymbol{k},\sigma}|$ and $r_{\boldsymbol{k},\sigma}$).

Naturally, a displaced squeezed state has a nonzero degree of squeezing. Calculating the variance of the quadrature operator yields

$$\left\langle[\Delta\hat{X}^{\mathrm{SC}}_{\boldsymbol{k},\sigma}(\vartheta_{\boldsymbol{k},\sigma})]^2\right\rangle=\frac{1}{4}[1+2\sinh^2(r_{\boldsymbol{k},\sigma}) -2\cosh(r_{\boldsymbol{k},\sigma})\sinh(r_{\boldsymbol{k},\sigma})\cos(2\vartheta_{\boldsymbol{k},\sigma}-\theta_{\boldsymbol{k},\sigma})]. \tag{2.67}$$

In particular, if we take $\vartheta_{\boldsymbol{k},\sigma}=0$ and the canonical conjugate $\vartheta_{\boldsymbol{k},\sigma}=\pi/2$ in Eq. (2.67) and further choose the squeezing to be along $\theta_{\boldsymbol{k},\sigma}=0$, we find that

$$\left\langle[\Delta\hat{X}^{\mathrm{SC}}_{\boldsymbol{k},\sigma}(0)]^2\right\rangle=\frac{1}{4}e^{-2r_{\boldsymbol{k},\sigma}}, \tag{2.68}$$

$$\left\langle[\Delta\hat{X}^{\mathrm{SC}}_{\boldsymbol{k},\sigma}(\pi/2)]^2\right\rangle=\frac{1}{4}e^{2r_{\boldsymbol{k},\sigma}}, \tag{2.69}$$

which is independent of $\alpha_{\boldsymbol{k},\sigma}$ and where we see that the variance of one quadrature is reduced below the vacuum variance due to the squeezing operator at the expense of anti-squeezing in the conjugate quadrature while the product still satisfies the Heisenberg relation in Eq. (2.36). Note in particular that since one of the quadratures can fluctuate less than a coherent state (or vacuum), a squeezed state has applications in, e.g., quantum sensing [91, 92].

A displaced squeezed state has a mean electric field identical to that of a coherent state in Eq. (2.57) under the evolution of the free field, but with fluctuations given by

$$\left\langle[\Delta\hat{\boldsymbol{E}}^{\mathrm{SC}}_{\boldsymbol{k},\sigma}]^2\right\rangle=g_0^2\omega_k[1+2\sinh^2(r_{\boldsymbol{k},\sigma}) +2\cosh(r_{\boldsymbol{k},\sigma})\sinh(r_{\boldsymbol{k},\sigma})\cos(2\omega_k t-\theta_{\boldsymbol{k},\sigma})], \tag{2.70}$$

which shows that the variance of the electric field can be less than that of vacuum at certain times, depending on the value of $\theta_{\boldsymbol{k},\sigma}$ as seen in Fig. 2.2. Note that the fluctuations oscillate with twice the frequency of the mean field in Eq. (2.57). If the minimum variance occurs at maximum field amplitude, which occurs for $2\phi_{\boldsymbol{k},\sigma}-\theta_{\boldsymbol{k},\sigma}=0$, the light is amplitude squeezed, while if it is minimum at zero field amplitude, which occurs for $2\phi_{\boldsymbol{k},\sigma}-\theta_{\boldsymbol{k},\sigma}=\pm\pi$, it is phase squeezed. Squeezing in amplitude (phase) will be at the expense of anti-squeezing in phase (amplitude). This is also seen in Fig. 2.2, where the mean electric field with its fluctuations is shown for amplitude squeezed light [Fig. 2.2(a)] and phase squeezed light [Fig. 2.2(b)].

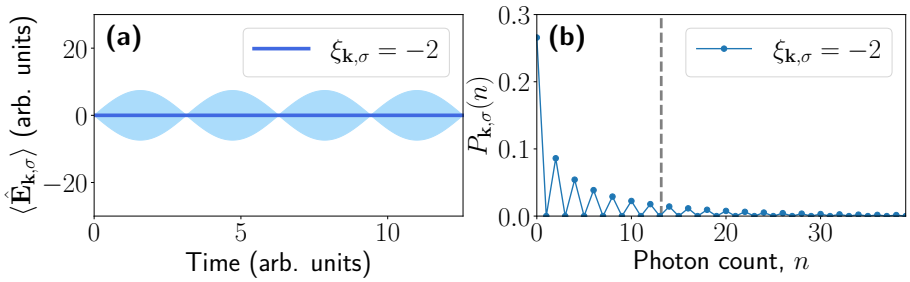

Figure 2.3: Characteristics of a squeezed vacuum state with squeezing parameter defined in Eq. (2.60). (a) The vanishing mean electric field with its fluctuations [Eq. (2.70)]. (b) The probability distribution [Eq. (2.71)] where we note only nonzero values for even photon numbers. The dashed vertical line indicates the mean photon number [Eq. (2.64)].

A special case of a displaced squeezed state is the coherent state ($\xi_{\boldsymbol{k},\sigma} = 0$) from above. Similarly, another special case is the squeezed vacuum state ($\alpha_{\boldsymbol{k},\sigma} = 0$). For intense large degrees of squeezing, this is also referred to as BSV, which has been considered as a nonclassical driver of HHG [5, 160, 165]. Squeezed vacuum is a special kind of state consisting of an even-number photon distribution given by

$$P^{\mathrm{SV}}_{\boldsymbol{k},\sigma}(2m) = \frac{(2m)!}{2^{2m}(m!)^2} \frac{[\tanh(r_{\boldsymbol{k},\sigma})]^{2m}}{\cosh(r_{\boldsymbol{k},\sigma})}, \qquad P^{\mathrm{SV}}_{\boldsymbol{k},\sigma}(2m+1) = 0, \tag{2.71}$$

where the superscript refers to *squeezed vacuum*. A squeezed vacuum state has super-Poissonian statistics as seen from the Mandel-Q parameter [using Eq. (2.65)] $Q^{\mathrm{SV}}_{\boldsymbol{k},\sigma} = 2\sinh^2(r_{\boldsymbol{k},\sigma}) + 1 = 2\langle \hat{n}_{\boldsymbol{k},\sigma} \rangle + 1 > 1$. Identical to a squeezed coherent state, a squeezed vacuum state has reduced fluctuations given by Eq. (2.70), i.e., $\left\langle [\Delta \hat{\boldsymbol{E}}^{\mathrm{SV}}_{\boldsymbol{k},\sigma}]^2 \right\rangle = \left\langle [\Delta \hat{\boldsymbol{E}}^{\mathrm{SC}}_{\boldsymbol{k},\sigma}]^2 \right\rangle$ but in contrast it has no mean electric field, i.e., $\langle \hat{\boldsymbol{E}}^{\mathrm{SV}}_{\boldsymbol{k},\sigma} \rangle = 0$. The characteristics of the squeezed vacuum state are seen in Fig. 2.3. Note that the probability distributions for a phase-squeezed state [Fig. 2.2(d)] and the squeezed vacuum [Fig. 2.3(b)] has a long tail reaching to high photon numbers. This will be relevant when discussing nonclassical driving fields in Ch. 5.

2.2.3.3 Fock state

A previously introduced, the Fock states are denoted $|n_{\boldsymbol{k},\sigma}\rangle$ for mode $(\boldsymbol{k},\sigma)$. It is a state with a well-defined number of excitation, or, as is the case here, the number of photons. In other words, for a Fock state, $|n_{\boldsymbol{k},\sigma}\rangle$, the probability to

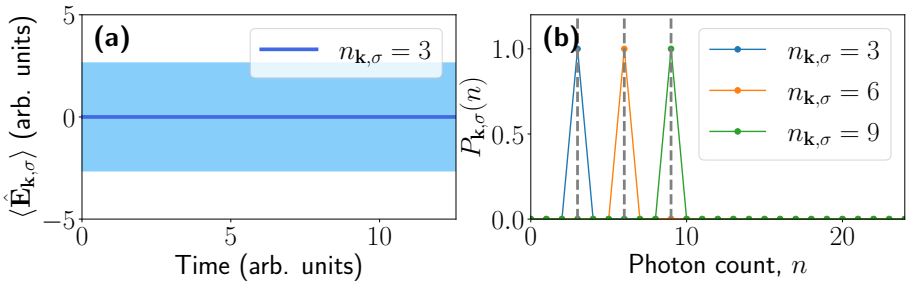

Figure 2.4: Characteristics of a Fock state. (a) The vanishing mean electric field with its fluctuations [Eq. (2.74)]. (b) The probability distribution [Eq. (2.72)] for different values of $n_{\boldsymbol{k},\sigma}$. The dashed vertical lines indicate the mean photon numbers [Eq. (2.73)].

measure m photons is

$$P^{\text{Fock}}_{\boldsymbol{k},\sigma}(m) = \delta_{m,n}, \tag{2.72}$$

and consequently

$$\langle \hat{n}_{\boldsymbol{k},\sigma} \rangle = n_{\boldsymbol{k},\sigma}. \tag{2.73}$$

As a Fock state has no variance in the photon number, it is the *most* sub-Poissonian state with the Mandel-Q parameter $Q^{\text{Fock}}_{\boldsymbol{k},\sigma} = -1$ for any n, showing that it is highly nonclassical. Despite this, a Fock state has no quadrature squeezing as $\left\langle [\Delta \hat{X}_{\boldsymbol{k},\sigma}(\vartheta_{\boldsymbol{k},\sigma})]^2 \right\rangle = \frac{1}{4}(2n+1) > \frac{1}{4}$. Additionally, a Fock state has no mean electric field $\langle \hat{\boldsymbol{E}}^{\text{Fock}}_{\boldsymbol{k},\sigma} \rangle = 0$ but has nonvanishing fluctuations

$$\left\langle [\Delta \hat{\boldsymbol{E}}^{\text{Fock}}_{\boldsymbol{k},\sigma}]^2 \right\rangle = g_0^2 \omega_k (2n+1). \tag{2.74}$$

In general, it is experimentally hard to generate Fock states with more than a few photons. It is, however, considered theoretically as a nonclassical driving field in quantum optical HHG. The characteristics of a Fock state are seen in Fig. 2.4.

2.2.3.4 Thermal state

A last quantum optical state of interest is the thermal state. This is the state of light emitted by an ideal black body in equilibrium described by Planck's radiation law. A thermal state is not a pure state, in contrast to the states introduced above, but it is instead a statistical mixture of pure states and is characterized by random phases and amplitude fluctuations. A thermal state is

described by the density matrix [74]

$$\hat{\rho}^{\mathrm{Th}}_{\boldsymbol{k},\sigma} = \frac{1}{1+\bar{n}_{\boldsymbol{k},\sigma}} \sum_{n=0}^{\infty} \left(\frac{\bar{n}_{\boldsymbol{k},\sigma}}{1+\bar{n}_{\boldsymbol{k},\sigma}} \right)^{n} |n_{\boldsymbol{k},\sigma}\rangle\langle n_{\boldsymbol{k},\sigma}|, \tag{2.75}$$

where the superscript indicates a thermal state and

$$\langle \hat{n}_{\boldsymbol{k},\sigma} \rangle = \bar{n}_{\boldsymbol{k},\sigma} \tag{2.76}$$

denotes the mean photon number. As the state describes a statistical mixture, it is easily seen that the probability of measuring m photons is given by

$$P^{\mathrm{Th}}_{\boldsymbol{k},\sigma}(m) = \frac{\bar{n}^{m}_{\boldsymbol{k},\sigma}}{(1+\bar{n}_{\boldsymbol{k},\sigma})^{m+1}}. \tag{2.77}$$

Thermal light has the property that $\langle \hat{n}^2_{\boldsymbol{k},\sigma} \rangle = \bar{n}^2_{\boldsymbol{k},\sigma} + \bar{n}_{\boldsymbol{k},\sigma}$ and it then follow that $Q^{\mathrm{Th}}_{\boldsymbol{k},\sigma} = \bar{n}_{\boldsymbol{k},\sigma}$, showing super-Poissonian photon statistics. Further, the variance of the quadrature operator for thermal light is

$$\left\langle [\Delta \hat{X}_{\boldsymbol{k},\sigma}(\vartheta_{\boldsymbol{k},\sigma})]^2 \right\rangle = \frac{1}{4}(2\bar{n}_{\boldsymbol{k},\sigma}+1), \tag{2.78}$$

which is larger than the fluctuations of the vacuum, and, consequently, a thermal state has no degree of squeezing. Finally, the mean electric field of a thermal state vanishes, $\langle \hat{\boldsymbol{E}}^{\mathrm{Th}}_{\boldsymbol{k},\sigma} \rangle = 0$ with the variance

$$\left\langle [\Delta \hat{\boldsymbol{E}}^{\mathrm{Th}}_{\boldsymbol{k},\sigma}]^2 \right\rangle = g_0^2 \omega_k (2\bar{n}_{\boldsymbol{k},\sigma}+1), \tag{2.79}$$

which again are constant in time and larger than the variance of the vacuum. The characteristics of a thermal state are summarized in Fig. 2.5. Similarly to the photon distribution for squeezed coherent states [Eq. (2.66)] and in squeezed vacuum states [Eq. (2.71)] the distribution in Eq. (2.77) has a longer tail in the photon distribution. This will be of importance when discussing nonclassical driving fields in Ch. 5.

2.2.4 Phase-space representation of quantum optical states

For many purposes, it can be beneficial and instructive to describe quantum optics in a phase-space representation. Often, the coordinates of such phase space are the quadratures in Eq. (2.35) with $\vartheta_{\boldsymbol{k},\sigma} = 0, \pm\pi$. For the present purpose in strong-field quantum optics, the use of the quantum optical phase space allows one to express nonclassical states of light in terms of the more familiar coherent states. This will be central for nonclassical driving fields in

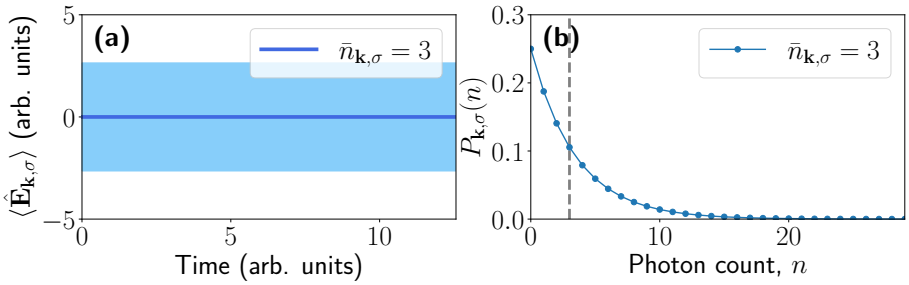

Figure 2.5: Characteristics of a thermal state. (a) The vanishing mean electric field with its fluctuations [Eq. (2.79)]. (b) The probability distribution [Eq. (2.77)]. The dashed vertical line indicates the mean photon number [Eq. (2.76)].

HHG, as will be discussed in Ch. 5, and we choose to introduce the general and central equations here.

Consider the state $\hat{\rho}_{\boldsymbol{k},\sigma} = |\psi_{\boldsymbol{k},\sigma}\rangle\langle\psi_{\boldsymbol{k},\sigma}|$ in mode $(\boldsymbol{k},\sigma)$. By inserting two complete sets of coherent states, one can express the single-mode state as

$$\hat{\rho}_{\boldsymbol{k},\sigma} = \int d\mu_{\boldsymbol{k},\sigma}\; P(\alpha_{\boldsymbol{k},\sigma}, \beta_{\boldsymbol{k},\sigma}) \frac{|\alpha_{\boldsymbol{k},\sigma}\rangle\langle\beta^*_{\boldsymbol{k},\sigma}|}{\langle\beta^*_{\boldsymbol{k},\sigma}|\alpha_{\boldsymbol{k},\sigma}\rangle}, \tag{2.80}$$

where $P(\alpha,\beta)$ is a P distribution and $d\mu$ is the integration measure. Equation (2.80) is called a *general P representation*. Due to the fact that the coherent states are non-orthogonal and form an overcomplete set, $d\mu$ can be chosen in different ways which also determines the form of $P(\alpha_{\boldsymbol{k},\sigma}, \beta_{\boldsymbol{k},\sigma})$ [172]. The existence of such measures is discussed in Ref. [178]. The representations of interest in the thesis are

Glauber-Sudarshan representation: In the Glauber-Sudarshan (GS) representation, the integration measure is chosen as $d\mu_{\boldsymbol{k},\sigma} = \delta^{(2)}(\alpha_{\boldsymbol{k},\sigma} - \beta^*_{\boldsymbol{k},\sigma})$, where $\delta^{(2)}$ denotes a two-dimensional delta function. This choice of integration measure gives the diagonal representation

$$\hat{\rho}_{\boldsymbol{k},\sigma} = \int d^2\alpha_{\boldsymbol{k},\sigma} P(\alpha_{\boldsymbol{k},\sigma}) |\alpha_{\boldsymbol{k},\sigma}\rangle\langle\alpha_{\boldsymbol{k},\sigma}|. \tag{2.81}$$

The advantage of the GS representation is that it is relatively simple, as it is diagonal, such that only a two-dimensional integral has to be evaluated. Unfortunately, the GS representation can be highly singular for nonclassical states, as seen below. Therefore, it is not always possible to calculate expectation values using the GS representation.

Positive P representation: In the positive P representation, the integration measure is chosen as $d\mu_{\boldsymbol{k},\sigma} = d^2\alpha_{\boldsymbol{k},\sigma} d^2\beta_{\boldsymbol{k},\sigma}$ which gives the

representation

$$\hat{\rho}_{\boldsymbol{k},\sigma} = \int d^2\alpha_{\boldsymbol{k},\sigma} d^2\beta_{\boldsymbol{k},\sigma} P(\alpha_{\boldsymbol{k},\sigma}, \beta_{\boldsymbol{k},\sigma}) \frac{|\alpha_{\boldsymbol{k},\sigma}\rangle\langle\beta^*_{\boldsymbol{k},\sigma}|}{\langle\beta^*_{\boldsymbol{k},\sigma}|\alpha_{\boldsymbol{k},\sigma}\rangle}, , \tag{2.82}$$

which involves a four-dimensional integral and is hence more demanding with respect to numerical evaluation. The advantage of the positive P representation is that $P(\alpha_{\boldsymbol{k},\sigma}, \beta_{\boldsymbol{k},\sigma})$ always exists, is smooth and positive, and can therefore be interpreted as a true probability distribution.

The positive P representation is proportional to the Husimi-Q function via [179]

$$P(\alpha_{\boldsymbol{k},\sigma}, \beta_{\boldsymbol{k},\sigma}) = \frac{1}{4\pi} e^{-\frac{\left|\alpha_{\boldsymbol{k},\sigma} - \beta^*_{\boldsymbol{k},\sigma}\right|^2}{4}} \mathcal{Q}\left(\frac{\alpha_{\boldsymbol{k},\sigma} + \beta^*_{\boldsymbol{k},\sigma}}{2}\right), \tag{2.83}$$

where the Husimi-Q function is given as

$$\mathcal{Q}(\alpha_{\boldsymbol{k},\sigma}) = \frac{\langle\alpha_{\boldsymbol{k},\sigma}|\rho_{\boldsymbol{k},\sigma}|\alpha_{\boldsymbol{k},\sigma}\rangle}{\pi}. \tag{2.84}$$

Note that we use the symbol $\mathcal{Q}$ for the Husimi-Q function to distinguish it from the Mandel-Q parameter, $Q_{\boldsymbol{k},\sigma}$ in Eq. (2.32). In the research papers, the symbol Q is used to express both, but the two concepts do not appear in the same research papers. The Husimi-Q function often appears when calculating anti-normal ordered expectation values and is normalized as seen from

$$1 = \mathrm{Tr}(\hat{\rho}_{\boldsymbol{k},\sigma}) = \int \frac{d^2\alpha_{\boldsymbol{k},\sigma}}{\pi} \langle\alpha_{\boldsymbol{k},\sigma}|\rho_{\boldsymbol{k},\sigma}|\alpha_{\boldsymbol{k},\sigma}\rangle = \int d^2\alpha_{\boldsymbol{k},\sigma} \mathcal{Q}(\alpha_{\boldsymbol{k},\sigma}), \tag{2.85}$$

resembling the normalization of a probability distribution. Due to the fact that the positive P function, $P(\alpha_{\boldsymbol{k},\sigma}, \beta_{\boldsymbol{k},\sigma})$ is four-dimensional, it is not possible to plot it. However, as it is related to the Husimi-Q function [Eq. (2.83)], one can illustrate the Husimi-Q function instead, as done in Fig. 2.6 for the quantum states of interest.

Using the phase-space representations, expectation values for an operator $\hat{O}_{\boldsymbol{k},\sigma}$ can be calculated as (using the GS representation as an example)

$$\begin{aligned}
\left\langle \hat{O}_{\boldsymbol{k},\sigma} \right\rangle &= \mathrm{Tr}\left(\hat{\rho}_{\boldsymbol{k},\sigma} \hat{O}_{\boldsymbol{k},\sigma}\right) \\
&= \frac{1}{\pi} \int d^2\alpha_{\boldsymbol{k},\sigma} d^2\beta_{\boldsymbol{k},\sigma} P(\alpha_{\boldsymbol{k},\sigma}) \langle\beta_{\boldsymbol{k},\sigma}|\hat{O}_{\boldsymbol{k},\sigma}|\alpha_{\boldsymbol{k},\sigma}\rangle \langle\alpha_{\boldsymbol{k},\sigma}|\beta_{\boldsymbol{k},\sigma}\rangle \\
&= \int d^2\alpha_{\boldsymbol{k},\sigma} P(\alpha_{\boldsymbol{k},\sigma}) \langle\alpha_{\boldsymbol{k},\sigma}|\hat{O}_{\boldsymbol{k},\sigma}|\alpha_{\boldsymbol{k},\sigma}\rangle,
\end{aligned} \tag{2.86}$$

where it has been used that $\mathbb{I} = \pi^{-1} \int d^2\beta_{\boldsymbol{k},\sigma} |\beta_{\boldsymbol{k},\sigma}\rangle\langle\beta_{\boldsymbol{k},\sigma}|$. Equation (2.86) highlights one of the main advantages of a phase-space representation of (nonclassical)

states of light: Expectation values are obtained by calculating the expectation value from a coherent state weighted by an appropriate probability distribution. In this sense, the expectation values from nonclassical light become a weighted average of classical expectation values. We will now introduce the GS P function and the Husimi-Q function for the quantum states of interest below.

Coherent state. For a coherent state given by $|\beta_{\boldsymbol{k},\sigma}\rangle$, the GS P and Husimi-Q functions are given as

$$P_{\mathrm{GS}}^{\mathrm{Coh}}(\alpha_{\boldsymbol{k},\sigma}) = \delta^{(2)}(\alpha_{\boldsymbol{k},\sigma} - \beta_{\boldsymbol{k},\sigma}), \tag{2.87}$$

$$\mathcal{Q}^{\mathrm{Coh}}(\alpha_{\boldsymbol{k},\sigma}) = \frac{1}{\pi} e^{-|\alpha_{\boldsymbol{k},\sigma} - \beta_{\boldsymbol{k},\sigma}|^2}. \tag{2.88}$$

Squeezed coherent state. For a squeezed coherent state given by $|\beta_{\boldsymbol{k},\sigma}, \xi_{\boldsymbol{k},\sigma}\rangle$, no GS P function is found in the literature. The Husimi-Q function is given as

$$\begin{aligned}\mathcal{Q}^{\mathrm{SC}}(\alpha_{\boldsymbol{k},\sigma}) =& \frac{1}{\pi \cosh(r_{\boldsymbol{k},\sigma})} \exp\big\{ - |\alpha_{\boldsymbol{k},\sigma}|^2 - |\beta_{\boldsymbol{k},\sigma}|^2 \\ &+ (\beta^*_{\boldsymbol{k},\sigma}\alpha_{\boldsymbol{k},\sigma} + \beta_{\boldsymbol{k},\sigma}\alpha^*_{\boldsymbol{k},\sigma})/\cosh(r_{\boldsymbol{k},\sigma}) \\ &+ \frac{\tanh(r_{\boldsymbol{k},\sigma})}{2} \\ &\times [e^{i\theta_{\boldsymbol{k},\sigma}}(\beta^{*2}_{\boldsymbol{k},\sigma} - \alpha^{*2}_{\boldsymbol{k},\sigma}) + e^{-i\theta_{\boldsymbol{k},\sigma}}(\beta^2_{\boldsymbol{k},\sigma} - \alpha^2_{\boldsymbol{k},\sigma})]\big\}. \end{aligned} \tag{2.89}$$

Squeezed vacuum state. For a squeezed vacuum state given by $|\xi_{\boldsymbol{k},\sigma}\rangle$, the GS P and Husimi-Q functions are given as (see a derivation in App. A).

$$P_{\mathrm{GS}}^{\mathrm{SV}}(\alpha_{\boldsymbol{k},\sigma}) = \frac{e^{|\alpha_{\boldsymbol{k},\sigma}|^2}}{\pi} \sum_{m,n=0}^{\infty} C_{2m} C^*_{2n} \frac{\partial^{2m+2n}}{\partial \alpha^{2m}_{\boldsymbol{k},\sigma} \partial \alpha^{*2n}_{\boldsymbol{k},\sigma}} \delta^{(2)}(\alpha_{\boldsymbol{k},\sigma}), \tag{2.90}$$

$$\begin{aligned}\mathcal{Q}^{\mathrm{SV}}(\alpha_{\boldsymbol{k},\sigma}) =& \frac{1}{\pi \cosh(r_{\boldsymbol{k},\sigma})} \exp\big\{ - |\alpha_{\boldsymbol{k},\sigma}|^2 \\ &- \frac{\tanh(r_{\boldsymbol{k},\sigma})}{2} [e^{i\theta_{\boldsymbol{k},\sigma}} \alpha^{*2}_{\boldsymbol{k},\sigma} + e^{-i\theta_{\boldsymbol{k},\sigma}} \alpha^2_{\boldsymbol{k},\sigma}]\big\} \end{aligned} \tag{2.91}$$

where $C_{2m} = (-1)^m [e^{i\theta_{\boldsymbol{k},\sigma}} \tanh(r_{\boldsymbol{k},\sigma})]^m / [2^m m! \sqrt{\cosh(r_{\boldsymbol{k},\sigma})}]$ in Eq. (2.90) and where the derivative of the δ-function is understood in the distributional sense.

Fock state. For a Fock state given by $|n_{\boldsymbol{k},\sigma}\rangle$, the GS P and the Husimi-Q

functions are given as

$$P_{\mathrm{GS}}^{\mathrm{Fock}}(\alpha_{\boldsymbol{k},\sigma}) = \frac{e^{|\alpha|^2}}{n_{\boldsymbol{k},\sigma}!}\frac{\partial^{2n}}{\partial\alpha_{\boldsymbol{k},\sigma}^{n}\partial\alpha_{\boldsymbol{k},\sigma}^{*n}}\delta^{(2)}(\alpha_{\boldsymbol{k},\sigma}), \tag{2.92}$$

$$\mathcal{Q}^{\mathrm{Fock}}(\alpha_{\boldsymbol{k},\sigma}) = \frac{1}{\pi}e^{-|\alpha_{\boldsymbol{k},\sigma}^2|}\frac{|\alpha|^{2n_{\boldsymbol{k},\sigma}}}{n_{\boldsymbol{k},\sigma}!}. \tag{2.93}$$

Thermal state. For a thermal state characterized by mean photon number $\bar{n}_{\boldsymbol{k},\sigma}$, the GS P and Husimi-Q functions are given as

$$P_{\mathrm{GS}}^{\mathrm{Th}}(\alpha_{\boldsymbol{k},\sigma}) = \frac{1}{\pi\bar{n}_{\boldsymbol{k},\sigma}}e^{-|\alpha_{\boldsymbol{k},\sigma}^2|/(\bar{n}_{\boldsymbol{k},\sigma})}, \tag{2.94}$$

$$\mathcal{Q}^{\mathrm{Th}}(\alpha_{\boldsymbol{k},\sigma}) = \frac{1}{\pi(1+\bar{n}_{\boldsymbol{k},\sigma})}e^{-|\alpha_{\boldsymbol{k},\sigma}^2|/(1+\bar{n}_{\boldsymbol{k},\sigma})}. \tag{2.95}$$

We note that the GS P representations for both squeezed vacuum [Eq. (2.90)] and Fock states [2.92] are highly singular and not useful for the calculation of expectation values.

The Husimi-Q function is shown for the various states in Fig. 2.6. Note that $\langle\hat{X}_{\boldsymbol{k},\sigma}(0)\rangle = \mathrm{Re}(\alpha_{\boldsymbol{k},\sigma})$ and $\langle\hat{X}_{\boldsymbol{k},\sigma}(\pi/2)\rangle = \mathrm{Im}(\alpha_{\boldsymbol{k},\sigma})$. From the figures in Fig. 2.6, one can see that only the states that are not symmetric around the origin yield a nonvanishing mean electric field.

2.2.5 Quantum-optical light-matter coupling

In a fully quantum optical description of light-matter coupling, both the electrons *and* the light are quantized. This means that in a quantum optical description, the classical vector potential in the semiclassical description in the velocity gauge in Eq. (2.8) is now promoted to the quantized field operator given in Eq. (2.18). The quantum optical Hamiltonian for N particles with identical charge Q and mass m is then, in the velocity gauge, given as

$$\hat{H}_{\mathrm{VG}} = \frac{1}{2m}\sum_{j}^{N}[\hat{\boldsymbol{p}}_j - Q\hat{\boldsymbol{A}}(\hat{\boldsymbol{r}})]^2 + \hat{U} + \hat{H}_F, \tag{2.96}$$

where the explicit dependence of the particle coordinates has been neglected for clarity. Further, in the quantum optical description, the Hamiltonian of the free field [Eq. (2.17)] has to be included. In total, this yields the TDSE

$$i\partial_t|\Psi(\boldsymbol{r},t)\rangle = \hat{H}_{VG}(\hat{\boldsymbol{r}})|\Psi(\boldsymbol{r},t)\rangle, \tag{2.97}$$

where we note that the total wavefunction of the system, $|\Psi(\boldsymbol{r},t)\rangle$, describes the combined state of both electrons and photons. Further, we point out that

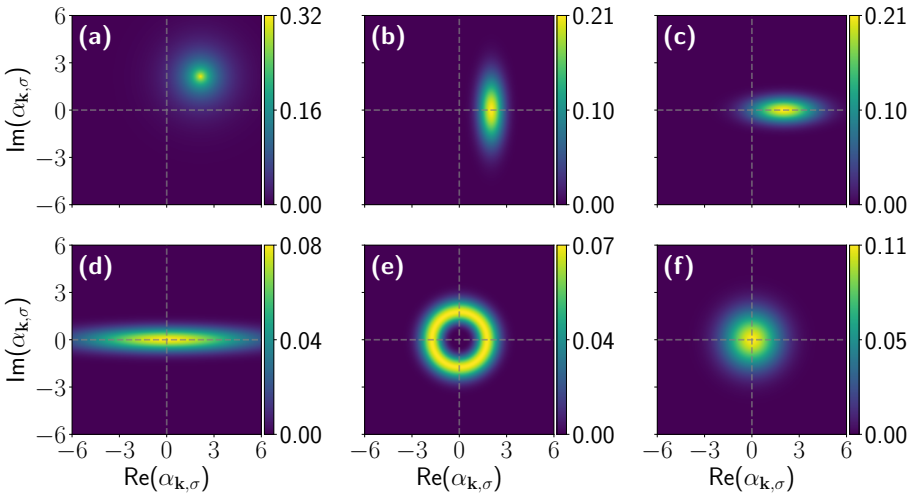

Figure 2.6: The Husimi-Q function for (a) a coherent state, (b) an amplitude squeezed coherent state, (c) a phase squeezed coherent state, (d) a squeezed vacuum state, (e) a Fock state, and (f) a thermal state. Gray dashed lines are inserted at $\mathrm{Re}(\alpha_{\boldsymbol{k},\sigma}) = \mathrm{Im}(\alpha_{\boldsymbol{k},\sigma}) = 0$ to guide the eye.

expanding the first term in Eq. (2.96) will yield a term $\propto [\hat{\boldsymbol{A}}(\hat{\boldsymbol{r}})]^2$, which, different to the semiclassical case, does not only yield a time dependent phase on the wavefunction. However, this term is often neglected in quantum optical HHG [2–4, 132]. This matter is discussed in detail in Sec. 4.1.1.

Furthermore, a length-gauge description of quantum-optical light-matter coupling can be obtained within the dipole approximation. By defining the unitary operator

$$\hat{T} = \exp\left[-i\sum_j \hat{\boldsymbol{d}}_j \cdot \hat{\boldsymbol{A}}(0)\right] = \exp\left[\sum_{\boldsymbol{k},\sigma}(\lambda^*_{\boldsymbol{k},\sigma}\hat{a}_{\boldsymbol{k},\sigma} - \lambda_{\boldsymbol{k},\sigma}\hat{a}^\dagger_{\boldsymbol{k},\sigma})\right], \tag{2.98}$$

where we have recognized the form of a displacement operator similar to Eq. (2.44) with displacement parameter given by

$$\lambda_{\boldsymbol{k},\sigma} = \frac{g_0}{\sqrt{\omega_k}}\boldsymbol{e}_\sigma \cdot \sum_j \hat{\boldsymbol{d}}_j, \tag{2.99}$$

where $\hat{\boldsymbol{d}} = \sum_j Q\hat{\boldsymbol{r}}_j$ is the electric dipole moments of identical particles of charge Q. Using the operator in Eq. (2.98) to transform the VG Hamiltonian in Eq.

(2.96) yields the LG Hamiltonian [170]

$$\begin{aligned}\hat{H}_{\mathrm{LG}} =& \hat{T}\hat{H}_{\mathrm{VG}}\hat{T}^{\dagger} \\ &= \sum_j \frac{\hat{\boldsymbol{p}}_j^2}{2m} + \hat{U} + \hat{H}_F - \hat{\boldsymbol{d}}\cdot\hat{\boldsymbol{E}} + \epsilon_{\mathrm{dip}},\end{aligned} \tag{2.100}$$

where ϵ_{dip} is a correction term given by

$$\epsilon_{\mathrm{dip}} = \sum_{\boldsymbol{k},\sigma} g_0^2(\boldsymbol{e}_\sigma \cdot \sum_j \hat{\boldsymbol{d}}_j)^2, \tag{2.101}$$

which, just like the term proportional to $\hat{\boldsymbol{A}}^2$ in the VG description, is neglected in quantum optical HHG [137] (See Sec. 4.1.1).

Equation (2.96) will be the starting point for quantum optical HHG in the thesis. As will become apparent, the VG description is particularly suitable for describing systems with periodic boundary conditions, as is the case for the electronic system considered in the thesis.

CHAPTER 3

The Hubbard Model - a semiclassical description

The electronic system considered in this thesis and in the associated research papers is the Fermi-Hubbard model. This prototypical model captures beyond-mean-field electron dynamics and has been shown to capture important physical properties of real materials. In particular, it is used to model cuprates, which include high-T_c superconductors [180, 181]. This model has been used extensively to study electron-electron correlation effects in HHG semiclassically [63–66, 182]. For the prospect of the present thesis, the motivation to consider the Fermi-Hubbard model is the effect of electron-electron correlations on the quantum nature of the emitted harmonics.

This chapter first derives the Fermi-Hubbard model in Sec. 3.1 followed by an analysis of the different phases of the model in Sec. 3.2 and a brief explanation of the numerical implementation in Sec. 3.3. Finally, the Fermi-Hubbard model will be employed as the generating medium for HHG from a semiclassical perspective in its different phases in Sec. 3.4. Here, the results from Paper I will be presented. Note that the Fermi-Hubbard model will also be referred to as the Hubbard model.

3.1 Derivation of the Hubbard Model

The Fermi-Hubbard model will now be derived. This derivation builds on Ref. [183] and first considers the field-free system before adding the driving field afterwards in Sec. 3.1.1.

We start by considering a generic Hamiltonian of N_e interacting electrons

$$\hat{H} = \sum_{j=1}^{N_e} \left[\frac{\hat{\boldsymbol{p}}_j^2}{2} + \hat{V}_{\text{N-e}}(\hat{\boldsymbol{r}}_j) \right] + \frac{1}{2} \sum_{i,j}^{N_e} \hat{V}_{\text{e-e}}(\hat{\boldsymbol{r}}_i, \hat{\boldsymbol{r}}_j), \tag{3.1}$$

where again the $\hat{\boldsymbol{r}}_j$ and $\hat{\boldsymbol{p}}_j$ is the position and momentum of the j'th electron, respectively, $\hat{V}_{\text{N-e}}(\hat{\boldsymbol{r}}_j)$ is the Coulomb interaction between the j'th electron and all atomic nuclei, and $\hat{V}_{\text{e-e}}(\hat{\boldsymbol{r}}_i, \hat{\boldsymbol{r}}_j)$ is the Coulomb interaction between the i'th and j'th electron. In Eq. (3.1), the coupling of the electrons' spin degree of freedom to the magnetic field has been neglected due to the lower energy contribution, and the nuclei have been assumed to be stationary as they are much heavier than the electrons. We now proceed by separating the interactions into mean-field interactions and beyond-mean-field interactions. This separates the Hamiltonian into

$$\hat{H} = \sum_j \hat{h}(\hat{\boldsymbol{r}}_j, \hat{\boldsymbol{p}}_j) + \frac{1}{2} \sum_{i,j} \hat{U}(\hat{\boldsymbol{r}}_i, \hat{\boldsymbol{r}}_j), \tag{3.2}$$

where

$$\hat{h}(\hat{\boldsymbol{r}}, \hat{\boldsymbol{p}}) = \frac{\hat{\boldsymbol{p}}^2}{2} + \hat{V}_{\text{N-e}}(\hat{\boldsymbol{r}}) + V_{\langle \text{e-e} \rangle}(\hat{\boldsymbol{r}}), \tag{3.3}$$

$$\hat{U}(\hat{\boldsymbol{r}}_i, \hat{\boldsymbol{r}}_j) = \hat{V}_{\text{e-e}}(\hat{\boldsymbol{r}}_i, \hat{\boldsymbol{r}}_j) - \frac{1}{N_e - 1} \left[V_{\langle \text{e-e} \rangle}(\hat{\boldsymbol{r}}_j) + V_{\langle \text{e-e} \rangle}(\hat{\boldsymbol{r}}_i) \right], \tag{3.4}$$

where $\hat{h}(\hat{\boldsymbol{r}}_j, \hat{\boldsymbol{p}}_j)$ describes the single-electron Hamiltonian in a Coulomb potential from the nuclei and the mean field of the other electrons denoted by $V_{\langle \text{e-e} \rangle}(\hat{\boldsymbol{r}})$. Equation (3.4) describes the beyond-mean-field contributions to the electron-electron interactions. We now assume that the electrons are ordered in a periodic lattice. One can think of this as the atoms being fixed in a regular lattice, each with a single active electron. In many cases, Eq. (3.4) is neglected and the system is modeled as a sum of single-electron operators [Eq. (3.3)] which massively simplifies the dynamics, yielding the familiar Bloch picture of noninteracting electrons. However, the Hubbard model keeps the beyond-mean-field terms [Eq. (3.4)] which correlate the electrons and, consequently, the electron dynamics becomes more involved.

Often in periodic systems, a convenient basis is the Bloch basis given by states on the form

$$|\phi_{\boldsymbol{q},m}(\boldsymbol{r})\rangle = e^{i\boldsymbol{q}\cdot\boldsymbol{r}} |u_{\boldsymbol{q},m}(\boldsymbol{r})\rangle, \tag{3.5}$$

where $\boldsymbol{q}$ is the crystal momentum of an electron, m is the band index, and $|u_{\boldsymbol{q},m}(\boldsymbol{r})\rangle$ is a lattice-periodic function, i.e., $|u_{\boldsymbol{q},m}(\boldsymbol{r}+R)\rangle = |u_{\boldsymbol{q},m}(\boldsymbol{r})\rangle$. A Bloch state satisfies the time-independent Schrödinger equation $\hat{h}|\phi_{\boldsymbol{q},m}(\boldsymbol{r})\rangle = \mathcal{E}_{m,\boldsymbol{q}}|\phi_{\boldsymbol{q},m}(\boldsymbol{r})\rangle$ with energy $\mathcal{E}_{m,\boldsymbol{q}}$.

However, as Eq. (3.4) correlates the electrons, the crystal momentum of the single electron is, in general, not preserved in the Hubbard model. Consequently, it is easier to proceed from a real-space basis. We use the Wannier basis, which is the Fourier transform of the Bloch basis

$$|\psi_{m,j}(\boldsymbol{r})\rangle = \frac{1}{\sqrt{L}} \sum_{\boldsymbol{q}} e^{-i\boldsymbol{q}\cdot\boldsymbol{R}_j} |\phi_{m,\boldsymbol{q}}(\boldsymbol{r})\rangle, \tag{3.6}$$

where L denotes the number of sites in the periodic lattice and i indicates that the wavefunction is localized on the lattice site at position $\boldsymbol{R}_i$. We now proceed by using the language of second quantization where we define the electronic annihilation operator $\hat{c}_{m,j,\mu}$ which annihilates an electron of spin $\mu = \uparrow, \downarrow$ on site with index j in band m with the Hermitian conjugate $\hat{c}^\dagger_{m,j,\mu}$ being the electronic creation operator. These operators satisfy the Fermionic anticommutation relations

$$\{\hat{c}_\alpha, \hat{c}_\beta\} = \{\hat{c}^\dagger_\alpha, \hat{c}^\dagger_\beta\} = 0, \quad \{\hat{c}_\alpha, \hat{c}^\dagger_\beta\} = \delta_{\alpha,\beta}, \tag{3.7}$$

where $\{\hat{A}, \hat{B}\} = \hat{A}\hat{B} + \hat{B}\hat{A}$ is the anticommutator and α, β are arbitrary indices. The Wannier state created by the operator $\hat{c}^\dagger_{m,j,\mu}$ is highly localized in real space (on site $\boldsymbol{R}_j$) and is related to a highly delocalized Bloch state in crystal-momentum space via the Fourier transform

$$\hat{c}^\dagger_{m,j,\mu} = \frac{1}{\sqrt{L}} \sum_{\boldsymbol{k}} e^{-i\boldsymbol{k}\cdot\boldsymbol{R}_j} \hat{c}^\dagger_{m,\boldsymbol{q},\mu}, \tag{3.8}$$

where $\hat{c}^\dagger_{m,\boldsymbol{q},\mu}$ creates an electron in band m, spin μ and crystal momentum $\boldsymbol{q}$. Expressing the Hamiltonian in Eq. (3.2) in second quantization yields [183]

$$\hat{H} = \sum_{\substack{i,j \\ m,n \\ \mu}} t^m_{i,j} \hat{c}^\dagger_{m,i,\mu} \hat{c}_{n,j,\mu} + \sum_{\substack{m,n,o,p \\ i,j,k,l \\ \mu,\gamma}} U^{m,n,o,p}_{i,j,k,l} \hat{c}^\dagger_{m,i,\mu} \hat{c}^\dagger_{n,j,\gamma} \hat{c}_{o,k,\gamma} \hat{c}_{p,l,\mu}, \tag{3.9}$$

where the matrix elements are given by

$$t^m_{i,j} = \int d\boldsymbol{r} \psi^*_m(\boldsymbol{r}-\boldsymbol{R}_i) \hat{h} \psi_m(\boldsymbol{r}-\boldsymbol{R}_j), \tag{3.10}$$

$$U^{m,n,o,p}_{i,k,k,l} = \int d\boldsymbol{r} d\boldsymbol{r}' \psi^*_m(\boldsymbol{r}-\boldsymbol{R}_i) \psi^*_n(\boldsymbol{r}'-\boldsymbol{R}_j) \hat{U}(\hat{\boldsymbol{r}}, \hat{\boldsymbol{r}}') \psi_o(\boldsymbol{r}'-\boldsymbol{R}_k) \psi_p(\boldsymbol{r}-\boldsymbol{R}_l), \tag{3.11}$$

where i, j, k, l are site indices, m, n, o, p band indices, and μ, σ are spin indices. As seen from the fact that Eq. (3.9) contains many site and band indexes, it contains too many states to be handled numerically. Consequently, approximations must be made on Eq. (3.9). Firstly, we assume the system to be one-dimensional. In the case of an applied electromagnetic field with linear polarization, the dominant electron dynamics will be along the polarization axis, motivating the approximation. Secondly, we restrict the model to only consider a single band. This approximation is justified when the Fermi surface lies inside a single band, and we then set $m = n = o = p = 1$ and hence only consider $t^1_{i,j}$ and $U^{1,1,1,1}_{i,j,k,l}$. Effectively, bands with energies above the Fermi surface are treated as higher-lying with much higher energy, and are unreachable during the system dynamics. Further, we assume a perfectly periodic lattice with inversion symmetry, and that the Wannier states are highly localized around a site such that only nearest-neighbor transitions are included and only onsite and nearest-neighbor interactions are accounted for. Further, we set the zero-point energy appropriately such that $t_{j,j} = 0$ and take all sites to be identical. Mathematically, this leaves only a few terms to consider. The hopping amplitude is set $t^m_{i,j} = -t_0\delta_{i,i\pm1}$, which means that the hopping is symmetric in space and only considers nearest-neighbor transitions. The sign is added to ensure a positive value of t_0. The interaction term is split into two parts: $U = U^{1,1,1,1}_{i,i,i,i}$ is the onsite electron-electron repulsion ($U > 0$) and $V = U^{1,1,1,1}_{i,i+1,i+1,i}$ is the nearest-neighbor electron-electron repulsion ($V > 0$). With these approximations, we finally arrive at the Fermi-Hubbard model

$$\hat{H}_{\mathrm{FH}} = \hat{H}_{\mathrm{Hop}} + \hat{H}_U + \hat{H}_V, \tag{3.12}$$

where

$$\hat{H}_{\mathrm{Hop}} = -t_0 \sum_{j,\mu} \left[\hat{c}^\dagger_{i,\mu} \hat{c}_{i+1,\mu} + \mathrm{h.c} \right], \tag{3.13}$$

$$\hat{H}_U = U \sum_j \hat{n}_{j,\uparrow} \hat{n}_{j,\downarrow}, \tag{3.14}$$

$$\hat{H}_V = V \sum_j \hat{n}_j \hat{n}_{j+1}, \tag{3.15}$$

are referred to as the *hopping term*, the *U term*, and the *V term*, respectively, and where $\hat{n}_{j,\mu} = \hat{c}^\dagger_{j,\mu}\hat{c}_{j,\mu}$ is the electron counting operator and $\hat{n}_j = \hat{n}_{j,\uparrow} + \hat{n}_{j,\downarrow}$. Note that in the literature, including the research papers, the model is often referred to as the *Fermi-Hubbard model* for $V = 0$ while for $V > 0$, it is called the *Extended Fermi-Hubbard model*. In the thesis, the model will be referred to as the former (or simply the *Hubbard model*) and the values of the parameters will be given in the specific context.

3.1.1 The driven Hubbard Model

The Hubbard model in Eq. (3.12) describes the interacting many-body system without any external field. Here, we derive the Hamiltonian for the model under the influence of an applied electromagnetic field, which is necessary to drive HHG. An electromagnetic field only modifies the momenta of individual electrons, and as such, it is only the hopping in Eq. (3.13) which is modified. As derived in Eq. (2.7), the effect of the electromagnetic field is to modify the electron momentum $\hat{\boldsymbol{p}} \to \hat{\boldsymbol{p}} + \boldsymbol{A}(\boldsymbol{r}, t)$ such that $\hat{h}(\hat{\boldsymbol{r}}, \hat{\boldsymbol{p}}) \to \hat{h}[\hat{\boldsymbol{r}}, \hat{\boldsymbol{p}} + \boldsymbol{A}(\hat{\boldsymbol{r}}, t)]$. Inserting this into the single-body Hamiltonian in Eq. (3.10), we obtain

$$\tilde{t}_{i,j}(t) = \int d\boldsymbol{r} \psi_m^*(\boldsymbol{r} - \boldsymbol{R}_i) \hat{h}[\hat{\boldsymbol{r}}, \hat{\boldsymbol{p}} + \boldsymbol{A}(\hat{\boldsymbol{r}}, t)] \psi_m(\boldsymbol{r} - \boldsymbol{R}_j). \tag{3.16}$$

By employing the Baker-Campbell-Hausdorff lemma [173], Eq. (3.16) can be restated as

$$\tilde{t}_{i,j}(t) = \int d\boldsymbol{r} \psi_m^*(\boldsymbol{r} - \boldsymbol{R}_i) e^{-i\lambda(\hat{\boldsymbol{r}}, t)} \hat{h}(\hat{\boldsymbol{r}}, \hat{\boldsymbol{p}}) e^{i\lambda(\hat{\boldsymbol{r}}, t)} \psi_m(\boldsymbol{r} - \boldsymbol{R}_j), \tag{3.17}$$

where the phase factor is given as

$$\lambda(\hat{\boldsymbol{r}}, t) = \int_{\boldsymbol{r}_0}^{\boldsymbol{r}} d\boldsymbol{r}' \boldsymbol{A}(\hat{\boldsymbol{r}}', t), \tag{3.18}$$

with $\boldsymbol{r}_0$ an arbitrary starting point for the integration. To proceed, we now assume that the Wannier functions, $\psi_m(\boldsymbol{r} - \boldsymbol{R}_j)$, are highly localized in real space on site $\boldsymbol{R}_j$ and assume that the vector potential does not change notably on the atomic scale such that the vector potential can be evaluated at the lattice site $\boldsymbol{R}_j$. We thus approximate

$$e^{i\lambda(\boldsymbol{r}, t)} \psi_m(\hat{\boldsymbol{r}} - \boldsymbol{R}_j) \simeq e^{i\lambda(\boldsymbol{R}_j, t)} \psi_m(\boldsymbol{r} - \boldsymbol{R}_j). \tag{3.19}$$

Inserting Eq. (3.19) into Eq. (3.17) and exploiting that the phase no longer contains any electronic operator, we obtain

$$\begin{aligned} \tilde{t}_{i,j}(t) &= e^{i[\lambda(\boldsymbol{R}_j, t) - \lambda(\boldsymbol{R}_i, t)]} \int d\boldsymbol{r} \psi_m^*(\boldsymbol{r} - \boldsymbol{R}_i) \hat{h}(\hat{\boldsymbol{r}}, \hat{\boldsymbol{p}}) \psi_m(\boldsymbol{r} - \boldsymbol{R}_j) \\ &= e^{i[\lambda(\boldsymbol{R}_j, t) - \lambda(\boldsymbol{R}_i, t)]} t_{i,j}, \end{aligned} \tag{3.20}$$

where we recognize that the effect of the applied electromagnetic field is merely a time-dependent phase, known as Peierls' phase. Assuming periodic boundary conditions and employing the dipole approximation, $\boldsymbol{A}(\boldsymbol{r}, t) \approx \boldsymbol{A}(t)$, we calculate

$$\lambda(\boldsymbol{R}_j, t) - \lambda(\boldsymbol{R}_i, t) = \int_{\boldsymbol{R}_i}^{\boldsymbol{R}_j} d\boldsymbol{r}' \boldsymbol{A}(t) = \boldsymbol{A}(t) a, \tag{3.21}$$

where a is the lattice spacing between any two neighboring sites. Inserting Eqs. (3.16)-(3.21) into Eq. (3.13), we obtain the modified hopping term with an applied electromagnetic field

$$\hat{H}_{\mathrm{FH}} = \hat{H}_{\mathrm{Hop}}(t) + \hat{H}_U + \hat{H}_V, \tag{3.22}$$

where

$$\hat{H}_{\mathrm{Hop}}(t) = -t_0 \sum_{j,\mu} \big(\, e^{iaA(t)} \, \hat{c}^\dagger_{j,\mu} \, \hat{c}_{j+1,\mu} + \mathrm{h.c.} \big), \tag{3.23}$$

where $\hat{H}_U$ and $\hat{H}_V$ are given in Eqs. (3.14) and (3.15), respectively, and where we have dropped the vector notation on the crystal momentum and the vector potential, as the model is one dimensional with the $A(t)$ being the vector potential with polarization projected onto the chain axis, i.e., in the direction of $\boldsymbol{q}$. As seen from Eq. (2.27), the signal from HHG is proportional to the induced current. For the Hubbard model, the current operator is given as [184]

$$\hat{\boldsymbol{j}}(t) = -i[\hat{H}_{FH}(t), \hat{\boldsymbol{R}}] = -iat_0 \sum_{j,\mu} \big(e^{iaA(t)} \hat{c}^\dagger_{j,\mu} \hat{c}_{j+1,\mu} - \mathrm{h.c.} \big) \hat{\boldsymbol{x}}, \tag{3.24}$$

where $\hat{\boldsymbol{x}}$ is along the chain, and $\hat{\boldsymbol{R}} = \Sigma_j \boldsymbol{R}_j \hat{n}_j$ is the electron counting operator in second quantization. The current is the expectation value of Eq. (3.24), $\boldsymbol{j}(t) = \langle \hat{\boldsymbol{j}}(t) \rangle$, which is relevant to calculate the HHG spectra using a semiclassical description of light-matter interactions.

3.2 Analysis of the Hubbard Model

With the Hamiltonian for the Hubbard model derived in Eq. (3.23), it is appropriate to further analyze the model and its characteristics before considering HHG from the model. First, some general symmetry considerations are in place that hold for all parameter values of the model. These will also be relevant when discussing selection rules for the emitted harmonics in Sec. 3.4. The symmetries relevant to the thesis are

> **Translation symmetry**: The Hamiltonian in Eq. (3.22) is symmetric under translation of all electrons. Such a translational invariant system comes with a conserved quantity, K, which in this case is the total crystal moment of all the electrons. This crystal momentum is only defined up to multiples of $\frac{2\pi}{a}$, and each choice of K can be block diagonalized, which yields L total blocks. The ground state of the system has $K = 0$, and we will, for the rest of the thesis, restrict ourselves to this subspace.

Inversion symmetry: When no field is applied, i.e., for $A(t) = 0$, the system is inversion symmetric around any one site. However, for a general applied field, $A(t) \neq 0$, this symmetry is broken and cannot be exploited to reduce the number of considered states.

Spin-inversion symmetry: As the Hamiltonian in Eq. (3.22) does not change the spin of any electrons, the total spin is conserved. This, like translational symmetry considered above, can be used to block diagonalize the system. In the thesis, we start with an equal number of spin-up and spin-down electrons to keep the system spin neutral.

Electron-hole symmetry: Though the intuitive understanding (and derivation) of the Hamiltonian [Eq. (3.22)] is about electrons, the system remains invariant if every electron is swapped with a hole and vice versa.

Now we will investigate different phases of the model. First, the tight-binding model ($U = V = 0$) will be considered, then the Hubbard model ($V = 0$), and finally, the extended Hubbard model will be investigated. We note in passing that $U > 0$ for physically realistic systems, and as onsite electron-electron repulsion is stronger than nearest neighbor electron-electron repulsion, due to the distance between the electrons, we always have $U > V$.

3.2.1 The tight-binding model

If one studies uncorrelated electrons by setting $U = V = 0$ in Eq. (3.22), the system is described by a simple tight-binding model described by Eq. (3.23). This limit is also sometimes referred to as the Bloch limit because, as shown below, it is described using Bloch waves. Using the Fourier relation in Eq. (3.8), the system is transformed into crystal-momentum space described by

$$\hat{H}_{\mathrm{Hop}}(t) = -2t_0 \sum_{q,\mu} \cos\{a[q + A(t)]\}\hat{n}_{q,\mu}. \tag{3.25}$$

Note that Eq. (3.25) preserves the crystal momentum for each individual electron. Likewise, the current operator [Eq. (3.24)] is given in crystal-momentum space as

$$\hat{\boldsymbol{j}}(t) = 2t_0 a \sum_{q,\mu} \sin\{a[q + A(t)]\}\hat{n}_{q,\mu}\hat{\boldsymbol{x}}, \tag{3.26}$$

which is also diagonal in crystal momentum space. Note that Eqs. (3.25) and (3.26) satisfy the semiclassical relation $\boldsymbol{j}(t) = -\frac{\partial \mathcal{E}(q)}{\partial q}|_{q=q_0+A(t)}$, where $\mathcal{E}(q) = -2t_0 \sum_{q,\mu} \cos\{a[q + A(t)]\}\hat{n}_{q,\mu}$ and q_0 is the initial crystal momentum and all is considered in the direction of the chain [185].

Due to the fact that both $\hat{H}_{\mathrm{Hop}}$ and $\hat{j}(t)$ are diagonal in momentum space, they commute at all times

$$[\hat{H}_{\mathrm{Hop}}(t), \hat{\boldsymbol{j}}(t)] = 0. \tag{3.27}$$

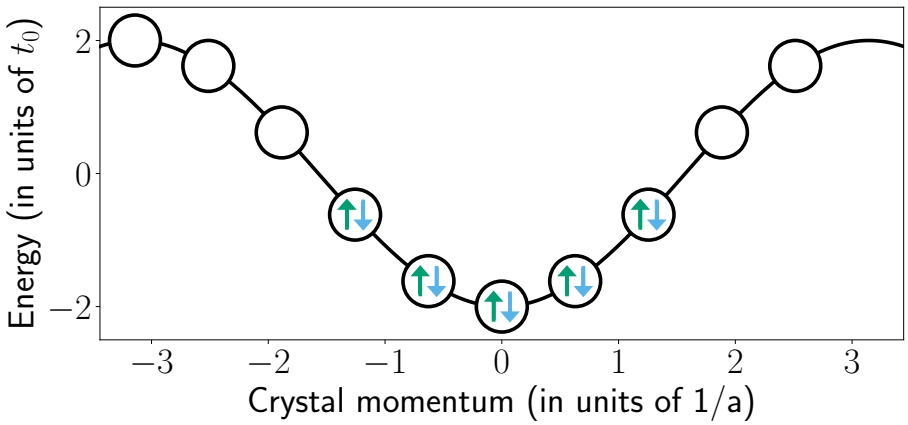

Figure 3.1: Crystal-momentum-space representation of the ground state of the tight-binding model [Eq. (3.13)] for $L = 10$ electrons. For total crystal momentum $K = 0$, the electrons are symmetrically distributed around $q = 0$. The directions of the arrows represent the spin orientation, up (green) and down (blue).

This peculiar fact will be of importance later in the thesis. The ground state of Eq. (3.22) is illustrated in Fig. 3.1 for no applied field. Here it is seen that the ground state is simply a product of Bloch states with different crystal momenta, minimizing the total energy according to Eq. (3.25). The allowed crystal momenta within a Brillouin zone are integer steps of $2\pi/(La)$ from $-\pi/a$ to π/a, where we in Fig. 3.1 only show an empty state for $q = -\pi/a$ and not for $q = \pi/a$, as they represent the same physical state. We note that the dispersion relation is a Bloch band with a width of $\Delta_{\text{Bloch}} = 4t_0$. Naturally, as the states are well localized in crystal-momentum space, they are highly delocalized in real space.

This simple model allows for further analytical considerations with an applied electromagnetic field. We now consider the Floquet limit with an applied electromagnetic field, i.e., we consider an infinite monochromatic laser. First, we calculate the current in the direction of the chain

$$\langle \hat{j}(t) \rangle = j(t) = 2t_0 a \sum_{q,\mu} \sin\{a[q + A(t)]\} n_{q,\mu}, \tag{3.28}$$

where it has been used that an eigenstate of the Hamiltonian [Eq. (3.25)] is an eigenstate for $\hat{n}_{q,\sigma}$ with eigenvalue $n_{q,\mu}$. Note that $n_{q,\mu}$ refers to the number of electrons populating a state with crystal momentum q and spin μ and is not to be confused with the order of the harmonics n below. Expanding the sinusoidal

function in Eq. (3.28), we obtain

$$j(t) = 2t_0 a \sum_{q,\mu} n_{q,\mu} \{\sin(aq)\cos[A(t)a] + \cos(qa)\sin[A(t)a]\}. \tag{3.29}$$

We now exploit that the ground state is symmetric around $q = 0$ (see Fig. 3.1), and note that $\sum_{q,\mu} n_{q,\mu} \sin(aq) = 0$ for any state with such symmetry. Further, we take the field of constant amplitude as

$$A(t) = A_0 \sin(\omega_L t + \phi), \tag{3.30}$$

where A_0 is the amplitude of the vector potential, ω_L is the laser frequency, and ϕ denotes the phase. Inserting this into Eq. (3.29) and further using the Jacobi-Anger expansion, we obtain

$$j(t) = 4t_0 a \sum_{q,\mu} n_{q,\mu} \cos(qa) \Big\{ \sum_{n=1}^{\infty} J_{2n-1}(A_0 a) \sin[(2n-1)(\omega_L t + \phi)] \Big\}, \tag{3.31}$$

where J_n denotes the n'th Bessel function of the first kind. The spectrum is obtained via the Fourier transform of the current as stated by Eq. (2.27). The Fourier transform of Eq. (3.31) is given by

$$\begin{aligned} \tilde{j}(\omega) = -4i\pi t_0 a \sum_{q,\mu} n_{q,\mu} \cos(qa) \\ \times \sum_{n=1}^{\infty} J_{2n-1}(A_0 a) \big\{ e^{i(2n-1)\phi}\ \delta[\omega - (2n-1)\omega_L] \\ - e^{-i(2n-1)\phi}\ \delta[\omega + (2n-1)\omega_L] \big\}. \end{aligned} \tag{3.32}$$

Inserting Eq. (3.32) into Eq. (2.27), we obtain the spectrum

$$S(\omega) \propto \sum_{n=1,3,5,\ldots}^{\infty} \omega^2 \delta(\omega - n\omega_L) [B J_n(A_0 a)]^2, \tag{3.33}$$

where $B = \sum_{q,\mu} n_{q,\mu} \cos(qa)$. We recognize the well-known selection rule in Eq. (3.33) allowing only odd harmonics in the spectrum, a selection rule found in systems with inversion symmetry.

3.2.2 On-site electron-electron repulsion

Going beyond the mean-field description above, we now consider the case of $U \neq 0$ while still keeping $V = 0$ in Eq. (3.22). First, we note that in crystal momentum space, $\hat{H}_U$ [Eq. (3.14)] is given as

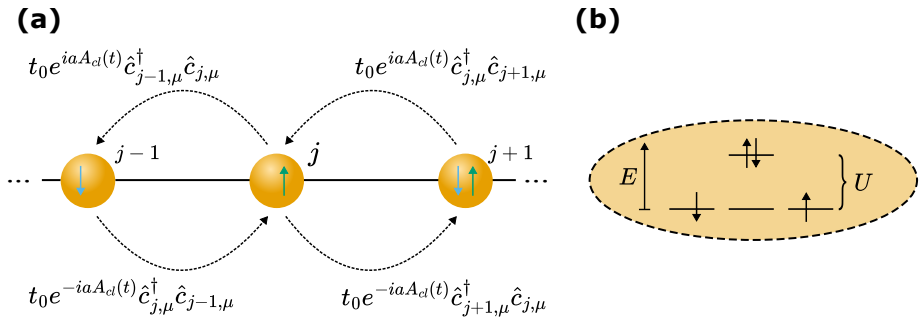

Figure 3.2: The Hubbard model with on-site electron-electron repulsion. (a) A real-space illustration indicates how the hopping operators generate electron hopping between neighboring sites. (b) An energy diagram for a single site showing that a double occupancy comes with an increased energy of U. Adapted with permission from Ref. [4]. Copyrighted by the American Physical Society.

$$\hat{H}_U = \frac{U}{L} \sum_{q_1,q_2,\Delta q} \hat{c}^\dagger_{q_1-\Delta q,\uparrow} \hat{c}_{q_1+\Delta q,\uparrow} \hat{c}^\dagger_{q_2-\Delta q,\downarrow} \hat{c}_{q_2+\Delta q,\downarrow}, \tag{3.34}$$

where we see that only the total crystal momentum is conserved, but not the individual crystal momenta of the electrons due to scattering and exchange of momenta Δq. Consequently, crystal momentum is no longer a good quantum number. In fact, the hopping term [Eq. (3.25)] is diagonal in crystal momentum space, while the U term is diagonal in real space [Eq. (3.14)], and a common eigenbasis for both parts of the Hamiltonian cannot be found. We are thus required to proceed numerically, and as $\hat{H}_U$ is arguably more complicated in crystal-momentum space than $\hat{H}_{\text{Hop}}$ in real space, we will continue the analysis in a real-space picture. An illustration of the system is given in Fig. 3.2. In Fig. 3.2(a), a real-space illustration of the Hubbard model is given, where the lattice sites along with the transition operators are given. In Fig. 3.2(b), an energy diagram shows that a doubly occupied site has an increased energy of U. We emphasize that all simulations in the thesis and research papers use a half-filled lattice, such that $N_e = L$, i.e., there are an equal number of electrons and sites.

With $U \neq 0$, it now requires more energy to have two electrons on the same site. Such a double occupancy can be thought of as a quasi particle called a *doublon* while an empty site is likewise called a *holon*. As seen in Fig. 3.3, for increasing values of U, the eigenstates of the system group into so-called *subbands*, where each subband is characterized by the number of doublon-holon pairs. The first of such subbands contains the ground state and is characterized by virtually no doublon-holon pairs, the second subband contains states with approximately one doublon-holon pair, and so on. In this large U limit, the ground state is

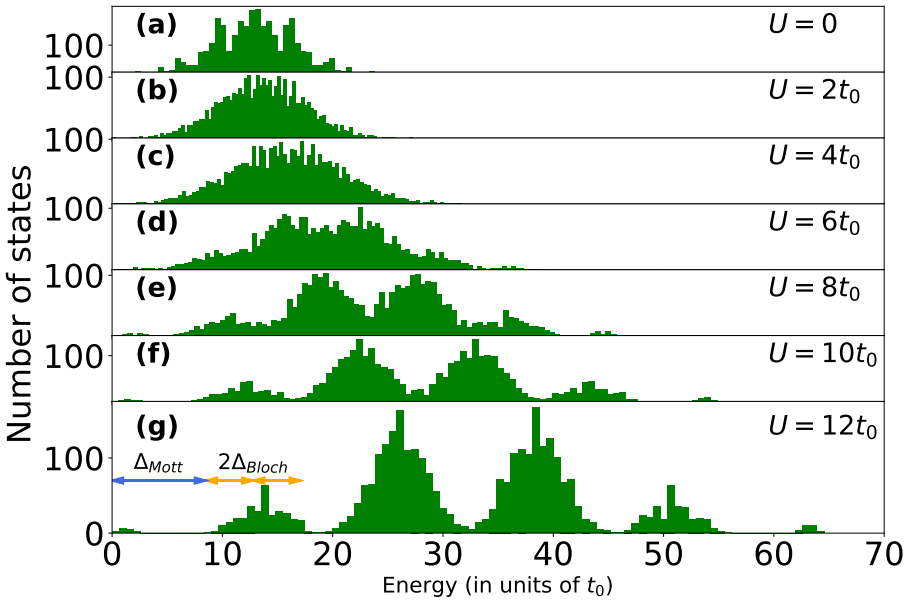

Figure 3.3: Histogram of energy eigenstates of the Fermi-Hubbard model for increasing values of U ($V = 0$). We note that for $U \geq 8t_0$, the subbands begin to emerge. This is the Mott-insulating limit of the system. In (g), the Mott gap, Δ_{Mott} (blue arrow) and the width of the first subband $2\Delta_{\text{Bloch}}$ (orange arrow) are shown. The histograms shown are for $L = 10$ electrons.

dominated by single-site occupancies and tends to be antiferromagnetic. Hence, at half filling, every first-order transition, i.e., a single electron transition to a neighboring site, involves the creation of a doublon-holon pair, which costs a lot of energy. Such a transition is from the first subband to the second subband, see Fig. 3.3. As such, for $U \gg t_0$, the system is gapped and is called a *Mott insulator*. The size of the gap is galled the *Mott gap*, denoted Δ_{Mott}, and can be calculated from [183, 186, 187]

$$\Delta_{\text{Mott}}(U) = E_{\text{GS}}^{\text{L}+1}(U) + E_{\text{GS}}^{\text{L-1}}(U) - 2E_{\text{GS}}^{\text{L}}(U), \tag{3.35}$$

where $E_{\text{GS}}^{\text{L}}(U)$ is the ground-state energy of a system of size L (at half filling). Equation (3.35) estimates the energy to create a doublon-holon pair. The creation of a doublon is $E_{\text{GS}}^{\text{L}+1}(U) - E_{\text{GS}}^{\text{L}}(U)$, that is, it is the energy cost of adding an extra electron to an already half-filled lattice. Similarly, $E_{\text{GS}}^{\text{L-1}}(U) - E_{\text{GS}}^{\text{L}}(U)$ is the energy to remove an electron from an already half-filled lattice. The sum of the two is thus the creation of a doublon-holon pair which, for $U \gg t_0$, is the energy difference between the first and second Hubbard subband, Δ_{Mott}. Note

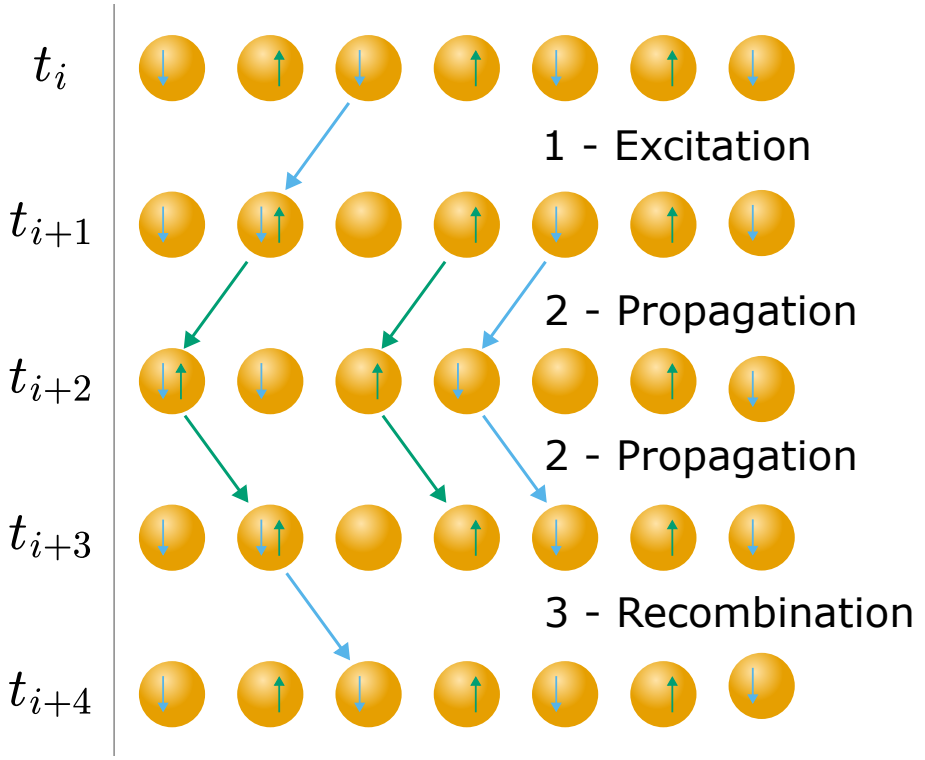

Figure 3.4: The three-step model in the Hubbard model. In the first step, starting from an anti-ferromagnetic state, any first-order excitation of the system results in the creation of a doublon-holon pair. Then, the doublon and holon propagate around in the lattice. Finally, the doublon and holon recombine. As for band-gap materials, both the propagation and recombination step generates current, resulting in the emission of harmonic radiation.

that Eq. (3.35) neglects the influence of the kinetic energy and is thus only valid in the Mott-insulating phase, i.e., for $U \gg t_0$.

With the Mott gap, HHG from the Hubbard model in the Mott-insulating phase can be understood from a three-step model analogous to the semiclassical three-step model for band-gap materials presented in Sec. 1.1.2. For the Mott-insulating phase of the Hubbard model, the three-step model is shown in Fig. 3.4 and consists of the following steps: First, the system is excited across the Mott gap by the creation of a doublon-holon pair. Then, the doublon-holon pair propagates freely within the subband (analogous to intraband current). Finally, the doublon-holon pair recombines (analogous to the interband current). As a single electron can have a maximal energy of $\Delta_{\text{Bloch}} = 4t_0$, heuristically, a

doublon-holon pair can, upon recombination during the laser-induced dynamics, release a photon with energy between Δ_{Mott} and $\Delta_{\text{Mott}} + 2\Delta_{\text{Bloch}} = \Delta_{\text{Mott}} + 8t_0$. This consideration is consistent with the numerical results presented in the thesis. Note also that as the ground state of the Mott-insulating phase is dominated by single-site configurations, any first-order transitions involve the creation of a doublon-holon pair, and, consequently, the transitions within the first subband are highly suppressed.

Finally, we note that Eq. (3.35) is only valid for $V = 0$, as the nearest-neighbor interactions change the gapped nature of the system.

3.2.3 Nearest-neighbor electron-electron repulsion: The Mott exciton

We now proceed to include nearest-neighbor interactions by including $\hat{H}_V$. Naturally, as on-site electron-electron repulsion is stronger than nearest-neighbor electron-electron repulsion, it is physically motivated to only consider $U > V$. In fact, it turns out that many different phases exist for the extended Hubbard model depending on the parameter values. The discussion of the different phases is beyond the scope of the thesis but can be found in, e.g., Ref. [188]. Relevant for the thesis and for Paper IV is to consider $U = 12t_0$ and $V = 4t_0$, which puts the system in a spin-density-wave phase.

For these parameters, a new quasi particle, the exciton, emerges. As seen in Fig. 3.5(a), the exciton is an effective bound state between the doublon and the holon, i.e., it is a quasi particle consisting of two different quasi particles. In Fig. 3.5(a), three different electron configurations are shown with their beyond-mean-field potential energy given on the right (periodic boundary conditions). The first row shows an antiferromagnetic state. Any first-order transition will create a doublon-holon pair (second row). If another single-electron transition occurs again, such that the doublon is spatially separated from the holon, we note that the total energy of the system is increased (third row). In this sense, the doublon and holon are effectively bound to each other, giving rise to the (Mott) exciton. Note that this does not occur for $V = 0$. The presence of the exciton changes the characteristics of the system drastically. For instance, the exciton is highly dominant in the linear optical response as seen in Fig. 3.5(b), where the signal is strongest at the exciton energy (vertical dashed line). The linear response, $\sigma(\omega)$, is calculated by applying a perturbative, single-cycle, and high-frequency pulse and calculating

$$\sigma(\omega) = \frac{\tilde{j}(\omega)}{\tilde{E}(\omega)}, \tag{3.36}$$

where $\tilde{E}(\omega)$ is the Fourier transform of the applied electric field, and the direction is along the chain. As will be evident later, the exciton is also central in the

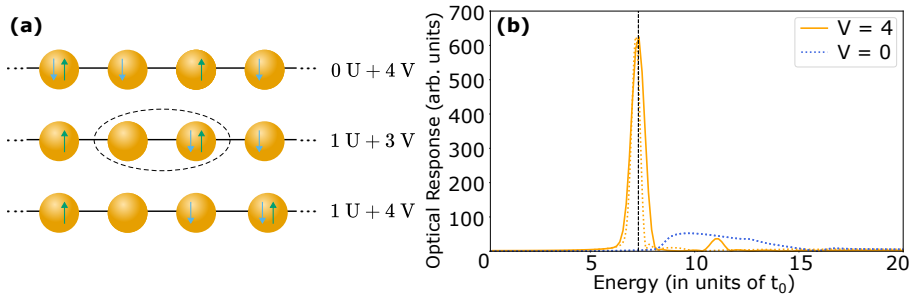

Figure 3.5: Illustration and properties of the extended Hubbard model. (a) An illustration of the potential energy of the extended Hubbard (with periodic boundary conditions). The inclusion of $V = 4$ effectively binds the doublon and holon together, giving rise to the Mott exciton. (b) The linear response [Eq. (3.36)] of the extended Hubbard model for $U = 12$. We see that the inclusion of $V = 4$ (orange lines) drastically enhances the linear optical response at a much more localized energy compared to $V = 0$ (blue line). The solid line is obtained for a finite system with $L = 10$, while the dashed lines are for an infinite system calculated using infinite time-evolving block decimation. As the two orange lines are very similar, the results are not due to finite lattice effects. Adapted with permission from Ref. [3]. Copyrighted by the American Physical Society.

nonlinear response of the system. Note that the dotted curves in Fig. 3.5(b) are the linear response from an infinite system, calculated using infinite time-evolving block decimation calculations [189, 190]. We note that these curves match the curves from the finite system of $L = 10$, showing that the involved physics is not a consequence of a finite system. The emission of HHG from a system with Mott excitons can be explained using a three-step model similar to the one for the usual Hubbard model ($V = 0$) explained above and in Fig. 3.4.

The central role of the exciton state can also be understood from the histogram of the energy eigenstates. Naturally, due to $V \neq 0$, the eigenenergies of the system are different from the Hubbard model with $V = 0$. Notably, looking at Fig. 3.6(a) and (b), the system is less gapped for $V = 4t_0$ than for $V = 0$ as eigenstates within the second subband are shifted to the left. As denoted by the orange dots in Fig 3.6(c), which is a zoom in of Fig. 3.6(b), we see that the states within the second subband with the lowest energy are also the ones containing ~ 1 exciton. This agrees with the physical picture in Fig. 3.5(a) showing that the lowest energy states, of the states that contain a single doublon-holon pair, are the exciton states. The energy of the peak signal from the linear response in Fig. (3.5)(b) is marked by the vertical dashed line in Fig. 3.6(c), proving that the strong signal is due to coupling with an eigenstate that contains an exciton. As for the case of $V = 0$, this shows that

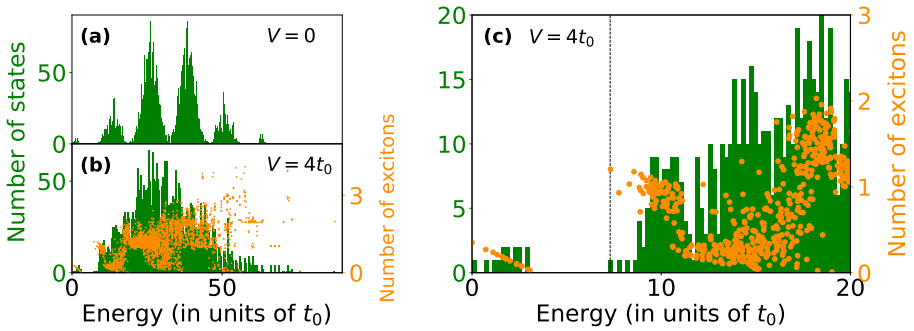

Figure 3.6: Histogram of energy eigenstates in the extended Hubbard model with the number of excitons in each eigenstate for $L = 10$ and $U = 12t_0$. (a) The energy for $V = 0$ [identical to Fig. 3.3(g)]. (b) The presence of $V = 4t_0$ changes the distribution of the energies in the eigenstates. (c) A zoom-in of (b) where we note that the lowest-lying energy eigenstates in the first subband contain ~ 1 exciton. The vertical dashed line is located at the same energy as in Fig. 3.5(b). Adapted with permission from Ref. [3]. Copyrighted by the American Physical Society.

first-order transitions from the ground state do not couple to states within the first subband.

3.3 Numerical implementation

As the Fermi-Hubbard model in general does not allow for analytical solutions when driven by an external field, one has to solve the system dynamics numerically. In this section, the numerical approach used will be outlined. First, the representation of the state will be presented, followed by an outline of the algorithm used to time evolve the quantum state. Though the Hubbard model is a model of real materials with many electrons, numerical constraints prohibit exact considerations of infinite lattices.

The Hubbard model is, as explained above, a lattice model with electron occupations on discrete sites. To build such a configuration, a product of fermionic creation operators has to be applied to the vacuum. Thus, any configuration of electrons can be written as

$$|\{x_j, \mu_j\}\rangle = \prod_j \hat{c}^\dagger_{x_j,\mu_j}|0\rangle, \tag{3.37}$$

where $|\{x_j, \mu_j\}\rangle$ is the multi-electron state with electrons of spin μ_j positioned on sites x_j. The creation operators do in general not commute [see Eq. (3.7)],

and thus, the ordering of the operators is important. We choose to separate the operators into two blocks differentiated by their spin orientation, e.g., such that all operators with $\mu =\uparrow$ are applied after all operators with $\mu =\downarrow$. As we employ periodic boundary conditions, one has to be careful when moving an electron of spin μ from site $j = L$ to site $j = 1$. This boundary condition simply applies the sign $(-1)^{N_\mu - 1}$, where N_μ is the number of electronic creation operators with spin index μ. We now restrict ourselves to the case of a spin-neutral lattice used in all the research papers where $N_\uparrow + N_\downarrow = L$ such that $N_\uparrow = N_\downarrow = L/2$, and hence L is an even integer. In general, without any further considerations, one can place $L/2$ electrons with, e.g., spin $\mu =\uparrow$ on L sites, giving $\binom{L}{L/2}$ different possible combinations. The same is true for electrons with spin $\mu =\downarrow$, such that the total number of states is $\binom{L}{L/2}^2$. As seen in Tab. 3.1, this number grows drastically with the asymptotic exponential scaling of 2^{2L}. Such a large number of states in a basis set quickly becomes unfeasible to handle numerically. Fortunately, the symmetries of $\hat{H}_{\mathrm{FH}}$ [Eq. (3.12)] introduced in Sec. 3.2 above, allow one to reduce the basis size drastically. First, as the system is translationally invariant, one can shift all electrons any number of sites in either direction and end up with a state translationally identical to the original state. By applying such a shift operator, and because all translational variants of a given state are identical, the number of required basis states can be reduced by grouping translational identical states as

$$|\{x_j, \mu_j\}, K\rangle = \frac{1}{\sqrt{N^K_{x_j,\mu_j}}} \sum_m e^{-iKma} |\{x_j + m, \mu_j\}\rangle, \tag{3.38}$$

where K again is the total crystal momentum of the entire system, and $N^K_{x_j,\mu_j}$ is the appropriate normalization constant. The state $|\{x_j + m, \mu_j\}\rangle$ is a translation of all electrons by m sites from the state $|\{x_j, \mu_j\}\rangle$. As the Hamiltonian $\hat{H}_{\mathrm{FH}}$ conserves K, we can choose any integer n and get $K = n\frac{2\pi}{La}$. For the systems used in the research papers, the ground state lies within the subspace with $K = 0$, and we will thus, for the rest of the thesis, only consider this subspace. The Hamiltonian, $\hat{H}_{\mathrm{FH}}$, is also invariant under spin flips. We can thus further reduce the number of states by

$$|\{x_j, \mu_j\}, K, P\rangle = \frac{1}{\sqrt{2}}(|\{x_j, \mu_j\}, K\rangle + P|\{x_j, -\mu_j\}, K\rangle), \tag{3.39}$$

where $P = \pm 1$ is the spin parity. As the ground state is within the subspace with parity $P = 1$, this is the only considered subspace in the thesis. The total number of states in both the full and symmetry-adapted basis for different values of L is given in Tab. 3.1, showing that the symmetry-adapted basis is significantly smaller than the full basis.

With the basis in hand, it is now possible to simulate the system by propagating the states according to the TDSE. First, however, the ground state of the

L/Number of states	4	6	8	10	12
Full basis	36	400	4,900	63,504	853,776
Symmetry-adapted basis	6	38	318	3,202	35,670

Table 3.1: The number of states in the full basis (top row) and symmetry-adapted basis (bottom row) as a function of the lattice length L at half filling with periodic boundary conditions. We note that the symmetries of the system drastically reduce the required basis size.

system must be found. In the results presented in the research papers and in the thesis, this is done using exact diagonalization techniques. Alternatively, one could also use imaginary time propagation, which will converge to the ground state. The time-evolution operator evolving a state from time t to time $t + \Delta t$, $\hat{\mathcal{U}}(t + \Delta t, t)$, is in general given by the Dyson series. Unfortunately, the form of the Dyson series involves many nonvanishing commutation relations when the Hamiltonian does not commute with itself at different times, as is the case for the Hubbard model. To proceed, the time-evolution operator is approximated using a commutator-free expansion to 4'th order. We thus approximate

$$\hat{\mathcal{U}}(t + \Delta t, t) \simeq e^{-i[v_- \hat{H}_{\mathrm{FH}}(t_-) + v_+ \hat{H}_{\mathrm{FH}}(t_+)]\frac{\Delta t}{2}} e^{-i[v_+ \hat{H}_{\mathrm{FH}}(t_-) + v_- \hat{H}_{\mathrm{FH}}(t_+)]\frac{\Delta t}{2}}, \quad (3.40)$$

where $v_\pm = \frac{3 \pm 2\sqrt{3}}{6}$ and $t_\pm = t + \dfrac{3 \pm \sqrt{3}}{6}\Delta t$ [191]. Equation (3.40) drastically simplifies the effort required to time evolve the system, as the time-evolution operator is approximated as a product of two time-evolution operators for a time-independent Hamiltonian. Nonetheless, matrix exponentials are numerically expensive, and further approximations are needed. Here, we apply the *Arnoldi-Lancoz* algorithm, which time-evolves the state in a *Krylov subspace* [192–195]. The idea is to Taylor expand the time-evolution operator for a time-independent Hamiltonian as

$$\begin{aligned} e^{-i\hat{H}\Delta t} &= \sum_n \frac{(-i\Delta t)^n}{n!} \hat{H}^n \\ &\simeq \sum_{n=0}^{N_{\mathrm{Krylov}}} \frac{(-i\Delta t)^n}{n!} \hat{H}^n, \end{aligned} \quad (3.41)$$

where $N_{\mathrm{Krylov}} + 1$ is the dimension of the Krylov subspace (since the summation starts with $n = 0$). The idea of the Arnoldi-Lanczos algorithm is the following. The states are evolved within the subspace with dimension N_{Krylov}. A basis within this subspace is created using the Gram-Schmidt procedure. Using this

basis, the state is then propagated by the approximated time-evolution operator in Eq. (3.40). This procedure introduces an error of $(\Delta t)^{N_{\text{Krylov}}}$, and it is thus useful to match N_{Krylov} with the precision of the approximated time-evolution operator via the size of the time step Δt. Further discussion about the numerical implementation of the Hubbard model can be found in [196]. As a final note, the algorithm presented above is the most efficient version of the Arnoldi-Lanczos algorithm. In some of the research papers, a less efficient version of the algorithm has been used, which is why different values of Δt and N_{Krylov} are used in the research papers.

3.4 High-order harmonic generation in the Hubbard Model

The Fermi-Hubbard model has been subject to many considerations with respect to HHG [63–66]. However, a comparison and explanation of the nature of the HHG spectra from the different phases of the model has not been fully covered. This chapter aims to understand the HHG spectra from different phases of the model, i.e., for different values of U (for $V = 0$), and presents the main results of Paper I. These considerations, though obtained from a semiclassical calculation, will aid in the understanding of the system which also will be useful for the quantum optical considerations in Chs. 4 and 5.

The motivation for such a study is emphasized by the HHG spectra [Eq. (2.27)] shown in Fig. 3.7 generated by driving with a typical intense femtosecond laser pulse. Here, we consider three different phases of the model: the uncorrelated phase ($U = 0$), a moderately correlated phase ($U = t_0$), and the strongly correlated Mott-insulating phase ($U = 10t_0$). Note that we set $V = 0$ in Eq. (3.22) in the remainder of this chapter. As seen in Fig. 3.7, the spectra from the three different phases are widely different: The uncorrelated phase (blue curve) shows regular peaks at odd harmonics up to energy Δ_{Bloch} as expected. In contrast, the moderately correlated phase (red curve) shows no regular structure, while the Mott-insulating phase (green curve) shows a clear signal at odd harmonics up to $\omega/\omega_L \sim 21$ and an irregular spectral structure for the harmonics above. Seemingly, this is inconsistent with the symmetry-based selection rules for harmonic generation which should be adhered to independent of the strength of the electron-electron correlation. It is thus interesting to investigate the reason for the disappearance and partial reappearance of harmonic structure with increasing degree of electron-electron correlations. A more detailed analysis of the spectra will be given in Ch. 4. The focus of this chapter is the appearance of noninteger harmonics.

These noninteger harmonics have been observed in works on theoretical considerations from HHG and have been hypothesized to be either due to the

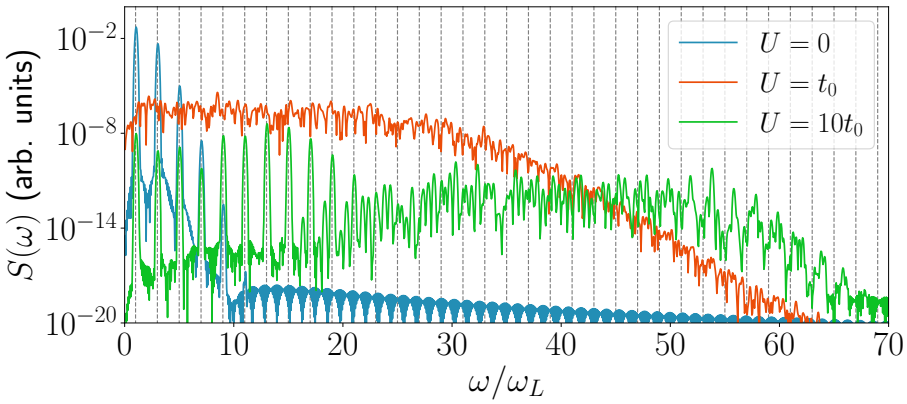

Figure 3.7: HHG spectra for the Hubbard model with different degrees of electron-electron correlation of $U = 0$ (blue), $U = t_0$ (red), and $U = 10t_0$ (green). We note how the spectra differ widely in their structure. To generate these spectra, a pulse of $N_{on} = 3$ and $N_{pl} = 10$ has been used with other parameters specified in the text. Adapted with permission from Ref. [1]. Copyrighted by the American Physical Society.

presence of correlations [63], or due to a finite pulse and missing dephasing channels [182], but for the most part, the presence of noninteger harmonics has simply not been commented on [2, 64–66, 197–200]. One may infer that the lack of clear (odd) harmonics is due to the fact that dephasing effects are not taken into account, which is typically added phenomenologically when working with semiconductor Bloch equations (SBE) in order to reproduce experimental results [201]. However, the primary source of such decoherence in the SBE formalism is the electron-electron interactions [202], and as electron-electron interactions are already included in the Hubbard model, it is unmotivated to further include such phenomenological decoherence. The effect of dephasing is to suppress long electron trajectories [203], which are likewise suppressed when including electron-electron interactions as seen by a short correlation length for the Hubbard model. Thus, the reason for the appearance of noninteger harmonics is not due to the lack of decoherence terms but has a different explanation.

In the remainder of the chapter, the dynamical symmetries and the relevant selection rules are outlined for the Hubbard model. This is followed by a discussion of Floquet theory and its relation to the appearance of the noninteger harmonics before concluding and summarizing the findings.

3.4.1 Symmetries and selection rules

For a time-dependent system such as the driven Hubbard model [Eq. (3.22)], one has to consider not only spatial symmetries but dynamical symmetries, i.e., both spatial and temporal symmetries at the same time. Relevant for the Hubbard model is the symmetry operator $\hat{C}_2 = \hat{R} \cdot \hat{\tau}_2$, where $\hat{R}$ is space inversion of all electronic coordinates, and $\hat{\tau}_2$ is time translational symmetry of half a period, i.e., $\hat{\tau}_2\ t\ \hat{\tau}_2^{-1} = t + T/2$, where $\hat{\tau}_2^{-1}$ is the inverse operation of $\hat{\tau}_2$, i.e., $\hat{\tau}_2\hat{\tau}_2^{-1} = \mathbb{I}$. It can be shown that the Hubbard model is invariant under the application of $\hat{C}_2$ [1]

$$\hat{C}_2\hat{H}_{\mathrm{FH}}(t)\hat{C}_2^{-1} = \hat{H}_{\mathrm{FH}}(t). \tag{3.42}$$

Similarly, the current operator can be considered with respect to symmetries. By going to the Floquet limit by considering an infinitely long pulse, $A(t) = A_0 \sin(\omega_l t)$, the current operator can be expressed in a Floquet decomposition as

$$\hat{j}(t) = \sum_m J_m(aA_0)e^{im\omega_l t}\hat{j}_m, \tag{3.43}$$

which is taken along the chain, and where

$$\hat{j}_m = \sum_{j,\mu}[\hat{c}^\dagger_{j,\mu}\hat{c}_{j+1,\mu} - (-1)^m\hat{c}^\dagger_{j+1,\mu}\hat{c}_{j,\mu}], \tag{3.44}$$

is the m'th term in the sum. It can then be shown that

$$\hat{C}_2\hat{j}_m\hat{C}_2^{-1} = (-1)^{m+1}\hat{j}_m, \tag{3.45}$$

where we see that $\hat{j}_m$ is odd for even m and vice versa. The symmetry considerations in Eqs. (3.42)-(3.45) will be relevant when deriving the selection rules based on the $\hat{C}_2$ symmetry of the model.

To derive the selection rules, we consider the Floquet limit of the model. In this limit, the Hubbard model is time periodic with the period of the vector potential $T = 2\pi/\omega_L$, i.e., $\hat{H}_{\mathrm{FH}}(t) = \hat{H}_{\mathrm{FH}}(t+T)$. The solution to the TDSE of a time-periodic Hamiltonian is given by Floquet states on the form [204, 205]

$$|\psi_j(t)\rangle = e^{-i\mathcal{E}_j t}|v_j(t)\rangle, \tag{3.46}$$

where $|v_j(t)\rangle = |v_j(t+T)\rangle$ are T-periodic states similar to the R-periodic states in the Bloch-states in Eq. (3.5) and $\mathcal{E}_j$ are quasienergies which are only defined up to integer multiples of the laser frequency. Note that the set of quasienergies $\{\mathcal{E}_j\}$ and their corresponding Floquet functions are determined not only by the properties of the electronic system but also by A_0 and ω_L of the applied field [204]. As Eq. (3.46) is laser periodic, it can be decomposed into Fourier components

$$|\psi(t)\rangle = e^{-i\mathcal{E}t}\sum_l e^{i\omega_L t}|\phi_l\rangle, \tag{3.47}$$

where $|\phi_l\rangle$ is an appropriate time-independent state of the full electronic system, and where the index denoting the Floquet eigenstate has been dropped for convenience. By inserting Eq. (3.46) into the TDSE with appropriate identity operations, $\hat{C}_2\hat{C}_2^{-1} = \mathbb{I}$, and using that $\hat{H}_{\mathrm{FH}}(t)$ is invariant under $\hat{C}_2$, one can obtain the relation [1]

$$|v(t)\rangle = e^{i\theta}\hat{R}|v(t+T/2)\rangle, \tag{3.48}$$

where θ is a phase. By Fourier expanding Eq. (3.48) and comparing it with Eq. (3.47), we obtain the relation

$$|\phi_l\rangle = e^{i\theta}\ (-1)^l\hat{R}|\phi_l\rangle. \tag{3.49}$$

Using this relation in the Fourier expansion of the Floquet state in Eq. (3.47) with the current operator in Eq. (3.43) to calculate the spectrum [Eq. (2.27)], we obtain

$$S(\omega) = \left|\omega^2 \sum_{l,m,n} \delta(w - n\omega_l) J_m(aA_0)\langle\phi_{m+l-m}|\hat{j}_k|\phi_l\rangle\right|^2. \tag{3.50}$$

Focusing on the matrix element in Eq. (3.50), we insert the symmetries of the states [Eq. (3.49)] and current operator [Eq. (3.45)] and obtain

$$\langle\phi_{m+l-m}|\hat{j}_k|\phi_l\rangle = (-1)^{n+1}\langle\phi_{m+l-m}|\hat{j}_m|\phi_l\rangle, \tag{3.51}$$

where it has been used that $\hat{R} = \hat{R}^{-1} = \hat{R}^\dagger$. We thus see from Eq. (3.51) that the matrix element vanishes for even values of n. Inserting this into Eq. (3.50), we see that the signal, in the Floquet limit, should only appear at odd integer values of the laser frequency. We emphasize that this result is independent of the values of U and V and is only based on the dynamical symmetries of the model. However, the spectra for $U = t_0$ and $U = 10t_0$ in Fig. 3.7 are seemingly in contradiction with this fact, as no clear harmonic structure is seen across all frequencies. To investigate this further, we again turn to Floquet theory as a suitable framework to explain this apparent discrepancy.

3.4.2 Floquet theory and noninteger harmonics

The above symmetry-based selection rules assume a Floquet Hamiltonian, i.e, a time-periodic Hamiltonian. When driving the Hubbard model, it is initially in its ground state, which can be thought of as a Floquet state of the driven model with vanishing field amplitude. Thus, by turning up the vector potential as required to generate a pulse, the amplitude becomes time dependent and, consequently, it is only approximately a Floquet state. However, it should be the case that only odd-integer harmonics appear in the spectrum in the Floquet limit. It thus remains to investigate how long the driving field should be and

how slowly varying the amplitude should be before the Floquet description is suitable, and how this all depends on the value of U.

By first investigating the uncorrelated limit ($U = 0$), we find, since the ground state is an eigenstate of the Hamiltonian as discussed in Sec. 3.2.1, that the state at all times is given analytically as

$$\begin{aligned} |\psi(t)\rangle &= \hat{\mathcal{U}}(t)|\psi(0)\rangle \\ &= e^{-i\int_0^t \hat{H}_{\mathrm{Hop}}(t')dt'}|\psi(0)\rangle \\ &= e^{-i\int_0^t E_g(t')dt'}|\psi(0)\rangle, \end{aligned} \tag{3.52}$$

where we have assumed the initial time to be at $t = 0$ and where $E_g(t)$ is the ground-state energy of the system, which can be found analytically via Eq. (3.25). Notably, Eq. (3.52) allows one to calculate the current along the chain as

$$\langle\hat{j}(t)\rangle = \langle\psi(t)|\hat{j}(t)|\psi(t)\rangle = \langle\psi(0)|\hat{j}(t)|\psi(0)\rangle, \tag{3.53}$$

which only contains frequency components determined by the vector potential $A(t)$. Hence, no Floquet theory is required for further analysis for $U = 0$, as the sharpness of the peaks is only limited by the Fourier transform of Eq. (3.53).

We now turn our attention to the general case of $U \neq 0$. As we drive the Hubbard model by applying a laser pulse, the vector potential is also a function of time. This means that the set of quasi energies and Floquet functions depends on the instantaneous values of the amplitude of the vector potential, i.e., $\mathcal{E}_j(t) = \mathcal{E}[A_0(t)]$. We can formally expand a general state of the system as

$$|\psi(t)\rangle = \sum c_j(t)e^{-i\int_0^t \mathcal{E}_j(t')dt'}|v_{\mathcal{E}_j(t)}(t)\rangle, \tag{3.54}$$

where the sum runs over all Floquet states with the time-dependent expansion coefficient $c_j(t)$. It is illustrative to consider the expectation value of the current operator for the general state in Eq. (3.54)

$$\begin{aligned} \langle\hat{j}(t)\rangle = &\sum_{i,j} c_i^*(t)c_j(t)e^{-i\int_0^t[\mathcal{E}_j(t')-\mathcal{E}_i(t')]dt'} \\ &\times \langle v_{\mathcal{E}_i(t)}(t)|\hat{j}(t)|v_{\mathcal{E}_j(t)}(t)\rangle. \end{aligned} \tag{3.55}$$

We note that the phase $\exp\Big(-i\int_0^t[\mathcal{E}_j(t') - \mathcal{E}_i(t')]dt'\Big)$ in contains frequency components that in general are not integer multiples of the laser frequency. In other words, if more than a single Floquet state is populated, this phase will generate noninteger harmonics in the spectrum. These have previously been found in studies on HHG from atomic gases, and are referred to as hyper-Raman lines [206–210]. Unfortunately, due to the size of the electronic system and the

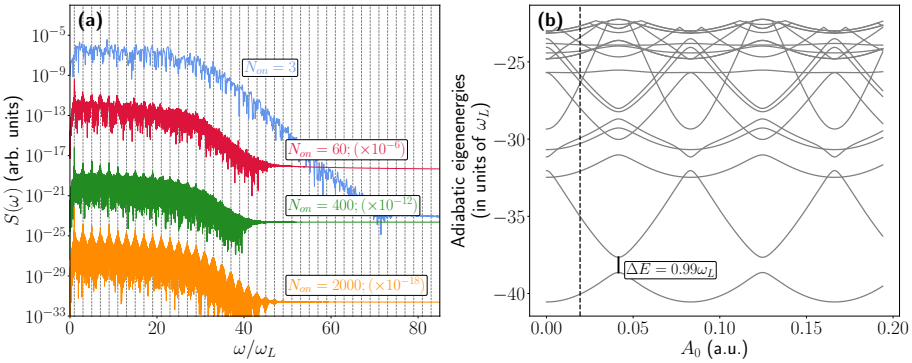

Figure 3.8: The moderately correlated phase of the model ($U = t_0$). (a) HHG spectra. The system is driven by a flat-top laser pulse with $N_{pl} = 10$ and a different number of cycles in the ramp. Note that the spectra are shifted by the number in the parentheses for visual clarity. (b) The adiabatic eigenvalues of the system as a function of the instantaneous amplitude of the vector potential, A_0. We note that a nonadiabatic resonance occurs for different values of A_0. Adapted with permission from Ref. [1]. Copyrighted by the American Physical Society.

low frequency of the laser, it is not possible to perform a full diagonalization of the Floquet Hamiltonian in order to obtain the entire spectrum of quasienergies. Fortunately, we can use the adiabatic eigenenergies of the system by diagonalizing $\hat{H}_{\mathrm{FH}}(t)$ for a given value of $A(t)$

$$\hat{H}_{\mathrm{FH}}(t)|\psi_j(t)\rangle = E_j(t)|\psi_j(t)\rangle, \tag{3.56}$$

for a fixed value of t and where $|\psi_j(t)\rangle$ is the adiabatic eigenstate with energy $E_j(t)$. The adiabatic eigenenergies are related to the Floquet quasi energies via an expansion in even powers of the small laser frequency ω_L^{2n} [204].

We now present the results. We drive the Hubbard model consisting of $L = 10$ electrons (periodic boundary conditions) with a linearly polarized pulse in the form

$$A(t) = A_0 f(t) \sin\left(\omega_L t + \frac{\pi}{2}\right), \tag{3.57}$$

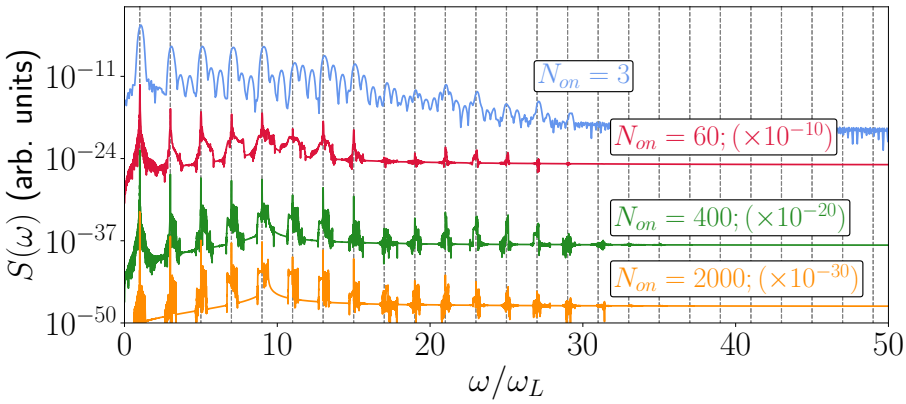

Figure 3.9: Spectra for the moderately correlated phase of the model ($U = t_0$). The system is driven by the same parameters as in Fig. 3.8(a) but with a reduced vector potential amplitude of $A_0' = 0.1A_0$ to avoid the nonadiabatic resonance seen in Fig. 3.8(b). Adapted with permission from Ref. [1]. Copyrighted by the American Physical Society.

where the envelope function is given by

$$f(t) = \begin{cases} \sin^2\left(\dfrac{\omega_L t}{4N_{on}}\right), & 0 < \frac{t}{T} < N_{on} \\ 1, & N_{on} < \frac{t}{T} < (N_{on} + N_{pl}) \\ \sin^2\left(\dfrac{\omega_L (t - N_{pl}T)}{4N_{on}}\right), & (N_{on} + N_{pl}) < \frac{t}{T} \\ & < (2N_{on} + N_{pl}) \\ 0, & \text{otherwise,} \end{cases} \tag{3.58}$$

which describes a flat-top pulse of N_{pl} plateau cycles with a $\sin^2$ ramp (turn-on and turn-off) of N_{on} cycles. In the presented results, $N_{pl} = 10$ is fixed and we study the effect of varying N_{on}. All simulations use $t_0 = 0.0191$ a.u. and $a = 7.5588$ a.u. chosen to model the curprate Sr_2CuO_3 [211]. The field amplitude is $A_0 = 0.194$ a.u. with a frequency of $\omega_L = 0.005$ a.u.. The simulations used a timestep of $\Delta t = 1/\sqrt{10}$ and a Krylov Subspace of dimension 4.

We first consider the case of a moderate degree of correlation $U = t_0$. In Fig. 3.8(a), see the spectra for various pulse lengths of $N_{on} = 3, 60, 400, 2000$. We note that only for very long laser pulses ($N_{on} \geq 400$), peaks begin to emerge at odd-integer harmonics across the spectrum, while, as previously noted, a short driving pulse generates an irregular spectrum. It is curious that such long pulses are required in order for odd-integer harmonics to appear. We explain this by the fact that the adiabatic eigenenergies of the system are spectrally close for

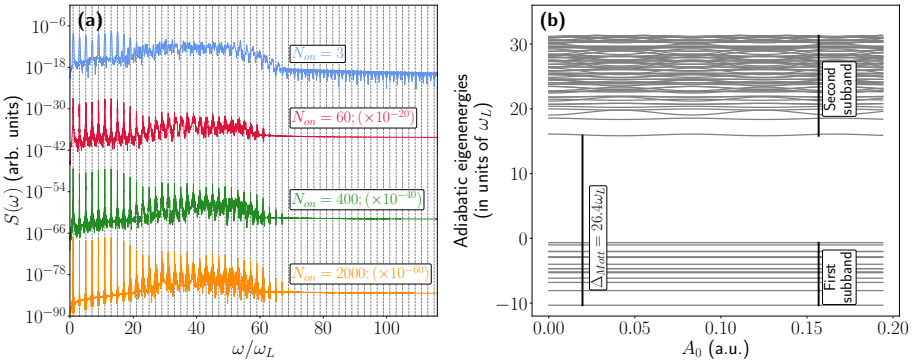

Figure 3.10: The Mott-insulating phase of the Hubbard model ($U = 10t_0$). (a) HHG spectra. The same parameters as in Fig. 3.8(a) have been used. We note that harmonic peaks appear for longer pulse durations. (b) The adiabatic eigenvalues as a function of the vector potential amplitude. We note that the adiabatic eigenvalues are virtually constant for different values of A_0. The left vertical line indicates the Mott gap, while the two right vertical lines show the first and part of the second Hubbard subbands. Adapted with permission from Ref. [1]. Copyrighted by the American Physical Society.

certain values of $A(t)$ as seen in Fig. 3.8(b). Here, a one-photon nonadiabatic resonance allows multiple Floquet states to become populated. Of course, such a nonadiabatic transition is suppressed for a longer pulse, which is why more regular peaks are seen for prolonged pulses in Fig. 3.8(a). Based on the insights from Fig. 3.8, we again drive the system of $U = t_0$ but with a reduced field amplitude of $A_0' = 0.1A_0$ to avoid the one-photon resonance. The results are shown in Fig. 3.9 where we note that odd-integer harmonics appear already for shorter pulse durations.

Before concluding, we also investigate the Mott-insulating phase of $U = 10t_0$. In Fig. 3.10(a), we see the spectra for the same pulse durations as in Figs. 3.8 and 3.9. First, we note that integer harmonics appear already for a short pulse as previously seen in Fig. 3.7. We ascribe this to the fact that it is due to inter-subband current in the second subband (propagation step in Fig. 3.4) and that the difference in quasi-energies is larger than Δ_{Mott} such that noninteger harmonics do not appear below this energy. At higher frequencies, curiously, clear integer harmonics appear with increasing sharpness for longer pulses without any need to change the peak amplitude. This is explained by Fig. 3.10(b), where we see that the adiabatic eigenvalues are practically constant as a function of the field amplitude, and nonadiabatic transitions are thus equally likely for all field amplitudes. However, different from the case of $U = t_0$, here the energy difference between the states is Δ_{Mott}, which strongly suppresses

nonadiabatic transitions. These transitions are more strongly suppressed for increasing pulse durations, which is why clear harmonic peaks are seen in Fig. 3.10.

Concluding, we have investigated the appearance of noninteger harmonics in the HHG spectra from the Hubbard model. In the uncorrelated phase, only odd harmonics appeared, consistent with the fact that only a single (Floquet) state is populated at all times. For the moderately correlated phase ($U = t_0$), even for very prolonged ramps, signal was found at noninteger harmonics in the spectrum. This is due to the population of multiple Floquet states, which is not in contradiction to the symmetry-based selection rules for HHG, as these assume the population of only a single Floquet state. Though the nature of the system impeded a diagonalization to obtain the set of quasienergies, insights could still be obtained by investigating the related adiabatic eigenenergies. Here, it was found that resonances occur during the dynamics, allowing for nonadiabatic transitions that couple different Floquet states. The population of multiple Floquet states is thus due to the combination of energy levels of the system and short pulse duration. By lowering the amplitude of the time-dependent vector potential, such resonances were avoided, and a clear signal at odd-integer harmonics is found, see Fig. 3.9. Similar findings hold in the Mott-insulating phase ($U = 10t_0$). In contrast, the adiabatic eigenenergies in this phase are virtually unaffected by the varying vector potential amplitude, and a longer pulse was thus sufficient to generate odd-integer harmonics across all harmonics (see Fig. 3.10).

CHAPTER 4

Quantum light from correlated materials

With an understanding of the Hubbard model and the HHG spectra generated from the model from Ch. 3, this chapter goes beyond the semiclassical theory and considers the quantum optical nature of the HHG process. Considering the quantum degrees of freedom may improve our understanding of the HHG process and increase the utility of HHG as a spectrographic tool. Further, studying HHG from a quantum-optical perspective allows one to investigate if and what the system requirements are in order to generate pulses of nonclassical light. If these requirements are well understood, this has further engineering applications, as one would be able to design ultrashort pulses of quantum light with desirable properties.

As the main focus of the thesis and Papers II-V is quantum-optical HHG, the theoretical considerations are introduced and discussed in greater detail in this chapter. This chapter will first derive the central equations for quantum optical HHG in Sec. 4.1 starting from a general light-matter coupling Hamiltonian. Then, the results from Papers II and III will be presented in Sec. 4.2, where the quantum-optical nature of the emitted HHG from the Hubbard model is investigated. This is followed by more theoretical considerations where approximations are applied and verified numerically in Sec. 4.3, presenting the results of Paper IV. These approximations both ease the numerical effort for the simulations and yield more insights into the requirements for the generation

of nonclassical light.

In the thesis, and in this chapter especially, the notion *nonclassical* and *quantum* light will be used interchangeably.

4.1 Quantum-optical description of high-order harmonic generation

The starting point for describing quantum optical HHG is the VG Hamiltonian with a quantized vector potential in Eq. (2.96). The derivation presented in this chapter is also found in, e.g., Refs. [2, 132]. For N_e electrons, the Hamiltonian is given as

$$\hat{H} = \frac{1}{2}\sum_{j}^{N_e}[\hat{\boldsymbol{p}}_j + \hat{\boldsymbol{A}}(\hat{\boldsymbol{r}})]^2 + \hat{U} + \hat{H}_F, \tag{4.1}$$

where $\hat{\boldsymbol{A}}(\hat{\boldsymbol{r}})$ is the quantized vector potential [Eq. (2.18)], U is a general electron potential, and $\hat{H}_F$ is the Hamiltonian of the free electromagnetic field [Eq. (2.17)]. The state of the system, $|\Psi(t)\rangle$, is now a state of both electrons and photons, allowing for possible entanglement between the two subsystems. The state satisfies the TDSE

$$i\partial_t|\Psi(t)\rangle = \hat{H}|\Psi(t)\rangle, \tag{4.2}$$

with the Hamiltonian given in Eq. (4.1).

The state of the driving field is initially ($t = 0$) a coherent state.

$$|\psi_{\text{laser}}(t=0)\rangle = \bigotimes_{\substack{\boldsymbol{k},\sigma \\ =\boldsymbol{k}_L,\sigma_L}} |\alpha_{\boldsymbol{k},\sigma}\rangle = \hat{D}(\alpha)|0\rangle, \tag{4.3}$$

where the tensor product is over all modes $\boldsymbol{k}, \sigma = \boldsymbol{k}_L, \sigma_L$ populated by the laser, i.e., $\alpha_{\boldsymbol{k},\sigma} = 0$ for modes not populated by the laser, and where we for convenience define

$$\hat{D}[\alpha(t)] = \bigotimes_{\substack{\boldsymbol{k},\sigma \\ =\boldsymbol{k}_L,\sigma_L}} \hat{\mathcal{D}}\big(\alpha_{\boldsymbol{k},\sigma}e^{-i\omega_k t}\big) \tag{4.4}$$

as the displacement operator for the laser with $\alpha = \alpha(t = 0)$ for notational convenience. The initial state of the combined system is the product state of the electronic initial state $|\phi_i(t)\rangle$, which typically is the ground state, and the laser state

$$|\Psi(0)\rangle = |\phi_i(0)\rangle \otimes |\psi_{\text{laser}}(0)\rangle. \tag{4.5}$$

As we are interested in a strong-field process, namely HHG, the laser will contain a macroscopic number of photons. Such a large number of photons is

not feasible to handle numerically, and further theoretical treatment is required. To simplify the expressions, the state is transformed by displacing away the driving field and by going to the frame of the free field. Mathematically, the transformations are given as

$$|\tilde{\Psi}(t)\rangle_I = \hat{\mathcal{U}}_F^\dagger(t)\hat{D}^\dagger[\alpha(t)]|\Psi(t)\rangle, \tag{4.6}$$

such that $|\tilde{\Psi}(0)\rangle_I = |\phi_i\rangle \otimes |0\rangle$ the initial state contains the photonic vacuum state. In Eq. (4.6), $\hat{\mathcal{U}}_F(t) = \exp\left(-i\hat{H}_F t\right)$ is the time-evolution operator for the free field with initial time $t = 0$. In Eq. (4.6), the tilde denotes that the state is displaced, and the subscript denotes that it rotates with $\hat{\mathcal{U}}_F(t)$. We now exploit that

$$\hat{\mathcal{U}}_F^\dagger(t)\hat{D}^\dagger[\alpha(t)]\hat{\mathcal{U}}_F(t)\hat{\mathcal{U}}_F^\dagger(t) = \hat{D}^\dagger(\alpha)\hat{\mathcal{U}}_F^\dagger(t), \tag{4.7}$$

i.e., the commutation of $\hat{D}^\dagger[\alpha(t)]$ and $\hat{\mathcal{U}}_F^\dagger(t)$ removes the time dependence on the displacement operator. This approach, though different from the one used in Refs. [2, 132], only contains the simple time dependence of $\hat{\mathcal{U}}_F^\dagger(t)$ and is thus simpler to handle analytically. By inserting the relation in Eq. (4.7) into Eq. (4.6) and taking the time derivative, we obtain the transformed TDSE

$$\begin{aligned} i\partial_t|\tilde{\Psi}(t)\rangle_I &= \left\{\frac{1}{2}\sum_j^{N_e}[\hat{\boldsymbol{p}}_j + \hat{\boldsymbol{A}}(\hat{\boldsymbol{r}},t) + \boldsymbol{A}_{cl}(r,t)]^2 + \hat{U}\right\}|\tilde{\Psi}(t)\rangle_I \\ &= \left\{\hat{H}_{\mathrm{sc}}(t) + \frac{\hat{\boldsymbol{A}}(\hat{\boldsymbol{r}},t)}{2}\cdot\sum_j^{N_e}[\hat{\boldsymbol{p}}_j + \boldsymbol{A}_{cl}(\hat{\boldsymbol{r}},t)]\right. \\ &\quad \left. + \sum_j^{N_e}[\hat{\boldsymbol{p}}_j + \boldsymbol{A}_{cl}(\hat{\boldsymbol{r}},t)]\cdot\frac{\hat{\boldsymbol{A}}(\hat{\boldsymbol{r}},t)}{2} + \frac{N_e}{2}\hat{\boldsymbol{A}}^2(\hat{\boldsymbol{r}},t)\right\}|\tilde{\Psi}(t)\rangle_I, \end{aligned} \tag{4.8}$$

where Eq. (4.2) has been used, and where we have recognized the semiclassical Hamiltonian

$$\hat{H}_{\mathrm{sc}}(t) = \frac{1}{2}\sum_j^{N_e}[\hat{\boldsymbol{p}}_j + \boldsymbol{A}_{cl}(\hat{\boldsymbol{r}},t)]^2 + \hat{U}. \tag{4.9}$$

In Eq. (4.8), the time-dependent quantized vector-potential operator is given by

$$\begin{aligned} \hat{\boldsymbol{A}}(\hat{\boldsymbol{r}},t) &= \hat{\mathcal{U}}_F^\dagger(t)\hat{\boldsymbol{A}}(\hat{\boldsymbol{r}})\hat{\mathcal{U}}_F \\ &= \sum_{\boldsymbol{k},\sigma}\frac{g_0}{\sqrt{\omega_k}}\left[\boldsymbol{e}_\sigma\hat{a}_{\boldsymbol{k},\sigma}e^{i(\boldsymbol{k}\cdot\hat{\boldsymbol{r}}-\omega_k t)} + \mathrm{h.c}\right] \end{aligned} \tag{4.10}$$

with the coherent-state expectation value

$$\begin{aligned}\boldsymbol{A}_{cl}(\hat{\boldsymbol{r}},t) &= \langle\psi_{\text{laser}}(0)|\hat{\boldsymbol{A}}(\hat{\boldsymbol{r}},t)|\psi_{\text{laser}}(0)\rangle \\ &= \langle 0|\hat{D}^{\dagger}(\alpha)\hat{\boldsymbol{A}}(\hat{\boldsymbol{r}},t)\hat{D}(\alpha)|0\rangle \\ &= \sum_{\boldsymbol{k},\sigma=\boldsymbol{k}_L,\sigma_L} \frac{g_0}{\sqrt{\omega_k}}\left[\boldsymbol{e}_{\sigma}\alpha_{\boldsymbol{k},\sigma}e^{i(\boldsymbol{k}\cdot\hat{\boldsymbol{r}}-\omega_k t)} + \text{c.c}\right] \end{aligned} \tag{4.11}$$

being the quantum optical description of the classical driving field used in Eq. (4.9). Note that the sum in Eq. (4.11) only runs over modes populated by the laser, i.e., the same modes transformed by the operator $\hat{D}(\alpha)$. Continuing from Eq. (4.8), we now neglect the last term as it is proportional to g_0^2, i.e., much smaller compared to the other terms (see Sec. 4.1.1 below for a discussion), and further transform the state into rotating the frame of the semiclassical Hamiltonian [Eq. (4.9)] and obtain the TDSE

$$i\partial_t|\tilde{\Psi}(t)\rangle_I = \hat{V}_I(t)|\tilde{\Psi}(t)\rangle_I, \tag{4.12}$$

where the subscript now denotes the interaction picture with respect to both $\hat{\mathcal{U}}_F(t)$ and $\hat{\mathcal{U}}_{\text{sc}}(t)$, and where we have defined

$$\begin{aligned}\hat{V}_I(t) &= \frac{\hat{\boldsymbol{A}}(\hat{\boldsymbol{r}},t)}{2}\cdot\hat{\mathcal{U}}_{\text{sc}}^{\dagger}(t)\hat{\boldsymbol{j}}(\boldsymbol{r},t)\hat{\mathcal{U}}_{\text{sc}}(t) + \hat{\mathcal{U}}_{\text{sc}}^{\dagger}(t)\hat{\boldsymbol{j}}(\boldsymbol{r},t)\hat{\mathcal{U}}_{\text{sc}}(t)\cdot\frac{\hat{\boldsymbol{A}}(\hat{\boldsymbol{r}},t)}{2} \\ &\approx \hat{\boldsymbol{A}}(t)\cdot\hat{\mathcal{U}}_{\text{sc}}^{\dagger}(t)\hat{\boldsymbol{j}}(t)\hat{\mathcal{U}}_{\text{sc}}(t)\end{aligned} \tag{4.13}$$

where the dipole approximation have been invoked and with the current operator given by $\hat{\boldsymbol{j}}(t) = \Sigma_{j=1}^{N_e}[\hat{\boldsymbol{p}}_j + \boldsymbol{A}_{cl}(t)]$. By inserting a complete set of electronic states, $\Sigma_m|\phi_m\rangle\langle\phi_m| = \mathbb{I}$, where each state is time evolved via

$$|\phi_m(t)\rangle = \hat{\mathcal{U}}_{\text{sc}}(t)|\phi_m(0)\rangle, \tag{4.14}$$

we rewrite the right-hand side of Eq. (4.13) as

$$\hat{V}_I(t) = \hat{\boldsymbol{A}}(t)\cdot\sum_{m,n}\boldsymbol{j}_{m,n}(t)|\phi_m\rangle\langle\phi_n|. \tag{4.15}$$

In Eq. (4.15) we have defined the *transition current elements*

$$\boldsymbol{j}_{m,n}(t) = \langle\phi_m(t)|\hat{\boldsymbol{j}}(t)|\phi_n(t)\rangle, \tag{4.16}$$

which sometimes are also referred to as *cross currents*. Finally, we expand the combined state of the system in terms of field-free eigenstates of the electronic system

$$|\tilde{\Psi}(t)\rangle_I = \sum_m |\phi_m\rangle|\chi^{(m)}(t)\rangle, \tag{4.17}$$

where $|\chi^{(m)}(t)\rangle$ is the photonic state of interest correlated to the m'th electronic eigenstate, $|\phi_m\rangle$. The ansatz for the wavefunction in Eq. (4.17) is similar to a Born-Huang expansion for molecules with known electronic states and unknown states of the nuclei. Inserting Eqs. (4.15)-(4.17) into Eq. (4.12) and then projecting onto $\langle\phi_m|$ yields the equation of motion for the photonic state correlated to the m'th eigenstate

$$i\partial_t|\chi^{(m)}(t)\rangle = \hat{\boldsymbol{A}}(t)\cdot\sum_n \boldsymbol{j}_{m,n}(t)|\chi^{(n)}(t)\rangle, \tag{4.18}$$

which is the central equation for quantum optical HHG, as it describes the evolution of the quantum state of light coupled to an electronic system. A few comments are in order with respect to Eq. (4.18). First, we emphasize that this state is the generated light that is "on top" of the driving field, as this state is displaced with respect to the driving field, see Eq. (4.6). We also note that due to the projection onto an electronic state, Eq. (4.18) is not a TDSE, as it is not the same state on the left-hand side and right-hand side of the equation. Further we note that, different to semiclassical theory, not only is the expectation value of the current, $\langle\hat{\boldsymbol{j}}(t)\rangle = \boldsymbol{j}_{i,i}(t)$, required but *all* transition current elements are required to obtained the full dynamics. In fact, as will be discussed in Sec. 4.2, it is the presence of these off-diagonal transition currents that will generate nonclassical light. Note that the inclusion of the off-diagonal transition currents puts greater numerical demands on the system. Not only must one be able to diagonalize the full system, but one must also be able to subsequently time propagate all states of the system according to Eq. (4.14). For many purposes, including the Hubbard model, this limits the possible system size for numerical simulation. We also note that a completely equivalent derivation can be made for the LG Hamiltonian [Eq. (2.100)] where the dipole and electric field operators appear instead of the current and vector potential operators in Eq. (4.18). Finally, we note that one does not simply solve Eq. (4.17) no matter how small the considered electronic system is. This is due to the fact that photons in all considered modes have to be numerically handled, e.g., in a Fock basis, and as the state in general is not a product state, all possible combinations of photon numbers in all considered modes have to be considered which is unfeasible if more than a few modes and a few photons are considered. Thus, approximations have to be employed in order to be able to perform simulations. This matter will be discussed in greater detail in Sec. 4.3.

We can, however, use perturbation theory to gain analytical insights into the quantum optical nature of HHG. This was first presented in Ref. [132]. Going back to Eq. (4.12), the total state of the system is given by $|\tilde{\Psi}(t)\rangle_I = \hat{T}\exp\left[-i\int_0^t \hat{V}_I(t')dt'\right]$ where $\hat{T}$ is the time-ordering operator and $\hat{V}_I(t)$ given in Eq. (4.13). Going to first order in the interaction, $\hat{V}_I$, the state of the system is given as

$$|\tilde{\Psi}(t)\rangle_I = \left[1 - i\int_0^t \hat{V}_I(t')dt'\right]|\tilde{\Psi}(0)\rangle_I$$
$$= |\phi_i\rangle|0\rangle - i\sum_m |\phi_m\rangle \sum_{\boldsymbol{k},\sigma} \frac{g_0}{\sqrt{\omega_k}} \times \left[\int_0^t e^{i\omega_k t'} \boldsymbol{j}_{m,i}(t') \cdot \boldsymbol{e}_\sigma^* dt'\right]|1_{\boldsymbol{k},\sigma}\rangle \tag{4.19}$$

where $|1_{\boldsymbol{k},\sigma}\rangle$ is a single-photon state in the mode $(\boldsymbol{k},\sigma)$. Interestingly, Eq. (4.19) shows that the photon is in a superposition of all frequency modes with an amplitude given by the Fourier transform (for $t \to \infty$) of relevant cross-current matrix elements. Furthermore, Eq. (4.19) also shows that the photonic state is correlated to the electronic state, i.e., the nature (frequency) of the photon is entangled to the field-free eigenstate of the electronic system weighted by the aforementioned Fourier transform. We can thus already conclude that HHG is of quantum nature even in a first-order interaction. Unfortunately, due to the fact that Eq. (4.19) only contains at most a single photon, it is not possible to calculate higher moments of photonic operators as required to calculate the Mandel-Q parameter [Eq. (2.32)] and degree squeezing [Eq. (2.39)]. Equation (4.19) thus further motivates more exact studies on the quantum optical nature of HHG and also shows that one has to rely on numerical simulations.

Before showing the more exact numerical results from quantum optical HHG in the Hubbard model, we first discuss the $\hat{\boldsymbol{A}}^2$ term neglected when going from Eq. (4.8) to Eq. (4.12).

4.1.1 The role of the $\hat{A}^2$ term

In this section, the $\hat{\boldsymbol{A}}^2$ term arising from the VG Hamiltonian [Eq. (4.1)] will be investigated, building on Ref. [18]. For this analysis, it is convenient to expand the square in the first term of Eq. (4.1) to obtain

$$\hat{H} = \frac{1}{2}\sum_{j=1}^{N_e} \hat{\boldsymbol{p}}_j^2 + \hat{\boldsymbol{A}} \cdot \sum_{j=1}^{N_e} \hat{\boldsymbol{p}}_j + \frac{N_e}{2}\hat{\boldsymbol{A}}^2 + \hat{U} + \hat{H}_F, \tag{4.20}$$

where the dipole approximation has been assumed for simplicity. Inverting the expression for the photonic operator in Eq. (2.14), we now want to express Eq. (4.20) in terms of the canonical variables

$$\hat{q}_{\boldsymbol{k},\sigma} = \frac{1}{\sqrt{2\omega_k}}(\hat{a}_{\boldsymbol{k},\sigma} + \hat{a}_{\boldsymbol{k},\sigma}^\dagger), \qquad \hat{p}_{\boldsymbol{k},\sigma} = i\sqrt{\frac{\omega_k}{2}}(\hat{a}_{\boldsymbol{k},\sigma}^\dagger - \hat{a}_{\boldsymbol{k},\sigma}). \tag{4.21}$$

For simplicity, we focus on a single-mode quantized field. Expressing the vector potential [Eq. (2.18)] and the free-field Hamiltonian [Eq. (2.17)] in terms of the

canonical variables in Eq. (4.21), we obtain

$$\hat{\boldsymbol{A}}_{\boldsymbol{k},\sigma} = \boldsymbol{e}_\sigma \sqrt{2} g_0 \ \hat{q}_{\boldsymbol{k},\sigma}, \tag{4.22}$$

where linear polarization has also been assumed, and where

$$\begin{aligned} \hat{H}_F &= \frac{1}{2}\omega_k (\hat{a}^\dagger_{\boldsymbol{k},\sigma}\hat{a}_{\boldsymbol{k},\sigma} + \hat{a}_{\boldsymbol{k},\sigma}\hat{a}^\dagger_{\boldsymbol{k},\sigma}) \\ &= \frac{1}{2}(\omega_k^2 \hat{q}^2_{\boldsymbol{k},\sigma} + \hat{p}^2_{\boldsymbol{k},\sigma}). \end{aligned} \tag{4.23}$$

Inserting Eqs. (4.22) and (4.23) into Eq. (4.20) and defining $\hat{H}_e = \Sigma_{j=1}^{N_e} \frac{\hat{\boldsymbol{p}}_j^2}{2} + \hat{U}$, we obtain

$$\begin{aligned} \hat{H} &= \hat{H}_e + \sqrt{2} g_0 \ \hat{q}_{\boldsymbol{k},\sigma} \boldsymbol{e}_\sigma \cdot \sum_{j=1}^{N_e} \hat{\boldsymbol{p}}_j + \frac{1}{2}(\omega_k^2 \hat{q}^2_{\boldsymbol{k},\sigma} + \hat{p}^2_{\boldsymbol{k},\sigma}) + 2N_e g_0^2 \hat{q}^2_{\boldsymbol{k},\sigma} \\ &= \hat{H}_e + \sqrt{2} g_0 \ \hat{q}_{\boldsymbol{k},\sigma} \boldsymbol{e}_\sigma \cdot \sum_{j=1}^{N_e} \hat{\boldsymbol{p}}_j + \frac{1}{2}[(\omega_k^2 + \omega_p^2)\hat{q}^2_{\boldsymbol{k},\sigma} + \hat{p}^2_{\boldsymbol{k},\sigma}], \end{aligned} \tag{4.24}$$

where we have defined the so-called plasma frequency

$$\omega_p^2 = 2 g_0^2 N_e. \tag{4.25}$$

Looking at Eq. (4.24), we note that it is the same Hamiltonian as Eq. (4.20) but with the free-field Hamiltonian [Eq. (4.23)] replaced by a dressed free-field Hamiltonian

$$\hat{H}'_F = \frac{1}{2}(\omega'^2 \hat{q}^2_{\boldsymbol{k},\sigma} + \hat{p}^2_{\boldsymbol{k},\sigma}), \tag{4.26}$$

where the perturbed frequency is given as $\omega' = \sqrt{\omega_k^2 + \omega_p^2}$. We see that the effect of the $\hat{\boldsymbol{A}}^2$ term is to perturb the field mode from frequency ω_k to ω'. Essentially, this is a second-order coupling of the photons to themselves via the electrons. We can define new operators of the dressed mode

$$\hat{a}' = \frac{1}{2\omega'}(\omega' \hat{q}_{\boldsymbol{k},\sigma} + i\hat{p}_{\boldsymbol{k},\sigma}), \tag{4.27}$$

and rewrite the Hamiltonian in Eq. (4.24) as

$$\hat{H} = \hat{H}_e + \frac{g_0}{\sqrt{\omega'}}(\hat{a}' + \hat{a}'^\dagger) \cdot \sum_{j=1}^{N_e} \hat{\boldsymbol{p}}_j + \omega' \hat{a}'^\dagger \hat{a}. \tag{4.28}$$

Comparing Eq. (4.28) to Eq. (4.20), we see that the quadratic dependence of the field operator has disappeared at the cost of perturbing the field to be described

by the primed modes. Semiclassically, this difference is irrelevant, as the $\boldsymbol{A}^2$ term in a semiclassical Hamiltonian will only yield a time-dependent phase on the wavefunction. However, in quantum optics, it is known that quadratic photon operators induce squeezing [74], but by comparing Eq. (4.28) to Eq. (4.20), this is curiously not the case for the $\hat{\boldsymbol{A}}^2$-operator. We note that the parameter relating the perturbed and unperturbed field modes is the plasma frequency in Eq. (4.25). As $g_0^2 = 2\pi/V$ where V is the quantization volume, we note that the plasma frequency depends on the ratio N_e/V. In dilute atomic gases, this ratio is usually very small, and the perturbation will consequently be negligible. However, in condensed-matter systems, the plasma frequency might yield a noticeable contribution and perturb the field modes. Though each mode is shifted to the primed modes, this does seemingly not matter, as the summation in Eq. (4.20) is over all modes, i.e., the sum over all modes remains the sum over all modes. The only difference is that modes with very low frequency are not considered anymore, as the smallest primed mode is ω_p, which we still take to be way smaller than the frequency of the driving field, such that, in the context of HHG, the sum over all considered modes remains the same. A full derivation for multimode fields is found in Ref. [18]. We also note that a similar analysis in the LG formulation [Eq. (2.100)] will lead to a term proportional to g_0^2, namely the dipole-correction term in Eq. (2.101). This term, different from the $\hat{\boldsymbol{A}}^2$ term, is quadratic in the electron operators and is interpreted as the interaction of electrons with themselves via the photonic field.

In the context of quantum optical HHG, the above analysis presents a challenge. It turns out that it matters at which point in the derivation the considerations above are made. If the considerations to change into the primed modes are made on the level of Eq. (4.20), we obtain the Hamiltonian (in the dipole approximation)

$$\hat{H} = \frac{1}{2}\sum_{j=1}^{N_e} \hat{\boldsymbol{p}}_j^2 + \hat{\boldsymbol{A}} \cdot \sum_{j=1}^{N_e} \hat{\boldsymbol{p}}_j + \hat{U} + \hat{H}_F, \tag{4.29}$$

where no quadratic photon operator appears. Following the steps of the derivation in Sec. 4.1 by transforming into the frame of the free field and the subsequent displacement of the laser field, transforms Eq. (4.29) into

$$\begin{aligned}\hat{H}'(t) &= \frac{1}{2}\sum_{j=1}^{N_e} \hat{\boldsymbol{p}}_j^2 + [\hat{\boldsymbol{A}}(t) + \boldsymbol{A}_{cl}(t)] \cdot \sum_{j=1}^{N_e} \hat{\boldsymbol{p}}_j + \hat{U}, \\ &= \hat{H}'_{\mathrm{sc}}(t) + \hat{\boldsymbol{A}}(t) \cdot \sum_{j=1}^{N_e} \hat{\boldsymbol{p}}_j,\end{aligned} \tag{4.30}$$

where we have defined a semiclassical Hamiltonian, $\hat{H}'_{\mathrm{sc}}(t)$, different from Eq.

(4.9) as

$$\hat{H}'_{\rm sc}(t) = \frac{1}{2}\sum_{j=1}^{N_e}\hat{\boldsymbol{p}}_j^2 + \hat{U} + \boldsymbol{A}_{cl}(t)\cdot\sum_{j=1}^{N_e}\hat{\boldsymbol{p}}_j. \tag{4.31}$$

Note that Eq. (4.30) is *not* the same Hamiltonian appearing in Eq. (4.8). Specifically, the term $\hat{\boldsymbol{A}}(t)\cdot\boldsymbol{A}_{cl}(t)$ is absent from Eq. (4.30). However, as is shown below, this only modifies the driving mode and not the generated harmonics. Without the transformation into the primed modes, the Hamiltonian is given as [using Eq. (4.8) in the dipole approximation, and neglecting the $\hat{\boldsymbol{A}}^2$ term]

$$\hat{H}(t) = \hat{H}_{\rm sc}(t) + \hat{\boldsymbol{A}}(t)\cdot\sum_{j=1}^{N_e}[\hat{\boldsymbol{p}}_j + \boldsymbol{A}_{cl}(t)], \tag{4.32}$$

where $\hat{H}_{\rm sc}(t)$ is given in Eq. (4.9). We note that the difference between the two semiclassical Hamiltonians is simply

$$\hat{H}_{\rm sc}(t) - \hat{H}'_{\rm sc}(t) = \frac{N_e}{2}\boldsymbol{A}_{cl}^2(t), \tag{4.33}$$

which can be neglected due to the fact that it only induces a time-dependent phase on the wavefunction. With this transformation, the semiclassical time evolution is thus identical using either semiclassical Hamiltonians, and we can thus go to the same semiclassical rotating frame. We first go into the semiclassical frame of Eq. (4.30) which has transformed into the primed modes via the $\hat{\boldsymbol{A}}^2$ term, and obtain

$$\hat{H}'_I(t) = \hat{\boldsymbol{A}}(t)\cdot\sum_{j=1}^{N_e}\hat{U}^\dagger_{sc}(t)\hat{\boldsymbol{p}}_j\hat{U}_{sc}(t), \tag{4.34}$$

whereas Eq. (4.32) transforms into

$$\hat{H}_I(t) = \hat{\boldsymbol{A}}(t)\cdot\sum_{j=1}^{N_e}[\hat{U}^\dagger_{sc}(t)\hat{\boldsymbol{p}}_j\hat{U}_{sc}(t) + \boldsymbol{A}_{cl}(t)]. \tag{4.35}$$

We note that the only difference between Eqs. (4.34) and (4.35) is the semiclassical vector potential, which will only affect the fundamental driving field and *not* the harmonics. We have thus found that the $\hat{\boldsymbol{A}}^2$ term does not contribute to the dynamics for most systems. However, it remains to be studied how large the plasma frequency is and if it perturbs the modes significantly. We remind ourselves that the summation in the vector potential [Eq. (2.18)] is over all modes, so shifting all modes by a given amount, δ, will still result in a summation over all modes except for an offset by δ, which might be of importance. The value of ω_p [Eq. (4.25)] is system dependent, but is larger for solid-state systems where many electrons are involved. This is a topic to

be investigated in future studies. Going forward, the $\hat{\boldsymbol{A}}^2$ term is neglected in the following and in the research papers, if not for other reasons, due to its g_0^2 dependence, which makes it significantly weaker than the other terms for reasonable values of the coupling strength, g_0.

4.2 Quantum light from high-order harmonic generation

Taking $\hat{H}_{\mathrm{sc}}(t) = \hat{H}_{\mathrm{FH}}(t)$ and by using the equation of motion for the photonic states [Eq. (4.18)], it is possible to calculate the various observables of interest: the HHG spectrum [Eq. (2.31)], the Mandel-Q parameter [Eq. (2.32)], and the degree of squeezing [Eq. (2.39)]. Unfortunately, as alluded to in Sec. 4.1, it is not possible to solve Eq. (4.18) if one wishes to consider more than a few photons in a few modes. To proceed, we thus make the approximation, that the photonic modes are uncorrelated, $|\chi^{(m)}(t)\rangle = \otimes_{\boldsymbol{k},\sigma}|\chi^{(m)}_{\boldsymbol{k},\sigma}(t)\rangle$, where each mode follows the equation of motion

$$i\partial_t|\chi^{(m)}_{\boldsymbol{k},\sigma}(t)\rangle = \hat{\boldsymbol{A}}_{\boldsymbol{k},\sigma}(t)\cdot\sum_n \boldsymbol{j}_{m,n}(t)|\chi^{(n)}_{\boldsymbol{k},\sigma}(t)\rangle, \tag{4.36}$$

and where $|\chi^{(m)}_{\boldsymbol{k},\sigma}(t)\rangle$ is the photonic state in mode $(\boldsymbol{k},\sigma)$ correlated to the m'th electronic eigenstate. In Eq. (4.18), the vector potential only couples to mode $(\boldsymbol{k},\sigma)$ via the vector potential operator

$$\hat{\boldsymbol{A}}_{\boldsymbol{k},\sigma} = \frac{g_0}{\sqrt{\omega_k}}(\hat{a}_{\boldsymbol{k},\sigma}e^{-i\omega_k t} + \hat{a}^\dagger_{\boldsymbol{k},\sigma}e^{i\omega_k t}). \tag{4.37}$$

where the dipole approximation has been assumed. This *decoupling ansatz* in Eq. (4.36) is the first step in a hierarchy of approximations, which is the topic of Sec. 4.3. Using Eq. (4.36), the HHG emission from the Hubbard model can be calculated by inserting the current matrix elements, $\boldsymbol{j}_{m,n}(t)$ [see Eq. (4.16)], calculated from the Hubbard model. Conveniently, this allows the use of numerical tools and techniques already developed to propagate the electronic states, $|\phi_m(t)\rangle$, according to the semiclassical TDSE, see Eq. (4.14). As shown in Fig. 4.1, where the Mott-insulating phase is considered ($U = 10t_0$), the transition current matrix elements have widely different spectral structure, and some are even many orders of magnitude greater than the classical current, $\tilde{\boldsymbol{j}}_{i,i}(\omega)$, at certain frequencies [2]. With all current matrix elements in hand, the photonic states can be obtained from Eq. (4.36). We express each state, $|\chi^{(m)}_{\boldsymbol{k},\sigma}(t)\rangle$, in a Fock basis containing up to 50 photons and integrate Eq. (4.36) for each mode with a spacing of $\omega/\omega_L = 0.1$ using a standard fourth-order Runge-Kutta routine.

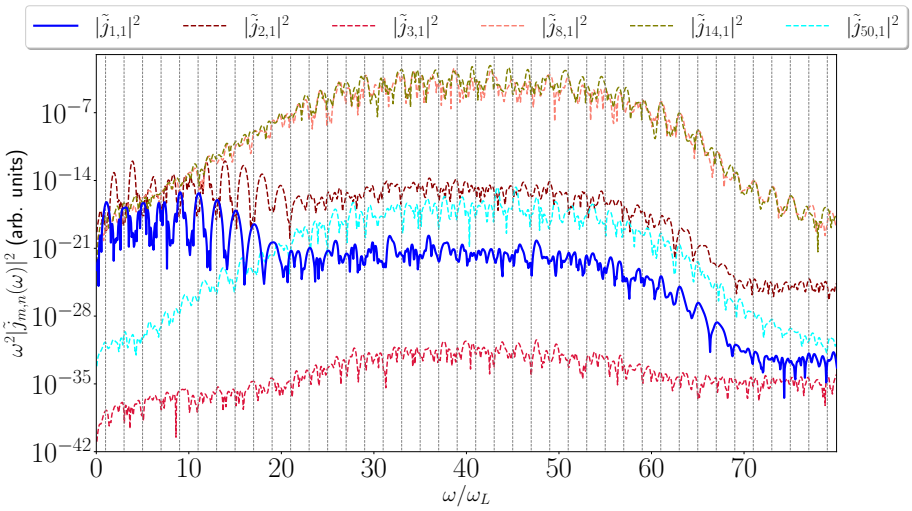

Figure 4.1: The Fourier transform of selected transition current matrix elements, $\boldsymbol{j}_{m,n}$ [Eq. (4.16)]. We note that different elements yield signal even orders of magnitude larger than the classical current, $\boldsymbol{j}_{1,1}$, at certain frequencies. The characteristics of the system are described in the text. Adapted with permission from Ref. [2]. Copyrighted by the American Physical Society.

We consider three different phases of the model. First, we consider the uncorrelated case of $U = V = 0$. Then we consider the Mott-insulating phase with $U = 10t_0$ with $V = 0$. Both of these phases are presented in Paper II. Finally, we consider the phase supporting the Mott exciton $U = 12t_0$ and $V = 4t_0$, highlighting the results from Paper III. For details on the calculation of expectation values, see App. B. Note that all results show the light generated "on top" of the driving field, i.e., the results are shown in the frame where the initial photon state is displaced to vacuum.

4.2.1 Uncorrelated phase

The uncorrelated phase with $U = V = 0$ allows for further analytical considerations as discussed in Sec. 3.2.1. The time-evolution operator for the uncorrelated phase is given by $\hat{\mathcal{U}}_{\text{Hop}}(t) = \exp\left[-i\int_0^t dt' \hat{H}_{\text{Hop}}(t')\right]$ and due to the fact that the current operator commutes with $\hat{H}_{\text{Hop}}(t)$ [Eq. (3.27)], it follows that it also commutes with the time-evolution operator, i.e., $[\hat{\boldsymbol{j}}(t), \hat{H}_{\text{Hop}}(t)] = 0$. With these

relations, we can now calculate the current matrix elements [Eq. (4.16)]

$$\begin{aligned}\boldsymbol{j}_{m,n}(t) &= \langle\phi_m(0)|\hat{\mathcal{U}}^\dagger_{\mathrm{Hop}}(t)\hat{\boldsymbol{j}}(t)\hat{\mathcal{U}}_{\mathrm{Hop}}(t)|\phi_n(0)\rangle \\ &= \boldsymbol{j}_{m,m}(t)\delta_{m,n},\end{aligned} \tag{4.38}$$

where it was used that $|\phi_n(t)\rangle$ is an eigenstate for the current operator. We thus see that only the diagonal current elements are involved in the uncorrelated phase. As the system is initially in the state $|\phi_i(0)\rangle$, which typically is the ground state, and the dynamics do not couple to other states with $m \neq i$, only $|\phi_i(t)\rangle$ is populated during the dynamics. This simplifies the equation of motion [Eq. (4.18)]

$$i\partial_t|\chi^{(i)}(t)\rangle = \hat{\boldsymbol{A}}(t)\cdot\boldsymbol{j}_{i,i}(t)|\chi^{(i)}(t)\rangle. \tag{4.39}$$

Equation (4.39) is linear in the photonic operators and has the closed-form solution [169]

$$|\chi^{(i)}(t)\rangle = \bigotimes_{\boldsymbol{k},\sigma}\hat{\mathcal{D}}[\beta^{(i)}_{\boldsymbol{k},\sigma}(t)]|0\rangle, \tag{4.40}$$

where $\beta^{(i)}_{\boldsymbol{k},\sigma}(t)$ is the time-dependent coherent-state amplitude is given by

$$\beta^{(i)}_{\boldsymbol{k},\sigma}(t) = -i\frac{g_0}{\sqrt{\omega_k}}\int_0^t e^{i\omega_k t'}\boldsymbol{j}_{i,i}(t')\cdot\boldsymbol{e}^*_\sigma dt'. \tag{4.41}$$

This result fits well with the fact that the field emitted from a classical current is a coherent state [169]. The mean photon number for Eq. (4.41) is $\langle\hat{n}_{\boldsymbol{k},\sigma}\rangle = \left|\beta^{(i)}_{\boldsymbol{k},\sigma}\right|^2$. Inserting this into the expression for the spectrum [Eq. (2.31)] and taking the polarization to be along the chain, we obtain (taking $t\to\infty$)

$$S(\omega_k) = \frac{\omega_k^2}{(2\pi)^2c^3}\sum_\sigma|\boldsymbol{j}_{i,i}(\omega_k)\cdot\boldsymbol{e}^*_\sigma|^2, \tag{4.42}$$

which is proportional to the semiclassical expression for the spectrum [Eq. (2.27)], see Fig. 3.7. Further, as Eq. (4.40) is a coherent state, it will have Poissonian photon statistics and no squeezing, i.e., $Q_{\boldsymbol{k},\sigma} = \eta_{\boldsymbol{k},\sigma} = 0$ for all modes. Thus, no quantum optical treatment is necessary when modeling uncorrelated electrons in an intraband model. We further note, that adding beyond-nearest-neighbor hopping in $\hat{H}_{\mathrm{Hop}}$ [Eq. (3.23)] will not change these conclusions as it will still commute with the current operator. This means that uncorrelated electrons in an intraband model will *always* yield classical light no matter the dispersion relation.

This result is in disagreement with the Ref. [148] where they measure $g^{(2)}(0) > 2$ from band-gap materials. The disagreement with Ref. [148] lies in the theoretical modeling, which only considers the intraband contribution. There,

the quantum optical vector potential is inserted into the dispersion relation of the band, which, due to its nonlinearity, generates squeezing in the emitted light. However, simply promoting the vector potential in the dispersion relation to a quantum operator is, in our opinion, not justified. In contrast, as shown from first principles, the derivation presented above does not make such a prediction. Additionally, the harmonics considered in the measurements of $g^{(2)}(0)$ have energies above the bandgap energy of the considered material. While intraband current can produce harmonics with this energy, one must also consider the contribution from interband current in order to accurately model the generated light. As our theory predicts classical light from intraband currents, we believe that the experimental results are to be explained with interband contributions. Interestingly, a complete theory for the quantum-optical description from bandgap materials is still to be derived (see Ref. [147]).

4.2.2 Mott-insulating phase

We now consider the Mott-insulating phase with $U = 10t_0$ and $V = 0$ introduced in Sec. 3.2.2. This system is driven by a linearly polarized pulse with the vector potential in the form $A_{cl}(t) = A_0 \sin(\omega_L t + \pi/2) \times \sin^2(\omega_L t/2N_c)$, where $N_c = 10$ is the number of cycles in the pulse. All other parameters are the same as the ones used in Sec. 3.4, except for a reduced lattice of $L = 8$ sites. The reduced lattice size is due to the fact that the numerical requirements are drastically increased in the quantum-optical treatment of HHG, as the full current matrix, $\boldsymbol{j}_{m,n}(t)$, must be calculated for all times. In Fig. 4.2(a), we see both the spectrum obtained from the quantum optical analysis by integrating Eq. (4.36) and calculating Eq. (2.31) (solid blue line), and the semiclassically obtained spectrum [Eq. (2.27), dashed orange]. We note that the two spectra (up to normalization) show good agreement, and the quantum-optical nature of HHG can hence not be deduced by looking solely at the spectra. In the spectrum in Fig. 4.2(a), we notice that the harmonics below the Mott gap (middle vertical black line) show clear peaks at odd harmonics as expected due to the selection rules discussed in Sec. 3.4. We also note that this clear signal extends beyond Δ_{Bloch} (left vertical black line) which lies in the middle of an exponential drop in signal strength, which shows that the heuristic argument of intra-subband current yielding harmonics up to $\omega/\omega_L \lesssim \Delta_{\text{Bloch}}$ in the Mott-insulating phase is indeed only heuristic. In real space, this intra-subband current is the propagation of doublon-holon pairs within a subband, which, for the current simulation, is the second subband, see Figs. 3.3 and 3.4. Above the Mott gap, we see that the signal increases. This is due to the contribution from the inter-subband current, i.e., the recombination of a doublon with a hole, see Fig. 3.4. This energy releases radiation with $\omega/\omega_L \geq \Delta_{\text{Mott}}$. Note that above the Mott gap, noninteger harmonics appear. This is due to the population of multiple Floquet

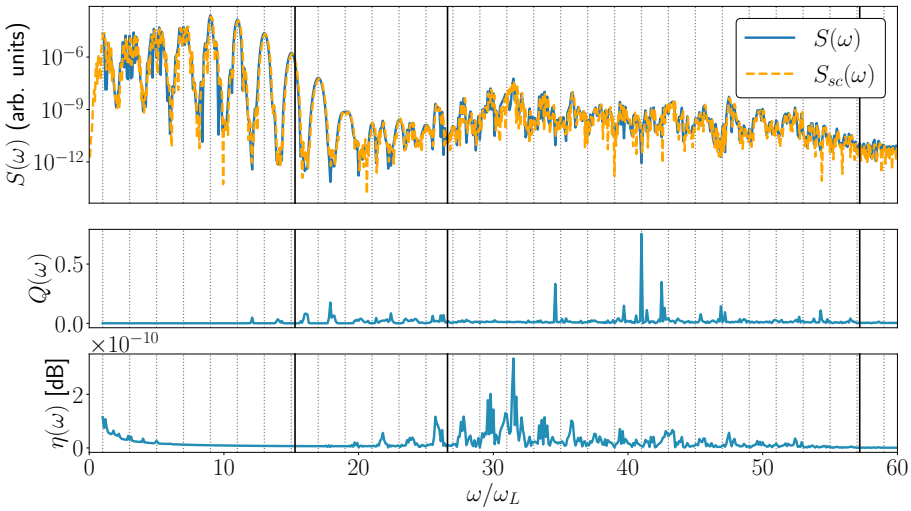

Figure 4.2: Observables for the Mott-insulating phase ($U = 10t_0$) of the Hubbard model for $L = 8$ sites with periodic boundary conditions. The vertical black lines indicate Δ_{Bloch} (left), Δ_{Mott} (middle), and $\Delta_{\text{Mott}} + 2\Delta_{\text{Bloch}}$ (right). (a) The HHG spectrum obtained from both quantum optical [Eq. (2.31)] and semiclassical [Eq. (2.27)] analysis. We see that the two spectra show good agreement. Note that the signal at energies below Δ_{Mott} shows clear peaks at odd harmonics while noninteger harmonics appear above the Mott gap. (b) The Mandel-Q parameter [Eq. (2.32)] where only super-Poissonian statistics is seen across the spectrum. (c) The degree of squeezing [Eq. (2.39)] where we see a clear signal, especially above the Mott gap, showing that the light is nonclassical. Adapted with permission from Ref. [2]. Copyrighted by the American Physical Society.

states as discussed in Sec. 3.4. Finally, we note that the spectrum drops for energies larger than $\Delta_{\text{Mott}} + 2\Delta_{\text{Bloch}}$ (right vertical black line).

Looking at the Mandel-Q parameter in Fig. 4.2(b), we see that only positive values appear at certain discrete frequencies. Especially, we note a clear peak at $\omega/\omega_L = 41$. However, the expression for the Mandel-Q parameter [Eq. (2.32)] is inversely proportional to $S(\omega_k) \propto \langle \hat{n}_{\boldsymbol{k},\sigma} \rangle$, so this high value of $Q_{\boldsymbol{k},\sigma}$ is found at a frequency where the HHG signal is weak. Further, as the $Q_{\boldsymbol{k},\sigma} > 0$, the light has super-Poissonian statistics and can, on that account, not be deemed nonclassical.

However, looking at the degree of squeezing in Fig. 4.2(c), we note nonzero values of $\eta_{\boldsymbol{k},\sigma}$ which proves that the light indeed is nonclassical. In particular, we note that the degree of squeezing occurs at energies above the Mott gap. This

shows that electron-electron correlations induce squeezing and hence nonclassical light at higher harmonics and at wavelengths typically not considered in quantum optics. We note that the degree of squeezing is fairly weak ($\sim 10^{-10}$ dB), but one must keep in mind that the provided results are based on simulations of $L = 8$ electrons. As shown in Eq. (2.64), the degree of squeezing is related to the mean photon number, and as the signal is already weak due to the limited system size, it is to be expected that the degree of squeezing is likewise small. However, for any experimental realistic system size, the degree of squeezing will increase. This is consistent with the fact that the degree of squeezing is larger for $L = 8$ than found for $L = 6$.

4.2.3 Mott-exciton phase

We now consider the phase supporting the Mott exciton ($U = 12t_0$, $V = 4t_0$) for $L = 8$ sites as introduced in Sec. 3.2. For this system, a linearly polarized pulse is used with a vector potential given by $A_{cl}(t) = (F_0/\omega_L)\exp\left[-(t-t_c)^2/2\sigma_L^2\right]$ $\times \sin[\omega_L(t-t_c)]$ with $F = 0.0025$ a.u, $\omega_L = t_0/2 = 0.00955$a.u., $\sigma_L = 3T_c$, and $t_c = 15T_L$, where $T_L = 2\pi/\omega_L$ is the period of the laser frequency. The parameters for the electron system are the same as those used in Figs. 4.2 given in Sec. 3.4. This pulse form and parameters are chosen to compare to semiclassical simulations [212]. The results are seen in Fig. 4.3. In Fig. 4.3(a), the spectrum is shown. Here we first note that the semiclassical spectrum [Eq. (2.27), dashed orange] to a good degree matches the quantum optical spectrum [Eq. (2.31), solid blue]. We note that the spectrum peaks exactly at the exciton energy (vertical dashed line), the same energy shown in the linear response in Fig. 3.5(b). This shows that the exciton is also central to the nonlinear dynamics of the system. We further note that the spectrum shows clear peaks at odd harmonics, which shows that for this system with the applied pulse, only a single Floquet state is populated.

Looking at the Mandel-Q parameter [Eq. (2.32)] in Fig. 4.3(b), we note that only very small positive values are found. Curiously, no clear signal is seen at the exciton energy. As was the case for the Mott-insulating phase in Fig. 4.2(b), the Mandel-Q parameter does not reveal any quantum nature of the emitted light.

Again, this is different when considering the degree of squeezing [Eq. (2.39)]. In particular, we note that the degree of squeezing clearly spikes at the exciton energy, with a value much higher than for the $V = 0$ in Fig. 4.2(c). In this sense, the presence of the exciton clearly enhances the degree of squeezing, a quite interesting result. Experimentally, this clear signal at the exciton energy in Fig. 4.3(c) is easier to detect than the squeezing for the Mott-insulating phase in Fig. 4.2(c) as the signal is both stronger and spectrally more localized, which puts fewer demands on the experimental equipment. Again, we note that the degree

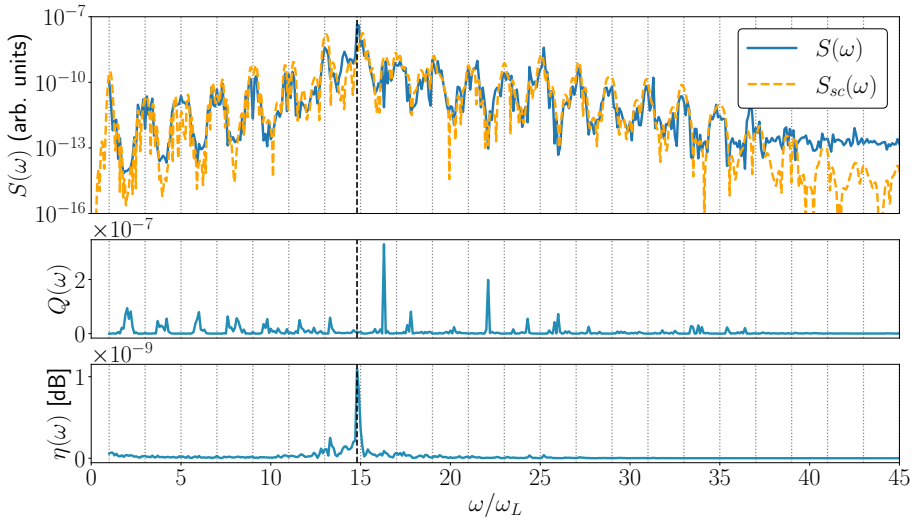

Figure 4.3: Observables for the Mott-exciton phase ($U = 12t_0$, $V = 4t_0$) of the Hubbard model for $L = 8$ sites with periodic boundary conditions. The vertical dashed line indicates the exciton energy as shown in Fig. 3.5(b). (a) The HHG spectrum obtained from both quantum optical [Eq. (2.31)] and semiclassical [Eq. (2.27)] analysis. We see that the two spectra show good agreement. We note that clear odd harmonics are seen across the spectrum and that the signal peaks exactly at the exciton energy close to $\omega/\omega_L \approx 15$, showing that the exciton is central in the nonlinear dynamics. (b) The Mandel-Q parameter [Eq. (2.32)] where only super-Poissonian statistics is seen across the spectrum, but with very small values. (c) The degree of squeezing [Eq. (2.39)] where we see a clear signal as the exciton energy. Adapted with permission from Ref. [3]. Copyrighted by the American Physical Society.

of squeezing, though low in the simulations, is expected to be much greater in any physically realistic systems. Finally, we note that the qualitative shape of the squeezing parameter for both the Mott-exciton phase (Fig. 4.3) and the Mott-insulating phase (Fig. 4.3) resembles the linear response function in Fig. 3.5(b). For both the Mott-insulating phase in Fig. 4.2 and the Mott-exciton phase in Fig. 4.3, we see that it is the presence of electron-electron correlations that generates nonclassical light from HHG.

4.3 Hierarchy of approximations

As stated in Ch. 1, different works have used different types of approximations to proceed from Eq. (4.18), which in general is not solvable. One type of approximation is to neglect the current correlations (or dipole correlations in the case of atoms). This approximation, also sometimes referred to as *negligible depletion of the ground state*, takes $\hat{\boldsymbol{j}}(t) = \langle \hat{\boldsymbol{j}}(t) \rangle$, i.e., considers only the classical current. This approximation yields a closed-form solution where all harmonic radiation is in a coherent state [133–137]. Another kind of approximation is to consider only two quantum optical states, the so-called *two-channel approximation* [138]. Note that this is not the same as a two-level system, as the former involves two time-propagated states, which in general populate all electronic states, including the continuum states, during the dynamics. In the two-channel approximation and under certain conditions for the applied laser pulse, a perturbative solution is possible, allowing for a closed-form expression for the quantum optical state [138–140, 147]. Other works [2–4, 132] consider all quantum optical states, but assume all photonic states to be product states such that the dynamics of a photonic mode, $(\boldsymbol{k}, \sigma)$, is independent from all other modes, $(\boldsymbol{k}', \sigma') \neq (\boldsymbol{k}, \sigma)$ as done in Sec. 4.2.

We will, in the remainder of this chapter, proceed with the latter approximation as also done in Papers II-IV. As seen in Figs. 4.2(a) and 4.3(a), the quantum optical spectrum matches the semiclassical spectrum. We can thus conclude that the semiclassical expression for the spectrum [Eq. (2.27)] yields accurate results, and that the spectrum is proportional to the Fourier transformed current. However, as seen in Figs. 4.2(b)-(c) and 4.3(b)-(c), the Mandel-Q parameter and the degree of squeezing do not follow the same "structure" as the spectra. This naturally raises the question: If the spectrum is related to the Fourier transform of the current, what electronic quantity are the photon statistics and the degree of squeezing related to? We are thus motivated to investigate the underlying electronic properties that generate these (possible) nonclassical features. In order to investigate the origin of the generation of nonclassical light, we make further approximations to obtain analytical expressions for the quantum optical state. This will yield a hierarchy of approximations, with the final and simplest expression being the MSA. The MSA was first presented in Ref. [150] but numerically verified for the Hubbard model in Paper IV.

Before deriving the hierarchy of approximations, we first turn our attention to the exact expression in Eq. (4.18). The states required to solve this equation would be on the following form when expanded in, e.g., a Fock basis

$$|\chi^{(m)}(t)\rangle = \sum_{\{n\}} c^{(m)}_{\{n\}}(t) |n_{\boldsymbol{k}_1,\sigma_1}, n_{\boldsymbol{k}_2,\sigma_2}, \ldots\rangle, \tag{4.43}$$

where the sum is over all $\{n\}$ possible combinations of photon numbers in all considered modes. The number of required basis states scale exponentially on

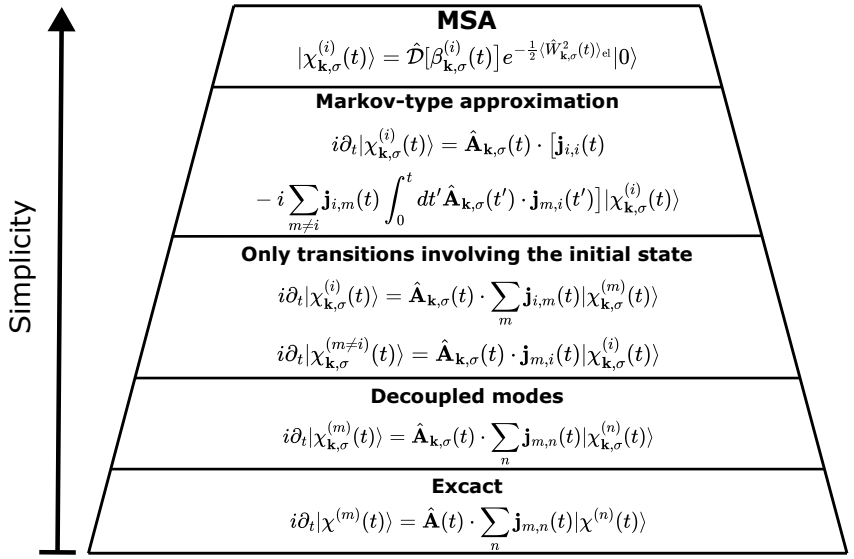

Figure 4.4: Hierarchy of approximations for the quantum optical state emitted from HHG with related equations as discussed in text. Each successive approximation builds upon and includes all the assumptions made in the previous ones, with increasing simplicity. Adapted with permission from Ref. [4]. Copyrighted by the American Physical Society.

the form $p^{\boldsymbol{k}_{\max}}$, where p is the maximum number of photons allowed in a given mode, and $\boldsymbol{k}_{\max}$ denotes the mode with the highest wavenumber considered. We emphasize that this exponential scaling is independent of the nature of the electronic system. Even for a two-level system, Eq. (4.43) would be the required basis, which is not numerically possible to employ. For this reason, Eq. (4.18) remains practically unsolvable in general. To be able to proceed, even numerically, approximations are required. This further motivates the hierarchy of approximations shown in Fig. 4.4, which will be derived below, followed by numerical verification.

Decoupled modes

The first approximation employed is the already-presented decoupling of modes $|\chi^{(m)}(t)\rangle = \otimes_{\boldsymbol{k},\sigma}|\chi^{(m)}_{\boldsymbol{k},\sigma}(t)\rangle$ with the dynamics shown in Eq. (4.36). This approximation drastically reduces the required basis size. Expanded in a Fock basis,

the state is expressed as

$$|\chi^{(m)}_{\boldsymbol{k},\sigma}(t)\rangle = \sum_{n_{\boldsymbol{k},\sigma}}^{p_{\boldsymbol{k},\sigma}} c^{(m)}_{n_{\boldsymbol{k},\sigma}}(t)|n_{\boldsymbol{k},\sigma}\rangle, \tag{4.44}$$

where the summation is now simply over photon numbers up to a given maximum of $p_{\boldsymbol{k},\sigma}$ photons. In contrast to Eq. (4.43), Eq. (4.36) requires only $p_{\boldsymbol{k},\sigma} \times \boldsymbol{k}_{\max}$ states for a given electronic index m, as $\boldsymbol{k}_{\max}$ modes are considered each with a maximum of $p_{\boldsymbol{k},\sigma}$ photons. The prize for such a significant reduction of the required basis states is neglecting harmonic correlations, i.e., that the dynamics of each mode is independent of other modes. This decoupled ansatz is the most exact formulation which allows for numerical simulations, see Fig. 4.4.

Keeping only transitions involving the initial state

As a next approximation, we now only keep couplings that involve the initial electronic state. This is motivated by the fact that the coupling constant, g_0, typically is very small, such that higher-order couplings via excited states are negligible. We thus only keep couplings that involve the initial state directly, $i \to i$ and to first order, $i \to m \to i$, but neglect couplings on the form $i \to m \to n \to i$ and higher order couplings, where i denotes the initial electronic state and $m, n \neq i$. Mathematically, we set $\boldsymbol{j}_{m,n}(t) = 0$ when both $m \neq i$ and $n \neq i$. Inserting this into Eq. (4.36), we obtain

$$i\partial_t|\chi^{(i)}_{\boldsymbol{k},\sigma}(t)\rangle = \hat{\boldsymbol{A}}_{\boldsymbol{k},\sigma} \cdot \sum_m \boldsymbol{j}_{i,m}(t)|\chi^{(m)}_{\boldsymbol{k},\sigma}(t)\rangle, \tag{4.45a}$$

$$i\partial_t|\chi^{(m\neq i)}_{\boldsymbol{k},\sigma}(t)\rangle = \hat{\boldsymbol{A}}_{\boldsymbol{k},\sigma} \cdot \boldsymbol{j}_{m,i}(t)|\chi^{(i)}_{\boldsymbol{k},\sigma}(t)\rangle, . \tag{4.45b}$$

We note that Eq. (4.45) only requires M matrix elements, where M is the number of electronic states, while Eq. (4.36) requires M^2 matrix elements. As such, the approximation significantly eases the numerical effort. The approximation of only including transitions involving the ground state is also found in Fig. 4.4.

Markov-type approximation

To proceed, we bring Eq. (4.45) onto a simpler form by first formally integrating Eq. (4.45b)

$$|\chi^{(m\neq i)}_{\boldsymbol{k},\sigma}(t)\rangle = -i\int_0^t dt' \hat{\boldsymbol{A}}_{\boldsymbol{k},\sigma}(t') \cdot \boldsymbol{j}_{m,i}(t')|\chi^{(i)}_{\boldsymbol{k},\sigma}(t')\rangle, \tag{4.46}$$

where the initial time is taken to be $t = 0$ for simplicity. Inserting Eq. (4.46) into Eq. (4.45a), we obtain

$$i\partial_t|\chi^{(i)}_{\boldsymbol{k},\sigma}(t)\rangle = \hat{\boldsymbol{A}}_{\boldsymbol{k},\sigma}(t)\cdot\Bigg[\boldsymbol{j}_{i,i}(t)|\chi^{(i)}_{\boldsymbol{k},\sigma}(t)\rangle - i\sum_{m\neq i}\int_0^t dt'\,\hat{\boldsymbol{A}}_{\boldsymbol{k},\sigma}(t')\cdot\boldsymbol{j}_{m,i}(t')|\chi^{(i)}_{\boldsymbol{k},\sigma}(t')\rangle\Bigg]. \tag{4.47}$$

We note that Eq. (4.47) is just as exact as Eq. (4.45). We now proceed by making a Taylor expansion of the state $|\chi^{(i)}_{\boldsymbol{k},\sigma}(t')\rangle$ around the time $t' = t$

$$|\chi^{(i)}_{\boldsymbol{k},\sigma}(t')\rangle \simeq |\chi^{(i)}_{\boldsymbol{k},\sigma}(t)\rangle + (t'-t)\;\;\partial_{t'}|\chi^{(i)}_{\boldsymbol{k},\sigma}(t')\rangle|_{t'=t} + \frac{(t'-t)^2}{2!}\frac{\partial^2}{\partial t'^2}|\chi^{(i)}_{\boldsymbol{k},\sigma}(t')\rangle|_{t'=t} + \ldots, \tag{4.48}$$

where we only keep the first term. Inserting this into Eq. (4.47), we obtain

$$i\partial_t|\chi^{(i)}_{\boldsymbol{k},\sigma}(t)\rangle = \hat{\boldsymbol{A}}_{\boldsymbol{k},\sigma}(t)\cdot\left[\boldsymbol{j}_{i,i}(t) - i\sum_{m\neq i}\int_0^t dt'\,\hat{\boldsymbol{A}}_{\boldsymbol{k},\sigma}(t')\cdot\boldsymbol{j}_{m,i}(t')\right]|\chi^{(i)}_{\boldsymbol{k},\sigma}(t)\rangle, \tag{4.49}$$

which is different from Eq. (4.47) as only the state $|\chi^{(i)}_{\boldsymbol{k},\sigma}(t)\rangle$ is required on the right-hand side of Eq. (4.61). Consequently, only the integration of a single quantum optical state of $m = i$, i.e., the state $|\chi^{(i)}_{\boldsymbol{k},\sigma}(t)\rangle$, is required, which again drastically eases the required numerical effort. The effect of only keeping the first term in Eq. (4.48) is to neglect the memory of the state and is hence a Markov approximation. Comparing Eq. (4.49) to Eq. (4.47), the approximation amounts to approximating the cumulative effect of interaction from time $t' = 0$ to time $t' = t$ as the application of a single instantaneous operator at time t.

By considering higher-order terms in Eq. (4.48), the Markov approximation used to obtain Eq. (4.49) can be quantified. If one includes the first-order term in Eq. (4.48), one would obtain terms on the form

$$\hat{a}_{\boldsymbol{k},\sigma}\sum_{m\neq i}\boldsymbol{j}_{i,m}(t)\left[\int_0^t dt' e^{-i\omega_k t'}\boldsymbol{j}_{m,i}(t')(t'-t)\right]\times\partial_t|\chi^{(i)}_{\boldsymbol{k},\sigma}(t)\rangle, \tag{4.50}$$

with a similar expression proportional to $\hat{a}^\dagger_{\boldsymbol{k},\sigma}$. The integral in Eq. (4.50) will, in general, yield a larger value, due to the fact that it consists of two terms, where one of them is linear with the time t. However, since Eq. (4.50) is proportional to $\partial_t|\chi^{(i)}_{\boldsymbol{k},\sigma}(t)\rangle \propto g_0$ it will be negligible compared to the first term in Eq. (4.48).

If one considers sufficiently long pulses, however, the integrals proportional to higher-order terms in Eq. (4.48) might be on the order of $1/g_0$ and the Markov-type approximation will consequently not be valid. Finally, we note that one might consider including these higher-order terms for better accuracy. However, due to the nature of the equations, all higher order terms will be on the same order of g_0, and an infinite number of terms must hence be considered as detailed in App. C. Hence, as there is no natural and controlled truncation, such a beyond-Markov approximation is not pursued further. The Markov-state approximation is seen in the hierarchy of approximations shown in Fig. 4.4.

Markov-state approximation

To get more physical insights, we now make further approximations to bring Eq. (4.49) onto a closed form. Following Ref. [150], we first define

$$\hat{W}_{\boldsymbol{k},\sigma}(t) = \int_0^t dt' \hat{\boldsymbol{A}}_{\boldsymbol{k},\sigma}(t') \cdot [\hat{\boldsymbol{j}}_H(t') - \langle \hat{\boldsymbol{j}}(t') \rangle], \tag{4.51}$$

where we have defined the Heisenberg-type operator

$$\hat{\boldsymbol{j}}_H(t) = \hat{\mathcal{U}}_{\rm sc}^\dagger(t) \hat{\boldsymbol{j}}(t) \hat{\mathcal{U}}_{\rm sc}(t). \tag{4.52}$$

Note that $\langle \hat{\boldsymbol{j}}_H(t) \rangle = \langle \phi_i | \hat{\mathcal{U}}_{\rm sc}^\dagger(t) \hat{\boldsymbol{j}}(t) \hat{\mathcal{U}}_{\rm sc}(t) | \phi_i \rangle = \langle \hat{\boldsymbol{j}}(t) \rangle = \boldsymbol{j}_{i,i}(t)$, where the states are time independent when a Heisenberg operator is considered.
Using $\sum_{m \neq i} |\phi_m\rangle\langle\phi_m| = \mathbb{I} - |\phi_i\rangle\langle\phi_i|$, we rewrite Eq. (4.49) as

$$i\partial_t |\chi_{\boldsymbol{k},\sigma}^{(i)}(t)\rangle = \left[\hat{\boldsymbol{A}}_{\boldsymbol{k},\sigma}(t) \cdot \boldsymbol{j}_{i,i}(t) - i \langle \dot{\hat{W}}_{\boldsymbol{k},\sigma}(t) \hat{W}_{\boldsymbol{k},\sigma}(t) \rangle_{\rm el} \right] |\chi_{\boldsymbol{k},\sigma}^{(i)}(t)\rangle, \tag{4.53}$$

where $\langle \cdot \rangle_{\rm el}$ denotes the expectation value only of the electronic operators. By only keeping commutators up to order g_0^2 and neglecting the commutator $[\dot{\hat{W}}_{\boldsymbol{k},\sigma}(t), \hat{W}_{\boldsymbol{k},\sigma}(t)]$ (which expresses the fluctuations of the fluctuations), the solution to Eq. (4.53) is given by

$$|\chi_{\boldsymbol{k},\sigma}^{(i)}\rangle = \hat{\mathcal{D}}[\beta_{\boldsymbol{k},\sigma}^{(i)}(t)] e^{-\frac{1}{2}\langle \hat{W}_{\boldsymbol{k},\sigma}^2(t) \rangle_{\rm el}} |0\rangle, \tag{4.54}$$

where $\beta_{\boldsymbol{k},\sigma}^{(i)}(t)$ is given in Eq. (4.41). Equation (4.54) is the MSA (see App. D for a derivation), which we now investigate in greater detail.

First, we note that if $\langle \hat{W}_{\boldsymbol{k},\sigma}^2(t) \rangle_{\rm el}(t) = 0$, the MSA will simply be a coherent state and have no nonclassical features. Consequently, $\langle \hat{W}_{\boldsymbol{k},\sigma}^2(t) \rangle_{\rm el}(t)$ is the origin of the nonclassical properties of the generated HHG within the MSA. Writing out $\langle \hat{W}_{\boldsymbol{k},\sigma}^2(t) \rangle_{\rm el}(t)$ explicitly yields

$$\langle \hat{W}_{\boldsymbol{k},\sigma}^2(t) \rangle_{\rm el} = \int_0^t dt' \int_0^t dt'' \hat{\boldsymbol{A}}_{\boldsymbol{k},\sigma}(t') \hat{\boldsymbol{A}}_{\boldsymbol{k},\sigma}(t'') C(t', t''), \tag{4.55}$$

where we have defined the time-correlation function of the current

$$C(t', t'') = \langle \hat{\boldsymbol{j}}_H(t') \hat{\boldsymbol{j}}_H(t'') \rangle - \langle \hat{\boldsymbol{j}}_H(t') \rangle \langle \hat{\boldsymbol{j}}_H(t''). \tag{4.56}$$

We note that Eq. (4.55) is reminiscent of similar quantum optical expressions obtained in the Heisenberg picture [119, 152]. Equation (4.55) shows that the origin of nonclassical light is due to the time correlations of the current. If $C(t', t'') = 0$, there would be no quantum signatures on the generated light. This is exactly the case for the uncorrelated case of $U = 0$, where the ground state is an eigenstate of the time-evolution operator and the current operator. In this case, the current contains no fluctuations, and the emitted radiation contains no quantum signatures. Conversely, if the current fluctuates a lot, i.e., if $C(t', t'')$ is large, the quantum signatures in the emitted HHG will likewise be large. The electronic mechanism connected to the nonclassical nature of the emitted radiation is thus the fluctuations of the current. To connect Eq. (4.55) to the transition current elements, we note that by inserting an identity into Eq. (4.56), we obtain

$$C(t', t'') = \sum_{m \neq i} \boldsymbol{j}_{i,m}(t') \boldsymbol{j}_{m,i}(t''), \tag{4.57}$$

which gives a clear physical interpretation of the transition-current elements: The transition-current elements are related to the time-correlations of the current. Inserting Eq. (4.57) into Eq. (4.55), we obtain the expression (for $t \to \infty$)

$$\langle \hat{W}^2_{\boldsymbol{k},\sigma} \rangle_{\mathrm{el}} = B_{\boldsymbol{k},\sigma} (\hat{a}^2_{\boldsymbol{k},\sigma} e^{-i\phi_k} + \hat{a}^{\dagger 2}_{\boldsymbol{k},\sigma} e^{i\phi_k}) + C_{\boldsymbol{k},\sigma} \hat{a}^\dagger_{\boldsymbol{k},\sigma} \hat{a}_{\boldsymbol{k},\sigma} + D_{\boldsymbol{k},\sigma} \hat{a}_{\boldsymbol{k},\sigma} \hat{a}^\dagger_{\boldsymbol{k},\sigma}, \tag{4.58}$$

where we have defined

$$B_{\boldsymbol{k},\sigma} = \left| \sum_{m \neq i} J^{(\boldsymbol{k},\sigma,+)}_{i,m} J^{(\boldsymbol{k},\sigma,+)}_{m,i} \right|, \tag{4.59a}$$

$$\varphi_{\boldsymbol{k},\sigma} = \arg \left[\sum_{m \neq i} J^{(\boldsymbol{k},\sigma,+)}_{i,m} J^{(\boldsymbol{k},\sigma,+)}_{m,i} \right], \tag{4.59b}$$

$$C_{\boldsymbol{k},\sigma} = \sum_{m \neq i} |J^{(\boldsymbol{k},\sigma,+)}_{i,m}|^2, \tag{4.59c}$$

$$D_{\boldsymbol{k},\sigma} = \sum_{m \neq i} |J^{(\boldsymbol{k},\sigma,-)}_{i,m}|^2, \tag{4.59d}$$

with the integrated transition current elements

$$J^{(\boldsymbol{k},\sigma,\pm)}_{m,n} = \frac{g_0}{\sqrt{\omega_k}} \int_{t_i}^{\infty} dt' e^{\pm i\omega_k t'} \boldsymbol{j}_{m,n}(t') \cdot \boldsymbol{e}^{(*)}_\sigma, \tag{4.60}$$

where the polarization vector has to be conjugated for the positive phase.

With Eq. (4.58), we can now calculate expectation values. However, as $\langle \hat{W}^2_{\boldsymbol{k},\sigma}\rangle_{\mathrm{el}}$ is Hermitian, the operator $\exp\Big(-1/2\langle \hat{W}^2_{\boldsymbol{k},\sigma}\rangle_{\mathrm{el}}\Big)$ is not unitary, and hence, typical tools such as the Baker-Campbell-Hausdorff formula cannot be applied. Instead, we expand the operator to second order in g_0 and obtain

$$|\chi^{(i)}_{\boldsymbol{k},\sigma}\rangle = \hat{D}[\beta^{(i)}_{\boldsymbol{k},\sigma}(t)]\left[\left(1-\frac{1}{2}D_{\boldsymbol{k},\sigma}\right)|0\rangle_{\boldsymbol{k},\sigma} - \frac{1}{\sqrt{2}}B_{\boldsymbol{k},\sigma}e^{i\varphi_{\boldsymbol{k},\sigma}}|2\rangle_{\boldsymbol{k},\sigma}\right]. \tag{4.61}$$

Using Eq. (4.61), we obtain the expression for the spectrum [Eq. (2.31)] to lowest order in g_0

$$\begin{aligned} S^{(\mathrm{MSA})}(\omega_k) &= \frac{\omega_k^3}{g_0^2(2\pi)^2c^3}\sum_\sigma \left|\beta^{(i)}_{\boldsymbol{k},\sigma}\right|^2 \\ &= \frac{\omega_k^2}{(2\pi)^2c^3}\sum_\sigma \left|\tilde{\boldsymbol{j}}_{i,i}(\omega_k)\cdot\boldsymbol{e}_\sigma\right|^2, \end{aligned} \tag{4.62}$$

which completely coincides with the spectrum for the uncorrelated phase [Eq. (4.42)] and the semiclassical spectrum [Eq. (2.27)]. This finding is consistent with previous results: The HHG spectrum is dominated by the classical response, and no quantum optical nature is seen from the spectrum alone. The expression for the Mandel-Q parameter is given as

$$Q^{(\mathrm{MSA})}_{\boldsymbol{k},\sigma} = \frac{B^2_{\boldsymbol{k},\sigma} + \left|\beta^{(i)}_{\boldsymbol{k},\sigma}\right|^4 - 2B_{\boldsymbol{k},\sigma}\mathrm{Re}[(\beta^{(i)}_{\boldsymbol{k},\sigma})^2 e^{i\phi_{\boldsymbol{k},\sigma}}]}{\left|\beta^{(i)}_{\boldsymbol{k},\sigma}\right|^2(1-D_{\boldsymbol{k},\sigma}) + B^2_{\boldsymbol{k},\sigma}} - \left|\beta^{(i)}_{\boldsymbol{k},\sigma}\right|^2, \tag{4.63}$$

where, due to numerical stability, it is necessary to include higher-order terms in g_0. Finally, the expression for the variance of the quadrature operator is

$$\langle[\Delta\hat{X}^{(\mathrm{MSA})}_{\boldsymbol{k},\sigma}(\vartheta_{\boldsymbol{k},\sigma})]^2\rangle = \frac{1}{4}[1-2B_{\boldsymbol{k},\sigma}\cos(2\vartheta_{\boldsymbol{k},\sigma}-\varphi_{\boldsymbol{k},\sigma})], \tag{4.64}$$

which has to be minimized over angles $\vartheta_{\boldsymbol{k},\sigma}$ as given by Eq. (2.39).

A few comments are in order as the MSA yields closed-form expressions subject to analysis. First, we note that the Mandel-Q parameter [Eq. (4.63)] depends both on the classical current, $\boldsymbol{j}_{i,i}(t)$ and nondiagonal transition currents, $\boldsymbol{j}_{m,n}(t)$, while the quadrature variance required to calculate the squeezing [Eq. (4.64)] depends *only* on the nondiagonal transition currents and not the classical current. Again, the MSA highlights that the mechanism generating the nonclassical properties of the emitted radiation is different from the one responsible for the spectrum. As previously shown in Eqs. (4.55) and (4.57), the underlying physical reason are the quantum fluctuations or nonvanishing time

correlations of the induced current, which in the equations for the observables [Eqs. (4.62)-(4.64)] is restated as transition current elements. Further, we note that in order to obtain the observables in the MSA [Eqs. (4.62)-(4.64)], no integration of equations of motion for a quantum optical state is required, different from the previous levels of approximations [Eqs. (4.36), (4.45), (4.49)], which again eases the numerical effort, see Fig. 4.4.

Results

We test the different levels of approximations by calculating the spectrum, Mandel-Q parameter, and degree of squeezing first for the Mott-insulating system with $U = 10t_0$ and $V = 0$. In Fig. 4.5, we show the observables for $N_c = 10$ cycles (using the same pulse as in Sec. 4.2.2 and Fig. 4.2). Looking first at the spectrum in Fig. 4.5(a), we clearly see that all levels of approximations agree. Likewise, the Mandel-Q parameter in Fig. 4.5 is qualitatively the same for all methods, with the MSA [Eq. (4.63)] showing a little deviation in some of the peaks. Looking at the degree of squeezing in Fig. 4.5(c), we note a good agreement between all levels of approximations. Notably, however, we see that the MSA does not capture the degree of squeezing at the lower harmonics very well. We note that the blue solid line in Fig. 4.5 is the same result shown in Fig. 4.2.

As the Markov-type approximation [Eq. (4.49)] and the MSA [Eq. (4.54)] both rely on a Markov-type approximation; we expect these to perform worse for a longer pulse. For this reason, we consider in Fig. 4.6 the results from the same system but with a pulse of $N_c = 18$ cycles. As for Fig. 4.5(a), all methods match in the predictions of the spectrum in Fig. 4.6(a). Looking at the Mandel-Q parameter for the longer pulse, we see in Fig. 4.6(b), that the MSA does not capture all peaks in the signal. However, these peaks all occur at frequencies with vanishing signal, which is to be expected as the Mandel-Q parameter is inversely proportional to the photon counting operator [Eq. (2.32)]. Interestingly, we see in Fig. 4.6(c), that while the MSA captures the degree of squeezing at the higher harmonics ($\omega/\omega_L \geq 25$), it does not capture the degree of squeezing at the lower harmonics ($\omega/\omega_L \leq 5$), showing the limits of the approximation. Curiously, the Markov-type approximation shows good agreement with more exact methods across the entire range of frequencies, and the reason for the disagreement with the MSA is hence not due to the Markov-type approximation but must come from neglecting higher-order terms in g_0 in the derivation of the MSA.

We are now interested in quantifying how the predictions by the MSA deviate from more exact calculations for increased pulse lengths. To this end, we compute the Mandel-Q parameter from the MSA [Eq. (4.63)], Q_{MSA} and from the decoupled ansatz [Eq. (4.36)], Q_{dec}, which the most exact obtainable result. We average the difference between the two methods and average over

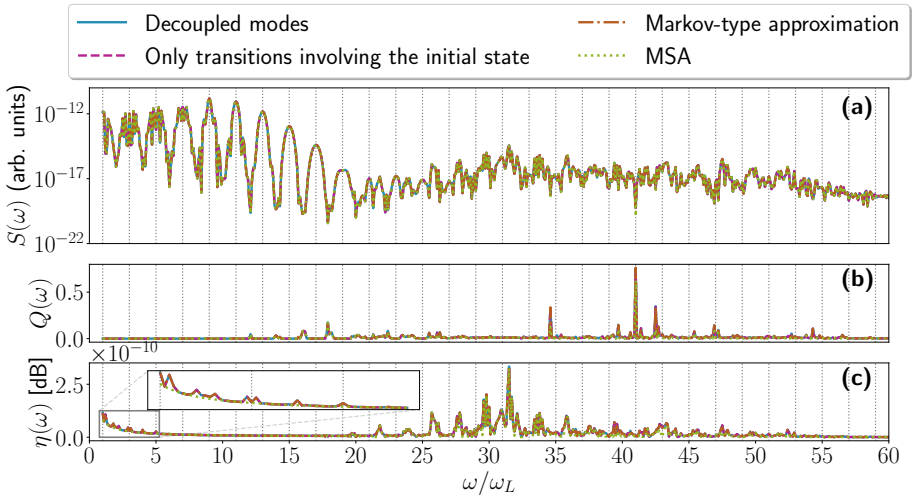

Figure 4.5: Results from the different levels of approximations for the Mott-insulating phase ($U = 10t_0$, $V = 0$) with $N_c = 10$ laser cycles: The decoupled modes [Eq. (4.36), solid blue], including only transitions involving the ground state [Eq. (4.45), dashed purple], the Markov-type approximation [Eq. (4.49), dashed red] and the MSA [Eq. (4.54), dotted green]. (a) The spectrum [Eq. (2.31)]. We note that all levels of approximations show good agreement. (b) The Mandel-Q parameter. We note that all levels of approximations show good agreement with the MSA [Eq. (4.63)] not capturing all peaks. (c) The degree of squeezing. Again, all levels of approximations show good agreement with MSA [Eq. (4.64)] deviating in particular at lower harmonics. Adapted with permission from Ref. [4]. Copyrighted by the American Physical Society.

all considered harmonics ($\omega/\omega_L \leq 60$). This measure, $\overline{|Q_{\mathrm{MSA}} - Q_{\mathrm{dec}}|}$, with a similar expression for η, indicates how the MSA deviates on average for increased pulse lengths. However, the measure does not reveal whether this deviation is small across all frequencies or if it is due to distinct harmonics where the Mandel-Q parameter or the degree of squeezing is not captured. Due to this fact, and due to the fact that the MSA does not seem to capture the degree of squeezing for lower harmonics as seen in Figs. 4.5(c) and 4.6(c), we also consider this measure, where the lower harmonics ($\omega/\omega_L \leq 10$) are excluded. The results are shown in Fig. 4.7. We first note that the MSA expression for the Mandel-Q parameter consistently gets worse for increased pulse length, both with and without the inclusion of the lower harmonics. The degree of squeezing also deviates from more exact results with increased pulse lengths. We note that the difference is worse when the lower harmonics are included, consistent

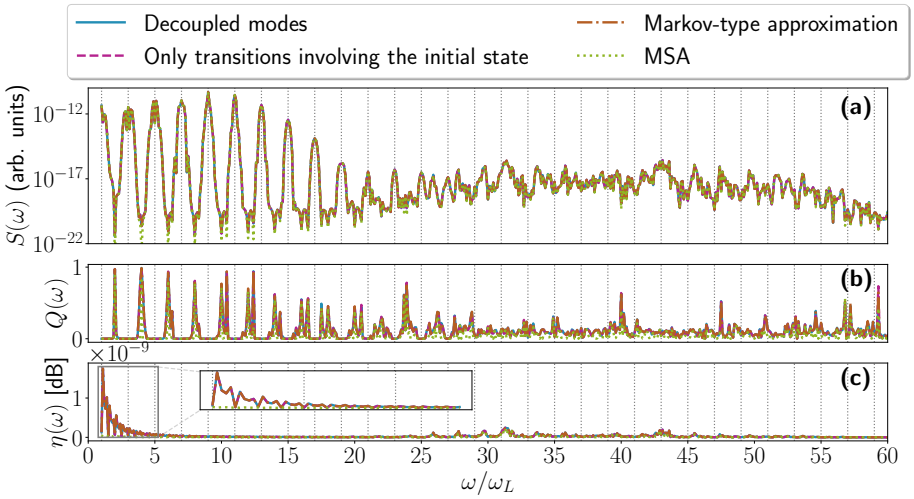

Figure 4.6: Results from the different levels of approximations for the Mott-insulating phase ($U = 10t_0$, $V = 0$) with $N_c = 18$ laser cycles: The decoupled modes [Eq. (4.36), solid blue], including only transitions involving the ground state [Eq. (4.45), dashed purple], the Markov-type approximation [Eq. (4.49), dashed red] and the MSA [Eq. (4.54), dotted green]. (a) The spectrum [Eq. (2.31)]. We note that all levels of approximations show good agreement. (b) The Mandel-Q parameter. Like in Fig. 4.5(b), all levels of approximations show good agreement. However, the MSA [Eq. (4.63)] shows deviations for certain harmonics. (c) The degree of squeezing. Again, all levels of approximations show good agreement with MSA, deviating in particular at lower harmonics. (c) The degree of squeezing. While all other levels of approximations show good agreement, the MSA [Eq. (4.64)] deviates noticeably at the lower harmonics. Adapted with permission from Ref. [4]. Copyrighted by the American Physical Society.

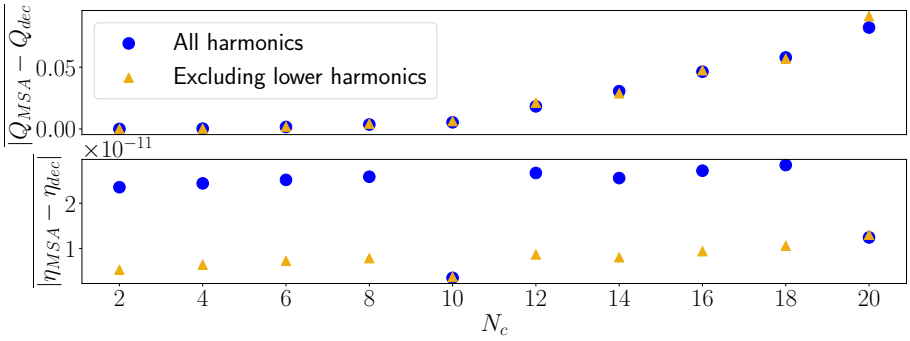

Figure 4.7: The absolute difference of the Mandel-Q parameter (upper panel) between the MSA [Eq. (4.63)] and the decoupled ansatz [Eq. (4.36)] averaged over all harmonics up to $\omega/\omega_L \leq 60$. We see a greater deviation for increased pulse length both when including the lower harmonics ($\omega/\omega_L \leq 10$, blue dots) and when excluding the lower harmonics (orange triangles). Similar results are found for the degree of squeezing (lower panel) using Eq. (4.64) for the MSA. Curiously, for $N_c = 10$ and $N_c = 20$, the system has a lower degree of squeezing at lower harmonics, which makes the MSA perform better as it does not, to a good degree, capture the degree of squeezing at lower harmonics. Nonetheless, we still see that the deviation increases for increased pulse length. Adapted with permission from Ref. [4]. Copyrighted by the American Physical Society.

with Fig. 4.6(c) where the lower harmonics were not captured. Curiously, the MSA captures the lower harmonics for $N_c = 10$ and $N_c = 20$. This is due to the fact that the Hubbard model generates a lower degree of squeezing at the lower harmonics for these pulse lengths, compare Figs. 4.5(c) and 4.6(c). Consequently, the MSA, which does not capture the degree of squeezing at lower harmonics very well, deviates less from more exact results. We believe this has to do with the nature of the Hubbard model and is not a general characteristic of the method. This finding is not pursued further. Conclusively, Fig. 4.7 shows that the MSA agrees less with more accurate results for increasing pulse lengths when considering the Mandel-Q parameter and the degree of squeezing.

For completeness, we also consider how the MSA performs for the system with a Mott exciton, i.e., for $U = 12t_0$ and $V = 4t_0$, shown in Fig. 4.8. For this system, the same pulse and parameters for Fig. 4.3 are used. In Fig. 4.8(a), we see that the MSA perfectly captures the spectrum, while it also accurately predicts the degree of squeezing across all harmonics as seen in Fig. 4.8(b).

Concluding, the MSA gives an accurate description of the spectrum while also qualitatively capturing the Mandel-Q parameter and the degree of squeezing. The analytical insights gained by the MSA show that the nonclassical features of the emitted HHG radiation are due to the quantum fluctuations or time

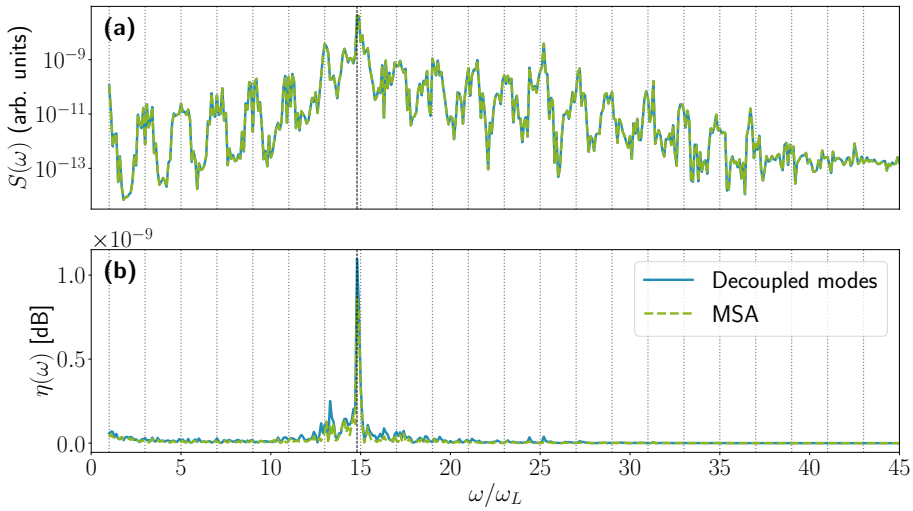

Figure 4.8: The MSA (dashed green) compared to the decoupled ansatz (solid blue) for the exciton system with $U = 12t_0$ and $V = 4t_0$ with other parameters specified in the text. (a) We note that the MSA perfectly captures the spectrum [Eq. (4.62)] and (b) also to accurately predict the degree of squeezing [Eq. (4.64)]. Adapted with permission from Ref. [3]. Copyrighted by the American Physical Society.

correlations of the induced current given in Eq. (4.56). This correlation can be restated in terms of the transition-current elements, which are also present in the equations of motion, e.g., in Eq. (4.18), providing a physical interpretation of these.

CHAPTER 5

Quantum-light-driven high-order harmonic generation

The quantum-optical considerations of HHG allow one to study both fundamental electron dynamics while also having potential applications in the generation of ultrashort pulses of quantum light. As shown in Ch. 4, this can be achieved by driving, e.g., a strongly-correlated material modeled by the Hubbard model with a strong coherent light field. In addition, as introduced in Ch. 1, the other route to generate ultrashort pulses of quantum light is to use a nonclassical driving field. By driving HHG with a nonclassical (that is, noncoherent) driving field, new regimes become accessible, and research questions can be asked. In literature, as well as in Paper V, four different types of driving fields are considered: coherent states, Fock states, thermal light, and BSV. While Fock and thermal light are included mainly for theoretical curiosity, both coherent and BSV driving fields are experimentally relevant as presented in Ch. 1. We will consider all four types of driving fields here. The theoretical framework for the inclusion of a noncoherent driving field is introduced in Sec. 5.1 with the results presented in Sec. 5.2, including analytical insights in the Floquet limit. Then, the nature of the generated electric field is studied in Sec. 5.3. The chapter concludes with a discussion of necessary theoretical approximations made and the limits of the presented theoretical framework in Sec. 5.4. This chapter builds on and presents the findings of Paper V.

5.1 Including a noncoherent driving field

To represent a nonclassical driving field, we exploit the phase-space representations of nonclassical quantum optical states presented in Sec. 2.2 and follow the derivation presented in Refs. [164, 165]. We again consider a general light-matter Hamiltonian [Eq. (4.1)] where both the electric and photonic degrees of freedom are quantized. At the initial time ($t = 0$), prior to any interactions, the state of the system is described by the density matrix

$$\hat{\rho}(t=0) = |\phi_i\rangle\langle\phi_i| \bigotimes_{\substack{(\boldsymbol{k},\sigma) \\ \neq(\boldsymbol{k}_L\sigma_L)}} |0_{\boldsymbol{k},\sigma}\rangle\langle 0_{\boldsymbol{k},\sigma}| \otimes \int d\mu P(\alpha,\beta) \frac{|\alpha\rangle\langle\beta^*|}{\langle\beta^*|\alpha\rangle}, \tag{5.1}$$

where, again, $|\phi_i\rangle$ is the initial electronic state, $|0_{\boldsymbol{k},\sigma}\rangle$ denotes the vacuum state of the mode $(\boldsymbol{k},\sigma)$, and where the driving field is described by a single mode expanded in a general P representation as detailed in Sec. 2.2.4. Note that we suppress the index of the laser mode for clarity. To determine the time evolution of Eq. (5.1), we make the ansatz that the time-dependent density matrix can be written as

$$\hat{\rho}(t) = \int d\mu \frac{P(\alpha,\beta)}{\langle\beta^*|\alpha\rangle} \hat{\rho}_{\alpha\beta^*}(t), \tag{5.2}$$

where $\hat{\rho}_{\alpha\beta^*}(t)$ is the time evolution of the state $\hat{\rho}_{\alpha\beta^*}(t=0) = |\phi_i\rangle\langle\phi_i| \otimes |\alpha\rangle\langle\beta^*| \otimes_{(\boldsymbol{k},\sigma)\neq(\boldsymbol{k}_L\sigma_L)} |0_{\boldsymbol{k},\sigma}\rangle\langle 0_{\boldsymbol{k},\sigma}|$. The state evolves according to the general Hamiltonian in Eq. (4.1) and as done in Sec. 4.1, we now go into the interaction picture with respect to $\hat{H}_F$, employ the dipole approximation, and displace the driving field to the vacuum state, i.e., we define

$$\hat{\tilde{\rho}}_{\alpha\beta^*}(t) = \hat{\mathcal{D}}^\dagger(\alpha)\hat{\rho}_{\alpha\beta^*}(t)\hat{\mathcal{D}}(\beta), \tag{5.3}$$

such that $\hat{\tilde{\rho}}_{\alpha\beta^*}(0) = |\phi_i\rangle\langle\phi_i| \otimes_{(\boldsymbol{k},\sigma)} |0_{\boldsymbol{k},\sigma}\rangle\langle 0_{\boldsymbol{k},\sigma}|$. Equation (5.3) satisfies the TDSE

$$i\partial_t \hat{\tilde{\rho}}_{\alpha\beta^*}(t) = \hat{H}_\alpha(t)\hat{\tilde{\rho}}_{\alpha\beta^*}(t) - \hat{\tilde{\rho}}_{\alpha\beta^*}(t)\hat{H}_\beta(t), \tag{5.4}$$

where we, for convenience, have defined

$$\hat{H}_\zeta(t) = \frac{1}{2}\sum_{j=1}^{N_e} [\hat{\boldsymbol{p}}_j + \hat{\boldsymbol{A}}(t) + \boldsymbol{A}_{cl}^\zeta(t)]^2 + \hat{U}, \tag{5.5}$$

for $\zeta = \{\alpha, \beta\}$. In Eq. (5.5), the classical driving field is given by

$$\boldsymbol{A}_{\mathrm{cl}}^\zeta(t) = \langle\zeta|\hat{\boldsymbol{A}}(t)|\zeta\rangle = \frac{g_0}{\sqrt{\omega_L}}(\boldsymbol{e}_{\sigma_L}\zeta e^{-i\omega_L t} + \mathrm{H.c}), \tag{5.6}$$

where $|\zeta\rangle = \hat{\mathcal{D}}(\zeta)|0\rangle$ is a coherent state with amplitude ζ. Neglecting the term proportional to $\hat{\boldsymbol{A}}^2$ in Eq. (5.5), we obtain

$$\hat{H}_\zeta(t) = \hat{H}_{\mathrm{SC}}(t;\zeta) + \hat{\boldsymbol{A}}(t)\cdot\hat{\boldsymbol{j}}^\zeta(t), \tag{5.7}$$

where

$$\hat{H}_{\mathrm{SC}}(t;\zeta) = \frac{1}{2}\sum_{j=1}^{N_e}[\hat{\boldsymbol{p}}_j + \boldsymbol{A}^\zeta_{\mathrm{cl}}(t)]^2 + \hat{U} \tag{5.8}$$

is the semiclassical Hamiltonian and

$$\hat{\boldsymbol{j}}^\zeta(t) = \sum_{j=1}^{N_e}[\hat{\boldsymbol{p}}_j + \boldsymbol{A}^\zeta_{\mathrm{cl}}(t)] \tag{5.9}$$

is the current operator.

Letting $|\psi_\zeta(t)\rangle$ be the solution to the TDSE

$$i\partial_t|\psi_\zeta(t)\rangle = \hat{H}_\zeta(t)|\psi_\zeta(t)\rangle, \tag{5.10}$$

it follows that $|\psi_\alpha(t)\rangle\langle\psi_\beta(t)|$ is a solution to Eq. (5.4). Proceeding from Eq. (5.10) and following the same arguments as presented in Sec. 4.1, we expand the state as

$$|\psi_\zeta(t)\rangle = \sum_m |\phi_m\rangle \otimes |\chi^\zeta_m(t)\rangle, \tag{5.11}$$

which is a generalization to the expansion in Eq. (4.17) for a general classical driving field of coherent-state parameter ζ. Similarly, to Sec. 4.1, we find that the equation of motion for the quantum optical state is

$$i\partial_t|\chi^\zeta_m(t)\rangle = \hat{\boldsymbol{A}}(t)\cdot\sum_n \boldsymbol{j}^\zeta_{m,n}(t)|\chi^\zeta_n(t)\rangle, \tag{5.12}$$

where

$$\boldsymbol{j}^\zeta_{m,n} = \langle\phi^\zeta_m(t)|\hat{\boldsymbol{j}}^\zeta(t)|\phi^\zeta_n(t)\rangle, \tag{5.13}$$

are the generalized transition current matrix elements, similar to Eq. (4.16), where $|\phi^\zeta_m(t)\rangle = \hat{\mathcal{U}}_{\mathrm{SC}}(t;\zeta)|\phi_m\rangle$ are the propagated electronic states. We note that Eq. (5.12) shows that the problem has been reformulated in terms of coherent states. This allows us to use the already developed theory of quantum optical HHG, as presented in Ch. 4, while at the same time employing the numerical methods used to solve the TDSE with a semiclassical Hamiltonian.

We now specify the electronic system. We use a one-dimensional intraband model, which can be thought of as the Hubbard model with $U = V = 0$ and with beyond-nearest-neighbor hopping. In crystal-momentum space, it is given by

$$\hat{H}_{\mathrm{SC}}(t,\zeta) = \sum_{q,\mu}\mathcal{E}[q + A^\zeta_{\mathrm{cl}}(t)]\hat{c}^\dagger_{q,\mu}\hat{c}_{q,\mu}, \tag{5.14}$$

where all vector quantities are projected along the chain, and where

$$\mathcal{E}(q) = \sum_l b_l \cos(alq), \tag{5.15}$$

is the dispersion relation with b_l being the Fourier coefficient of the band structure. Note that Eq. (5.14) is a generalization of Eq. (3.25) as a general dispersion relation is now considered. Likewise, the current operator in this model is a generalization of Eq. (3.26) expressed by

$$\hat{\boldsymbol{j}}^{\zeta}(t) = \boldsymbol{e}_\sigma \sum_{q,\mu} \frac{\partial \mathcal{E}[q + A_{\mathrm{cl}^{\zeta}(t)}]}{\partial q} \hat{c}^{\dagger}_{q,\mu} \hat{c}_{q,\mu}. \tag{5.16}$$

As Eqs. (5.14) and (5.16) commute, the situation is much similar to the uncorrelated case in Sec. 3.2.1, and by the same arguments presented there, the equation of motion for the quantum optical state reduces to

$$i\partial_t |\chi_i^{\zeta}(t)\rangle = \hat{\boldsymbol{A}}(t) \cdot \boldsymbol{j}^{\zeta}_{i,i}(t) |\chi_i^{\zeta}(t)\rangle, \tag{5.17}$$

which has the solution

$$|\chi_i^{\zeta}(t)\rangle = \bigotimes_{\boldsymbol{k},\sigma} \hat{\mathcal{D}}\big[\gamma^{\zeta}_{\boldsymbol{k},\sigma}(t)\big] |0_{\boldsymbol{k},\sigma}\rangle, \tag{5.18}$$

i.e., all modes are in a coherent state with the amplitude

$$\gamma^{\zeta}_{\boldsymbol{k},\sigma}(t) = -i \frac{g_0}{\sqrt{\omega_k}} \int_0^t dt' \boldsymbol{j}^{\zeta}_{i,i}(t') \cdot \boldsymbol{e}_\sigma \; e^{i\omega_k t'}, \tag{5.19}$$

similar to the result in Eqs. (4.40) and (4.41). Note that this solution [Eq. (5.18)] is exact in the present model, whereas it is an approximative solution for atoms, due to the fact that the off-diagonal transitional current elements are nonvanishing for atoms [165, 166].

With Eq. (5.18) being the solution to the quantum optical state, and since the time-evolved electronic state is simply given by $|\phi_i^{\zeta}(t)\rangle = \exp[-iE_{\zeta}(t)]|\phi_i\rangle$ with $E_{\zeta}(t) = \int_0^t dt \Sigma_{q,\mu} \; \mathcal{E}[q + A^{\zeta}_{\mathrm{cl}}(t')] \langle \hat{c}^{\dagger}_{q,\mu} \hat{c}_{q,\mu} \rangle$, as shown in Eq. (3.52), we can now obtain an expression for the state of the photonic field from Eq. (5.2) as

$$\hat{\rho}_F(t) = \int d\mu \frac{P(\alpha,\beta)}{\langle \beta^* | \alpha \rangle} e^{-i[E_\alpha(t) - E_{\beta^*}(t)]} \otimes \hat{\mathcal{D}}(\alpha) |\gamma^{\alpha}_{\boldsymbol{k}_L,\sigma_L}(t)\rangle \langle \gamma^{\beta^*}_{\boldsymbol{k}_L,\sigma_L}(t)| \hat{\mathcal{D}}^{\dagger}(\beta) \bigotimes_{\substack{(\boldsymbol{k},\sigma) \\ \neq (\boldsymbol{k}_L,\sigma_L)}} |\gamma^{\alpha}_{\boldsymbol{k},\sigma}(t)\rangle \langle \gamma^{\beta^*}_{\boldsymbol{k},\sigma}(t)|, \tag{5.20}$$

where we have traced out the electronic states. Further, we neglect the displacement operators on the driving mode and only consider the field generated on

top of the driving field. This allows an identical treatment of all modes. We thus finally obtain

$$\hat{\rho}_F = \int d\mu \frac{P(\alpha,\beta)}{\langle\beta^*|\alpha\rangle} e^{-i[E_\alpha(t)-E_{\beta^*}(t)]} \bigotimes_{\boldsymbol{k},\sigma} |\gamma^{\alpha}_{\boldsymbol{k},\sigma}(t)\rangle\langle\gamma^{\beta^*}_{\boldsymbol{k},\sigma}(t)|. \tag{5.21}$$

Again, we see, that the state of the emitted field is a statistical mixture of fields generated by a coherent driver weighted by $P(\alpha,\beta)$. We now specify the measure $d\mu$ for the fields of interest.

5.1.1 The approximative positive P representation

Using the insights from Sec. 2.2.4, we know that a coherent state [Eq. (2.87)] and a thermal state [Eq. (2.94)] can be used in the GS representation, which is diagonal such that only a single phase-space variable, α, needs to be integrated. However, the GS representation for Fock states [Eq. (2.92)] and (bright) squeezed vacuum states [Eq. (2.90)] are not suited for numerical handling, prohibiting their use. Instead, we use the positive P representation and exploit its relation to the Husimi-Q function [Eq. (2.83)]. Unfortunately, this makes the representation nondiagonal as two phase spaces parameterized by α and β have to be integrated. However, by carefully studying the behavior of the positive P representation for both Fock and BSV states, we find that it has narrow peaks only when $\alpha = \beta^*$ and is otherwise vanishing. Approximating these narrow peaks as delta-functions, we can rewrite Eq. (2.83) as

$$P(\alpha,\beta) \approx \delta^{(2)}(\alpha-\beta^*)\mathcal{Q}\left(\frac{\alpha+\beta^*}{2}\right). \tag{5.22}$$

Later, we will discuss the implications and accuracy of this approximation in Sec. 5.4. We will refer to Eq. (5.22) as the *approximative positive P* (APP) representation. Note that we base the APP on the nature of the positive-P distribution, while other works base the APP on taking the limit of an infinite interaction volume for constant field amplitude, $\mathcal{E}_\alpha$ [165, 213]. However, the correct limit would be (using $\mathcal{E}_\alpha = 2g_0\alpha$)

$$\lim_{g_0\to 0} \mathcal{Q}^{\mathrm{Fock}}\left(\frac{\mathcal{E}_\alpha}{2g_0}\right)\frac{1}{4g_0^2} d^2\mathcal{E}_\alpha \propto d^2\mathcal{E}_\alpha \delta^{(2)}(\mathcal{E}_\alpha). \tag{5.23}$$

This limit, as seen below, would imply that no harmonic radiation is generated, and even more critically, that the driving field would contain no photons. However, we show that the results based on the APP agree with more exact analytical expressions in App. E. We thus base the APP on the nature of the Husimi-Q function and *not* on the limit of a large interaction volume.

Continuing from Eq. (5.22), we can, within the APP, express Fock and BSV states as

$$P^{(N)}_{\mathrm{Fock}}(\alpha,\beta) \approx \delta^{(2)}(\alpha-\beta^*)P^{(N)}_{\mathrm{Fock}}(\alpha), \tag{5.24}$$

where we have defined $P^{(N)}_{\mathrm{Fock}}(\alpha) = \mathcal{Q}^{(N)}_{\mathrm{Fock}}(\alpha)$ for notational convenience with $\mathcal{Q}^{(N)}_{\mathrm{Fock}}(\alpha)$ given in Eq. (2.93). Similarly, we define

$$P^{(r)}_{\mathrm{BSV}}(\alpha,\beta) \approx \delta^{(2)}(\alpha-\beta^*)P^{(r)}_{\mathrm{BSV}}(\alpha), \tag{5.25}$$

with $P^{(r)}_{\mathrm{BSV}}(\alpha) = \mathcal{Q}^{(r)}_{\mathrm{BSV}}(\alpha)$ given in Eq. (2.91).

Using the GS representation for coherent states [Eq. (2.87)] and thermal states [Eq. (2.94)], and the APP for Fock states [Eq. (5.24)] and BSV states [Eq. (5.25)], we can, exploiting that all representations are diagonal, i.e., only requiring the integration over a single phase space, express the emitted field as [following from Eq. (5.21)]

$$\hat{\rho}_F = \int d^2\alpha P(\alpha) \bigotimes_{\boldsymbol{k},\sigma} |\gamma^{\alpha}_{\boldsymbol{k},\sigma}(t)\rangle\langle\gamma^{\alpha}_{\boldsymbol{k},\sigma}(t)|, \tag{5.26}$$

where $P(\alpha)$ describes either of the driving fields of interest in the representation presented above. Equation (5.26) will be the starting point for calculating observables.

5.2 The harmonic spectrum

The primary observable of interest is the harmonic spectrum. Using Eq. (2.31), we find that the spectrum of the light emitted by the state in Eq. (5.26) can be expressed as

$$S(\omega) \propto \int d^2\alpha\ P(\alpha) S_{\mathrm{SC}}(\omega;\alpha), \tag{5.27}$$

where we have defined the generalized semiclassical spectrum

$$S_{\mathrm{SC}}(\omega;\alpha) = \omega^2 \left| \int_{-\infty}^{\infty} dt' j^{\alpha}_{i,i}(t') e^{i\omega t'} \right|^2, \tag{5.28}$$

as a function of coherent state amplitude α. Again, looking at Eq. (5.27), we see how the nonclassical signal is a weighted average over semiclassical spectra [Eq. (5.28)], each of which is driven by a classical field with coherent-state parameter α and appropriately weighted by the $P(\alpha)$ distribution. We will assume a sufficiently long pulse with an adiabatic envelope such that the phase of α does not affect the norm square of the Fourier transform of the current matrix element,

i.e., the carrier-envelope phase will be negligible. We may therefore rewrite Eq. (5.27) as

$$S(\omega) \propto \int_0^\infty d|\alpha|\ P(|\alpha|) S_{\mathrm{SC}}(\omega;\alpha), \tag{5.29}$$

where we have defined the radial distribution of α as

$$P(|\alpha|) = |\alpha| \int_0^{2\pi} d\phi P(\alpha), \tag{5.30}$$

where ϕ denotes the phase of α. We can thus perform the angular integral by only considering $P(\alpha)$, which lowers the complexity of the computation. The spectra for the different types of driving fields using Eq. (5.29) are shown in Fig. 5.1. Before commenting on the spectra, we exploit the Floquet limit to get further insights analytically.

Considering a monochromatic field $A_{cl}^{\alpha}(t) = 2g_0\omega_L^{-1/2}|\alpha|\sin(\omega_L t - \phi)$, we now perform the same considerations as in Sec. 3.2.1 by exploiting the nature of the uncorrelated electrons and obtain the analytical expression for the spectrum

$$S(\omega) \propto \sum_{n=1,3,5,\ldots}^{\infty} \omega^2 \delta(\omega - n\omega_L) \int d^2\alpha P(\alpha) \left[\sum_l C_l J_n(l\tilde{g}_0|\alpha|) \right]^2, \tag{5.31}$$

where $C_l = lb_l\Sigma_q \cos(alq)$ collects all the crystal-specific properties, and where $\tilde{g}_0 = 2ag_0\omega_L^{-1/2}$ is a lattice-modified coupling constant. We note that the Floquet expression for the spectrum in Eq. (5.31) adheres to the symmetry-based selection rules, emitting only odd harmonics. Curiously, we also see in Eq. (5.31) that the strength of a harmonic peak is determined by the overlap between the distribution function, $P(a)$, and the Bessel functions, J_n. We will return to this in Sec. 5.2.1.

We drive the system with a 16-cycle laser pulse on the form in Eq. (3.58) with $N_{on} = 3$ cycle $\sin^2$ turn-on and turn-off and $N_{pl} = 10$ cycles of constant amplitude in the middle of the pulse. Using the P functions for coherent [Eq. (2.87)], Fock [Eq. (5.24)], thermal [Eq. (2.94)], and BSV [Eq. (5.25)], we simulate the spectra using both the direct expression in Eq. (5.29) and the Floquet expression in Eq. (5.31). To be able to compare the spectra, we use the same mean photon number in the driving fields, $\langle \hat{a}^\dagger_{\boldsymbol{k}_L,\sigma_L} \hat{a}_{\boldsymbol{k}_L,\sigma_L} \rangle = 7.35 \times 10^{11}$ which corresponds to a coherent driver intensity of $I = 8.26 \times 10^{11}$ W/cm^2. We consider the first conduction band in ZnO crystal along the $\Gamma - M$ direction [52] and consider a population of $L = 10$ electrons, but note that the characteristics of the spectrum are independent of the number of considered electrons, as indicated by Eqs. (5.29) and (5.31). In this model, the lattice constant is $a = 5.52$ a.u. and the Fourier coefficients are $b_1 = 0 - 0.814$ a.u., $b_2 = -0.0024$ a.u., $b_3 = -0.0048$ a.u., $b_4 = -0.0003$ a.u., and $b_5 = -0.0009$ a.u. We use a spacing in crystal-momentum space of $\Delta q = \frac{2\pi}{10a}$. We note that for the BSV-driver, the squeezing parameter was $r_{\boldsymbol{k}_L,\sigma_L} = 14.35$, a number already exceeded experimentally [158].

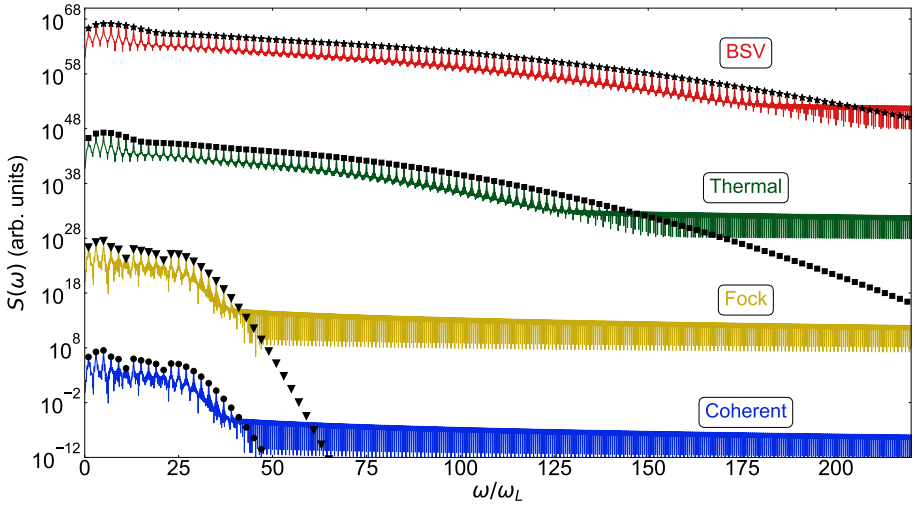

Figure 5.1: The harmonic spectrum [Eq. (5.29)] for coherent (blue), Fock (yellow), thermal (green), and BSV (red) driving fields. The black markers are results obtained in the analytical Floquet limit [Eq. (5.31)]. We note that the spectra generated by a thermal and BSV driver yield signal at extended harmonics compared to the spectra generated by a coherent state or Fock state. Adapted with permission from Ref. [5]. Copyrighted by the American Physical Society.

The spectra are shown in Fig. 5.1. We note that the overall structure of the spectra is much the same as for atomic gases [165]. We note that the spectra generated from coherent and Fock states are very similar, with a clear cutoff. In contrast, the spectra from both thermal light and BSV extend to much higher harmonics with no clear cutoff. The black markers show the results from the Floquet limit [Eq. (5.31)] proving that the Floquet description accurately reproduces the harmonic spectrum. We can thus proceed to study the nature of the spectra using the expression in Eq. (5.31). In particular, we are interested in investigating the origin of the different cutoffs seen in Fig. 5.1.

5.2.1 Harmonic cutoff

As stated and seen from Eq. (5.31), the strength of the n'th harmonic is determined by the integral of the product between the $P(|\alpha|)$ distribution and the square of the Bessel function of order n. The Bessel functions, $J_n(x)$, quickly vanish for arguments lower than their order, i.e., $J_n(x) \approx 0$ for $x < n$ [214]. Consequently, only if the P function is nonvanishing in the region where the

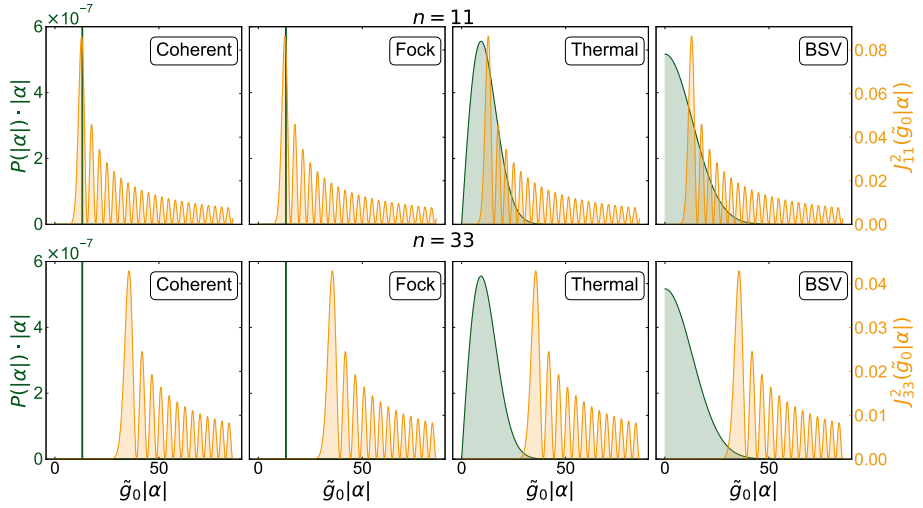

Figure 5.2: The overlap between the radial distribution [Eq. (5.30)] with the square of the Bessel functions as found in Eq. (5.31) for harmonic $n = 11$ (top row) and $n = 33$ (bottom row). Each column shows the radial P distribution for a different type of driving field. We note that the overlap due to the long tails for thermal and BSV light overlaps with the square of the Bessel functions for higher harmonics when compared to coherent and Fock driving fields. Adapted with permission from Ref. [5]. Copyrighted by the American Physical Society.

argument is larger than the order, will the signal be nonvanishing. In Eq. (5.31), the argument in the Bessel functions is $l\tilde{g}_0|\alpha|$. This means that Bessel functions of order n vanish for $|\alpha| < n/(l_{\max}\tilde{g}_0)$, where $l_{\max}$ denotes the most significant contribution in the Fourier expansion of the dispersion relation.

In Fig. 5.2, the $P(|\alpha|)$ distributions as well as the square of the Bessel functions $J_n^2(\tilde{g}_0|\alpha|)$ are shown for the four different types of light for harmonic order $n = 11$ (top row) and $n = 33$ (bottom row). The two columns on the most left-hand side show the $P(|\alpha|)$ distributions for coherent [Eq. (2.87)] and Fock [Eq. (5.24)] states, respectively. As the driving fields contain a macroscopic number of photons, the radial distribution becomes very narrow and is approximately a delta function on the $|\alpha|$ axis. As seen in the difference between order $n = 11$ and $n = 33$ in Fig. 5.2, the domain of no overlap is quickly reached which results in the clear cutoff for coherent and Fock driving fields seen in Fig. 5.1 while at the same time explaining why the spectra are so similar.

In contrast, the $P(|\alpha|)$ distributions for thermal and BSV light have a much longer tail extending far beyond their mean value as seen in the two columns on the right-hand side in Fig. 5.2. Due to these prolonged tails in the distributions,

the $P(|\alpha|)$ and the Bessel functions have a nonvanishing overlap for far higher values of $|\alpha|$, yielding a much higher cutoff. However, the notion of a cutoff in the case of thermal and BSV driving fields might be without meaning, as seen in Fig. 5.1, due to the fact that the signal falls off much more slowly when compared to coherent and Fock drivers. This is again explained by the nature of the $P(|\alpha|)$ distributions. The long tails in the distributions for thermal and BSV light mean that the overlap decreases much more gradually, meaning that no clear cutoff can be defined. Note, however, that the analytical expression for a cutoff used for coherent driving has been extended to nonclassical driving fields in Ref. [165], which are consistent with the present results. Figure 5.2 provides a physical explanation of how the quantum nature of the driving field affects the emitted spectra: Driving fields with larger photon-number fluctuations (thermal and BSV) have a broader $P(|\alpha|)$ distribution which consequently has a larger overlap with the squared Bessel functions for higher values of $|\alpha|$ compared to more narrow distributions (coherent, Fock). Physically, it is thus the photon-number fluctuations that are the root of the extended harmonics signal, though all driving fields have the same mean photon number.

5.3 Time-resolved electric field

One of the observables of interest when driving with a nonclassical field is the generated electric field from HHG. In particular, it is interesting to investigate if it resembles the driving field. Already, experimental work has measured the time-dependent electric field generated by HHG [215–219], motivating such an investigation. Using the expression in Eq. (2.19), we calculate the expectation value for the emitted electric field from the state

$$\begin{aligned}\langle \hat{\boldsymbol{E}}(t)\rangle_{\mathrm{HHG}} &= \mathrm{Tr}\left[\hat{\rho}_F(t)\hat{\boldsymbol{E}}(t)\right] \\ &= -\sum_{\boldsymbol{k},\sigma} g_0\sqrt{\omega_k}\int d^2\alpha P(\alpha)\ \ 2\,\mathrm{Im}[\boldsymbol{e}_\sigma \gamma^{\alpha}_{\boldsymbol{k},\sigma}(t)e^{-i\omega_k t}]. \end{aligned} \tag{5.32}$$

By inserting the expression for $\gamma^{\alpha}_{\boldsymbol{k},\sigma}(t)$ [Eq. (5.19)], going to the continuum limit [Eq. (2.30)], and executing the solid angle integral and the sum over polarizations, we obtain

$$\begin{aligned}\langle \hat{\boldsymbol{E}}(t)\rangle_{\mathrm{HHG}} &= -\frac{4}{3\pi c^3}\int d^2\alpha P(\alpha)\,\mathrm{Im}\left[-i\int_0^t dt' \boldsymbol{j}^{\alpha}_{i,i}(t')\int_0^\infty d\omega\ \omega^2 e^{i\omega(t'-t)}\right] \\ &= -\frac{4}{3c^3}\int d^2\alpha P(\alpha)\frac{d^2}{dt^2}\boldsymbol{j}^{\alpha}_{i,i}(t), \end{aligned} \tag{5.33}$$

where we have recognized the innermost integral in the first line as $-\pi\frac{d^2}{dt^2}\delta(t'-t)$ when the imaginary part is taken. We are also interested in computing the

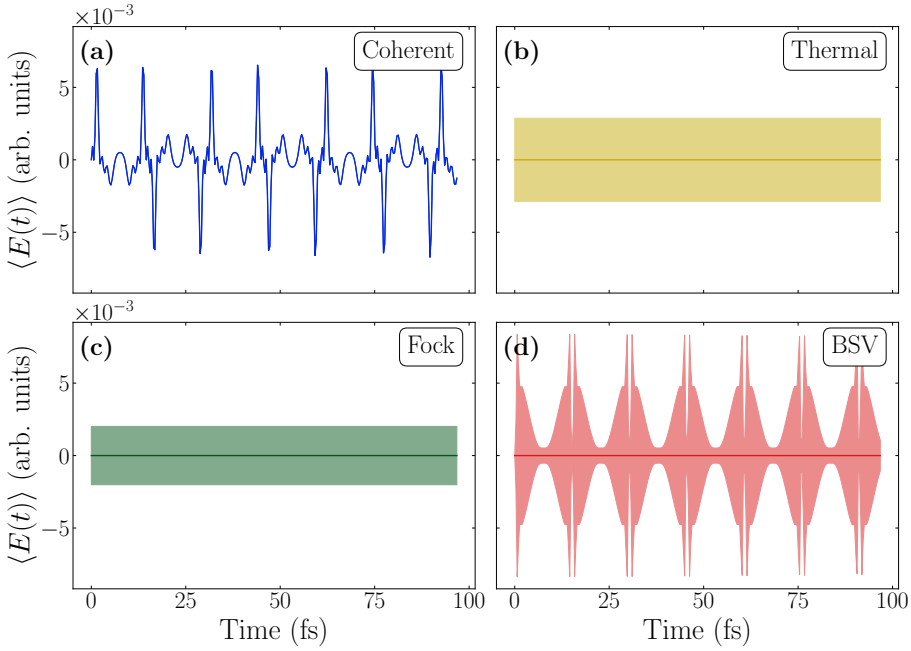

Figure 5.3: The mean electric field [Eq. (5.33)] and its uncertainty [Eq. (5.34)] for (a) coherent, (b) thermal, (c) Fock, and (d) BSV driving field. We note that the emitted field characteristics are similar to those of the driving field, shown in Sec. 2.2.3. Adapted with permission from Ref. [5]. Copyrighted by the American Physical Society.

variance. Without loss of generality, we take the current, $\boldsymbol{j}_{i,i}(t)$ along the one-dimensional chain to be the x direction and compute $\langle \hat{E}_x^2(t) \rangle$. Using Eqs. (2.41) and (2.42) and by neglecting the terms involving the driving field as well as the vacuum fluctuations, we obtain the expression for the variance (a full derivation can be found in Ref. [5])

$$\langle [\Delta \hat{E}_x(t)]^2 \rangle_{\mathrm{HHG}} = \frac{16}{9c^3} \Bigg\{ \int d^2\alpha P(\alpha) \left[\frac{d^2}{dt^2} j^{\alpha}_{i,i}(t) \right]^2 - \left[\int d^2\alpha P(\alpha) \frac{d^2}{dt^2} j^{\alpha}_{i,i}(t) \right]^2 \Bigg\}. \tag{5.34}$$

Curiously, we note that the distribution of the driving field, $P(\alpha)$, enters the expression for both the emitted field [Eq. (5.33)] and its variance [Eq. (5.34)]. This shows that, without any electron correlations, the emitted field inherits the quantum nature from the driving field, consistent with the findings

in Sec. 4.2.1. In Fig. 5.3, we show the generated fields with their uncertainties, i.e., $\sqrt{\langle[\Delta\hat{E}_x(t)]^2\rangle_{\mathrm{HHG}}}$. Comparing to the electric field characteristics shown in Sec. 2.2.3, we see that all fields are similar to their driving fields: the field emitted from a coherent driver [Fig. 5.3(a)] has a time-dependent mean field with minimum uncertainty, the fields emitted from Fock and thermal drivers [Fig. 5.3(b) and (c)] both have vanishing mean and constant uncertainty, while the field emitted from a BSV driver [Fig. 5.3(d)] has a vanishing mean but with large time-dependent fluctuations. It is thus reasonable to say that the emitted fields are of a similar nature to their nonclassical driving fields. As the spectral resolution of the fields shown in Fig. 5.3 is within experimental reach, using, e.g., TIPTOE [215, 219], the quantum nature of the electric field emitted from HHG driven by a nonclassical driving field can be experimentally investigated.

5.4 Accuracy of the approximative positive P representation

The results presented in Figs. 5.1, 5.2, and 5.3 rely on the APP for Fock and BSV driving fields. In order to verify this approximation, we calculate the expectation values of interest on the driving field within the APP and compare them to known exact results. Using the APP, we express the state as

$$\hat{\rho}_F^{(\mathrm{APP})} = \int d^2\alpha \mathcal{Q}(\alpha)|\alpha\rangle\langle\alpha|, \tag{5.35}$$

where all states are in the mode of the driving field. We first calculate the mean photon number, which is proportional to the spectrum [Eq. (2.31)]. For a Fock state, it is given by

$$\begin{aligned}
\langle\hat{a}^\dagger\hat{a}\rangle_{\mathrm{Fock}}^{(\mathrm{APP})} &= \mathrm{Tr}\left[\hat{a}^\dagger\hat{a}\hat{\rho}_F^{(\mathrm{APP})}\right] \\
&= \int d^2\alpha \mathcal{Q}_{\mathrm{Fock}}^{(N)}(\alpha)|\alpha|^2 \\
&= \int_0^{2\pi} d\phi \int_0^\infty d|\alpha| \frac{e^{-|\alpha|^2}}{\pi} \frac{|\alpha|^{2N}}{N!}|\alpha|^3 \\
&= N+1 \\
&\neq \langle\hat{a}^\dagger\hat{a}\rangle_{\mathrm{Fock}}^{(\mathrm{Exact})},
\end{aligned} \tag{5.36}$$

which does not equal the exact result. However, in the large photon-number limit, $N \gg 1$, as is relevant in HHG, it holds that $N+1 \approx N$ and the APP thus approximately yields the correct spectrum. Likewise, the spectrum for a BSV

driving field is

$$\begin{aligned}\langle \hat{a}^\dagger \hat{a} \rangle_{\mathrm{BSV}}^{(\mathrm{APP})} &= \mathrm{Tr}\left[\hat{a}^\dagger \hat{a} \hat{\rho}_F^{(\mathrm{APP})}\right] \\ &= \int_{-\infty}^{\infty} dx \int_{-\infty}^{\infty} dy \; \mathcal{Q}_{\mathrm{BSV}}^{(r)}(x,y)(x^2+y^2) \\ &= \cosh^2(r) \\ &\neq \langle \hat{a}^\dagger \hat{a} \rangle_{\mathrm{BSV}}^{(\mathrm{Exact})}, \end{aligned} \tag{5.37}$$

where we have parameterized $\alpha = x + iy$. Again the expression in Eq. (5.37) differs from the exact result, $\langle \hat{a}^\dagger \hat{a} \rangle_{\mathrm{BSV}}^{(\mathrm{Exact})} = \sinh^2(r)$, but in the large photon-number limit, we find that $\cosh^{(r)} = 1 + \sinh^2(r) \approx \sinh^2(r)$ and the spectrum for the BSV driver is thus approximately correct. Similarly, the driving fields yield the correct mean electric fields and variances.

We now consider the other quantum optical observables. First, we consider the photon statistics via the Mandel-Q parameter [Eq. (2.32)] for a Fock state. In the APP, we find that

$$\langle \hat{a}^\dagger \hat{a}^\dagger \hat{a} \hat{a} \rangle_{\mathrm{Fock}}^{(\mathrm{APP})} = N^2 + 3N + 2, \tag{5.38}$$

which yields a Mandel-Q parameter of $Q_{\mathrm{Fock}}^{(\mathrm{APP})} = 3 + 2/N \neq Q_{\mathrm{Fock}}^{(\mathrm{Exact})} = -1$. This is a significant deviation from the exact result, as a Fock state is the most number-squeezed state possible, with clear sub-Poissonian statistics; however, the APP predicts super-Poissonian statistics. This shows a clear limitation of the APP, and hence, the photon statistics are not considered for the emitted field.

Likewise, we also consider the degree of squeezing [Eq. (2.39)] for the BSV driving field. Calculating the variance of the quadrature operator [Eq. (2.37)] yields

$$\langle [\Delta \hat{X}(\vartheta)]^2 \rangle_{\mathrm{BSV}}^{(\mathrm{APP})} = \frac{1}{2}\cosh^2(r)[1 - \cos(2\vartheta)\tanh(r)] + \frac{1}{4}. \tag{5.39}$$

To obtain the squeezing, we minimize over the angle ϑ and find that

$$\lambda_{\mathrm{BSV}}^{(\mathrm{APP})} = \min_{\vartheta \in [0,\pi)]} \langle [\Delta \hat{X}(\vartheta)]^2 \rangle_{\mathrm{BSV}}^{(\mathrm{APP})} = \frac{1}{2}\cosh^2(r)[1 - \tanh(r)] + \frac{1}{4}. \tag{5.40}$$

Notice that since $r > 0$ it follows that $0 \leq \tanh(r) \leq 1$, which means that within the APP for a BSV driving field $\lambda_{\mathrm{BSV}}^{(\mathrm{APP})} \geq \frac{1}{4}$, which is clearly different from the exact result $\lambda_{\mathrm{BSV}}^{(\mathrm{Exact})} = \frac{1}{4}e^{-r}$. The APP does not, hence, capture the correct degree of squeezing, and we thus abstain from considering this observable for the emitted field.

In order to calculate the exact photon statistics and degree of squeezing, one needs to consider the full positive P representation and not use the APP. While this is not impossible, it drastically increases the numerical complexity, as an additional phase space has to be integrated over [see Eqs. (2.82) and (2.83)]. This approach is not pursued further.

CHAPTER 6

Summary and outlook

The thesis has examined the process of HHG from a quantum optical perspective and considered the quantum nature of the emitted light. Further, the required conditions for the generating electronic medium to generate nonclassical states of light have been identified. The thesis uses the Hubbard model to theoretically model strongly correlated systems and found that if the electrons are strongly correlated, the light emitted from the HHG process will have nonclassical properties.

In Ch. 1, the motivation to consider the process of HHG with emphasis on quantum optics is given, followed by an overview of the historical context and development of both strong-field physics and quantum optics. Finally, a more detailed overview of the works within the subfield of quantum optical HHG is given.

Chapter 2 provides an introduction to the theoretical description of light-matter coupling, both from a semiclassical and a quantum optical perspective. Further, an introduction to relevant quantum optical states, their properties, and phase-space representation is given, serving as a reference for later chapters.

In Ch. 3, the work-horse model of the thesis, the Fermi-Hubbard model, is derived and studied in its uncorrelated and correlated phases, including the Mott-insulating phase and the phase supporting a Mott exciton. Further, HHG from the model is studied using semiclassical considerations, and in particular, the appearance of noninteger harmonic peaks is investigated. These peaks at noninteger harmonics are explained by the population of multiple Floquet states,

which become populated due to a combination of energy levels and pulse lengths considered as presented in Paper I.

Chapter 4 dives into the quantum optical description of HHG by first deriving the general set of equations. Again, the Fermi-Hubbard model is considered as the generating medium, and it is found in Paper II that, without any electron correlations, the emitted light from HHG is a coherent state in all modes and thus has no quantum properties. However, in the strongly correlated Mott-insulating phase, the emitted light yields nonclassical characteristics. This is also seen in Paper III, where the nearest-neighbor interactions are considered, which supports the presence of a Mott exciton. Such an exciton is dominant in both the HHG spectrum and the degree of squeezing in the emitted HHG radiation. Finally, Paper IV considers further analytical approximations with numerical verification that provide a physical explanation of the origin of the nonclassical nature of HHG: the nonclassical response is due to nonvanishing time correlations or quantum fluctuations of the induced current.

Finally, Ch. 5 considers intraband HHG driven by nonclassical light. In Paper V, it is found that strongly driving the intraband model with thermal light or BSV light produces harmonic spectra that extend to harmonics much higher than when driving the system with a coherent or a Fock state. The mathematical reason for this finding is the overlap between the probability distribution of the driving field and the Bessel functions, which are function of the material properties. Due to large photon-number fluctuations in thermal and BSV fields, their probability distributions show a long tail, which explains both the extended harmonic spectrum and the lack of a clear cutoff. Finally, a discussion on the required approximations is given.

The main contribution of the PhD is to show that electron-electron correlations in an electronic medium generate nonclassical states of light when driven by an intense laser field and that this is due to fluctuations or nonvanishing time correlations of the induced current.

Many open questions remain in the field of quantum optical HHG. One of the main challenges is to improve the theoretical description of the process such that it relies on fewer approximations. In particular, it is unknown how accurate the approximation to decouple the dynamics of each harmonic mode is, or how accurate it is to consider just two quantum optical states in order to obtain a closed-form solution based on perturbation theory. This challenge is independent of the nature of the electronic system considered, as the challenge lies in the ability to numerically handle the large number of photonic basis states required for an exact simulation, as explained in Sec. 4.3.

Similarly, a new theory also has to be developed for HHG driven by nonclassical light. First, it would be highly interesting to investigate the interplay between electron-electron correlations in an electronic system with the nonclassical driving fields. However, nonvanishing electron-electron correlations mean

that light emitted from HHG driven by a coherent state is *not* itself a coherent state as shown in Ch. 4. As no analytical solutions to this case exist, one must be able to obtain numerical solutions for many different driving fields, which significantly complicates the required numerical effort. If a solution is found to this challenge, an even more important improvement might be possible: developing a theory that can consider the quantum optical nature of the light generated by a nonclassical driving field while also including the effect electron-electron correlations. So far, these two contributions, i.e., the generation of quantum light via electron-electron correlations and a quantum driving field, have only been considered independently. To consider both would open new fundamental research questions, as the interplay between these two quantum contributions has not been studied. Further, this interplay might allow for more efficient ways to generate ultrashort pulses of quantum light.

Another way to improve on the quantum optical nature of HHG is to consider other electronic systems. The purpose is twofold: First, the quantum optical considerations of HHG might improve HHG as a spectroscopic method by revealing more about the fundamental electron dynamics in the system, as the quantum nature of the emitted light is dictated by the fluctuations of the induced electron dynamics. However, the quantum optical observables are more expensive to compute numerically and also more expensive to measure experimentally, and as such, the quantum optical considerations in HHG must yield new insights about the electronic system and improve a semiclassical approach in order to justify the increased effort. Second, other electronic systems might be more suited to generate a stronger nonclassical signal at desirable frequencies, or in general, to generate ultrashort pulses of quantum light. As one of the main results of the thesis is that electron-electron correlations generate nonclassical light, one might also consider other "highly quantum" systems, such as, e.g., topological or superconducting systems.

Clearly, many open questions remain in the field of strong-field quantum optics, which will aid in the understanding of fundamental electron dynamics in complex systems while at the same time providing a novel platform for future quantum optical applications and innovations.

CHAPTER 7

Bibliography

[1] C. S. Lange, T. Hansen and L. B. Madsen, *Noninteger High-Order Harmonic Generation from Extended Correlated Systems*, Physical Review A **109**, 063103 (2024).

[2] C. S. Lange, T. Hansen and L. B. Madsen, *Electron-Correlation-Induced Nonclassicality of Light from High-Order Harmonic Generation*, Physical Review A **109**, 033110 (2024).

[3] C. S. Lange, T. Hansen and L. B. Madsen, *Excitonic Enhancement of Squeezed Light in Quantum-Optical High-Harmonic Generation from a Mott Insulator*, Phys. Rev. Lett. **135**, 043603 (2025).

[4] C. S. Lange and L. B. Madsen, *Hierarchy of approximations for describing quantum light from high-harmonic generation: A Fermi-Hubbard-model study*, Phys. Rev. A **111**, 013113 (2025).

[5] R. V. Gothelf, C. S. Lange and L. B. Madsen, *High-order harmonic generation in a crystal driven by quantum light*, Phys. Rev. A **111**, 063105 (2025).

[6] M. Planck, *Ueber das Gesetz der Energieverteilung im Normalspectrum*, Annalen der Physik **309**, 553 (1901).

[7] A. Einstein, *Über einen die Erzeugung und Verwandlung des Lichtes betreffenden heuristischen Gesichtspunkt*, Annalen der Physik **322**, 132 (1905).

[8] G. N. Lewis, *The Conservation of Photons*, Nature **118**, 874 (1926).

[9] N. Bohr, *I. On the constitution of atoms and molecules*, The London, Edinburgh, and Dublin Philosophical Magazine and Journal of Science **26**, 1 (1913).

[10] C. Nordling, E. Sokolowski and K. Siegbahn, *Precision Method for Obtaining Absolute Values of Atomic Binding Energies*, Phys. Rev. **105**, 1676 (1957).

[11] T. H. Maiman, *Stimulated Optical Radiation in Ruby*, Nature **187**, 493 (1960).

[12] F. J. McClung and R. W. Hellwarth, *Giant Optical Pulsations from Ruby*, Journal of Applied Physics **33**, 828 (1962).

[13] A. J. DeMaria, D. A. Stetser and H. Heynau, *Self Mode-Lokcing Of Lasers With Saturable Absorbers*, Applied Physics Letters **8**, 174 (1966).

[14] R. L. Fork, C. H. B. Cruz, P. C. Becker et al., *Compression of optical pulses to six femtoseconds by using cubic phase compensation*, Opt. Lett. **12**, 483 (1987).

[15] A. H. Zewail, *Femtochemistry: Atomic-Scale Dynamics of the Chemical Bond*, The Journal of Physical Chemistry A **104**, 5660 (2000).

[16] D. Strickland and G. Mourou, *Compression of amplified chirped optical pulses*, Optics Communications **55**, 447 (1985).

[17] L. V. Keldysh, *Ionization in the Field of a Strong Electromagnetic Wave*, J. Exp. Theor. Phys. **20**, 1307 (1965).

[18] F. H. M. Faisal, *Multiple absorption of laser photons by atoms*, Journal of Physics B: Atomic and Molecular Physics **6**, L89 (1973).

[19] M. V. Ammosov, N. B. Delone and V. P. Krainov, *Tunnel ionization of complex atoms and of atomic ions in an alternating electromagnetic field*, Soviet Journal of Experimental and Theoretical Physics **64**, 1191 (1986).

[20] H. R. Reiss, *Effect of an intense electromagnetic field on a weakly bound system*, Phys. Rev. A **22**, 1786 (1980).

[21] P. Agostini, F. Fabre, G. Mainfray et al., *Free-Free Transitions Following Six-Photon Ionization of Xenon Atoms*, Phys. Rev. Lett. **42**, 1127 (1979).

[22] A. L'Huillier, L. A. Lompre, G. Mainfray et al., *Multiply Charged Ions Formed by Multiphoton Absorption Processes in the Continuum*, Phys. Rev. Lett. **48**, 1814 (1982).

[23] A. McPherson, G. Gibson, H. Jara et al., *Studies of multiphoton production of vacuum-ultraviolet radiation in the rare gases*, J. Opt. Soc. Am. B **4**, 595 (1987).

[24] P. M. Paul, E. S. Toma, P. Breger et al., *Observation of a Train of Attosecond Pulses from High Harmonic Generation*, Science **292**, 1689 (2001).

[25] P. B. Corkum, *Plasma Perspective on Strong Field Multiphoton Ionization*, Physical Review Letters **71**, 1994 (1993).

[26] S. V. B. Jensen, *High-order harmonic generation from solids*, PhD thesis, Institut for Fysik og Astronomi, Aarhus Universitet (2024).

[27] D. M. Wolkow, *Über eine Klasse von Lösungen der Diracschen Gleichung*, Zeitschrift für Physik **94**, 250 (1935).

[28] B. Walker, B. Sheehy, L. F. DiMauro et al., *Precision Measurement of Strong Field Double Ionization of Helium*, Phys. Rev. Lett. **73**, 1227 (1994).

[29] M. Lewenstein, Ph. Balcou, M. Yu. Ivanov et al., *Theory of High-Harmonic Generation by Low-Frequency Laser Fields*, Physical Review A **49**, 2117 (1994).

[30] T. Gaumnitz, A. Jain, Y. Pertot et al., *Streaking of 43-attosecond soft-X-ray pulses generated by a passively CEP-stable mid-infrared driver*, Opt. Express **25**, 27506 (2017).

[31] N. H. Burnett, H. A. Baldis, M. C. Richardson et al., *Harmonic generation in CO2 laser target interaction*, Applied Physics Letters **31**, 172 (1977).

[32] R. L. Carman, D. W. Forslund and J. M. Kindel, *Visible Harmonic Emission as a Way of Measuring Profile Steepening*, Phys. Rev. Lett. **46**, 29 (1981).

[33] D. von der Linde, T. Engers, G. Jenke et al., *Generation of high-order harmonics from solid surfaces by intense femtosecond laser pulses*, Phys. Rev. A **52**, R25 (1995).

[34] P. A. Norreys, M. Zepf, S. Moustaizis et al., *Efficient Extreme UV Harmonics Generated from Picosecond Laser Pulse Interactions with Solid Targets*, Phys. Rev. Lett. **76**, 1832 (1996).

[35] A. H. Chin, O. G. Calderón and J. Kono, *Extreme Midinfrared Nonlinear Optics in Semiconductors*, Phys. Rev. Lett. **86**, 3292 (2001).

[36] S. Ghimire, A. D. DiChiara, E. Sistrunk et al., *Observation of High-Order Harmonic Generation in a Bulk Crystal*, Nature Physics **7**, 138 (2011).

[37] T. T. Luu, M. Garg, S. Y. Kruchinin et al., *Extreme Ultraviolet High-Harmonic Spectroscopy of Solids*, Nature **521**, 498 (2015).

[38] A. Korobenko, S. Saha, A. T. K. Godfrey et al., *High-harmonic generation in metallic titanium nitride*, Nature Communications **12**, 4981 (2021).

[39] Y.-Y. Lv, J. Xu, S. Han et al., *High-harmonic generation in Weyl semimetal β-WP_2 crystals*, Nature Communications **12**, 6437 (2021).

[40] S. Han, H. Kim, Y. W. Kim et al., *High-harmonic generation by field enhanced femtosecond pulses in metal-sapphire nanostructure*, Nature Communications **7**, 13105 (2016).

[41] N. Yoshikawa, T. Tamaya and K. Tanaka, *High-harmonic generation in graphene enhanced by elliptically polarized light excitation*, Science **356**, 736 (2017).

[42] V. E. Nefedova, S. Fröhlich, F. Navarrete et al., *Enhanced extreme ultraviolet high-harmonic generation from chromium-doped magnesium oxide*, Applied Physics Letters **118**, 201103 (2021).

[43] T. T. Luu, Z. Yin, A. Jain et al., *Extreme–ultraviolet high–harmonic generation in liquids*, Nature Communications **9**, 3723 (2018).

[44] Y. S. You, Y. Yin, Y. Wu et al., *High-harmonic generation in amorphous solids*, Nature Communications **8**, 724 (2017).

[45] B. Cheng, N. Kanda, T. N. Ikeda et al., *Efficient Terahertz Harmonic Generation with Coherent Acceleration of Electrons in the Dirac Semimetal* Cd_3As_2, Phys. Rev. Lett. **124**, 117402 (2020).

[46] G. Ndabashimiye, S. Ghimire, M. Wu et al., *Solid-state harmonics beyond the atomic limit*, Nature **534**, 520 (2016).

[47] Y. Bai, F. Fei, S. Wang et al., *High-Harmonic Generation from Topological Surface States*, Nature Physics **17**, 311 (2021).

[48] A. Annunziata, L. Becker, M. L. Murillo-Sánchez et al., *High-order harmonic generation in liquid crystals*, APL Photonics **9**, 060801 (2024).

[49] M. R. Bionta, E. Haddad, A. Leblanc et al., *Tracking ultrafast solid-state dynamics using high harmonic spectroscopy*, Phys. Rev. Res. **3**, 023250 (2021).

[50] K. Uchida, G. Mattoni, S. Yonezawa et al., *High-Order Harmonic Generation and Its Unconventional Scaling Law in the Mott-Insulating* Ca_2RuO_4, Phys. Rev. Lett. **128**, 127401 (2022).

[51] D. Golde, T. Meier and S. W. Koch, *High harmonics generated in semiconductor nanostructures by the coupled dynamics of optical inter- and intraband excitations*, Phys. Rev. B **77**, 075330 (2008).

[52] G. Vampa, C. R. McDonald, G. Orlando et al., *Semiclassical Analysis of High Harmonic Generation in Bulk Crystals*, Physical Review B **91**, 064302 (2015).

[53] D. Bauer and K. K. Hansen, *High-Harmonic Generation in Solids with and without Topological Edge States*, Phys. Rev. Lett. **120**, 177401 (2018).

[54] L. Yue and M. B. Gaarde, *Characterizing Anomalous High-Harmonic Generation in Solids*, Phys. Rev. Lett. **130**, 166903 (2023).

[55] K. K. Hansen, D. Bauer and L. B. Madsen, *Finite-system effects on high-order harmonic generation: From atoms to solids*, Phys. Rev. A **97**, 043424 (2018).

[56] C. Yu, K. K. Hansen and L. B. Madsen, *Enhanced high-order harmonic*

generation in donor-doped band-gap materials, Phys. Rev. A **99**, 013435 (2019).

[57] C. Yu, K. K. Hansen and L. B. Madsen, *High-order harmonic generation in imperfect crystals*, Phys. Rev. A **99**, 063408 (2019).

[58] I. Floss, C. Lemell, G. Wachter et al., *Ab initio multiscale simulation of high-order harmonic generation in solids*, Phys. Rev. A **97**, 011401 (2018).

[59] O. Neufeld, J. Zhang, U. D. Giovannini et al., *Probing phonon dynamics with multidimensional high harmonic carrier-envelope-phase spectroscopy*, Proceedings of the National Academy of Sciences **119**, e2204219119 (2022).

[60] M. Lysne, Y. Murakami, M. Schüler et al., *High-harmonic generation in spin-orbit coupled systems*, Phys. Rev. B **102**, 081121 (2020).

[61] N. Tancogne-Dejean, F. G. Eich and A. Rubio, *Effect of spin-orbit coupling on the high harmonics from the topological Dirac semimetal Na_3Bi*, npj Computational Materials **8**, 145 (2022).

[62] T. Ikemachi, Y. Shinohara, T. Sato et al., *Time-dependent Hartree-Fock study of electron-hole interaction effects on high-order harmonic generation from periodic crystals*, Phys. Rev. A **98**, 023415 (2018).

[63] R. E. F. Silva, I. V. Blinov, A. N. Rubtsov et al., *High-harmonic spectroscopy of ultrafast many-body dynamics in strongly correlated systems*, Nature Photonics **12**, 266 (2018).

[64] T. Hansen, S. V. B. Jensen and L. B. Madsen, *Correlation effects in high-order harmonic generation from finite systems*, Phys. Rev. A **105**, 053118 (2022).

[65] T. Hansen and L. B. Madsen, *Doping effects in high-harmonic generation from correlated systems*, Phys. Rev. B **106**, 235142 (2022).

[66] T. Hansen and L. Bojer Madsen, *Lattice imperfections and high-harmonic generation in correlated systems*, New Journal of Physics **26**, 063023 (2024).

[67] P. A. M. Dirac, *The quantum theory of the emission and absorption of radiation*, Proceedings of the Royal Society of London. Series A, Containing Papers of a Mathematical and Physical Character **114**, 243 (1927).

[68] P. A. M. Dirac, *The quantum theory of the electron*, Proceedings of the Royal Society of London. Series A, Containing Papers of a Mathematical and Physical Character **117**, 610 (1928).

[69] P. A. M. Dirac, *The quantum theory of the Electron. Part II*, Proceedings of the Royal Society of London. Series A, Containing Papers of a Mathematical and Physical Character **118**, 351 (1928).

[70] R. H. Brown and R. T. and, *LXXIV. A new type of interferometer for use in radio astronomy*, The London, Edinburgh, and Dublin Philosophical Magazine and Journal of Science **45**, 663 (1954).

[71] R. H. Brown and R. Q. Twiss, *Correlation between Photons in two Coherent Beams of Light*, Nature **177**, 27 (1956).

[72] R. H. Brown and R. Q. Twiss, *A Test of a New Type of Stellar Interferometer on Sirius*, Nature **178**, 1046 (1956).

[73] R. J. Glauber, *The Quantum Theory of Optical Coherence*, Phys. Rev. **130**, 2529 (1963).

[74] C. Gerry and P. Knight, *Introductory Quantum Optics* (Cambridge University Press, Cambridge, 2004).

[75] H. J. Carmichael and D. F. Walls, *Proposal for the measurement of the resonant Stark effect by photon correlation techniques*, Journal of Physics B: Atomic and Molecular Physics **9**, L43 (1976).

[76] H. J. Carmichael and D. F. Walls, *A quantum-mechanical master equation treatment of the dynamical Stark effect*, Journal of Physics B: Atomic and Molecular Physics **9**, 1199 (1976).

[77] J. Dalibard, Y. Castin and K. Mølmer, *Wave-function approach to dissipative processes in quantum optics*, Phys. Rev. Lett. **68**, 580 (1992).

[78] K. Mølmer, Y. Castin and J. Dalibard, *Monte Carlo wave-function method in quantum optics*, J. Opt. Soc. Am. B **10**, 524 (1993).

[79] J. C. Bergquist, R. G. Hulet, W. M. Itano et al., *Observation of Quantum Jumps in a Single Atom*, Phys. Rev. Lett. **57**, 1699 (1986).

[80] W. M. Itano, D. J. Heinzen, J. J. Bollinger et al., *Quantum Zeno effect*, Phys. Rev. A **41**, 2295 (1990).

[81] C. Monroe, D. M. Meekhof, B. E. King et al., *Demonstration of a Fundamental Quantum Logic Gate*, Phys. Rev. Lett. **75**, 4714 (1995).

[82] C. Monroe, D. M. Meekhof, B. E. King et al., *A "Schrödinger Cat" Superposition State of an Atom*, Science **272**, 1131 (1996).

[83] M. Brune, E. Hagley, J. Dreyer et al., *Observing the Progressive Decoherence of the "Meter" in a Quantum Measurement*, Phys. Rev. Lett. **77**, 4887 (1996).

[84] M. Brune, F. Schmidt-Kaler, A. Maali et al., *Quantum Rabi Oscillation: A Direct Test of Field Quantization in a Cavity*, Phys. Rev. Lett. **76**, 1800 (1996).

[85] J. F. Clauser, M. A. Horne, A. Shimony et al., *Proposed Experiment to Test Local Hidden-Variable Theories*, Phys. Rev. Lett. **23**, 880 (1969).

[86] S. J. Freedman and J. F. Clauser, *Experimental Test of Local Hidden-Variable Theories*, Phys. Rev. Lett. **28**, 938 (1972).

[87] A. Aspect, J. Dalibard and G. Roger, *Experimental Test of Bell's Inequalities Using Time-Varying Analyzers*, Phys. Rev. Lett. **49**, 1804 (1982).

[88] D. Bouwmeester, J.-W. Pan, K. Mattle et al., *Experimental quantum teleportation*, Nature **390**, 575 (1997).

[89] C. K. Hong, Z. Y. Ou and L. Mandel, *Measurement of subpicosecond time intervals between two photons by interference*, Phys. Rev. Lett. **59**, 2044 (1987).

[90] P. Kok, W. J. Munro, K. Nemoto et al., *Linear optical quantum computing with photonic qubits*, Rev. Mod. Phys. **79**, 135 (2007).

[91] J. Aasi, J. Abadie, B. P. Abbott et al., *Enhanced sensitivity of the LIGO gravitational wave detector by using squeezed states of light*, Nature Photonics **7**, 613 (2013).

[92] C. L. Degen, F. Reinhard and P. Cappellaro, *Quantum sensing*, Rev. Mod. Phys. **89**, 035002 (2017).

[93] S. Mukamel, M. Freyberger, W. Schleich et al., *Roadmap on quantum light spectroscopy*, Journal of Physics B: Atomic, Molecular and Optical Physics **53**, 072002 (2020).

[94] M. Kira, S. W. Koch, R. P. Smith et al., *Quantum spectroscopy with Schrödinger-cat states*, Nature Physics **7**, 799 (2011).

[95] S. L. Braunstein and P. van Loock, *Quantum Information with Continuous Variables*, Reviews of Modern Physics **77**, 513 (2005).

[96] C. Weedbrook, S. Pirandola, R. García-Patrón et al., *Gaussian quantum information*, Rev. Mod. Phys. **84**, 621 (2012).

[97] M. A. Nielsen and I. L. Chuang, *Quantum Computation and Quantum Information: 10th Anniversary Edition* (Cambridge University Press, 2010).

[98] J. L. O'Brien, A. Furusawa and J. Vučković, *Photonic quantum technologies*, Nature Photonics **3**, 687 (2009).

[99] I. Berson, *Electron in the quantized field of a monochromatic electromagnetic wave*, Sov. JETP **56**, 1627 (1969).

[100] J. Bergou and S. Varro, *Nonlinear scattering processes in the presence of a quantised radiation field. I. Non-relativistic treatment*, Journal of Physics A: Mathematical and General **14**, 1469 (1981).

[101] J. Bergou and S. Varro, *Nonlinear scattering processes in the presence of a quantised radiation field. II. Relativistic treatment*, Journal of Physics A: Mathematical and General **14**, 2281 (1981).

[102] P. Filipowicz, *Relativistic electron in a quantised plane wave*, Journal of Physics A: Mathematical and General **18**, 1675 (1985).

[103] O. Kfir, V. D. Giulio, F. J. G. de Abajo et al., *Optical coherence transfer mediated by free electrons*, Science Advances **7**, eabf6380 (2021).

[104] V. D. Giulio, M. Kociak and F. J. G. de Abajo, *Probing quantum optical excitations with fast electrons*, Optica **6**, 1524 (2019).

[105] R. Dahan, A. Gorlach, U. Haeusler et al., *Imprinting the quantum statistics of photons on free electrons*, Science **373**, eabj7128 (2021).

[106] A. B. Hayun, O. Reinhardt, J. Nemirovsky et al., *Shaping quantum photonic states using free electrons*, Science Advances **7**, eabe4270 (2021).

[107] V. D. Giulio and F. J. G. de Abajo, *Optical-cavity mode squeezing by free electrons*, Nanophotonics **11**, 4659 (2022).

[108] R. Dahan, G. Baranes, A. Gorlach et al., *Creation of Optical Cat and GKP States Using Shaped Free Electrons*, Phys. Rev. X **13**, 031001 (2023).

[109] A. Karnieli, S. Tsesses, R. Yu et al., *Quantum sensing of strongly coupled light-matter systems using free electrons*, Science Advances **9**, eadd2349 (2023).

[110] A. Gorlach, S. Malka, A. Karnieli et al., *Photonic Quantum State Tomography Using Free Electrons*, Phys. Rev. Lett. **133**, 250801 (2024).

[111] R. Ruimy, A. Karnieli and I. Kaminer, *Free-electron quantum optics*, Nature Physics **21**, 193 (2025).

[112] Y. Fang, F.-X. Sun, Q. He et al., *Strong-Field Ionization of Hydrogen Atoms with Quantum Light*, Phys. Rev. Lett. **130**, 253201 (2023).

[113] S. Wang and X. Lai, *High-order above-threshold ionization of an atom in intense quantum light*, Phys. Rev. A **108**, 063101 (2023).

[114] H. Liu, H. Zhang, X. Wang et al., *Atomic Double Ionization with Quantum Light*, Phys. Rev. Lett. **134**, 123202 (2025).

[115] M. Even Tzur and O. Cohen, *Motion of charged particles in bright squeezed vacuum*, Light: Science & Applications **13**, 41 (2024).

[116] J. Heimerl, A. Mikhaylov, S. Meier et al., *Multiphoton electron emission with non-classical light*, Nature Physics **20**, 945 (2024).

[117] J. Heimerl, A. Rasputnyi, J. Pölloth et al., *Driving electrons at needle tips strongly with quantum light* (2025), arXiv:2503.22464 [quant-ph] .

[118] M. Lewenstein, N. Baldelli, U. Bhattacharya et al., *Attosecond Physics and Quantum Information Science*, in *Proceedings of the 8th International Conference on Attosecond Science and Technology*, edited by L. Argenti, M. Chini and L. Fang (Springer International Publishing, Cham, 2024) pp. 27–44.

[119] B. Sundaram and P. W. Milonni, *High-order harmonic generation: Simplified model and relevance of single-atom theories to experiment*, Phys. Rev. A **41**, 6571 (1990).

[120] K. J. LaGattuta, *Radiation emitted by a resonantly driven hydrogen atom*,

Phys. Rev. A **48**, 666 (1993).

[121] H. Xu, *Non-perturbative theory of harmonic generation under a high-intensity laser field*, Zeitschrift für Physik D Atoms, Molecules and Clusters **28**, 27 (1993).

[122] G. Compagno, K. Dietz and F. Persico, *QED theory of harmonic emission by a strongly driven atom*, Journal of Physics B: Atomic, Molecular and Optical Physics **27**, 4779 (1994).

[123] F. I. Gauthey, C. H. Keitel, P. L. Knight et al., *Role of initial coherence in the generation of harmonics and sidebands from a strongly driven two-level atom*, Phys. Rev. A **52**, 525 (1995).

[124] A. Bogatskaya, E. Volkova and A. Popov, *Spontaneous transitions in atomic system in the presence of high-intensity laser field*, Europhysics Letters **116**, 14003 (2016).

[125] A. V. Bogatskaya, E. A. Volkova and A. M. Popov, *Spectroscopy of the atomic system driven by high intensity laser field* (2017), arXiv:1701.05777 [physics.atom-ph] .

[126] A. V. Bogatskaya, E. A. Volkova and A. M. Popov, *Spontaneous emission of atoms in a strong laser field*, Journal of Experimental and Theoretical Physics **125**, 587 (2017).

[127] I. A. Gonoskov, N. Tsatrafyllis, I. K. Kominis et al., *Quantum optical signatures in strong-field laser physics: Infrared photon counting in high-order-harmonic generation*, Scientific Reports **6**, 32821 (2016).

[128] N. Tsatrafyllis, I. K. Kominis, I. A. Gonoskov et al., *High-order harmonics measured by the photon statistics of the infrared driving-field exiting the atomic medium*, Nature Communications **8**, 15170 (2017).

[129] N. Tsatrafyllis, S. Kühn, M. Dumergue et al., *Quantum Optical Signatures in a Strong Laser Pulse after Interaction with Semiconductors*, Phys. Rev. Lett. **122**, 193602 (2019).

[130] A. Gombkötő, S. Varró, P. Mati et al., *High-order harmonic generation as induced by a quantized field: Phase-space picture*, Phys. Rev. A **101**, 013418 (2020).

[131] D. N. Yangaliev, V. P. Krainov and O. I. Tolstikhin, *Quantum theory of radiation by nonstationary systems with application to high-order harmonic generation*, Phys. Rev. A **101**, 013410 (2020).

[132] A. Gorlach, O. Neufeld, N. Rivera et al., *The Quantum-Optical Nature of High Harmonic Generation*, Nature Communications **11**, 4598 (2020).

[133] P. Stammer, J. Rivera-Dean, T. Lamprou et al., *High Photon Number Entangled States and Coherent State Superposition from the Extreme Ultraviolet to the Far Infrared*, Physical Review Letters **128**, 123603 (2022).

[134] J. Rivera-Dean, T. Lamprou, E. Pisanty et al., *Strong laser fields and their power to generate controllable high-photon-number coherent-state superpositions*, Phys. Rev. A **105**, 033714 (2022).

[135] M. Lewenstein, M. F. Ciappina, E. Pisanty et al., *Generation of Optical Schrödinger Cat States in Intense Laser–Matter Interactions*, Nature Physics **17**, 1104 (2021).

[136] P. Stammer, *Theory of entanglement and measurement in high-order harmonic generation*, Phys. Rev. A **106**, L050402 (2022).

[137] P. Stammer, J. Rivera-Dean, A. Maxwell et al., *Quantum Electrodynamics of Intense Laser-Matter Interactions: A Tool for Quantum State Engineering*, PRX Quantum **4**, 010201 (2023).

[138] S. Yi, N. D. Klimkin, G. G. Brown et al., *Generation of Massively Entangled Bright States of Light during Harmonic Generation in Resonant Media*, Phys. Rev. X **15**, 011023 (2025).

[139] J. Rivera-Dean, H. B. Crispin, P. Stammer et al., *Squeezed states of light after high-order harmonic generation in excited atomic systems*, Phys. Rev. A **110**, 063118 (2024).

[140] J. Rivera-Dean, P. Stammer, A. S. Maxwell et al., *Quantum-optical analysis of high-order harmonic generation in* $H_2{}^+$ *molecules*, Phys. Rev. A **109**, 033706 (2024).

[141] J. Sloan, A. Gorlach, M. E. Tzur et al., *Entangling extreme ultraviolet photons through strong field pair generation* (2023), arXiv:2309.16466 [quant-ph] .

[142] J. Rivera-Dean, *Role of short and long trajectories on the quantum-optical state after high-order harmonic generation*, Phys. Rev. A **110**, 063704 (2024).

[143] A. Gombkötő, S. Varró, B. G. Pusztai et al., *Parametric model for high-order harmonic generation with quantized fields*, Phys. Rev. A **109**, 053717 (2024).

[144] A. Gombkötő, P. Földi and S. Varró, *Quantum-optical description of photon statistics and cross correlations in high-order harmonic generation*, Phys. Rev. A **104**, 033703 (2021).

[145] A. Pizzi, A. Gorlach, N. Rivera et al., *Light Emission from Strongly Driven Many-Body Systems*, Nature Physics **19**, 551 (2023).

[146] I. Gonoskov, R. Sondenheimer, C. Hünecke et al., *Nonclassical light generation and control from laser-driven semiconductor intraband excitations*, Phys. Rev. B **109**, 125110 (2024).

[147] J. Rivera-Dean, P. Stammer, A. S. Maxwell et al., *Nonclassical states of light after high-harmonic generation in semiconductors: A Bloch-based*

perspective, Phys. Rev. B **109**, 035203 (2024).

[148] D. Theidel, V. Cotte, R. Sondenheimer et al., *Evidence of the Quantum Optical Nature of High-Harmonic Generation*, PRX Quantum **5**, 040319 (2024).

[149] S. Lemieux, S. A. Jalil, D. N. Purschke et al., *Photon bunching in high-harmonic emission controlled by quantum light*, Nature Photonics **19**, 767 (2025).

[150] P. Stammer, J. Rivera-Dean, A. S. Maxwell et al., *Entanglement and Squeezing of the Optical Field Modes in High Harmonic Generation*, Physical Review Letters **132**, 143603 (2024).

[151] S. de-la Peña, O. Neufeld, M. Even Tzur et al., *Quantum Electrodynamics in High-Harmonic Generation: Multitrajectory Ehrenfest and Exact Quantum Analysis*, Journal of Chemical Theory and Computation **21**, 283 (2025).

[152] P. Stammer, J. Rivera-Dean and M. Lewenstein, *Theory of quantum optics and optical coherence in high harmonic generation* (2025), arXiv:2504.13287 [quant-ph] .

[153] I. N. Agafonov, M. V. Chekhova and G. Leuchs, *Two-color bright squeezed vacuum*, Phys. Rev. A **82**, 011801 (2010).

[154] T. S. Iskhakov, A. M. Pérez, K. Y. Spasibko et al., *Superbunched bright squeezed vacuum state*, Opt. Lett. **37**, 1919 (2012).

[155] A. M. Pérez, T. S. Iskhakov, P. Sharapova et al., *Bright squeezed-vacuum source with 1.1 spatial mode*, Opt. Lett. **39**, 2403 (2014).

[156] M. Chekhova, G. Leuchs and M. Żukowski, *Bright squeezed vacuum: Entanglement of macroscopic light beams*, Optics Communications **337**, 27 (2015), macroscopic quantumness: theory and applications in optical sciences.

[157] M. A. Finger, T. S. Iskhakov, N. Y. Joly et al., *Raman-Free, Noble-Gas-Filled Photonic-Crystal Fiber Source for Ultrafast, Very Bright Twin-Beam Squeezed Vacuum*, Phys. Rev. Lett. **115**, 143602 (2015).

[158] M. Manceau, K. Y. Spasibko, G. Leuchs et al., *Indefinite-Mean Pareto Photon Distribution from Amplified Quantum Noise*, Physical Review Letters **123**, 123606 (2019).

[159] P. R. Sharapova, G. Frascella, M. Riabinin et al., *Properties of bright squeezed vacuum at increasing brightness*, Phys. Rev. Res. **2**, 013371 (2020).

[160] A. Rasputnyi, Z. Chen, M. Birk et al., *High-harmonic generation by a bright squeezed vacuum*, Nature Physics **20**, 1960 (2024).

[161] M. E. Tzur, C. Mor, N. Yaffe et al., *Measuring and controlling the birth of quantum attosecond pulses* (2025), arXiv:2502.09427 [physics.optics] .

[162] O. Pedatzur, G. Orenstein, V. Serbinenko et al., *Attosecond tunnelling*

interferometry, Nature Physics **11**, 815 (2015).

[163] T. Lamprou, P. Stammer, J. Rivera-Dean et al., *Recent developments in the generation of non-classical and entangled light states using intense laser-matter interactions* (2025), arXiv:2410.17452 [quant-ph] .

[164] M. Even Tzur, M. Birk, A. Gorlach et al., *Photon-Statistics Force in Ultrafast Electron Dynamics*, Nature Photonics **17**, 501 (2023).

[165] A. Gorlach, M. E. Tzur, M. Birk et al., *High-Harmonic Generation Driven by Quantum Light*, Nature Physics **19**, 1689 (2023).

[166] M. E. Tzur, M. Birk, A. Gorlach et al., *Generation of squeezed high-order harmonics*, Phys. Rev. Res. **6**, 033079 (2024).

[167] Y.-B. Wang and X.-B. Bian, *High-order harmonic generation in quantum light by a generalized von Neumann lattice method*, Phys. Rev. A **111**, 043111 (2025).

[168] D. J. Griffiths, *Introduction to Electrodynamics*, 4th ed. (Cambridge University Press, Cambridge, 2017).

[169] M. O. Scully and M. S. Zubairy, *Quantum Optics* (Cambridge University Press, Cambridge, 1997).

[170] C. Cohen-Tannoudji, G. Grynberg and J. Dupont-Roc, *Atom-Photon Interactions: Basic Processes and Applications* (Wiley, New York, 1998).

[171] R. Loudon, *The Quantum Theory of Light*, 2nd ed. (Clarendon Press, Oxford, 1983).

[172] D. Walls and G. J. Milburn, *Quantum Optics* (Springer Berlin, Heidelberg, 2008).

[173] J. J. Sakurai and J. Napolitano, *Modern Quantum Mechanics*, 2nd ed. (Cambridge University Press, Cambridge, 2017).

[174] J. Taylor, *Classical Mechanics* (University Science Books, Mill Valley, California, 2005).

[175] G. S. Agarwal, *Quantum Optics* (Cambridge University Press, Cambridge, 2012).

[176] J. Rivera-Dean, in *Non-classical States of Light: Generation via Strong-Field Processes and Applications in Quantum Key Distribution* (Springer Nature Switzerland, Cham, 2024).

[177] L. Yue and M. B. Gaarde, *Introduction to Theory of High-Harmonic Generation in Solids: Tutorial*, JOSA B **39**, 535 (2022).

[178] P. D. Drummond and C. W. Gardiner, *Generalised P-representations in Quantum Optics*, Journal of Physics A: Mathematical and General **13**, 2353 (1980).

[179] M. S. Kim, F. A. M. de Oliveira and P. L. Knight, *Properties of Squeezed*

Number States and Squeezed Thermal States, Physical Review A **40**, 2494 (1989).

[180] M. Imada, A. Fujimori and Y. Tokura, *Metal-insulator transitions*, Rev. Mod. Phys. **70**, 1039 (1998).

[181] P. A. Lee, N. Nagaosa and X.-G. Wen, *Doping a Mott insulator: Physics of high-temperature superconductivity*, Rev. Mod. Phys. **78**, 17 (2006).

[182] Y. Murakami, S. Takayoshi, A. Koga et al., *High-harmonic generation in one-dimensional Mott insulators*, Phys. Rev. B **103**, 035110 (2021).

[183] F. H. L. Essler, H. Frahm, F. Göhmann et al., *The One-Dimensional Hubbard Model* (Cambridge University Press, Cambridge, 2005).

[184] G. D. Mahan, *Many-Particle Physics* (Springer New York, New York, 2000).

[185] N. Ashcroft and N. Mermin, *Solid State Physics* (Saunders College Publishing, Fort Worth, 1976).

[186] F. Gebhard, *The Mott Metal-Insulator Transition: Models and Methods*, Vol. 137 (Springer Berlin, Heidelberg, 1997).

[187] S. Maekawa, *Physics of Transition Metal Oxides*, 1st ed., Springer Series in Solid-State Sciences (Springer Berlin, Heidelberg, 2004).

[188] E. Jeckelmann, *Optical excitations in a one-dimensional Mott insulator*, Phys. Rev. B **67**, 075106 (2003).

[189] G. Vidal, *Classical Simulation of Infinite-Size Quantum Lattice Systems in One Spatial Dimension*, Phys. Rev. Lett. **98**, 070201 (2007).

[190] J. A. Kjäll, M. P. Zaletel, R. S. K. Mong et al., *Phase diagram of the anisotropic spin-2 XXZ model: Infinite-system density matrix renormalization group study*, Phys. Rev. B **87**, 235106 (2013).

[191] A. Alvermann and H. Fehske, *High-order commutator-free exponential time-propagation of driven quantum systems*, Journal of Computational Physics **230**, 5930 (2011).

[192] T. J. Park and J. C. Light, *Unitary quantum time evolution by iterative Lanczos reduction*, J. Chem. Phys. **85**, 5870 (1986).

[193] E. S. Smyth, J. S. Parker and K. Taylor, *Numerical integration of the time-dependent Schrödinger equation for laser-driven helium*, Comput. Phys. Commun. **114**, 1 (1998).

[194] X. Guan, O. Zatsarinny, K. Bartschat et al., *General approach to few-cycle intense laser interactions with complex atoms*, Phys. Rev. A **76**, 053411 (2007).

[195] A. L. Frapiccini, A. Hamido, S. Schröter et al., *Explicit schemes for time propagating many-body wave functions*, Phys. Rev. A **89**, 023418 (2014).

[196] T. Hansen, *High-harmonic spectroscopy of strongly correlated systems*, PhD thesis, Institut for Fysik og Astronomi, Aarhus Universitet (2025).

[197] Y. Murakami, M. Eckstein and P. Werner, *High-Harmonic Generation in Mott Insulators*, Phys. Rev. Lett. **121**, 057405 (2018).

[198] Y. Murakami and P. Werner, *Nonequilibrium steady states of electric field driven Mott insulators*, Phys. Rev. B **98**, 075102 (2018).

[199] A. AlShafey, G. McCaul, Y.-M. Lu et al., *Ultrafast laser-driven dynamics in metal/magnetic-insulator interfaces*, Phys. Rev. B **108**, 144434 (2023).

[200] J. Masur, D. I. Bondar and G. McCaul, *Optical distinguishability of Mott insulators in the time versus frequency domain*, Phys. Rev. A **106**, 013110 (2022).

[201] G. Vampa, C. R. McDonald, G. Orlando et al., *Theoretical Analysis of High-Harmonic Generation in Solids*, Physical Review Letters **113**, 073901 (2014).

[202] U. Huttner, M. Kira and S. W. Koch, *Ultrahigh Off-Resonant Field Effects in Semiconductors*, Laser & Photonics Reviews **11**, 1700049 (2017).

[203] G. G. Brown, A. Jiménez-Galán, R. E. F. Silva et al., *Real-space perspective on dephasing in solid-state high harmonic generation*, Phys. Rev. Res. **6**, 043005 (2024).

[204] C. J. Joachain, N. J. Kylstra and R. M. Potvliege, *Atoms in Intense Laser Fields* (Cambridge University Press, Cambridge, 2011).

[205] M. Holthaus, *Floquet engineering with quasienergy bands of periodically driven optical lattices*, Journal of Physics B: Atomic, Molecular and Optical Physics **49**, 013001 (2015).

[206] T. Millack and A. Maquet, *Hyper-Raman Lines Produced During High Harmonic Generation*, *Journal of Modern Optics*, Journal of Modern Optics **40**, 2161 (1993).

[207] P. P. Corso, L. L. Cascio and F. Persico, *The role of hyper-Raman transitions in the radiation spectrum of a strongly driven two-level atom*, Journal of Modern Optics **44**, 819 (1997).

[208] A. Di Piazza and E. Fiordilino, *Why hyper-Raman lines are absent in high-order harmonic generation*, Phys. Rev. A **64**, 013802 (2001).

[209] N. Moiseyev and M. Lein, *Non-Hermitian Quantum Mechanics for High-Order Harmonic Generation Spectra*, The Journal of Physical Chemistry A **107**, 7181 (2003).

[210] E. Bloch, S. Beaulieu, D. Descamps et al., *Hyper-Raman lines emission concomitant with high-order harmonic generation*, New Journal of Physics **21**, 073006 (2019).

[211] N. Tomita and K. Nasu, *Quantum fluctuation effects on light absorption*

spectra of the one-dimensional extended Hubbard model, Phys. Rev. B **63**, 085107 (2001).

[212] M. Udono, K. Sugimoto, T. Kaneko et al., *Excitonic effects on high-harmonic generation in Mott insulators*, Phys. Rev. B **105**, L241108 (2022).

[213] P. Stammer, *Absence of Quantum Optical Coherence in High Harmonic Generation*, Physical Review Research **6**, L032033 (2024).

[214] A. T. Andersen, S. V. B. Jensen and L. B. Madsen, *Intra- and Intercycle Analysis of Intraband High-Order Harmonic Generation*, Physical Review A **109**, 063109 (2024).

[215] P. D. Keathley, S. V. B. Jensen, M. Yeung et al., *Uncovering Extreme Nonlinear Dynamics in Solids through Time-Domain Field Analysis*, Physical Review B **107**, 054302 (2023).

[216] S. Sederberg, D. Zimin, S. Keiber et al., *Attosecond optoelectronic field measurement in solids*, Nature Communications **11**, 430 (2020).

[217] D. A. Zimin, V. S. Yakovlev and N. Karpowicz, *Ultra-broadband all-optical sampling of optical waveforms*, Science Advances **8**, eade1029 (2022).

[218] A. Husakou, N. Karpowicz, V. S. Yakovlev et al., *Towards multi-petahertz all-optical electric field sampling* (2024), arXiv:2410.19196 [physics.optics] .

[219] M. R. Bionta, F. Ritzkowsky, M. Turchetti et al., *On-Chip Sampling of Optical Fields with Attosecond Resolution*, Nature Photonics **15**, 456 (2021).

[220] E. Merzbacher, *Quantum mechanics*, 3rd ed. (John Wiley and Sons, New York, 1998).

APPENDIX A

Glauber-Sudarshan P function for squeezed vacuum

In this appendix, the Glauber-Sudarshan P function for a squeezed vacuum state given in Eq. (2.90) will be derived. We consider a squeezed state, $|\xi_{\boldsymbol{k},\sigma}\rangle$, with squeezing parameter $\xi_{\boldsymbol{k},\sigma} = r_{\boldsymbol{k},\sigma}e^{i\theta_{\boldsymbol{k},\sigma}}$. From Ref. [74], we have the following

$$P_{\mathrm{GS}}(\alpha_{\boldsymbol{k}},\sigma) = \frac{e^{|\alpha_{\boldsymbol{k},\sigma}|^2}}{\pi^2}\int d^2u_{\boldsymbol{k},\sigma}e^{|u_{\boldsymbol{k},\sigma}|^2}\langle -u_{\boldsymbol{k},\sigma}|\hat{\rho}_{\boldsymbol{k},\sigma}|u_{\boldsymbol{k},\sigma}\rangle e^{u^*_{\boldsymbol{k},\sigma}\alpha_{\boldsymbol{k},\sigma}-u_{\boldsymbol{k},\sigma}\alpha^*_{\boldsymbol{k},\sigma}}, \tag{A.1}$$

$$|u_{\boldsymbol{k},\sigma}\rangle = e^{-\frac{1}{2}|u_{\boldsymbol{k},\sigma}|^2}\sum_{m=0}^{\infty}\frac{u^m_{\boldsymbol{k},\sigma}}{\sqrt{m!}}|m\rangle, \tag{A.2}$$

$$|\xi_{\boldsymbol{k},\sigma}\rangle = \sum_{m=0}^{\infty}C_{2m}\sqrt{(2m)!}|2m\rangle, \tag{A.3}$$

$$\delta^{(2)}(\alpha) = \int d^2u_{\boldsymbol{k},\sigma}e^{u^*_{\boldsymbol{k},\sigma}\alpha-u_{\boldsymbol{k},\sigma}\alpha^*_{\boldsymbol{k},\sigma}}, \tag{A.4}$$

where $|u_{\boldsymbol{k},\sigma}\rangle$ is a coherent state, $|m\rangle$ and $|2m\rangle$ denote Fock states in mode $(\boldsymbol{k},\sigma)$, and P_{GS} in Eq. (A.1) is a general expression for a GS P function. In Eq. (A.3), the expansion coefficients are given as $C_{2m} = \frac{(-1)^m[e^{im\theta_{\boldsymbol{k},\sigma}}\tanh(r_{\boldsymbol{k},\sigma})]^m}{2^m m!\sqrt{\cosh(r_{\boldsymbol{k},\sigma})}}$. Inserting $\hat{\rho}_{\boldsymbol{k},\sigma} = |\xi_{\boldsymbol{k},\sigma}\rangle\langle\xi_{\boldsymbol{k},\sigma}|$ into Eq. (A.1), we calculate the overlaps using Eqs. (A.2)

and (A.3)

$$\langle \xi_{\boldsymbol{k},\sigma} | u_{\boldsymbol{k},\sigma} \rangle = e^{-\frac{1}{2}|u_{\boldsymbol{k},\sigma}|^2} \sum_{m=0}^{\infty} C_{2m}^* u_{\boldsymbol{k},\sigma}^{2m}, \tag{A.5}$$

$$\langle -u_{\boldsymbol{k},\sigma} | \xi_{\boldsymbol{k},\sigma} \rangle = e^{-\frac{1}{2}|u_{\boldsymbol{k},\sigma}|^2} \sum_{m=0}^{\infty} C_{2m} u_{\boldsymbol{k},\sigma}^{*2m}. \tag{A.6}$$

Inserting Eqs. (A.5) and (A.6) into Eq. (A.1), we obtain

$$\begin{aligned} P_{\mathrm{GS}}(\alpha_{\boldsymbol{k},\sigma}) &= \frac{e^{|\alpha_{\boldsymbol{k},\sigma}|^2}}{\pi^2} \sum_{m,n=0}^{\infty} C_{2m} C_{2n}^* \int d^2 u_{\boldsymbol{k},\sigma} u_{\boldsymbol{k},\sigma}^{*2m} u_{\boldsymbol{k},\sigma}^{2n} e^{u_{\boldsymbol{k},\sigma}^* \alpha_{\boldsymbol{k},\sigma} - u_{\boldsymbol{k},\sigma} \alpha_{\boldsymbol{k},\sigma}^*} \\ &= \frac{e^{|\alpha_{\boldsymbol{k},\sigma}|^2}}{\pi^2} \sum_{m,n=0}^{\infty} C_{2m} C_{2n}^* \frac{\partial^{2m+2n}}{\partial \alpha_{\boldsymbol{k},\sigma}^{2m} \partial \alpha_{\boldsymbol{k},\sigma}^{*2n}} \int d^2 u_{\boldsymbol{k},\sigma}^2 e^{u_{\boldsymbol{k},\sigma}^* \alpha - u_{\boldsymbol{k},\sigma} \alpha_{\boldsymbol{k},\sigma}^*} \\ &= \frac{e^{|\alpha_{\boldsymbol{k},\sigma}|^2}}{\pi^2} \sum_{m,n=0}^{\infty} C_{2m} C_{2n}^* \frac{\partial^{2m+2n}}{\partial \alpha_{\boldsymbol{k},\sigma}^{2m} \partial \alpha_{\boldsymbol{k},\sigma}^{*2n}} \delta^{(2)}(\alpha_{\boldsymbol{k},\sigma}), \end{aligned} \tag{A.7}$$

where Eq. (A.4) has been used in the last line, where the delta function is to be understood in the distributional sense. Equation (A.7) is the GS P function for a squeezed vacuum state shown in Eq. (2.90).

APPENDIX B

Calculation of expectation values

In Chs. 4, expectation values for different observables are calculated. This appendix shows how this is done in practice. We start from the general state [Eq. (4.17)] expanded in field-free eigenstates of the electronic system

$$|\tilde{\Psi}(t)\rangle_I = \sum_m |\phi_m\rangle|\chi^{(m)}(t)\rangle, \tag{B.1}$$

from where we make the decoupling ansatz (see Sec. 4.3)

$$|\chi^{(m)}(t)\rangle = \otimes_{\boldsymbol{k},\sigma}|\chi^{(m)}_{\boldsymbol{k},\sigma}(t)\rangle, \tag{B.2}$$

where each state is expanded in Fock states

$$|\chi^{(m)}_{\boldsymbol{k},\sigma}(t)\rangle = \sum_{n_{\boldsymbol{k},\sigma}=0}^{p_{\boldsymbol{k},\sigma}} c^{(m)}_{n_{\boldsymbol{k},\sigma}}|n_{\boldsymbol{k},\sigma}\rangle, \tag{B.3}$$

with $p_{\boldsymbol{k},\sigma}$ being the maximum number of photons considered in mode $(\boldsymbol{k},\sigma)$ and where the time has been suppressed for convenience. As the state in Eq. (B.1) is in the interaction picture, the quantum topical observables have to transform accordingly

$$\hat{\mathcal{U}}_F^\dagger(t,t_0)\hat{a}_{\boldsymbol{k},\sigma}\hat{\mathcal{U}}_F(t,t_0) = \hat{a}_{\boldsymbol{k},\sigma}e^{-i\omega_k t}, \tag{B.4}$$

$$\hat{\mathcal{U}}_F^\dagger(t,t_0)\hat{a}_{\boldsymbol{k}^\dagger,\sigma}\hat{\mathcal{U}}_F(t,t_0) = \hat{a}^\dagger_{\boldsymbol{k},\sigma}e^{i\omega_k t}. \tag{B.5}$$

Using the number operator, $(\hat{n}_{\boldsymbol{k}',\sigma'})^l = (\hat{a}_{\boldsymbol{k}',\sigma'}\hat{a}^\dagger_{\boldsymbol{k}',\sigma'})^l$, to the power of l as an example, we can then calculate

$$\begin{aligned}\langle(\hat{n}_{\boldsymbol{k}',\sigma'})^l\rangle &= {}_I\langle\tilde{\Psi}(t)|\hat{\mathcal{U}}_F^\dagger(t,t_0)(\hat{n}_{\boldsymbol{k}',\sigma'})^l\hat{\mathcal{U}}_F(t,t_0)|\tilde{\Psi}(t)\rangle_I \\ &= \sum_{m,m'}\langle\phi_{m'}|\phi_m\rangle\,\langle\chi^{(m')}|(\hat{n}_{\boldsymbol{k}',\sigma'})^l|\chi^{(m)}\rangle \\ &= \sum_m\langle\chi^{(m)}|(\hat{n}_{\boldsymbol{k}',\sigma'})^l|\chi^{(m)}\rangle, \end{aligned} \tag{B.6}$$

where we have used the fact that the electronic eigenstates are orthogonal in the last line. Using the product ansatz in Eq. (B.2) in Eq. (B.6), we obtain

$$\langle(\hat{n}_{\boldsymbol{k}',\sigma'})^l\rangle = \sum_m\langle\chi^{(m)}_{\boldsymbol{k}',\sigma'}|(\hat{n}_{\boldsymbol{k}',\sigma'})^l|\chi^{(m)}_{\boldsymbol{k}',\sigma'}\rangle\prod_{\substack{\boldsymbol{k},\sigma\\\neq\boldsymbol{k},\sigma}}\langle\chi^{(m)}_{\boldsymbol{k},\sigma}|\chi^{(m)}_{\boldsymbol{k},\sigma}\rangle. \tag{B.7}$$

Using the Fock-state expansion in Eq. (B.3), we can calculate the two factors in Eq. (B.7) as

$$\begin{aligned}\langle\chi^{(m)}_{\boldsymbol{k}',\sigma'}|(\hat{n}_{\boldsymbol{k}',\sigma'})^l|\chi^{(m)}_{\boldsymbol{k}',\sigma'}\rangle &= \sum_{n'_{\boldsymbol{k}',\sigma'}=0}^{p_{\boldsymbol{k}',\sigma}}\sum_{n''_{\boldsymbol{k}',\sigma'}}^{p_{\boldsymbol{k}',\sigma}}\left(c^{(m)}_{n'_{\boldsymbol{k}',\sigma'}}\right)^* c^{(m)}_{n''_{\boldsymbol{k}',\sigma'}}\langle n'_{\boldsymbol{k}',\sigma'}|(\hat{n}_{\boldsymbol{k}',\sigma'})^l|n''_{\boldsymbol{k}',\sigma'}\rangle \\ &= \sum_{n'_{\boldsymbol{k}',\sigma'}=0}^{p_{\boldsymbol{k}',\sigma}}\left|c^{(m)}_{n'_{\boldsymbol{k}',\sigma'}}\right|^2(n_{\boldsymbol{k}',\sigma'})^l, \end{aligned} \tag{B.8}$$

and

$$\langle\chi^{(m)}_{\boldsymbol{k},\sigma}|\chi^{(m)}_{\boldsymbol{k},\sigma}\rangle = \sum_{n_{\boldsymbol{k},\sigma}}\left|c^{(m)}_{n_{\boldsymbol{k},\sigma}}\right|^2. \tag{B.9}$$

Inserting Eqs. (B.8) and (B.9) into Eq. (B.7), we obtain the final expression

$$\begin{aligned}\langle(\hat{n}_{\boldsymbol{k}',\sigma'})^l\rangle = \sum_m\Bigg\{\Bigg[\sum_{n'_{\boldsymbol{k}',\sigma'}=0}^{p_{\boldsymbol{k}',\sigma}}\left|c^{(m)}_{n'_{\boldsymbol{k}',\sigma'}}\right|^2(n_{\boldsymbol{k}',\sigma'})^l\Bigg] \\ \times\prod_{\substack{\boldsymbol{k},\sigma\\\neq\boldsymbol{k},\sigma}}\left(\sum_{n_{\boldsymbol{k},\sigma}}\left|c^{(m)}_{n_{\boldsymbol{k},\sigma}}\right|^2\right)\Bigg\}, \end{aligned} \tag{B.10}$$

where similar expressions are obtained for other observables.

APPENDIX C

Higher-order terms in the Markov-type approximation

In this Appendix, we consider the possibility of including more terms in the expansion of the quantum optical state in Eq. (4.48). Inserting this into Eq. (4.47), we obtain

$$\begin{aligned} i\partial_t|\chi^{(i)}_{\boldsymbol{k},\sigma}(t)\rangle =& \hat{\boldsymbol{A}}_{\boldsymbol{k},\sigma}(t)\cdot\boldsymbol{j}_{i,i}(t)|\chi^{(i)}_{\boldsymbol{k},\sigma}(t)\rangle - i\hat{\boldsymbol{A}}_{\boldsymbol{k},\sigma}(t)\cdot\sum_{m\neq i}\int_0^t dt'\,\hat{\boldsymbol{A}}_{\boldsymbol{k},\sigma}(t')\cdot\boldsymbol{j}_{m,i}(t') \\ &\times\Bigg[|\chi^{(i)}_{\boldsymbol{k},\sigma}(t)\rangle + (t'-t)\;\;\partial_{t'}|\chi^{(i)}_{\boldsymbol{k},\sigma}(t')\rangle|_{t'=t} \\ &\quad + \frac{(t'-t)^2}{2!}\frac{\partial^2}{\partial t'^2}|\chi^{(i)}_{\boldsymbol{k},\sigma}(t')\rangle|_{t'=t} + \dots\Bigg]. \end{aligned} \tag{C.1}$$

As the time-derivative of the state, $\partial_t|\chi^{(i)}_{\boldsymbol{k},\sigma}(t)\rangle$, enters on both sides of Eq. (C.1), this equation is not in a closed form. Calculating both the first and second-order time derivative, we find to lowest order in g_0

$$\partial_t|\chi^{(i)}_{\boldsymbol{k},\sigma}(t')\rangle|_{t'=t} \simeq -i\hat{\boldsymbol{A}}_{\boldsymbol{k},\sigma}(t)\cdot\boldsymbol{j}_{i,i}(t)|\chi^{(i)}_{\boldsymbol{k},\sigma}(t)\rangle, \tag{C.2}$$

$$\frac{\partial^2}{\partial t'^2}|\chi^{(i)}_{\boldsymbol{k},\sigma}(t')\rangle|_{t'=t} \simeq -i\Big\{\Big[\partial_t\hat{\boldsymbol{A}}_{\boldsymbol{k},\sigma}(t)\Big]\cdot\boldsymbol{j}_{i,i}(t) + \hat{\boldsymbol{A}}_{\boldsymbol{k},\sigma}(t)\;\partial_t\boldsymbol{j}_{i,i}(t)\Big\}|\chi^{(i)}_{\boldsymbol{k},\sigma}(t)\rangle. \tag{C.3}$$

We note that all higher-order terms are linear in g_0 as seen from Eq. (C.2) and (C.3). However, for the Hubbard model, we find that the two terms in Eq. (C.3) are similar in numerical value, and we can thus not consistently neglect either of the two terms. Consequently, as higher order terms in the expansion would yield derivatives of Eq. (C.3), we see that all time derivatives would be on the same form as the right-hand side of Eq. (C.3) which will all be to the same order in the coupling g_0. Consequently, one cannot truncate the expansion in Eq. (4.48) consistently to a given order in g_0. Hence, one can only use the leading order as done in Eq. (4.49). Of course, one could numerically investigate the higher-order terms in Eq. (C.3) in order to obtain higher precision. However, such considerations rely on the characteristics of the electronic system and will not be pursued further.

APPENDIX D

Derivation of the Markov-state approximation

In this Appendix, we show how the MSA [Eq. (4.54)] is derived and that it satisfies the equation of motion in Eq. (4.53). Before calculating the time derivative, we first multiply the state by a time-dependent phase, $e^{-ib(t)}$, and obtain

$$\begin{aligned} i\partial_t e^{-ib(t)}|\chi^{(i)}_{\boldsymbol{k},\sigma}(t)\rangle =& b(t)e^{-ib(t)}|\chi^{(i)}_{\boldsymbol{k},\sigma}(t)\rangle \\ &+ ie^{-ib(t)}\left\{\partial_t\hat{\mathcal{D}}[\beta^{(i)}_{\boldsymbol{k},\sigma}(t)]\right\}e^{-\frac{1}{2}\langle\hat{W}^2(t)\rangle_{\mathrm{el}}}|0\rangle \\ &+ ie^{-ib(t)}\hat{\mathcal{D}}[\beta^{(i)}_{\boldsymbol{k},\sigma}(t)]\partial_t e^{-\frac{1}{2}\langle\hat{W}^2(t)\rangle_{\mathrm{el}}}|0\rangle. \end{aligned} \tag{D.1}$$

We note that the right-hand side of Eq. (D.1) consists of three terms. The first term does not contribute to the dynamics. The time derivative of the displacement operator in Eq. (D.1) is calculated as

$$\begin{aligned} \partial_t\hat{\mathcal{D}}[\beta^{(i)}_{\boldsymbol{k},\sigma}(t)] = \Big\{ &\frac{1}{2}\left[\dot{\beta}^{(i)*}_{\boldsymbol{k},\sigma}(t)\beta^{(i)}_{\boldsymbol{k},\sigma}(t) - \beta^{(i)*}_{\boldsymbol{k},\sigma}(t)\dot{\beta}^{(i)}_{\boldsymbol{k},\sigma}(t)\right] \\ &+ \dot{\beta}^{(i)}_{\boldsymbol{k},\sigma}(t)\hat{a}^\dagger_{\boldsymbol{k},\sigma} - \dot{\beta}^{(i)*}_{\boldsymbol{k},\sigma}(t)\hat{a}_{\boldsymbol{k},\sigma}\Big\}\hat{\mathcal{D}}[\beta^{(i)}_{\boldsymbol{k},\sigma}(t)] \end{aligned} \tag{D.2}$$

By comparing Eq. (D.2) with Eq. (4.53), we see that the two last terms on the right-hand side of Eq. (D.2) with the definition of $\beta^{(i)}_{\boldsymbol{k},\sigma}(t)$ given in Eq. (4.41) match the first term on the right-hand side of Eq. (4.53). The terms in the square brackets on the right-hand side of Eq. (D.2) are absorbed into $b(t)$ and hence only contribute with a time-dependent phase.

As the first term on the right-hand side of Eq. (4.53) is accounted for, the second term must come from the last term in Eq. (D.1). This term involves the time derivative of an exponential operator. Such a derivative of an exponential operator, $\hat{F}(t)$, is given by [220]

$$\frac{d}{dt}e^{\hat{F}(t)} = \left\{\dot{\hat{F}}(t) + \frac{1}{2!}[\hat{F}(t),\dot{\hat{F}}(t)] + \frac{1}{3!}[\hat{F}(t),[\hat{F}(t),\dot{\hat{F}}(t)]] + \dots\right\}e^{\hat{F}(t)}. \quad \text{(D.3)}$$

The operator relevant in the present case is $\exp\left[-\frac{1}{2}\langle\hat{W}^2(t)\rangle_{\text{el}}\right]$, and we hence obtain

$$\frac{d}{dt}e^{-\frac{1}{2}\langle\hat{W}^2(t)\rangle_{\text{el}}} = -\langle\dot{\hat{W}}_{\boldsymbol{k},\sigma}(t)\hat{W}_{\boldsymbol{k},\sigma}(t)\rangle_{\text{el}}e^{-\frac{1}{2}\langle\hat{W}^2(t)\rangle_{\text{el}}} + \mathcal{O}(g_0^3), \quad \text{(D.4)}$$

where only terms up to second order in g_0 has been kept, and where we have neglected the commutator $[\dot{\hat{W}}_{\boldsymbol{k},\sigma}(t),\hat{W}_{\boldsymbol{k},\sigma}(t)]$. Inserting Eq. (D.4) into Eq. (D.1) yields the term

$$\begin{aligned}&\hat{\mathcal{D}}[\beta^{(i)}_{\boldsymbol{k},\sigma}(t)\langle\dot{\hat{W}}_{\boldsymbol{k},\sigma}(t)\hat{W}_{\boldsymbol{k},\sigma}(t)\rangle_{\text{el}}e^{-\frac{1}{2}\langle\hat{W}^2(t)\rangle_{\text{el}}}\\ &\overset{!}{=}\langle\dot{\hat{W}}_{\boldsymbol{k},\sigma}(t)\hat{W}_{\boldsymbol{k},\sigma}(t)\rangle_{\text{el}}\hat{\mathcal{D}}[\beta^{(i)}_{\boldsymbol{k},\sigma}(t)e^{-\frac{1}{2}\langle\hat{W}^2(t)\rangle_{\text{el}}},\end{aligned} \quad \text{(D.5)}$$

where the right-hand side is the required form as dictated by the equation of motion [Eq. (4.53)]. It can be shown that $[\hat{\mathcal{D}}[\beta^{(i)}_{\boldsymbol{k},\sigma}(t)],\langle\dot{\hat{W}}_{\boldsymbol{k},\sigma}(t)\hat{W}_{\boldsymbol{k},\sigma}(t)\rangle_{\text{el}}] = \mathcal{O}(g_0^3)$, and the equality in Eq. (D.5) holds up to second order in g_0. Consequently, Eq. (4.54) is a solution to Eq. (4.53) to second order in g_0. The time-dependent phase of $b(t)$ can simply be ignored as it carries no physical meaning.

APPENDIX E

Analytical expression for the HHG spectrum

In this appendix, an exact analytical expression for the HHG spectrum driven by an arbitrary state of light is provided. Note that the following does *not* rely on the APP for Fock and BSV driving fields.

It is not possible to evaluate Eq. (5.31) directly in the GS representation for Fock or BSV driving fields. However, by expanding the Bessel functions, further insights can be gained. The power-series expansion of the Bessel function is given as

$$J_n(x) = \sum_k \frac{(-1)^k}{k!(n+k)!}\left(\frac{x}{2}\right)^{n+2k}. \tag{E.1}$$

Inserting Eq. (E.1) into Eq. (5.31), and considering the n'th harmonic, we obtain

$$S(n\omega_L) \propto \sum_{k_1,k_2} \frac{(-1)^{k_1+k_2} K_{n,k_1,k_2}}{k_1!k_2!(n+k_1)!(n+k_2)!}\left(\frac{\tilde{g}_0}{2}\right)^{2(n+k_1+k_2)} \times \int d^2\alpha P(a)|\alpha|^{2(n+k_1+k_2)}, \tag{E.2}$$

where we again suppress the index of the laser mode on α, and where $K_{n,k_1,k_2} = \sum_{l_1,l_2} l_1^{n+2k_1} l_2^{n+2k_2} C_{l_1} C_{l_2}$ is a material constant with $C_l = lb_l\Sigma_q \cos(alq)$. We

recognize the integral in Eq. (E.2) as

$$\langle : (\hat{a}^\dagger \hat{a})^{n+k_1+k_2} : \rangle = \int d^2\alpha P(a) |\alpha|^{2(n+k_1+k_2)}, \tag{E.3}$$

where $\langle : \hat{O} : \rangle$ denotes the normal-ordered expectation value of the operator $\hat{O}$. Using the definition of the normalized m'th order coherence function

$$g^{(m)}(0) = \frac{\langle : (\hat{a}^\dagger \hat{a})^m : \rangle}{\langle \hat{a}^\dagger \hat{a} \rangle^m}, \tag{E.4}$$

we can rewrite Eq. (E.2) as

$$\begin{aligned} S(n\omega_L) \propto \sum_{k_1,k_2} \frac{(-1)^{k_1+k_2} K_{n,k_1,k_2}}{k_1! k_2! (n+k_1)! (n+k_2)!} \left(\frac{\tilde{g}_0}{2}\right)^{2(n+k_1+k_2)} \\ \times g^{n+k_1+k_2}(0) \ \langle \hat{a}^\dagger \hat{a} \rangle^{n+k_1+k_2}, \end{aligned} \tag{E.5}$$

which shows that the quantum nature of the driving field affects the harmonics via its coherence functions. Unfortunately, due to the infinite sums, Eq. (E.5) cannot be numerically evaluated. However, knowing the coherence functions for the different types of driving fields, further insights can be gained.

First we know that for a coherent field $g^{(m)}_{\text{Coh}}(0) = 1$. For a Fock state, the coherence function is

$$g^{(m)}_{\text{Fock}}(0) = 1 - \frac{m(m+1)}{2N} + \mathcal{O}\left(\frac{1}{N^2}\right), \tag{E.6}$$

which in the limit of the large photon number $N = \langle \hat{a}^\dagger \hat{a} \rangle = 7.35 \times 10^{11}$ used in the simulations in Ch. 5 yields $g^{(m)}_{\text{Fock}}(0) \approx 1$. We thus have $g^{(m)}_{\text{Fock}}(0) \approx g^{(m)}_{\text{Coh}}(0)$ even for very large m. This explains why the spectra generated from a coherent driver are very similar to those generated from a Fock state. This agrees with the numerical results in Fig. 5.1, which rely on the APP. Hence, the above calculation validates the APP results. For completeness, we see that the extended tails of the P distributions for thermal and BSV light are also explained by their coherence functions

$$g^{(m)}_{\text{Th}}(0)) = m!, \tag{E.7}$$

$$g^{(m)}_{\text{BSV}}(0)) = (2m-1)!! + \mathcal{O}\left(\frac{1}{\langle \hat{a}^\dagger \hat{a} \rangle}\right), \tag{E.8}$$

which are drastically different from those of a coherent or a Fock state, explaining the extended spectra in Fig. 5.1. Again, this calculation validates the use of the APP for a BSV driving field.

Publications

PAPER O

Phys. Rev. A 109, 063103 (2024)

Paper information

Author contributions

I participated in performing the numerical simulations and contributed to the analysis and interpretation of the research results. Furthermore, I contributed to the manuscript including preparation of the figures.

PHYSICAL REVIEW A **109**, 063103 (2024)

Noninteger high-order harmonic generation from extended correlated systems

Christian Saugbjerg Lange,* Thomas Hansen,* and Lars Bojer Madsen
Department of Physics and Astronomy, Aarhus University, Ny Munkegade 120, DK-8000 Aarhus C, Denmark

(Received 20 March 2024; accepted 15 May 2024; published 3 June 2024)

The spectra produced by high-order harmonic generation (HHG) typically exhibit well-defined peaks at odd integers times the laser frequency. However, in recent investigations of HHG from correlated materials, spectra exhibit signals at noninteger harmonics which do not conform to the well-known symmetry-based selection rules for HHG spectra. Here, we use the Fermi-Hubbard model to study HHG from a linear chain of atoms. This model allows us to study both the correlated and uncorrelated phases through a specification of the amount of onsite electron-electron repulsion. The presence of signal at noninteger harmonics can be interpreted as originating from the population of multiple Floquet states. We show how this coupling to different Floquet states depends on the characteristics of the driving pulse and the strength of the electron-electron interaction in the system.

DOI: 10.1103/PhysRevA.109.063103

I. INTRODUCTION

In the process of high-order harmonic generation (HHG), a medium (atomic gas, molecules, solid) is driven by an intense laser pulse causing highly nonlinear electron dynamics. The result is the emission of electromagnetic radiation in pulses that can be subfemtoseconds in duration. The attosecond pulses and the HHG process itself enable the study of electrons at their natural timescale [1,2]. If the high-harmonic generating system is inversion symmetric and if the driving pulse is sufficiently long, selection rules are imposed on the HHG spectrum allowing only odd harmonics [3]. This is verified in both atomic gases [4], molecules [5], and solids [6–8].

In recent years, there has been an increasing interest in HHG from correlated materials, i.e., materials where a beyond mean-field electron-electron repulsion is of significance. These systems cannot be described by a multiband picture but are instead described by effective models, such as the Fermi-Hubbard model [9], which allows for a description of electrons moving in a chain of atoms in terms of effective hopping and onsite electron-electron repulsion parameters. With this model it was found that the electron-electron correlation can lead to an enhanced signal for certain harmonics [10–18]. Curiously, however, HHG spectra from these types of systems show noninteger harmonics [10–19] which do not obey the symmetry-imposed selection rules [3]. Furthermore, even if these symmetries are broken, signal is still only expected to be found at (both even and odd) integer harmonics. The origin of these noninteger harmonics has been hypothesized to be the presence of correlations [10] or due to a short pulse or missing dephasing channels [15], or has simply not been discussed [11–14,16–19]. Thus, a satisfactory explanation of the reported signal at noninteger harmonics in HHG spectra from correlated systems is lacking.

In this work, therefore, we discuss the physical origin of the signal at noninteger harmonics. To do so, we use the prototypical Fermi-Hubbard model [9]. This model captures aspects of physics relevant to real materials, including cuprates and some high-T_c superconductors [20,21]. Conveniently, this model allows us to treat the electron-electron correlation strength, the Hubbard U, as a tunable parameter which enables us to study the model with various degrees of electron-electron correlations, ranging from the uncorrelated tight-binding limit to the highly correlated Mott-insulating limit, where the electrons are distributed evenly among the sites.

The paper is organized as follows. First, in Sec. II, the Fermi-Hubbard model is discussed. The results are presented in Sec. III. Here, the uncorrelated case, a case with intermediate correlation strength, and finally the highly correlated Mott-insulating phase are investigated. We conclude and summarize our findings in Sec. IV. Throughout this paper atomic units are used unless explicitly stated otherwise.

II. MODEL AND OBSERVABLES

We study HHG spectra generated by strong-field driving of the Fermi-Hubbard model [9]. We consider a one-dimensional chain of atoms corresponding to a one-band system at half-filling with the Hamiltonian given as

$$\hat{H}(t) = \hat{H}_{\text{hop}}(t) + \hat{H}_U. \tag{1}$$

Here

$$\hat{H}_{\text{hop}}(t) = -t_0 \sum_{j,\mu} (e^{iaA(t)} \hat{c}^\dagger_{j,\mu} \hat{c}_{j+1,\mu} + \text{H.c.}), \tag{2}$$

$$\hat{H}_U = U \sum_j (\hat{c}^\dagger_{j,\uparrow} \hat{c}_{j,\uparrow})(\hat{c}^\dagger_{j,\downarrow} \hat{c}_{j,\downarrow}) \tag{3}$$

describes the electron hopping and onsite electron-electron repulsion, respectively. The parameter t_0 describes the strength of an electron hop from site j to its neighboring sites $j \pm 1$ (with periodic boundary conditions), a is the lattice spacing, $A(t)$ is the vector potential of the driving laser polarized along

*These authors contributed equally to this work.

the lattice dimension, and U is the onsite electron-electron repulsion strength. The electronic annihilation operator for an electron with spin $\mu \in \{\uparrow, \downarrow\}$ on site j is denoted $\hat{c}_{j,\mu}$ with the creation operator $\hat{c}^{\dagger}_{j,\mu}$. We treat U as a tunable parameter allowing us to study the system with various degrees of electron-electron correlation. As apparent from Eq. (2), the laser-matter interaction is described through the Peierls phase $\exp[iaA(t)]$ [9,22]. In the limiting case of vanishing U, the system is simply a tight-binding model as the Hamiltonian of the system in Eq. (1) reduces to Eq. (2). For a finite $U \neq 0$, however, onsite electron-electron interactions are apparent, making the system more involved.

The current operator for this model is given as [13,15,17]

$$\hat{j}(t) = -iat_0 \sum_{j,\mu} (e^{iaA(t)} \hat{c}^{\dagger}_{j,\mu} \hat{c}_{j+1,\mu} - \text{H.c.}). \tag{4}$$

The expectation value of the current is calculated as

$$j(t) = \langle \Psi(t) | \hat{j}(t) | \Psi(t) \rangle, \tag{5}$$

where $|\Psi(t)\rangle$ is the time-dependent wave function evolved according to the time-dependent Schrödinger equation (TDSE)

$$i \frac{\partial}{\partial t} |\Psi(t)\rangle = \hat{H}(t) |\Psi(t)\rangle, \tag{6}$$

with the Hamiltonian given in Eq. (1). The many-electron state $|\Psi(t)\rangle$ is expanded in configurations $|\Phi_I\rangle$, specifying the site occupations through the multi-index I, i.e.,

$$|\Psi(t)\rangle = \sum_I C_I(t) |\Phi_I\rangle, \tag{7}$$

where $C_I(t)$ is the time-dependent amplitude to be solved for.

To drive the system, we use a linearly polarized pulse of the form

$$A(t) = A_0 f(t) \sin\left(\omega_L t + \frac{\pi}{2}\right), \tag{8}$$

where A_0 is the amplitude of the vector potential and where the dipole approximation is assumed to be valid. The envelope function of the vector potential is given by

$$f(t) = \begin{cases} \sin^2\left(\dfrac{\omega_L t}{4N_{\text{on}}}\right), & 0 < \frac{t}{T} < N_{\text{on}} \\ 1, & N_{\text{on}} < \frac{t}{T} < (N_{\text{on}} + N_{\text{pl}}) \\ \sin^2\left(\dfrac{\omega_L (t - N_{pl} T)}{4N_{\text{on}}}\right), & (N_{\text{on}} + N_{\text{pl}}) < \frac{t}{T} \\ & < (2N_{\text{on}} + N_{\text{pl}}) \\ 0, & \text{otherwise,} \end{cases} \tag{9}$$

i.e., as a flat top pulse with a $\sin^2$ ramp. Here N_{on} and N_{pl} are the number of cycles in the ramp and plateau of the pulse, respectively, and $T = 2\pi/\omega_L$ is the period of the laser. We keep the number of cycles on the top constant, specifically $N_{\text{pl}} = 10$, and by changing N_{on} we can study the effect of a longer pulse with a less steep ramp.

The observable of interest is the spectrum generated from the HHG process. It is given by

$$S(\omega) = |\omega^2 \tilde{j}(\omega)|^2, \tag{10}$$

where $\tilde{j}(\omega)$ is the Fourier transform of the current in Eq. (5).

We note that for a laser pulse of constant amplitude [$f(t) = 1$], the Hamiltonian in Eq. (1) is periodic with the laser period, i.e., $\hat{H}(t) = \hat{H}(t + T)$. In this limit, the solution to the TDSE [Eq. (6)] is given by Floquet states on the form [23,24]

$$|\Psi_j(t)\rangle = e^{-i\mathcal{E}_j t} |u_j(t)\rangle, \tag{11}$$

where $|u_j(t)\rangle = |u_j(t + T)\rangle$ are T-periodic functions and $\mathcal{E}_j$ are the quasienergy levels which are only uniquely defined up to integer multiples of the laser frequency ω_L. The set of quasienergies $\{\mathcal{E}_j\}$ and their corresponding Floquet functions are determined by the parameters of the electronic system but also by the amplitude A_0 and frequency ω_L of the vector potential [24].

Furthermore, we note that for a constant vector potential amplitude and for all correlation strengths, the system is symmetric under reflection in space and time translation by half a period. That is $\hat{C}_2 \hat{H}(t) \hat{C}_2^{-1} = \hat{H}(t)$. Here $\hat{C}_2 = \hat{R}_2 \cdot \hat{\tau}_2$, where $\hat{R}_2$ is reflection of the electronic system and $\hat{\tau}_2$ is a time translation by $T/2$. With this symmetry and if the system only populates a single Floquet state, only odd harmonics are allowed in the spectrum as shown in Ref. [3]. A detailed symmetry calculation for the present model is found in Appendix A and the related selection rules are derived in Appendix B.

Here, we investigate a system of $L = 10$ sites with periodic boundary conditions with a lattice spacing of $a = 7.5588$ a.u., and $t_0 = 0.0191$ a.u. similar to Refs. [10,13,14,17,18]. These values are picked to fit those of the cuprate Sr_2CuO_3 [25]. The field has an amplitude of $A_0 = F_0/\omega_L = 0.194$ a.u. with angular frequency 0.005 a.u. = 33 THz. This choice of field strength corresponds to a peak intensity of $F_0 = 3.3 \times 10^{10}$ W/cm^2. To solve the dynamics of the system driven by the laser governed by the TDSE in Eq. (6), we use the Arnoldi-Lancoz algorithm [26–29] with a Krylov subspace of dimension 4. To simplify the numerical calculations, we exploit that the Hamiltonian in Eq. (1) is invariant under spin flip of all electrons and under translations of the entire system corresponding to spin-flip symmetry and conservation of total crystal momentum, respectively [9]. In this manner, the number of configurations entering the expansion in Eq. (7) is reduced. In our simulations, we start from a nondegenerate spin-symmetric ground state with vanishing total crystal momentum, and as such only states within that subspace are needed in the basis. All results have been checked for convergence.

III. RESULTS AND DISCUSSION

In this section, we show the effects of correlations and pulse characteristics on the generated HHG spectra. The results presented will be followed by a discussion based on Floquet theory to explain the observations. In Fig. 1 the spectra for an uncorrelated system ($U = 0$) and for a system with an intermediate correlation strength of $U = t_0$ are shown. We note how the clear peaks in the uncorrelated phase at lower odd harmonics ($\omega/\omega_L \leqslant 11$) completely disappear when correlations are introduced. Furthermore, we note that correlations enhance the spectrum and extend it to much higher harmonics without any clear peaks, indicating that the presence of correlations drastically changes the underlying

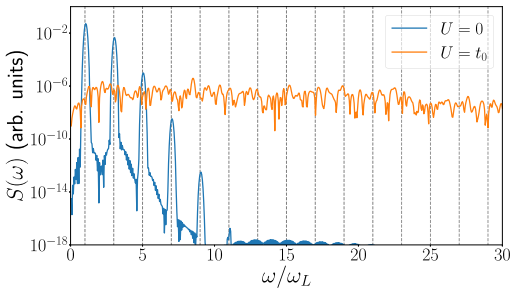

FIG. 1. Spectrum for an uncorrelated system ($U = 0$) and a correlated system ($U = t_0$). We note how the presence of correlations completely changes the spectrum. Both spectra have been obtained with an identical pulse with $N_{\text{on}} = 3$ [see Eq. (9)] and parameters specified in the text. The gray vertical dashed lines indicate odd harmonics to guide the eye.

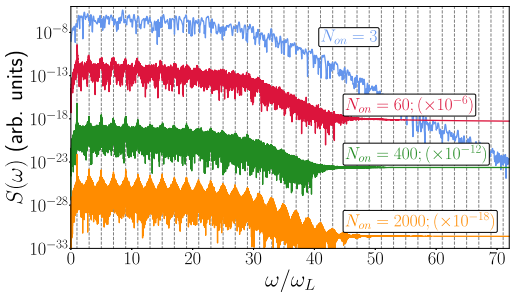

FIG. 2. Spectra for a correlated system with $U = t_0$ for turn-on cycles $N_{\text{on}} = 3, 60, 400, 2000$ [see Eq. (9)]. We note how peaks at odd harmonics become clearer with a more adiabatic (longer) turn-on of the pulse. The numbers in the parentheses in the inserts indicate that the spectra are scaled for visual clarity.

physics that generates the spectrum. While this enhancement and extension of the spectrum has already been observed and is well understood in the Mott-insulating phase [10,11,13–15], a satisfactory explanation of the absence of well-defined peaks is still missing. We will in this section first discuss the uncorrelated case before investigating the case with an intermediate correlation strength of $U = t_0$. At the end of the section also the Mott-insulating phase ($U = 10t_0$) will be investigated.

A. Uncorrelated phase

When $U = 0$ the Hamiltonian reduces to a simple tight-binding model with $\hat{H}(t) = \hat{H}_{\text{hop}}(t)$ in Eq. (2). This case corresponds to a one-band model, where only intraband harmonics can be generated. The importance of this limit in understanding experimental data is well documented [6,30,31]. It can be shown that $\hat{H}_{\text{hop}}(t)$ commutes with itself at all times [17]. It then follows that the time-evolution operator in this limit is given as $\hat{\mathcal{U}}(t, t_i) = \exp[-i\int_{t_i}^{t} \hat{H}_{\text{hop}}(t')dt']$. Taking the many-electron initial state $|\Psi(t_i)\rangle$ to be an eigenstate of the field-free system, the state in the uncorrelated phase at any time is therefore given as

$$|\Psi(t)\rangle = \hat{\mathcal{U}}(t, t_i)|\Psi(t_i)\rangle = e^{-i\int_{t_i}^{t} E(t')dt'}|\Psi(t_i)\rangle, \tag{12}$$

where $E(t)$ is the time-dependent energy and t_i is the initial time at which interactions between the laser and electronic system are turned on. It is seen from Eq. (12) that the time evolution is simply accounted for by a time-dependent phase applied to the initial state. As such, only a single many-electron Floquet state is populated at all times.

To reexpress Eq. (12) using Floquet theory, we define

$$\mathcal{E} = \frac{1}{T}\int_{t_i}^{t_i+T} E(t')dt', \tag{13}$$

which enables us to rewrite the phase in Eq. (12) as

$$e^{-i\int_{t_i}^{t}[E(t')-\mathcal{E}+\mathcal{E}]dt'} = e^{-i\mathcal{E}(t-t_i)}e^{-i\int_{t_i}^{t}[E(t')-\mathcal{E}]dt'}, \tag{14}$$

which by inserting into Eq. (12) yields

$$|\Psi(t)\rangle = e^{-i\mathcal{E}(t-t_i)}|u(t)\rangle, \tag{15}$$

where we have defined $|u(t)\rangle = e^{-i\int_{t_i}^{t}[E(t')-\mathcal{E}]dt'}|\Psi(t_i)\rangle$. We note that in the limit of periodic driving, i.e., when $E(t) = E(t+T)$ the state $|u(t)\rangle = |u(t+T)\rangle$ is periodic. Equation (15) expresses the formal solution to the many-electron Hamiltonian [Eq. (1)] in the $U = 0$ case in a Floquet picture, and since only a single Floquet state is populated [Eq. (15)], only odd harmonics are found in the spectrum [3]. This conclusion is also reached by noting that the expectation value of the current [Eq. (5)] is in this case simply

$$\langle\hat{j}(t)\rangle = \langle u(t)|\hat{j}(t)|u(t)\rangle, \tag{16}$$

which only contains frequency components determined by $A(t)$. The sharpness of the peaks is only limited by the integration limits of the Fourier transform involved in obtaining the spectra [Eq. (10)] and is hence determined by the bandwidth of the driving pulse. We note that it is not necessary to investigate the uncorrelated phase from the perspective of Floquet theory to conclude that only odd harmonics are visible in the spectrum. This can also be shown explicitly algebraically (see Appendix C).

B. Noninteger HHG in a correlated system

When we introduce correlations to the system, the spectrum changes completely, as seen in Fig. 1. For $U \neq 0$ no simple analytical expression for the wave function exists and we rely on numerical simulations. We first use a moderate electron-electron correlation strength of $U = t_0$. To study the effect of the pulse ramp and pulse length, we will in the remainder of this work consider pulses with various ramp lengths, starting from a typical ramp extending to an extremely long pulse with a highly adiabatic ramp by using $N_{\text{on}} = 3, 60, 400, 2000$ in Eq. (9).

Naively, one would think that the spectrum presented in Fig. 1 does not show clear harmonics due to a short pulse ($N_{\text{on}} = 3$). However, this is only partially true as seen in Fig. 2 where spectra for the various ramp lengths are shown. Here,

the spectra have been scaled for visual clarity as indicated by the number in the parentheses in the inserts to the right. To obtain a well-resolved spectrum, a window function of $\cos^8$ has been used in all figures for the case of a very short ramp of $N_{\rm on} = 3$. This is not necessary for $N_{\rm on} = 60, 400, 2000$. As seen in Fig. 2, the signal at odd harmonics becomes clearer with increasing pulse length. Surprisingly, however, we see how the peaks are accompanied by a broadening which does not disappear for a longer ramp though the spectrum becomes more regular. This behavior is different from the uncorrelated case where only sharp peaks are found at the odd harmonics without such a broadening (Fig. 1). As such, the presence of correlations introduces new phenomena not found in uncorrelated systems.

We will now explain the origin of the signal at noninteger harmonics. As discussed below, the presence of these indicates that, despite the extremely adiabatic turn-on of the laser, the system is still populated by more than a single Floquet state. Different from the uncorrelated case, the presence of correlations now allows coupling between (Floquet) states during the dynamics. In the present case where the amplitude of the vector potential changes with time, the set of quasienergies and corresponding Floquet functions depend on the instantaneous field amplitude, i.e., $\mathcal{E}(t) = \mathcal{E}[A_0(t)]$ [24], where we for simplicity define $A_0(t) = A_0 f(t)$ with $f(t)$ given in Eq. (9). We may formally expand a general state $|\Psi(t)\rangle$ in terms of Floquet states

$$|\Psi(t)\rangle = \sum_j c_j(t) e^{-i\int_{t_i}^{t}\mathcal{E}_j(t')dt'} |u_{\mathcal{E}_j(t)}(t)\rangle. \tag{17}$$

Here $c_j(t)$ is a time-dependent expansion coefficient to account for couplings between Floquet states. In the absence of couplings $c_j(t) = \delta_{j,i}$, where i denotes the Floquet state initially populated at $t = t_i$. We note that Eq. (17) reduces to the form of Eq. (15) for a constant field amplitude and no couplings. The time integrals of the quasienergies in Eq. (17) reflect that these quasienergies now depend on time through the time dependence of the field.

The expectation value of the current [Eq. (5)] for the state in Eq. (17) is readily calculated as

$$\langle \hat{j}(t)\rangle = \sum_{i,j} c_i^*(t) c_j(t) e^{-i\int_{t_i}^{t}[\mathcal{E}_j(t')-\mathcal{E}_i(t')]dt'} \times \langle u_{\mathcal{E}_i(t)}(t)|\hat{j}(t)|u_{\mathcal{E}_j(t)}(t)\rangle. \tag{18}$$

Equation (18) looks vastly different than if only a single Floquet state is populated as in Eq. (16). In particular, we see that the phase $\exp(-i\int_{t_i}^{t}[\mathcal{E}_j(t') - \mathcal{E}_i(t')]dt')$ contains frequency components which are in general not a multiple of the laser frequency. That is, if more than a single Floquet state is populated, this phase will generate noninteger harmonics in the spectrum. These are the so-called hyper-Raman lines previously found in HHG studies in atomic systems [32–36].

Based on the above discussion and the results presented in Fig. 2, it seems likely that the system indeed populates more than a single Floquet state throughout the dynamics. The population of multiple Floquet states can be explained by possible resonances in the quasienergy spectrum. However, the size of the system and the low frequency of the laser impede a numerical diagonalization of the full Floquet Hamiltonian to obtain the entire spectrum of quasienergies. Instead, we gain insight from the adiabatic eigenenergies which are obtained by diagonalizing $\hat{H}(t)$ in Eq. (1) for a fixed value of $A(t)$,

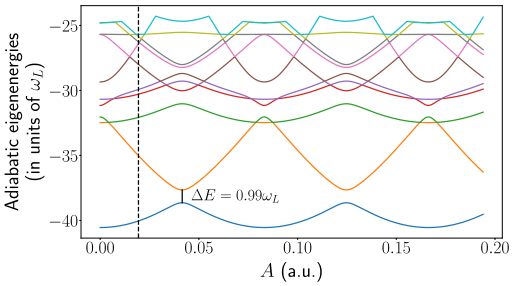

FIG. 3. Adiabatic eigenenergies as a function of the magnitude of the vector potential with an electron-electron correlation strength of $U = t_0$ and parameters specified in the main text. We note that for $A \approx 0.04$ a.u. the ground state is at a nonadiabatic one-photon resonance with the first excited state. The dashed vertical line indicates the reduced A_0' value considered (see text).

$$\hat{H}(t)|\psi_j(t)\rangle = E_j(t)|\psi_j(t)\rangle, \tag{19}$$

where t is a fixed parameter and $|\psi_j(t)\rangle$ is the adiabatic eigenstate with adiabatic eigenenergy $E_j(t)$. The adiabatic eigenenergies can be related to the Floquet quasienergies through a perturbative expansion of the latter in even powers of the small laser frequency ω_L^{2n} $(n = 0, 1, 2, \dots)$ p. 271 in Ref. [24]. Figure 3 shows the adiabatic eigenenergies for vector potential amplitudes up to the A_0 value of $A_0 = 0.194$ a.u. used in the TDSE simulations generating the spectra in Figs. 1, 2, and 6. We note how the gap in energies changes and especially that a one-photon resonance occurs between the two lowest-lying states at around $A \approx 0.04$ a.u., indicating a strong nonadiabatic coupling. We can examine these nonadiabatic couplings by expanding a general state in terms of adiabatic eigenstates $|\Psi(t)\rangle = \Sigma_j c_j(t) e^{-i\int_{t_i}^{t} dt' E_j(t')}|\psi_j\rangle$. The equation of motion for $c_j(t)$ then reads as [37]

$$\dot{c}_j(t) = -c_j\langle\psi_m|\dot{\psi}_m\rangle - \sum_{n\neq j} c_n \frac{\langle\psi_j|\dot{\hat{H}}(t)|\psi_n\rangle}{E_n - E_j} e^{-i\int_{t_i}^{t} dt'[E_n(t')-E_j(t')]}, \tag{20}$$

where the time derivative of the Hamiltonian in Eq. (1) is explicitly given as

$$\dot{\hat{H}}(t) = iat_0 F(t)\sum_{j,\mu}(e^{iaA(t)}\hat{c}_{j,\mu}^\dagger\hat{c}_{j+1,\mu} - \text{H.c.}) = -F(t)\,\hat{j}(t), \tag{21}$$

where it was used that the electric field is given by $F(t) = -\partial_t A(t)$. We first note that the nonadiabatic couplings are suppressed by the energy denominator in Eq. (20) which suppresses the influence of higher-lying energy states when only the ground state is initially populated. We further note that the strength of the adiabatic coupling is proportional to the amplitude of the electric field.

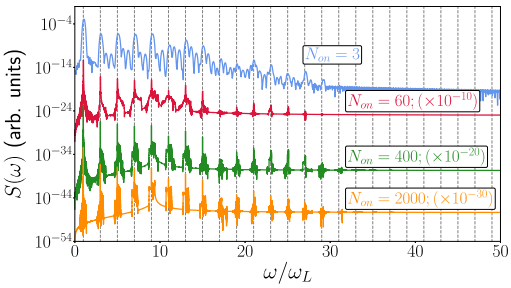

FIG. 4. Spectra for a correlated system with $U = t_0$. The same parameters as in Fig. 2 have been used except for a smaller vector potential amplitude of $A_0' = 0.1, A_0 = 0.0194$ a.u. We note that clear peaks are found at odd harmonics with a much smaller broadening when compared to Fig. 2.

Based on the above considerations, we now consider the results of a TDSE simulation for the same system driven with a weaker vector potential amplitude of $A_0' = 0.1A_0$. This is done in order to be off resonant with the one-photon transition between the two lowest-lying states (see Fig. 3). The spectra for the system driven with a vector potential of amplitude A_0' are seen in Fig. 4. Here we clearly see that for all the values of N_{on} considered, peaks are found at odd harmonics with increasing sharpness for longer pulse lengths. We ascribe this finding to the fact that the field strength remains far to the left of the resonance seen in Fig. 3, prohibiting many Floquet states from becoming populated. Naturally, n-photon resonances are also present for lower values of $A(t)$, e.g., a five-photon resonance at $A(t) \approx 0.015$ a.u., leading to some coupling to other Floquet states which is also seen in Fig. 4 where the peaks have some finite width. Nonetheless, as the spectrum in Fig. 4 is regular at odd harmonics, these higher n-photon resonances are sufficiently suppressed to not significantly impact the dynamics and we emphasize that the signal seen at odd harmonics of the laser frequency dominates the noninteger signal by orders of magnitude.

The origin of noninteger HHG in correlated systems can hence be ascribed to the population of multiple Floquet states due to resonances in the Floquet quasienergy spectrum. In the uncorrelated case, only the pulse length dictates the resolution of the peaks at odd harmonics, as only a single Floquet state is populated throughout the dynamics. In the correlated case, not only the length and the ramp of the pulse is of importance, but also its amplitude plays a role. This is due to the fact that when correlations are introduced, couplings are allowed and other Floquet states can become populated. The strength of this coupling depends both on the vector potential amplitude of the driving laser (compare Figs. 2 and 4) and on the degree of correlations in the target system. These findings can be used to study the quasienergy levels of a correlated system. In particular, the HHG spectrum can be used to study the presence of such resonances throughout the dynamics by varying the maximum amplitude of the vector potential.

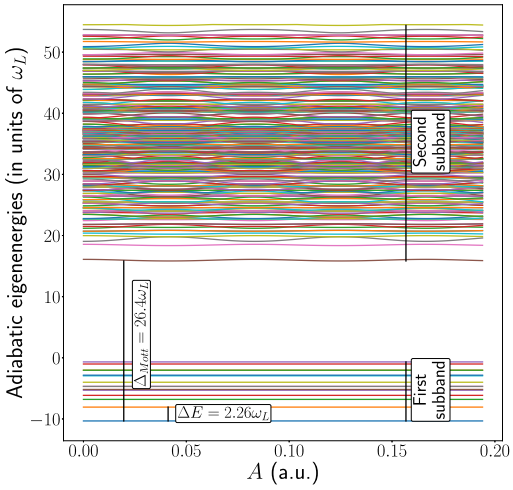

FIG. 5. Adiabatic eigenenergies as a function of the magnitude of the vector potential with an electron-electron correlation strength of $U = 10t_0$ and parameters specified in the main text. We note that in this Mott-insulating limit, Δ_{Mott} is largely independent of the strength of the electric field.

C. Noninteger HHG in Mott insulators

We now consider a system with an electron-electron correlation strength of $U = 10t_0$ which places the system in the Mott-insulating phase. Several works have observed noninteger harmonics and a general irregular spectrum above the so-called Mott gap [10,11,13–17]. As mentioned in the Introduction, the presence of noninteger HHG has been hypothesized to be due to missing dephasing channels and a short pulse length [15] or due to the presence of correlations [10], and some works have simply not discussed this aspect of the HHG spectrum [11,13,14,16,17,19]. In view of the symmetry-based constraints for the present system with $\hat{C}_2$ symmetry allowing only odd harmonics in the long pulse limit [3], it seems relevant to provide an explanation of the origin of the occurrence of noninteger HHG.

Before going into the discussion about HHG in this type of system, we first introduce the relevant physical quantities. In the Mott-insulating limit, the eigenenergies of the field-free system split into several Hubbard subbands (see Fig. 5). In the first subband, which contains the lowest-energy eigenstates including the ground state, the system is largely dominated by configurations with only a single electron on each site as it is energetically expensive to have two electrons on the same site due to the large value of the Hubbard U. Similarly, the states in the second subband are dominated by configurations that contain a single double occupancy of electrons on a site. Such a double occupancy is called a doublon and can be considered a quasiparticle. This doublon is accompanied by an empty site called a holon quasiparticle [11,14,15,17,18]. These two lowest subbands are the relevant ones in this work. Also of relevance is the energy difference between the ground state in the first subband and the lowest state in the second subband

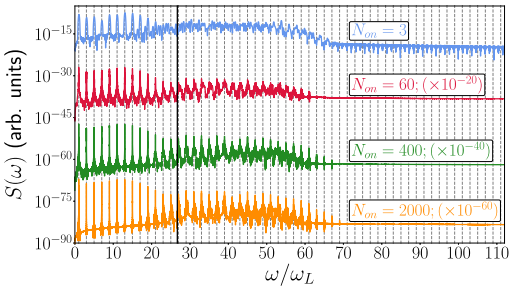

FIG. 6. Spectra for the Mott insulating phase with $U = 10t_0$ for various pulse lengths and parameters specified in the main text. Above the Mott gap (solid vertical line) clearer peaks are seen for longer pulse lengths.

described by Δ_{Mott} called the Mott gap (see Fig. 5). This separation gives rise to two different kinds of currents: the intrasubband and intersubband currents [11,15] reminiscent of intraband and interband currents for band-gap materials [6–8]. The intrasubband current originates from the propagation of the states with a single doublon-holon pair within the second subband which results in harmonics with energies below the Mott gap. The intersubband current originates from the recombination of a doublon-holon pair. Here transition occurs from the second subband to the first subband resulting in the emission of a harmonic with energy around or above Δ_{Mott} [11,15]. In this work $\Delta_{\text{Mott}} = 26.4\omega_L$. We note that the current operator in Eq. (4) involves moving a single electron which will create a single doublon-holon pair when applied to a state within the first subband. As all states within the first subband contain virtually no doublon-holon pairs, the matrix element $\langle\Psi_i|\hat{j}(t)|\Psi_j\rangle$, with $|\Psi_{i,j}\rangle$ being states within the first subband, is insignificant and there will be virtually no current contribution from couplings within the first subband (see Fig. 5). Further discussions about the Mott-insulating phase in the presence of intense laser pulses can be found, e.g., in Refs. [10–12,14,15,38].

The spectra obtained for the Mott-insulating phase are shown in Fig. 6. Here, clear peaks at odd harmonics in the intrasubband region with energies below Δ_{Mott} are seen for all considered pulse lengths. On the contrary, the peaks in the intersubband region above the Mott gap become more visible for longer ramp times. We further note that the broadening of the peaks for $U = t_0$ found in the spectra in Fig. 2 is not similarly found in Fig. 5. This indicates that no resonances between states occur with the varying strength of the vector potential in the Mott-insulating phase. Indeed, this is consistent with the adiabatic eigenenergies for the Mott-insulating phase shown in Fig. 5, where we see that the eigenenergies are virtually constant for a varying strength of the vector potential. In other words, the coupling between states does not change with a varying field strength prohibiting the same kind of field control of the dynamics as in the case of $U = t_0$. The possible population of multiple Floquet states will thus not change notably with a varying amplitude of the vector potential or with a longer pulse, the latter of which is also testified in Fig. 6. It is worth pointing out that it is primarily the peaks in the interband region that are broadened. This is due to the fact that though the dynamics populate multiple Floquet states, the states with a higher energy than the lowest state in the second subband in Fig. 5 have relatively little population. Consequently, the contribution to the current from terms which involve only states with a higher energy than the lowest state in the second subband (Fig. 5) is negligible when compared to terms which involve the lowest state in the second subband or states in the first subband as these are in general more populated. The off-diagonal terms contributing to the current in Eq. (18) will hence only have a phase with a difference in quasienergy at around or above Δ_{Mott} which broadens the signal only in the interband region of the spectrum. Similarly to the spectra in Fig. 4, the spectra in Fig. 6 become dominated by the signal at odd harmonics by orders of magnitude when compared to the signal at noninteger harmonics with increasing ramp time.

IV. SUMMARY AND CONCLUSION

In this work, we investigated the origin of noninteger harmonics found in spectra modeling the response of correlated solids. We employed the Fermi-Hubbard model and varied the Hubbard U, to analyze both the uncorrelated case and the correlated case. In the correlated case we investigated both an intermediate and high degree of electron-electron correlations, the latter known as the Mott-insulating phase. In the uncorrelated case, only odd harmonics were found in the spectrum, consistent with the population of a single Floquet state throughout the dynamics. Conversely, in the correlated phase with moderate electron-electron correlation ($U = t_0$), even with prolonged ramps, signal appeared at frequencies not an odd multiple of the laser frequency. This latter signal originates from the concurrent population of multiple Floquet states during the dynamics and is not at odds with the strong symmetry-based argument allowing only odd harmonics, as this assumes only a single Floquet state to be populated [3]. The varying amplitude of the vector potential causes states to become resonant, allowing multiple Floquet states to couple. Notably, reducing the maximum amplitude of the vector potential mitigated this resonance, resulting in predominantly odd harmonics with minimal broadening, indicating fewer populated Floquet states. The duration and bandwidth of the pulse crucially determine the resolution of the HHG peaks in the spectrum. However, changes in the vector potential amplitude via the pulse envelope can lead to resonances between states, populating multiple Floquet states which will generate a noninteger harmonic signal. Similar observations hold true for the Mott-insulating phase ($U = 10t_0$) where quasienergy levels remain largely unaffected by the magnitude of the vector potential amplitude. Thus, a longer pulse suffices to resolve the HHG peaks at odd harmonics in the interband regime of the spectrum. These findings are similar to the so-called hyper-Raman lines predicted [32–35] and recently observed [36] in studies of HHG in atoms, now reemerging in materials when accounting for beyond mean-field electron-electron correlations. However, the large energy gap in atoms between ground and excited states made it difficult to observe these noninteger spectral features in atomic HHG experiments

and necessitated a two-color approach for their observation [36]. In contrast, the energy difference between states in the present model can be much smaller, which could lead one to expect that experimental observations and potential technological applications of noninteger HHG are feasible in correlated materials.

ACKNOWLEDGMENTS

This work was supported by the Independent Research Fund Denmark (Grant No. 1026-00040B) and by the Danish National Research Foundation through the Center of Excellence for Complex Quantum Systems (Grant Agreement No. DNRF152).

APPENDIX A: DYNAMICAL SYMMETRIES OF THE FERMI-HUBBARD MODEL

In this Appendix, we show that the Fermi-Hubbard Hamiltonian in Eq. (1) is invariant in the continuous laser-field limit under the application of $\hat{C}_2 = \hat{R}\cdot\hat{\tau}_2$, where $\hat{R}$ is space inversion of all electronic coordinates and $\hat{\tau}_2$ is time translation by half a period, i.e., $\hat{\tau}_2\, t\, \hat{\tau}_2^{-1} = t + T/2$. We note that the spatial inversion does not affect the Peierls phase as this phase is still a coordinate of the vector potential [9].

The effect of space inversion on the electronic operators in Eq. (1) is readily calculated:

$$\hat{R}\Big[\sum_{j,\mu}\hat{c}^\dagger_{j,u}\hat{c}_{j+1,\mu}\Big]\hat{R}^{-1} = \sum_{j,\mu}\hat{c}^\dagger_{-j,u}\hat{c}_{-j-1,\mu} = \sum_{j',\mu}\hat{c}^\dagger_{j'+1,\mu}\hat{c}_{j',\mu}, \tag{A1}$$

where we have used the change of index $j' = -j+1$. Applying space inversion to the hopping Hamiltonian in Eq. (2) thus yields

$$\hat{R}\hat{H}_{\rm hop}(t)\hat{R}^{-1} = -t_0\sum_{j,\mu}(e^{iaA(t)}\hat{c}^\dagger_{j+1,\mu}\hat{c}_{j,\mu} + \text{H.c.}) \neq \hat{H}_{\rm hop}(t). \tag{A2}$$

We see that the Peierls phases in Eq. (A2) would also need to change sign for $\hat{H}_{\rm hop}(t)$ to be invariant. Hence, we also apply $\hat{\tau}_2$ and use that $A(t+T/2) = -A(t)$, in the Floquet limit of continuous monochromatic lasers. We then obtain that

$$\hat{C}_2\hat{H}_{\rm hop}(t)\hat{C}_2^{-1} = \hat{H}_{\rm hop}(t). \tag{A3}$$

As space inversion leaves the single-site dynamics invariant, it follows that the U term [Eq. (3)] is invariant under space inversion and hence under $\hat{C}_2$. We thus conclude that the Fermi-Hubbard Hamiltonian in Eq. (1) is $\hat{C}_2$ symmetric:

$$\hat{C}_2\hat{H}(t)\hat{C}_2^{-1} = \hat{H}(t). \tag{A4}$$

We now look at the current operator [Eq. (4)]. Here we assume $A(t) = A_0\sin(\omega_L t)$ and use the Jacobi-Anger expansion to decompose the Peierls phase

$$e^{iaA(t)} = \sum_m J_m(aA_0)e^{im\omega_L t}, \tag{A5}$$

where $J_m(z)$ is mth Bessel function of the first kind. We further note that

$$e^{-iaA(t)} = e^{iaA(t+T/2)} = \sum_m J_m(aA_0)(-1)^m e^{im\omega_L t}. \tag{A6}$$

Inserting Eqs. (A5) and (A6) into the current operator [Eq. (4)], it can be written in a decomposed form

$$\hat{j}(t) = \sum_m J_m(aA_0)e^{im\omega_L t}\,\hat{j}_m, \tag{A7}$$

where we have defined

$$\hat{j}_m = \sum_{j,\mu}[\hat{c}^\dagger_{j,\mu}\hat{c}_{j+1,\mu} - (-1)^m\hat{c}^\dagger_{j+1,\mu}\hat{c}_{j,\mu}]. \tag{A8}$$

By using Eq. (A1), we note that

$$\hat{R}\hat{j}_m\hat{R}^{-1} = \hat{C}_2\hat{j}_m\hat{C}_2^{-1} = (-1)^{m+1}\hat{j}_m, \tag{A9}$$

i.e., j_m is odd for even m and vice versa. The symmetries of both the Hamiltonian found in Eq. (A4) and of the current operator in Eqs. (A7) and (A9) will be used to derive the related selection rules of HHG in Appendix B.

APPENDIX B: SELECTION RULES FROM DYNAMICAL SYMMETRIES

In this Appendix, we show how the dynamical symmetries derived in Appendix A lead to selection rules for the harmonic spectrum. We start by investigating the electronic states. We consider the Floquet state in Eq. (11) and insert it into the TDSE [Eq. (6)] and obtain the Floquet Hamiltonian [39]

$$(-i\partial_t + \hat{H}(t))|u(t)\rangle = \mathcal{E}|u(t)\rangle, \tag{B1}$$

where the subscript has been dropped for notational convenience. By applying $\hat{C}_2$ from the left in Eq. (B1) and inserting that $\hat{C}_2^{-1}\hat{C}_2 = \mathbb{1}$ we find

$$\begin{aligned}\big(-i\partial_t + \hat{C}_2\hat{H}(t)\hat{C}_2^{-1}\big)\hat{C}_2|u(t)\rangle &= \mathcal{E}\hat{C}_2|u(t)\rangle\\ &= (-i\partial_t + \hat{H}(t))\hat{R}|u(t+T/2)\rangle\\ &= \mathcal{E}\hat{R}|u(t+T/2)\rangle,\end{aligned} \tag{B2}$$

where we have exploited the symmetry of the Hamiltonian [Eq. (A4)] and used that $\hat{C}_2|u(t)\rangle = \hat{R}|u(t+T/2)\rangle$. By comparing Eqs. (B1) and (B2), we obtain

$$|u(t)\rangle = e^{i\theta}\hat{R}|u(t+T/2)\rangle, \tag{B3}$$

where θ is a phase.

As the Floquet state in Eq. (11) is periodic with the laser frequency, it can be decomposed into its Fourier components

$$|\Psi(t)\rangle = e^{-i\mathcal{E}t}|u(t)\rangle = e^{-i\mathcal{E}t}\sum_l e^{il\omega_L t}|\phi_l\rangle, \tag{B4}$$

where l is an integer and the subscript of the Floquet state has been dropped for simplicity.

Using the Fourier decomposition in Eq. (B4) and comparing it with (B3) we obtain the relation

$$|\phi_l\rangle = e^{i\theta}(-1)^l\hat{R}|\phi_l\rangle. \tag{B5}$$

Using Eq. (10) the signal is readily calculated:

$$\begin{aligned} S(\omega) &= \left|\omega^2 \int_{-\infty}^{\infty} dt \langle\Psi(t)|\hat{j}(t)|\Psi(t)\rangle e^{-i\omega t}\right|^2 \\ &= \left|\omega^2 \int_{-\infty}^{\infty} dt \sum_{l,l',m} J_m(aA_0) e^{-i(\omega-(m+l-l')\omega_L)t} \langle\phi_{l'}|\hat{j}_m|\phi_l\rangle\right|^2 \\ &= \left|\omega^2 \sum_{l,l',m} J_m(aA_0)\, \delta[\omega-(m+l-l')\omega_L]\langle\phi_{l'}|\hat{j}_m|\phi_l\rangle\right|^2, \end{aligned} \tag{B6}$$

where we have used the Fourier decomposition of the Floquet state in Eq. (B4) and of the current operator in Eq. (A7). By defining $n = m + l - l'$, we can rewrite Eq. (B6) as

$$S(\omega) = \left|\omega^2 \sum_{l,m,n} \delta(\omega - n\omega_L)\, J_m(aA_0)\langle\phi_{m+l-n}|\hat{j}_m|\phi_l\rangle\right|^2. \tag{B7}$$

We now focus on the matrix element in Eq. (B7). Inserting the symmetries of the states and the current operator [Eqs. (B5) and (A9)] we obtain

$$\begin{aligned} \langle\phi_{m+l-n}|\hat{j}_m|\phi_l\rangle &= (-1)^{m+l-n+l+m+1} \\ &\quad \times \langle\phi_{m+l-n}|\hat{R}^{-1}\hat{R}\hat{j}_m\hat{R}^{-1}\hat{R}|\phi_l\rangle \\ &= (-1)^{n+1}\langle\phi_{m+l-n}|\hat{j}_m|\phi_l\rangle, \end{aligned} \tag{B8}$$

where we have used that $\hat{R} = \hat{R}^{-1} = \hat{R}^{\dagger}$. We see that Eq. (B8) vanishes for even n. Using this result in Eq. (B7) we conclude that due to the symmetries of the Hamiltonian, only odd harmonics are allowed in the spectrum when only a single Floquet state is populated during the dynamics.

APPENDIX C: EXPLICIT CALCULATION OF UNCORRELATED PHASE

In this Appendix, we show by algebraic derivations, without the use of Floquet theory, that the uncorrelated phase ($U = 0$) yields only odd harmonics. The state of the system at all times is given in Eq. (12) in the main text and is restated here for convenience:

$$|\Psi(t)\rangle = e^{-i\int_{t_i}^{t} E(t')dt'}|\Psi(t_i)\rangle. \tag{C1}$$

We start by transforming the fermionic creation operator from a site-specific description (site index j) to a crystal momentum-specific description (crystal momenta q)

$$\hat{c}^{\dagger}_{j,\mu} = \frac{1}{\sqrt{L}}\sum_{q} e^{-iR_j q}\hat{c}^{\dagger}_{q,\mu} \tag{C2}$$

and similarly for the annihilation operator. Here $R_j = ja$ is the position of the jth site with a being the lattice constant. The transformation in Eq. (C2) allows us to describe the system in the spatially delocalized Bloch basis instead of the localized Wannier basis underlying the representations in Eqs. (1)–(4). Inserting Eq. (C2) into the Hamiltonian in Eq. (2) yields

$$\hat{H}_{\text{hop}}(t) = -2t_0\sum_{q,\mu}\cos\{[q + A(t)]a\}\hat{c}^{\dagger}_{q,\mu}\hat{c}_{q,\mu}, \tag{C3}$$

and the current operator in Eq. (4) likewise transforms as

$$\hat{j}(t) = 2t_0 a\sum_{q,\mu}\sin\{[q + A(t)]a\}\hat{c}^{\dagger}_{q,\mu}\hat{c}_{q,\mu}. \tag{C4}$$

From Eqs. (C3) and (C4) it is clearly seen that the system is diagonal in q space. Further, we note from Eq. (C3) that the ground state has a symmetric distribution of electron crystal momenta around $q = 0$.

The expectation value of the current is calculated using Eq. (C4),

$$j(t) = \langle\hat{j}(t)\rangle = 2t_0 a\sum_{q,\mu}\sin\{[q + A(t)]a\}n_{q,\mu}, \tag{C5}$$

where $n_{q,\mu} = \langle\Psi(t)|\hat{c}^{\dagger}_{q,\mu}\hat{c}_{q,\mu}|\Psi(t)\rangle$ is the number of electrons with crystal momentum q and spin μ which remains constant throughout the dynamics. We now expand the sinusoidal function in Eq. (C5):

$$\begin{aligned} j(t) = 2t_0 a\sum_{q,\mu} n_{q,\mu}\{&\sin(qa)\cos[A(t)a] \\ &+ \cos(qa)\sin[A(t)a]\}. \end{aligned} \tag{C6}$$

We see that the first term in Eq. (C6) vanishes as $\Sigma_{q,\mu}\sin(qa)n_{q,\mu} = 0$ for all distributions symmetric around $q = 0$ which includes the ground state for $L = 10$. Taking a field of constant amplitude, $A(t) = A_0\sin(\omega_L t + \phi)$, we then expand the sine function in Eq. (C6) using the Jacobi-Anger expansion and obtain

$$\begin{aligned} j(t) = 4t_0 a\sum_{q,\mu} n_{q,\mu}\cos(qa) \\ \times\left(\sum_{n=1}^{\infty} J_{2n-1}(A_0 a)\sin[(2n-1)(\omega_L t + \phi)]\right), \end{aligned} \tag{C7}$$

where J_n is the nth Bessel function of the first kind. The spectrum is finally obtained from the norm square of the Fourier transform of Eq. (C7):

$$\begin{aligned} \tilde{j}(\omega) &= 4t_0 a\sum_{q,\mu} n_{q,\mu}\cos(qa)\sum_{n=1}^{\infty} J_{2n-1}(A_0 a)\int_{-\infty}^{\infty} e^{-i\omega t}\sin[(2n-1)(\omega_L t + \phi)]dt \\ &= -4i\pi t_0 a\sum_{q,\mu} n_{q,\mu}\cos(qa)\sum_{n=1}^{\infty} J_{2n-1}(A_0 a)\{e^{i(2n-1)\phi}\delta[\omega - (2n-1)\omega_L] - e^{-i(2n-1)\phi}\delta[\omega + (2n-1)\omega_L]\}, \end{aligned} \tag{C8}$$

where we have assumed an infinitely long pulse for simplicity. We see that Eq. (C8) is only nonvanishing for odd integer values of ω showing that only odd harmonics are found in the spectrum in the uncorrelated phase. For a finite pulse (also with an envelope), still only odd harmonics will be found in the spectrum, though less sharply peaked. In that case, the equations become more involved and are not included here.

[1] F. Krausz and M. Ivanov, Attosecond physics, Rev. Mod. Phys. **81**, 163 (2009).

[2] P. M. Kraus, B. Mignolet, D. Baykusheva, A. Rupenyan, L. Horný, E. F. Penka, G. Grassi, O. I. Tolstikhin, J. Schneider, F. Jensen, L. B. Madsen, A. D. Bandrauk, F. Remacle, and H. J. Wörner, Measurement and laser control of attosecond charge migration in ionized iodoacetylene, Science **350**, 790 (2015).

[3] O. Neufeld, D. Podolsky, and O. Cohen, Floquet group theory and its application to selection rules in harmonic generation, Nat. Commun. **10**, 405 (2019).

[4] M. Ferray, A. L'Huillier, X. F. Li, L. A. Lompre, G. Mainfray, and C. Manus, Multiple-harmonic conversion of 1064 nm radiation in rare gases, J. Phys. B: At. Mol. Opt. Phys. **21**, L31 (1988).

[5] C. Lyngå, A. L'Huillier, and C.-G. Wahlström, High-order harmonic generation in molecular gases, J. Phys. B: At. Mol. Opt. Phys. **29**, 3293 (1996).

[6] S. Ghimire, A. D. DiChiara, E. Sistrunk, P. Agostini, L. F. DiMauro, and D. A. Reis, Observation of high-order harmonic generation in a bulk crystal, Nat. Phys. **7**, 138 (2011).

[7] S. Ghimire and D. A. Reis, High-harmonic generation from solids, Nat. Phys. **15**, 10 (2019).

[8] E. Goulielmakis and T. Brabec, High harmonic generation in condensed matter, Nat. Photonics **16**, 411 (2022).

[9] F. H. L. Essler, H. Frahm, F. Göhmann, A. Klümper, and V. E. Korepin, *The One-Dimensional Hubbard Model* (Cambridge University Press, Cambridge, 2005).

[10] R. E. F. Silva, I. V. Blinov, A. N. Rubtsov, O. Smirnova, and M. Ivanov, High-harmonic spectroscopy of ultrafast many-body dynamics in strongly correlated systems, Nat. Photonics **12**, 266 (2018).

[11] Y. Murakami, M. Eckstein, and P. Werner, High-harmonic generation in Mott insulators, Phys. Rev. Lett. **121**, 057405 (2018).

[12] Y. Murakami and P. Werner, Nonequilibrium steady states of electric field driven Mott insulators, Phys. Rev. B **98**, 075102 (2018).

[13] T. Hansen, S. V. B. Jensen, and L. B. Madsen, Correlation effects in high-order harmonic generation from finite systems, Phys. Rev. A **105**, 053118 (2022).

[14] T. Hansen and L. B. Madsen, Doping effects in high-harmonic generation from correlated systems, Phys. Rev. B **106**, 235142 (2022).

[15] Y. Murakami, S. Takayoshi, A. Koga, and P. Werner, High-harmonic generation in one-dimensional Mott insulators, Phys. Rev. B **103**, 035110 (2021).

[16] A. AlShafey, G. McCaul, Y.-M. Lu, X.-Y. Jia, S.-S. Gong, Z. Addison, D. I. Bondar, M. Randeria, and A. S. Landsman, Ultrafast laser-driven dynamics in metal/magnetic-insulator interfaces, Phys. Rev. B **108**, 144434 (2023).

[17] C. S. Lange, T. Hansen, and L. B. Madsen, Electron-correlation-induced nonclassicality of light from high-order harmonic generation, Phys. Rev. A **109**, 033110 (2024).

[18] T. Hansen and L. B. Madsen, Effects of lattice imperfections on high-harmonic generation from correlated systems, arXiv:2306.08379.

[19] J. Masur, D. I. Bondar, and G. McCaul, Optical distinguishability of Mott insulators in the time versus frequency domain, Phys. Rev. A **106**, 013110 (2022).

[20] P. A. Lee, N. Nagaosa, and X.-G. Wen, Doping a Mott insulator: Physics of high-temperature superconductivity, Rev. Mod. Phys. **78**, 17 (2006).

[21] M. Imada, A. Fujimori, and Y. Tokura, Metal-insulator transitions, Rev. Mod. Phys. **70**, 1039 (1998).

[22] R. P. Feynman, R. B. Leighton, and M. Sands, *The Feynman Lectures on Physics* (Addison-Wesley, Reading, MA, 1966), Vol. 3.

[23] M. Holthaus, Floquet engineering with quasienergy bands of periodically driven optical lattices, J. Phys. B: At. Mol. Opt. Phys. **49**, 013001 (2016).

[24] C. J. Joachain, N. J. Kylstra, and R. M. Potvliege, *Atoms in Intense Laser Fields* (Cambridge University Press, Cambridge, 2011).

[25] N. Tomita and K. Nasu, Quantum fluctuation effects on light absorption spectra of the one-dimensional extended Hubbard model, Phys. Rev. B **63**, 085107 (2001).

[26] T. J. Park and J. C. Light, Unitary quantum time evolution by iterative Lanczos reduction, J. Chem. Phys. **85**, 5870 (1986).

[27] E. S. Smyth, J. S. Parker, and K. Taylor, Numerical integration of the time-dependent Schrödinger equation for laser-driven helium, Comput. Phys. Commun. **114**, 1 (1998).

[28] X. Guan, O. Zatsarinny, K. Bartschat, B. I. Schneider, J. Feist, and C. J. Noble, General approach to few-cycle intense laser interactions with complex atoms, Phys. Rev. A **76**, 053411 (2007).

[29] A. L. Frapiccini, A. Hamido, S. Schröter, D. Pyke, F. Mota-Furtado, P. F. O'Mahony, J. Madroñero, J. Eiglsperger, and B. Piraux, Explicit schemes for time propagating many-body wave functions, Phys. Rev. A **89**, 023418 (2014).

[30] S. Ghimire, A. D. DiChiara, E. Sistrunk, G. Ndabashimiye, U. B. Szafruga, A. Mohammad, P. Agostini, L. F. DiMauro, and D. A. Reis, Generation and propagation of high-order harmonics in crystals, Phys. Rev. A **85**, 043836 (2012).

[31] T. T. Luu, M. Garg, S. Y. Kruchinin, A. Moulet, M. T. Hassan, and E. Goulielmakis, Extreme ultraviolet high-harmonic spectroscopy of solids, Nature (London) **521**, 498 (2015).

[32] T. Millack and A. Maquet, Hyper-Raman lines produced during high harmonic generation, J. Mod. Opt. **40**, 2161 (1993).

[33] P. P. Corso, L. L. Cascio, and F. Persico, The role of hyper-Raman transitions in the radiation spectrum of a strongly driven two-level atom, J. Mod. Opt. **44**, 819 (1997).

[34] A. Di Piazza and E. Fiordilino, Why hyper-Raman lines are absent in high-order harmonic generation, Phys. Rev. A **64**, 013802 (2001).

[35] N. Moiseyev and M. Lein, Non-Hermitian quantum mechanics for high-order harmonic generation spectra, J. Phys. Chem. A **107**, 7181 (2003).

[36] E. Bloch, S. Beaulieu, D. Descamps, S. Petit, F. Légaré, A. Magunov, Y. Mairesse, and V. Strelkov, Hyper-Raman lines emission concomitant with high-order harmonic generation, New J. Phys. **21**, 073006 (2019).

[37] J. Sakurai and J. Napolitano, *Modern Quantum Mechanics* (Cambridge University Press, Cambridge, 2017).

[38] T. Oka, Nonlinear doublon production in a Mott insulator: Landau-Dykhne method applied to an integrable model, Phys. Rev. B **86**, 075148 (2012).

[39] N. Ben-Tal, N. Moiseyev, and A. Beswick, The effect of Hamiltonian symmetry on generation of odd and even harmonics, J. Phys. B: At., Mol. Opt. Phys. **26**, 3017 (1993).

PAPER II

Phys. Rev. A 109, 033110 (2024)

Paper information

By the terms and conditions of the American Physical Society's Reuse and Permissions License, the paper Digital Object Identifier (DOI) is provided: 10.1103/PhysRevA.109.033110. Reprinted with permission from C. S. Lange, Thomas Hansen, and L. B. Madsen, *Electron-correlation-induced nonclassicality of light from high-order harmonic generation*, Phys. Rev. A **109**, 033110 (2024).

Author contributions

I conducted the numerical simulations and contributed to the analysis and interpretation of the research findings. Additionally, I was involved in preparing the manuscript, including the creation of figures.

PHYSICAL REVIEW A **109**, 033110 (2024)

Editors' Suggestion

Electron-correlation-induced nonclassicality of light from high-order harmonic generation

Christian Saugbjerg Lange, Thomas Hansen, and Lars Bojer Madsen

Department of Physics and Astronomy, Aarhus University, Ny Munkegade 120, DK-8000 Aarhus C, Denmark

(Received 18 December 2023; accepted 26 February 2024; published 15 March 2024)

We study the effect of electron-electron correlations on the quantum state of the light emitted from high-harmonic generation (HHG). The quantum state of the emitted light is obtained by using a fully quantum-mechanical description of both the optical modes as well as the electronic system. This is different from the usual semiclassical description of HHG, which only treats the electronic target system quantum mechanically. Using the generic Fermi-Hubbard model, the strength of the electron-electron correlation can be treated as a parameter enabling us to investigate the two limiting cases of a completely uncorrelated phase and a correlated Mott-insulating phase. In the completely uncorrelated phase, the model reduces to a single-band tight-binding model in which only intraband currents contribute to the spectrum. In this limit, we analytically find that the emitted light is in a classical coherent state. In the Mott-insulating phase, a consideration of the photon statistics and squeezing of the emitted photonic state shows that the inter-Hubbard-subband current generates nonclassical light. In this sense, we show that electron-electron correlation can induce the generation of nonclassical states of light.

DOI: 10.1103/PhysRevA.109.033110

I. INTRODUCTION

High-harmonic generation (HHG) is a well-studied process in which a system (atom, molecule, solid) is driven by an intense laser field resulting in the emission of higher harmonics at integer values times the frequency of the laser. HHG has been observed in numerous experiments and has led to the field of attosecond physics [1] that was awarded the Nobel Prize in physics in 2023 [2–4]. The experimental progress has opened the door to study electron dynamics at their natural times scales as well as using the HHG spectrum to study the generating process within the HHG sample [1]. HHG in atomic and molecular gases is typically rationalized in terms of the three-step model [5–7], with ionization, propagation and recombination, and associated emission of light as essential elements. HHG in solids [8–10] can often be understood as originating from two different but coupled kinds of currents, namely, the inter- and intraband currents. Similarly to HHG in atoms, the interband current can be explained semiclassically by the three-step-model for HHG in band-gap materials [11–14]. In this model, (i) an electron is promoted to the conduction band due to the interaction with the driving field, leaving a hole in the valance band; (ii) both the electron and the hole are accelerated in their respective bands by the strong laser field; and (iii) the electron and hole can recombine, resulting in the emission of light. This process typically occurs in semiconductors with a valence band and at least one conduction band, which is why such a process cannot be included in one-band models. Intraband currents, on the other hand, can exist also in one-band models and emerge from the acceleration of an electron in the nonparabolic band of the solid. The two mechanisms are intrinsically coupled as the intraband mechanism is the second step in the three-step model for interband current generation.

Though the above-mentioned physical pictures have allowed for accurate descriptions of the emitted photonic spectrum and have found a wide range of applications, they are not entirely complete as they cannot account for a possible quantum-mechanical nature of the emitted light. In recent years, much attention has been given to the inclusion of a quantized electromagnetic field in the context of HHG both theoretically [15–29] and experimentally [28,30–32], merging the fields of strong-field physics and quantum optics. In this fully quantum-mechanical setting it was found that nonclassical states of light can be generated when including transitions between the initial and different final electronic states in atomic gasses, e.g., in a gas of helium atoms [17]. It was also found that a nonclassical catlike state, a coherent-state superposition (CSS), can be generated if one performs a conditional measurement subsequent to the HHG process as shown for both atomic gasses [19,26,28,32] and solids [20,21,29]. Furthermore, there have been investigations in the direction of a nonclassical driving field [22,23,27], which is also not possible within a conventional semiclassical framework. Investigating the quantum features of the emitted HHG light is not only of interest to fundamental research and understanding of the HHG process itself but is also important with regards to quantum information science, as a fully quantized theory could enable HHG to be a feasible way to reliably create nonclassical states of light (e.g., squeezed states, Fock states, CSS [33–35]). These could serve as a great resource in quantum technology [36,37] and quantum metrology [38,39] linking the fields of attosecond science and quantum information [19].

In parallel with these developments, there has recently been an increasing interest in HHG in correlated materials, that is, materials with a beyond mean-field electron-electron repulsion. These materials, including cuprates and high-temperature superconductors, are of great interest and they

can lead to a signal enhancement for certain harmonics [40–45]. HHG is hence relevant as a spectroscopic tool to resolve the dynamics of electrons in correlated materials. Mott insulators in particular have recently been investigated both theoretically [40–54] and experimentally [55–57], although not with quantum optical considerations. Generally, a correlated quantum system exhibits nonclassical behavior, motivating the use of correlations to generate nonclassical light in HHG. This is also indicated by recent theoretical studies where it has been shown that by preparing a gas of atoms in a highly correlated (superradiant) state nonclassical light was emitted from HHG [18]. It was also shown that including correlations between atoms can generate entangled and squeezed light [24] or entangled photon pairs [58]. In this paper, we focus on correlated materials and ask the question of how electron-electron correlations affect the generated photonic state. Specifically, we ask how the HHG spectrum in a fully quantum-mechanical calculation differs from semiclassical calculations when including electron correlations and how the presence of these correlations affects the photon statistics and squeezing of the emitted light, the latter two of which would not be possible to address in a usual semiclassical HHG setting.

To capture generic effects of electron correlation we use the prototypical Fermi-Hubbard model [59]. This model has been shown to capture important physical properties of real materials, such as cuprates, which include high-T_c superconductors [60,61]. In this model the on-site electron-electron correlation is included via the so-called Hubbard U term and the correlation strength can thus be treated as a changeable parameter allowing us to study how the quantum-mechanical nature of the generated light changes when increasing the correlation strength, U. This allows us to study both the uncorrelated phase and the highly correlated Mott-insulating phase where the electrons are highly real-space localized with only one electron per site as doubly occupied sites are energetically unfavorable.

The paper is organized as follows. In Sec. II the general fully quantum-mechanical theory and the Fermi-Hubbard model are presented as well as the measures of interest. Then in Sec. III we present the results for the two limiting cases of an uncorrelated phase and a Mott-insulating phase followed by a discussion in Sec. IV before summarizing and concluding in Sec. V. In the Appendices further details on the derivation and application of the formalism are given. Throughout this paper atomic units ($\hbar = m_e = 4\pi\epsilon_0 = e = 1$) are used unless explicitly stated otherwise.

II. THEORY

A. Quantum optical description of HHG

In this section, we describe a fully quantum-mechanical framework that includes the quantum optical state of the light emitted from an electronic system driven by an intense time-dependent electromagnetic field. The steps involved in this theory can be found, e.g., in Refs. [17,19]. We have chosen to include some details of the derivations to make the presentation self-contained. The theory goes beyond usual semiclassical HHG theory by considering the quantum state of both the emitted light and the coherent state of the driving laser. This quantum optical calculation consists of three parts. In the first step, the state of the laser is transformed into vacuum [62,63]. This in consequence separates the vector potential into a classical and a quantum part and is accompanied by a transformation of the time-dependent Schrödinger equation (TDSE). In the second step, the TDSE is solved for electrons driven only by the classical field. This is only possible due to the transformation performed in the first step and enables one to use conventional TDSE solvers as only the classical field is considered. Here we specifically calculate all transition currents and not only the time-dependent expectation value of the current. The third and final step is to integrate an equation of motion for the photonic state, which is coupled to the current generated by the response of the electrons to the classical part of the vector potential. From the photonic degrees of freedom one can calculate all expectation values of interest. This protocol will now be explained in greater detail.

We investigate a system driven by a multimode coherent-state laser, $|\psi_{\text{laser}}(t)\rangle = \otimes_{\boldsymbol{k},\sigma} |\alpha_{\boldsymbol{k}\sigma} e^{-i\omega_k t}\rangle$ where $\omega_k = c|\boldsymbol{k}|$ is the angular frequency with the wave number $\boldsymbol{k}$, c being the speed of light in vacuum, and σ the polarization. The distribution of the complex coherent-state parameters $\{\alpha_{\boldsymbol{k}\sigma}\}$ determines the properties of the field. We note that the coherent-state amplitude vanishes for modes far away from the laser mode, i.e., $\alpha_{\boldsymbol{k}\sigma} = 0$ for $\boldsymbol{k}, \sigma \gg \boldsymbol{k}_L, \sigma_L$ where $\boldsymbol{k}_L, \sigma_L$ is the wave number and polarization of the laser mode, respectively.

We consider a case where, under field-free conditions, N electrons move subject to an electrostatic potential $\hat{U}$ generated by other electrons and static nuclei. The state of the combined electronic and photonic system, denoted by $|\Psi(t)\rangle$, satisfies the TDSE

$$i\frac{\partial}{\partial t}|\Psi(t)\rangle = \hat{H}|\Psi(t)\rangle\,, \tag{1}$$

where the full Hamiltonian is given by $\hat{H} = \frac{1}{2}\sum_{j=1}^{N}(\hat{\boldsymbol{p}}_j + \boldsymbol{A})^2 + \hat{U} + \hat{H}_F$, where $\hat{\boldsymbol{p}}_j$ is the momentum operator for electron j, $\hat{U}$ is the potential accounting for the Coulomb interaction between the particles,

$$\hat{\boldsymbol{A}} = \sum_{\boldsymbol{k},\sigma} \frac{g_0}{\sqrt{\omega_k}}(\hat{\boldsymbol{e}}_\sigma \hat{a}_{\boldsymbol{k},\sigma} e^{i\boldsymbol{k}\cdot\boldsymbol{r}} + \hat{\boldsymbol{e}}^*_\sigma \hat{a}^\dagger_{\boldsymbol{k},\sigma} e^{-i\boldsymbol{k}\cdot\boldsymbol{r}}) \tag{2}$$

is the quantized vector potential, and

$$\hat{H}_F = \sum_{\boldsymbol{k},\sigma} \omega_k \hat{a}^\dagger_{\boldsymbol{k},\sigma}\hat{a}_{\boldsymbol{k},\sigma} \tag{3}$$

is the Hamiltonian for the free photonic field. In Eqs. (2) and (3) the effective coupling strength is denoted $g_0 = \sqrt{2\pi/V}$ with quantization volume V, $\boldsymbol{r}$ is the position, $\Sigma_{\boldsymbol{k},\sigma}$ is the sum over all photon momenta and polarizations with photon unit vector $\hat{\boldsymbol{e}}_\sigma$, and $\hat{a}_{\boldsymbol{k},\sigma}$ and $\hat{a}^\dagger_{\boldsymbol{k},\sigma}$ are the photonic annihilation and creations operators, respectively. In order to solve Eq. (1) we follow the same procedure as in Refs. [17,19] for a quantized electromagnetic field. The first step follows a transformation originally introduced by Ref. [62] and later used in the context of HHG [17,19,20,28,32], which is to transform away the laser field by considering the time-dependent unitary displacement

operator

$$\hat{D}(t) = \otimes_{\boldsymbol{k},\sigma} \hat{\mathcal{D}}[\alpha_{\boldsymbol{k}\sigma}(t)] \tag{4}$$

with

$$\hat{\mathcal{D}}[\alpha_{\boldsymbol{k},\sigma}(t)] = \exp[\alpha_{\boldsymbol{k}\sigma}(t)\hat{a}^\dagger_{\boldsymbol{k},\sigma} - \alpha^*_{\boldsymbol{k}\sigma}(t)\hat{a}_{\boldsymbol{k},\sigma}], \tag{5}$$

with $\alpha_{\boldsymbol{k},\sigma}(t) = \alpha_{\boldsymbol{k},\sigma} e^{-i\omega_k t}$ such that $\hat{D}^\dagger(t)\,|\psi_{\text{laser}}(t)\rangle = |0\rangle$. Due to this transformation the vector potential $\hat{\boldsymbol{A}}$ now splits up into a classical part $\boldsymbol{A}_{\text{cl}}(t) = \langle\psi_{\text{laser}}(t)|\,\hat{\boldsymbol{A}}\,|\psi_{\text{laser}}(t)\rangle$ as well as a quantum part:

$$\hat{\boldsymbol{A}}_Q = \sum_{\boldsymbol{k},\sigma} \frac{g_0}{\sqrt{\omega_k}} (\hat{\boldsymbol{e}}_\sigma \hat{a}_{\boldsymbol{k},\sigma} e^{i\boldsymbol{k}\cdot\boldsymbol{r}} + \hat{\boldsymbol{e}}^*_\sigma \hat{a}^\dagger_{\boldsymbol{k},\sigma} e^{-i\boldsymbol{k}\cdot\boldsymbol{r}}). \tag{6}$$

Consequently, the Hamiltonian is now separated into three parts:

$$\hat{\tilde{H}}(t) = \hat{H}_{\text{TDSE}}(t) + \hat{V}(t) + \hat{H}_F, \tag{7}$$

where $\hat{H}_{\text{TDSE}}(t) = \sum_{j=1}^N \frac{1}{2}[\hat{\boldsymbol{p}}_j + \boldsymbol{A}_{\text{cl}}(t)]^2 + \hat{U}$ is the Hamiltonian governing the electronic system subject to a classical driving, $\hat{V}(t) = \sum_{j=1}^N \hat{\boldsymbol{A}}_Q \cdot [\hat{\boldsymbol{p}}_j + \boldsymbol{A}_{\text{cl}}(t)]$ is the electronic interaction with the quantum field, and $\hat{H}_F$ is the free-field Hamiltonian given in Eq. (3). In Eq. (7) a tilde has been used on the left-hand site to denote the fact that the Hamiltonian is transformed due to the application of the displacement operator in Eq. (4). A full derivation of the result in Eq. (7) can be found in the Supplementary Information of Ref. [17] and is included in Appendix A for completeness.

The full Hamiltonian in Eq. (7) is now further transformed by going to a rotating frame with respect to $\hat{H}_{\text{TDSE}}(t)$ and $\hat{H}_F$, i.e., by applying the unitary time evolution operator $\hat{\mathcal{U}}_0^\dagger(t,t_0) = \hat{\mathcal{U}}^\dagger_{\text{TDSE}}(t,t_0)\cdot\hat{\mathcal{U}}^\dagger_F(t,t_0)$ with t_0 being the initial time such that

$$|\tilde{\Psi}(t)\rangle_I = \hat{\mathcal{U}}_0^\dagger(t,t_0)\,|\tilde{\Psi}(t)\rangle_S\,, \tag{8}$$

where the subscripts refer to the frame of reference with S denoting the Schrödinger picture and I the interaction picture. The transformation in Eq. (8) separates the dynamics of the classical and quantum parts of the electromagnetic potential and transforms the TDSE into

$$i\frac{\partial}{\partial t}\,|\tilde{\Psi}(t)\rangle_I = \hat{V}_I(t)\,|\tilde{\Psi}(t)\rangle_I\,, \tag{9}$$

with

$$\begin{aligned}\hat{V}_I(t) = {}& \hat{\mathcal{U}}_F^\dagger(t,t_0)\,\hat{\boldsymbol{A}}_Q\,\hat{\mathcal{U}}_F(t,t_0)\\ & \cdot\hat{\mathcal{U}}^\dagger_{\text{TDSE}}(t,t_0)\,\hat{\boldsymbol{j}}(t)\,\hat{\mathcal{U}}_{\text{TDSE}}(t,t_0)\end{aligned} \tag{10}$$

where we have defined the current operator $\hat{\boldsymbol{j}}(t) = \Sigma_{j=1}^N[\hat{\boldsymbol{p}}_j + \boldsymbol{A}_{\text{cl}}(t)]$ and where the tilde denotes that the state is displaced with respect to the laser modes. The quantized vector potential in the rotating frame within the dipole approximation is given by

$$\begin{aligned}\hat{\boldsymbol{A}}_{Q,I}(t) &= \hat{\mathcal{U}}_0^\dagger(t,t_0)\,\hat{\boldsymbol{A}}_Q\,\hat{\mathcal{U}}_0(t,t_0) = \hat{\mathcal{U}}_F^\dagger(t,t_0)\,\hat{\boldsymbol{A}}_Q\,\hat{\mathcal{U}}_F(t,t_0)\\ &= \sum_{\boldsymbol{k},\sigma}\frac{g_0}{\sqrt{\omega_k}}\big[\hat{\boldsymbol{e}}_\sigma\hat{a}_{\boldsymbol{k},\sigma}e^{-i\omega_k(t-t_0)} + \hat{\boldsymbol{e}}^*_\sigma\hat{a}^\dagger_{\boldsymbol{k},\sigma}e^{i\omega_k(t-t_0)}\big].\end{aligned} \tag{11}$$

We rewrite the right-hand side of Eq. (10) by utilizing that an electronic state $|\phi_m\rangle$ is time evolved via

$$|\phi_m(t)\rangle = \hat{\mathcal{U}}_{\text{TDSE}}(t,t_0)\,|\phi_m(t_0)\rangle\,. \tag{12}$$

By inserting identity operators $\mathbb{1} = \Sigma_m\,|\phi_m\rangle\,\langle\phi_m|$ into Eq. (10) and using the definition in Eq. (12) we then express the interaction as

$$\hat{V}_I(t) = \sum_{m,n}\hat{\boldsymbol{A}}_{Q,I}(t)\cdot\boldsymbol{j}_{m,n}(t)\,|\phi_m\rangle\,\langle\phi_n|\,, \tag{13}$$

where we have defined the matrix element

$$\boldsymbol{j}_{m,n}(t) = \langle\phi_m(t)|\,\hat{\boldsymbol{j}}(t)\,|\phi_n(t)\rangle\,, \tag{14}$$

which is referred to as the transition current between two electronic states. Thus, the second step in the quantum optical protocol is to obtain a set of electronic states $\{|\phi_m(t)\rangle\}$ for all times using standard TDSE solving techniques to solve

$$i\frac{\partial}{\partial t}\,|\phi_m(t)\rangle = \hat{H}_{\text{TDSE}}(t)\,|\phi_m(t)\rangle\,, \tag{15}$$

where $|\phi_m(t)\rangle$ is a wave packet starting out in the mth state for the electronic part of the problem. The choice of basis, $\{|\phi_m(t)\rangle\}$, is in principle completely arbitrary. We have chosen the basis to be the eigenstates of the field-free Hamiltonian of the electronic system, as it enables the use of conventional numerical tools to solve the TDSE.

In the present paper, we investigate how correlations in a generic correlated material described by the Fermi-Hubbard model affect the emitted photonic state produced by HHG. To that end, we now specify the electronic Hamiltonian to be the field-driven Fermi-Hubbard Hamiltonian, i.e., $\hat{H}_{\text{TDSE}}(t) \to \hat{H}_{\text{FH}}(t)$. Specifically, we consider the one-dimensional, one-band Fermi-Hubbard model at half filling with periodic boundary conditions and with an equal number of spin-up and spin-down electrons to keep the whole system spin neutral. This model is chosen as it allows us to treat the correlation strength U as a parameter to study the effects of correlations. The system is driven by a classical laser pulse such that the system within the dipole approximation is described by the time-dependent Hamiltonian [59]

$$\hat{H}_{\text{FH}}(t) = \hat{H}_{\text{hop}}(t) + \hat{H}_U\,, \tag{16}$$

with

$$\hat{H}_{\text{hop}}(t) = -t_0\sum_{j,\mu}\big(e^{ia\boldsymbol{A}_{\text{cl}}(t)}\hat{c}^\dagger_{j,\mu}\hat{c}_{j+1,\mu} + \text{H.c.}\big), \tag{17}$$

$$\hat{H}_U = U\sum_j(\hat{c}^\dagger_{j,\uparrow}\hat{c}_{j,\uparrow})(\hat{c}^\dagger_{j,\downarrow}\hat{c}_{j,\downarrow}), \tag{18}$$

where t_0 is the hopping matrix element for an electron to move to the nearest-neighboring sites, i.e., from site j to site $j\pm1$; $A_{\text{cl}}(t)$ is the classical vector potential of the driving field along the lattice dimension; a is the lattice spacing; and U is the beyond mean-field onsite electron-electron repulsion. The fermionic creation (annihilation) operator for an electron on site j with spin $\mu\in\{\uparrow,\downarrow\}$ is denoted $\hat{c}^\dagger_{j,\mu}$ ($\hat{c}_{j,\mu}$). We work with nearest-neighbor hopping, which is the common limit of this model [43–45]. Inclusion of multiple bands and beyond-nearest-neighbor hopping terms becomes numerically very demanding. Note that each term in the sum in Eq. (18) counts the number of electrons on site j. In the

Fermi-Hubbard model, the current operator is explicitly given as

$$\hat{\boldsymbol{j}}(t) = -iat_0 \sum_{j,\mu} \left(e^{iaA_{\rm cl}(t)}\hat{c}^\dagger_{j,\mu}\hat{c}_{j+1,\mu} - \text{H.c.}\right)\hat{\boldsymbol{x}}, \tag{19}$$

which is in the direction of the Fermi-Hubbard chain taken to be the x direction; see Appendix B.

We are now ready to solve Eq. (9). To that end, it is convenient to expand the full state of the electronic and photonic degrees of freedom in terms of field-free electronic eigenstates:

$$|\tilde{\Psi}(t)\rangle_I = \sum_m |\tilde{\chi}^{(m)}(t)\rangle\, |\phi_m\rangle\,, \tag{20}$$

where m is the index corresponding to the mth electronic state and $|\tilde{\chi}^{(m)}(t)\rangle$ is the photonic state associated with the electronic state $|\phi_m\rangle$. Note that normalization of the state in Eq. (20) requires $\Sigma_m \langle\tilde{\chi}^{(m)}(t)\,|\tilde{\chi}^{(m)}(t)\rangle = 1$. The choice of basis in Eq. (20) can be completely arbitrary but it is convenient to expand in the same basis as the one used in Eq. (13) as we will exploit the orthogonality between basis states in the following. We now insert Eq. (20) into the transformed TDSE in Eq. (9), project onto $\langle\phi_m|$, write out $\hat{\boldsymbol{A}}_{Q,I}(t)$ explicitly, and obtain the following equation of motion for the emitted photonic field:

$$i\frac{\partial}{\partial t}|\tilde{\chi}^{(m)}(t)\rangle = \sum_{\boldsymbol{k},\sigma} \frac{g_0}{\sqrt{\omega_k}}\left[\hat{\boldsymbol{e}}_\sigma \hat{a}_{\boldsymbol{k},\sigma} e^{-i\omega_k t} + \hat{\boldsymbol{e}}^*_\sigma \hat{a}^\dagger_{\boldsymbol{k},\sigma} e^{i\omega_k t}\right] \cdot \sum_n \boldsymbol{j}_{m,n}(t)\,|\tilde{\chi}^{(n)}(t)\rangle\,, \tag{21}$$

where we have taken $t_0 = 0$ for convenience. Equation (21) has the same structure as the equations derived for the atomic case in Refs. [17,19,20,24,32] and it is in general difficult to solve as it couples all frequency modes and all electronic states. To proceed we now assume that each frequency component can be treated independently (that is, assuming no coupling between the different harmonics [17]), yielding the equation

$$i\frac{\partial}{\partial t}\left|\tilde{\chi}^{(m)}_{\boldsymbol{k}\sigma}(t)\right\rangle = \frac{g_0}{\sqrt{\omega_k}}\left[\hat{\boldsymbol{e}}_\sigma \hat{a}_{\boldsymbol{k},\sigma} e^{-i\omega_k t} + \hat{\boldsymbol{e}}^*_\sigma \hat{a}^\dagger_{\boldsymbol{k},\sigma} e^{i\omega_k t}\right] \cdot \sum_n \boldsymbol{j}_{m,n}(t)\left|\tilde{\chi}^{(n)}_{\boldsymbol{k}\sigma}(t)\right\rangle, \tag{22}$$

where $|\tilde{\chi}^{(m)}_{\boldsymbol{k}\sigma}(t)\rangle$ is the frequency component with wave number $\boldsymbol{k}$ and polarization σ of the photonic state associated to the field-free electronic eigenstate $|\phi_m\rangle$. The integration of Eq. (21) or (22) is the third step in the quantum optical description of HHG, and by using the full state of the system in Eq. (20) expectation values of interest can be calculated. Details on the calculation of expectation values are given in Appendix C.

We emphasize that Eq. (21) [or equivalently Eq. (22)] is the central equation in this fully quantum-mechanical framework, highlighting that it is not only the classical current, $\boldsymbol{j}_{i,i}(t)$ with i being the initial state [see Eq. (14)], that contributes to the photonic quantum state. In fact, for the system considered in this paper, we find that other elements of this transition current, $\boldsymbol{j}_{n,m}(t)$, are significantly greater than the classical contribution as seen in Fig. 1 where Fourier-transformed transition currents, $\tilde{\boldsymbol{j}}_{n,m}(\omega)$, are shown. At first glance, this may indicate that many transition currents contribute more than $\langle\boldsymbol{j}(t)\rangle = \boldsymbol{j}_{1,1}(t)$. However, as seen from Eqs. (21) and (22) the transition currents (together with g_0) determine how much population is transferred to a given state. As we take the initial condition to be the vacuum state associated with the electronic ground state, i.e., $|\tilde{\chi}^{(m)}_{\boldsymbol{k}\sigma}(t_0)\rangle = \delta_{m,i}\,|0\rangle$, and the coupling is in general weak (determined by g_0) most of the population remains in the photonic state associated with the initial electronic state. Note also that this formalism can be used to calculate the quantum features of any system once $\boldsymbol{j}_{n,m}(t)$ is known for all n and m. As will be shown in Sec. III, it is the inclusion of these off-diagonal transition currents that can potentially generate nonclassical light.

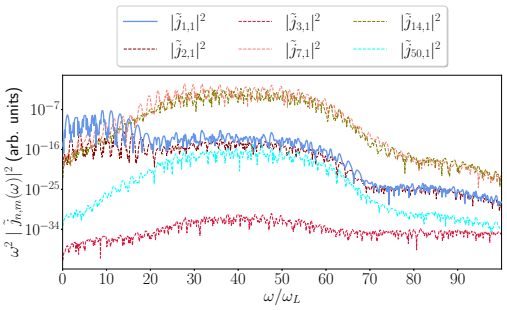

FIG. 1. The norm squared of the time derivative of the Fourier-transformed current, $\tilde{j}_{n,m}(\omega)$, for various transition currents. Note that some elements are comparable to or even larger than the classical current element, $\tilde{j}_{1,1}(\omega)$ (solid blue line). The results shown are for a Fermi-Hubbard model with $U = 10t_0$ and the parameters specified in the main text.

In other works further approximations have been made on the transition currents. For instance, the strong-field approximation (SFA) has been made to neglect transitions between excited states (or continuum-continuum transitions for atoms) [19,32], and a Markov-type approximation has been performed on the photonic state [24], allowing for an analytical solution of Eq. (21). However, we do not pursue this further here.

In the results presented in this paper, we use a one-dimensional lattice of $L = 8$ sites with periodic boundary conditions, a lattice spacing of $a = 7.5589$ a.u., and $t_0 = 0.0191$ a.u. picked to fit those of the cuprate Sr_2CuO_3 [64] as done previously in Refs. [40,43,44]. We use a linearly polarized pulse with polarization along the lattice dimension with $N_c = 10$ cycles and a $\sin^2$ envelope function in the dipole approximation

$$A_{\rm cl}(t) = A_0 \sin(\omega_L t + \pi/2)\sin^2\left(\frac{\omega_L t}{2N_c}\right). \tag{23}$$

Here, the vector potential amplitude is $A_0 = F_0/\omega_L = 0.194$ a.u. with the angular frequency $\omega_L = 0.005$ a.u. $= 33$ THz. With these choices the field strength, F_0, corresponds to a peak intensity of 3.3×10^{10} W/cm^2. To study the effects of

correlations, we treat the strength of the on-site electron-electron correlation, U, as a parameter. We solve the TDSE in Eq. (15) for all states $\{|\phi_m(t)\rangle\}$ using the Arnoldi-Lancoz algorithm [65–68] with a Krylov subspace dimension of 4. As this fully quantum-mechanical theory requires all time evolved states of the electronic system, $\{|\phi_m(t)\rangle\}$, it is computationally more demanding than the usual semiclassical calculation, limiting us to consider at most $L = 8$ electrons in the model. We found consistent results for smaller systems with $L = 4, 6$ electrons. Furthermore, to limit the dimensionality of the system, we utilize that the Hamiltonian in Eq. (16) possesses spin-flip symmetry and is invariant under translations of the entire system corresponding to conservation of the total crystal momentum [59]. The initial state is the spin-symmetric ground state with vanishing total crystal momentum, and due to the symmetries of the Hamiltonian only couplings to states within that subspace are needed.

B. Measures

Using a fully quantum-mechanical approach to calculate the quantum state of the emitted HHG allows one to calculate other measures than just the spectrum, which is the primary observable in usual HHG approaches. Particularly, since the photon distribution in each mode is obtained within this theory, the photon statistics of the emitted state can be calculated, enabling the study of nonclassicality in HHG. In this paper, we follow Ref. [17] to calculate the photonic spectrum, the Mandel Q parameter, and the squeezing of the photonic state, which we will explain in the following.

The spectrum can be calculated in the following way. The total energy of the emitted field after the HHG process is given by $\epsilon = \Sigma_{\boldsymbol{k},\sigma}\omega_k\langle\hat{n}_{\boldsymbol{k},\sigma}\rangle$, where $\hat{n}_{\boldsymbol{k},\sigma} = \hat{a}^\dagger_{\boldsymbol{k},\sigma}\hat{a}_{\boldsymbol{k},\sigma}$ is the photonic counting operator, and where we for simplicity have denoted $\langle\hat{n}_{\boldsymbol{k},\sigma}\rangle = {}_I\langle\tilde{\Psi}(\infty)|\hat{\mathcal{U}}_0^\dagger\,\hat{n}_{\boldsymbol{k},\sigma}\,\hat{\mathcal{U}}_0\,|\tilde{\Psi}(\infty)\rangle_I$ and include $\hat{\mathcal{U}}_0$ as the state is in a rotating frame as seen from Eq. (8). By taking the continuum limit, $\sum_{\boldsymbol{k}} \to V/(8c^3\pi^3)\int d\Omega d\omega\omega^2$, where V is the quantization volume, one can calculate the energy per frequency per solid angle:

$$S(\omega) \equiv \frac{d\epsilon}{d\omega d\Omega} = \frac{\omega^3}{g_0^2(2\pi)^2c^3}\langle\hat{n}_{\boldsymbol{k},\sigma}\rangle, \tag{24}$$

which we will refer to as the spectrum. To illustrate the effect of the quantum description of the photonic degrees of freedom, we also consider the conventional semiclassical prediction of the spectrum [69]:

$$S_{\rm cl}(\omega) = \omega^2|\tilde{\boldsymbol{j}}_{i,i}(\omega)|^2 \tag{25}$$

where $\tilde{\boldsymbol{j}}_{i,i}(\omega)$ is the Fourier transform of the classical current which in the present case is obtained from the time evolved ground state $|\phi_1(t)\rangle$ used in Eq. (14).

We note that the spectrum in Eq. (24) only contains the first moment of the photon counting operator, which does not reveal all the statistical properties of the underlying distribution from which it was calculated. Information about the photon statistics of the generated light is hence not found in the spectrum. The statistical properties of the generated light can instead be quantified via the so-called Mandel Q parameter. For a single mode it is given by [70]

$$Q_{\boldsymbol{k},\sigma} = \frac{\langle\hat{n}^2_{\boldsymbol{k},\sigma}\rangle - \langle\hat{n}_{\boldsymbol{k},\sigma}\rangle^2}{\langle\hat{n}_{\boldsymbol{k},\sigma}\rangle} - 1. \tag{26}$$

If $Q_{\boldsymbol{k},\sigma} > 0$ the photon statistics is called super-Poissonian while for $Q_{\boldsymbol{k},\sigma} < 0$ it is called sub-Poissonian, referring to a broader and narrower distribution than a Poissonian distribution, respectively. Note that a classical coherent state will have $Q_{\boldsymbol{k},\sigma} = 0$ as it has Poissonian statistics. While only a nonclassical state can produce sub-Poissonian statistics, both classical mixtures of coherent states, thermal states as well as nonclassical states can have super-Poissonian photon statistics. In other words, a super-Poissonian statistics is not necessarily a quantum feature [70]. The last measure of interest in this paper is the degree of squeezing, which is a clear nonclassical feature of light. The degree of squeezing in the unit of dB is given as [71,72]

$$\eta_{\boldsymbol{k},\sigma} = -10\log\left\{4\min_{\theta\in[0,\pi)}[\Delta X_{\boldsymbol{k},\sigma}(\theta)]^2\right\}, \tag{27}$$

where the minimum is found over angles $0 \leqslant \theta < \pi$ that minimizes the variance in the generalized quadrature operator $\hat{X}_{\boldsymbol{k},\sigma}(\theta) = (\hat{a}_{\boldsymbol{k},\sigma}e^{-i\theta} + \hat{a}^\dagger_{\boldsymbol{k},\sigma}e^{i\theta})/2$. We note that classical coherent light is not squeezed, i.e., $\eta_{\boldsymbol{k},\sigma} = 0$ for all modes and polarizations for coherent light.

Experimentally, one can measure the degree of squeezing with a homodyne detection scheme [70,73,74] and the Mandel Q parameter can be obtained by photon counting [75,76].

III. RESULTS

We now use this fully quantum-mechanical framework to study the harmonics generated by the field-driven Fermi-Hubbard model in two limiting cases, namely, the completely uncorrelated phase ($U = 0$) and a Mott-insulating phase ($U = 10t_0$). These cases are chosen as the dynamics is governed by two different mechanisms and the limiting cases allow us to present qualitatively physical pictures to explain the results. Additionally, the Mott-insulating phase will highlight the role of electron-electron correlations in the generation of nonclassical light when compared to the uncorrelated phase.

A. Uncorrelated phase

1. Qualitative physical picture

As a limiting case we consider a system without correlations, i.e., $U = 0$, as it allows for an exact analytic solution. In this case, the Fermi-Hubbard Hamiltonian reduces to a simple one-band tight-binding model described by the hopping Hamiltonian, $\hat{H}_{\rm hop}(t)$ in Eq. (17). Equation (17) can be diagonalized by transforming the creation operators as follows:

$$\hat{c}^\dagger_{j,\mu} = \frac{1}{\sqrt{L}}\sum_q e^{-iqR_j}\hat{c}^\dagger_{q,\mu}, \tag{28}$$

with a similar expression for the annihilation operators. Here R_j denotes the jth lattice position and q is the crystal momentum of the particle. The transformation reflects a shift from real space to momentum space corresponding to a shift from an underlying localized Wannier basis to a spatially delocalized Bloch basis. The result for $\hat{H}_{\rm hop}(t)$ in terms of the

new operators reads

$$\hat{H}_{\rm hop}(t) = \sum_{q,\mu} \mathcal{E}[q + A_{\rm cl}(t)] \hat{c}^\dagger_{q,\mu} \hat{c}_{q,\mu}, \tag{29}$$

with the dispersion relation describing the Bloch band given as

$$\mathcal{E}(q) = -2t_0 \cos(aq). \tag{30}$$

That is, the individual crystal momenta of the electrons are conserved and have a time-dependent dispersion determined by $A_{\rm cl}(t)$. Note that the energy bandwidth is

$$\Delta_{\rm band} = 4t_0 \tag{31}$$

as seen in Eq. (30).

2. Results

One can show that $[\hat{H}_{\rm hop}(t), \hat{\boldsymbol{j}}(t)] = 0$, which allows for a shared set of eigenstates. As the Hamiltonian also commutes with itself at different times, the time evolution operator is simply given as $\hat{\mathcal{U}}_{\rm hop}(t, t_0) = \exp[-i \int_{t_0}^{t} \hat{H}_{\rm hop}(t')dt']$ and it then follows that $[\hat{\mathcal{U}}_{\rm hop}(t, t_0), \hat{\boldsymbol{j}}(t)] = 0$. Because of these relations, all off-diagonal elements of the current vanish, i.e.,

$$\begin{aligned} \boldsymbol{j}_{m,n}(t) &= \langle \phi_m(t_0) | \hat{\mathcal{U}}^\dagger_{\rm hop}(t, t_0) \hat{\boldsymbol{j}}(t) \hat{\mathcal{U}}_{\rm hop}(t, t_0) | \phi_n(t_0) \rangle \\ &= \boldsymbol{j}_{n,n}(t) \delta_{m,n}, \end{aligned} \tag{32}$$

where it was used that $|\phi_n(t)\rangle$ is an eigenstate for the current operator. Equation (32) consequently decouples all the electronic states in Eq. (21). As the initial state prior to interaction with the laser is the field-free ground state, $|\phi_i(t_0)\rangle$, and there is no coupling to states $|\phi_m(t)\rangle$ with $m \neq i$, only $|\phi_i(t)\rangle$ is populated throughout the dynamics. That is, the equation of motion for the photonic state is now simply given as

$$\begin{aligned} i\frac{\partial}{\partial t} |\tilde{\chi}^{(i)}(t)\rangle = \sum_{\boldsymbol{k},\sigma} \frac{g_0}{\sqrt{\omega_k}} [\hat{\boldsymbol{e}}_\sigma \hat{a}_{\boldsymbol{k},\sigma} e^{-i\omega_k t} + \hat{\boldsymbol{e}}^*_\sigma \hat{a}^\dagger_{\boldsymbol{k},\sigma} e^{i\omega_k t}] \\ \cdot \boldsymbol{j}_{i,i}(t) |\tilde{\chi}^{(i)}(t)\rangle . \end{aligned} \tag{33}$$

As Eq. (33) is linear in the photonic creation and annihilation operators, it can be solved analytically [71]:

$$|\tilde{\chi}^{(i)}(t)\rangle = \otimes_{\boldsymbol{k},\sigma} \hat{\mathcal{D}}\big[\beta^{(i)}_{\boldsymbol{k},\sigma}(t)\big] |0\rangle , \tag{34}$$

where $\hat{\mathcal{D}}$ is the unitary displacement operator for the photonic field given in Eq. (5) and $\beta^{(i)}_{\boldsymbol{k},\sigma}(t)$ is the time-dependent coherent-state amplitude given by

$$\beta^{(i)}_{\boldsymbol{k},\sigma}(t) = -i\frac{g_0}{\sqrt{\omega_k}} \int_{t_0}^{t} e^{i\omega_k t'} \boldsymbol{j}_{i,i}(t') \cdot \hat{\boldsymbol{e}}^*_\sigma dt'. \tag{35}$$

This result is to be expected as the emitted light is generated by a classical current, $\langle \hat{\boldsymbol{j}} \rangle = \boldsymbol{j}_{i,i}$, and consequently the emitted HHG is a multimode coherent state. The mean photon number for a coherent state is readily evaluated $\langle \hat{n}_{\boldsymbol{k},\sigma} \rangle = |\beta^{(i)}_{\boldsymbol{k},\sigma}(t)|^2$, and using Eq. (24) it is found that the HHG spectrum for $U = 0$ is given by (taking $t \to \infty$)

$$S(\omega) = \frac{\omega^2}{(2\pi)^2 c^3} |\tilde{j}_{i,i}(\omega)|^2, \tag{36}$$

where $\tilde{j}_{i,i}(\omega)$ is the Fourier-transformed current. This result is identical to the classical spectrum in Eq. (25), proving that no quantum optical considerations are necessary when studying the uncorrelated phase. The spectrum can be seen in Fig. 2 where peaks are found at only odd harmonics as expected. We note that since the emitted HHG is in a coherent state it shows no nonclassical nature, and hence $Q_{\boldsymbol{k},\sigma} = \eta_{\boldsymbol{k},\sigma} = 0$ for all wave numbers and polarizations. We can thus conclude that in the uncorrelated phase, no quantum optical considerations are needed as usual semiclassical calculations are exact. We note that in the uncorrelated limit the inclusion of beyond-nearest-neighbor hopping would not change the classicality of the emitted light as these terms would simply modify the dispersion in Eq. (30). The hopping Hamiltonian in Eq. (29) would still remain diagonal in crystal momentum space and hence commute with the current operator.

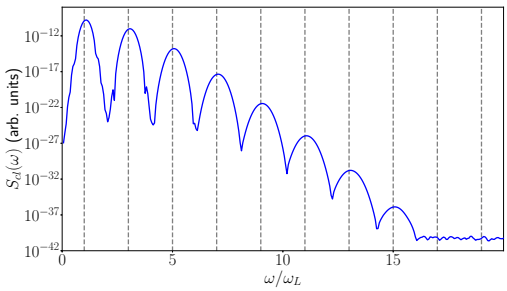

FIG. 2. HHG spectrum for the uncorrelated $U = 0$ case calculated via Eq. (36). Parameters for the system are given in the main text. The dashed lines are placed at odd harmonics to guide the eye. See text in Sec. II A for laser and system parameters.

A few additional notes for the uncorrelated phase are worth making. First, we find that a perturbative calculation to first order in $\hat{\boldsymbol{A}}_Q$, limiting the total state to contain at most one photon as done in Ref. [17], interestingly yields the exact analytical result for the spectrum though the photon distribution is a superposition of vacuum and one-photon modes and is hence not Poissonian. See Appendix D for details. Moreover, we find that even though the spectrum is peaked only at odd harmonics, we observe that during the interaction with the laser $\langle \hat{n}_{\boldsymbol{k},\sigma} \rangle(t) \neq 0$ also for even harmonics. Of course, due to the symmetry of the electronic system and laser, no peaks at even harmonics are observed in the final spectrum. See Appendix E for details. As a final note, one can perform a subsequent condition measurement of the emitted HHG signal. Due to the quantum back-action of this measurement, the state is no longer a single multimode coherent state but is a superposition of coherent states (similar to a cat state) as found in Refs. [19,21,28,32]. We will not discuss conditional measurement schemes further in the present paper.

B. Mott-insulating phase

1. Qualitative physical picture

We now investigate the so-called Mott-insulating phase where $U \gg t_0$ and where we use $U = 10t_0$ in the calculations. In Fig. 3 all the eigenenergies for the field-free Hamiltonian with $U = 10t_0$ are shown. Here we see how the spectrum is

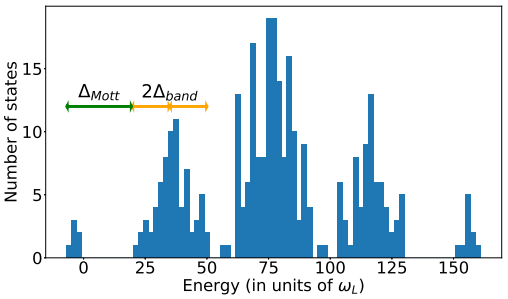

FIG. 3. The spectrum of the field-free Fermi-Hubbard model in the Mott-insulating phase with $U = 10t_0$ and parameters in the main text. We note how the spectrum is separated into so-called Hubbard subbands. The characteristic energies are given by the Mott gap $\Delta_{\text{Mott}} = 26.7\omega_L$ [Eq. (37)] (green arrow) and the bandwidth $\Delta_{\text{band}} = 4t_0 = 15.3\omega_L$ [Eq. (31)] (orange arrows).

grouped into the so-called Hubbard subbands [59]. We refer to the left most subband in Fig. 3 as the first subband, the second most left subband as the second subband, and so on. The energy difference between the ground state and the second subband is given by the Mott gap (green arrow) [59,77,78]:

$$\Delta_{\text{Mott}} = E_{\text{GS}}^{L+1} + E_{\text{GS}}^{L-1} - 2E_{\text{GS}}^{L}. \tag{37}$$

Here E_{GS}^{n} denotes the ground-state energy containing n electrons on a lattice with L sites. Further discussion can be found in Ref. [44]. The ground state of the system is dominated largely by configurations with only single site occupations as it requires a relatively large energy to have a doubly occupied site [41,42,44,45]. The Mott-insulating phase is therefore best analyzed in a quasiparticle picture with doublons (doubly occupied sites) and holons (empty sites). The states in the lowest-lying subband (most left band in Fig. 3) contain virtually no doublon-holon pairs while the states in the second subband are dominated by configurations that contain a single doublon-holon pair. Hence, the Mott gap in Eq. (37) approximates how much energy is needed to create a doublon-holon pair from the ground state. Furthermore, we note that the width of the second subband is approximately $2\Delta_{\text{band}}$ (orange arrows in Fig. 3), which is due to the fact that both the doublon and the holon can propagate within the band, each with an identical bandwidth similar to Δ_{band}. Details on the spectrum of the Mott-insulating phase are discussed further in Refs. [45,59,79].

Neglecting scattering between doublons and holons, we can qualitatively describe the HHG process in the Mott-insulating phase in a similar three-step model as the one for multiband models presented in Sec. I, where doublons now are analogous to electrons and holons are analogous to electron holes [45]. This three-step model for Mott insulators is described by the following.

(i) The creation of a doublon-holon pair as the external laser now transfers population from the ground state in the first subband to a state in the second subband. The two bands are energetically separated by Δ_{Mott} as seen in Fig. 3.

(ii) The doublon-holon pair then propagates within the second subband by coupling to different states in that subband whose eigenenergies are closely spaced when compared to Δ_{Mott} as seen in Fig. 3.

(iii) Finally, the doublon-holon pair recombines (annihilates), emitting a high-harmonic photon populating one of the states in the first subband.

The intraband current in step (ii) originates from both the doublon and holon propagating in their respective bands with a width similar to Δ_{band} and hence intraband harmonics can at most have an energy of Δ_{band}. The width of $2\Delta_{\text{band}}$ in the second subband in Fig. 3 comes from the fact that it contains both the holon and doublon band. Transitions from states in the top to the bottom of the second Hubbard subband in Fig. 3 are multielectron transitions which are not the dominant contributions to the intraband current. Interband harmonics originating from step (iii) are restricted to have an energy between Δ_{Mott} and $\Delta_{\text{Mott}} + 2\Delta_{\text{band}}$ as this is the smallest and largest possible energy when coupling from a state within the second subband to the ground state, respectively.

2. Results

With this physical picture in mind, we are now ready to look at the spectrum, the Mandel Q parameter, and the squeezing parameter for the Mott-insulating phase. We obtain the following results by integrating Eq. (22) for each harmonic mode with a frequency spacing of $\omega/\omega_L = 0.1$ with a fourth-order Runge-Kutta routine. In Fig. 4(a) the spectrum [Eq. (24)] is shown (blue line). The vertical dashed lines indicate selected frequencies of interest and the vertical dotted lines are placed at odd harmonic orders. The vertical solid black lines are placed at Δ_{band}, Δ_{Mott}, and $\Delta_{\text{Mott}} + 2\Delta_{\text{band}}$, respectively.

In Fig. 4(a), we find well-defined peaks at odd harmonics up until $\omega/\omega_L \approx 21$. These harmonics originate from the doublon-holon intraband current. For harmonics above this value we note an increasing signal which we attribute mainly to the interband current. We also note that the higher-lying peaks are not as clear as the lower ones, which is due to the length of the laser pulse. The less clear peaks are thus not a consequence of the quantum optical considerations as has previously been seen in usual semiclassical HHG calculations [44,45,80], and are indeed also present in the semiclassical result [Eq. (25)] shown by the dashed curve in Fig. 4(a). These peaks at noninteger harmonics are due to the laser pulse populating multiple Floquet states which generate noninteger harmonics at certain frequencies; a comprehensive analysis of this aspect of the HHG spectrum will be given elsewhere. The good agreement between the spectrum obtained by including quantum optical theory and the semiclassical spectrum shows that the quantum nature of the generated light cannot be seen clearly from HHG spectra.

Fortunately, using a quantum optical description allows one to investigate nonclassical properties through the calculation of, e.g., the Mandel Q parameter and squeezing defined in Eqs. (26) and (27), respectively. In Figs. 4(b) and 4(c) the results for $Q(\omega)$ and $\eta(\omega)$, respectively, are shown. These have been calculated at frequencies of interest, ω'/ω_L, and are averaged over a small region of $\omega'/\omega_L \pm 0.2$, where ω'

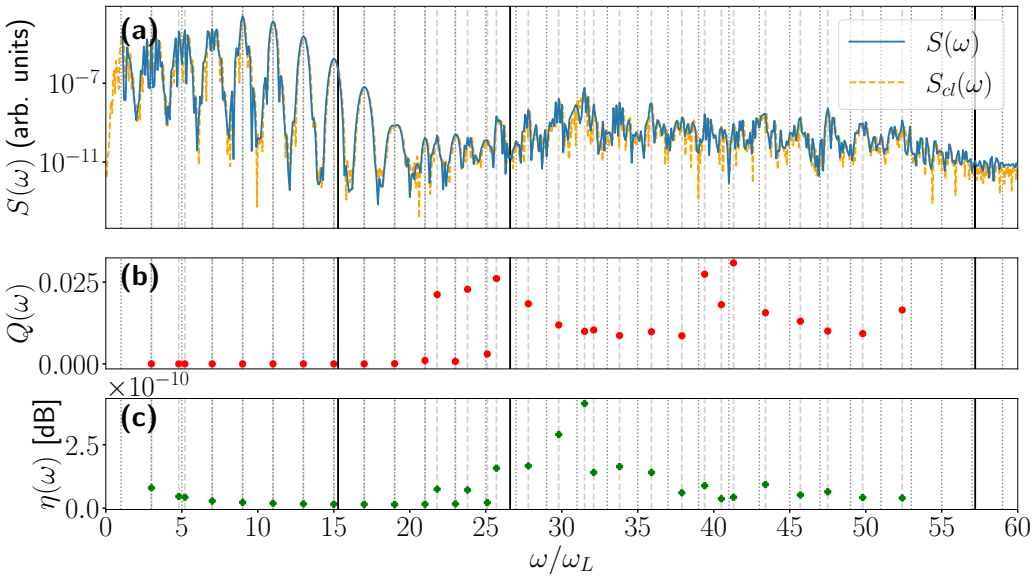

FIG. 4. Measures obtained for a system of $L = 8$ sites (periodic boundary conditions) with a correlation strength of $U = 10\ t_0$. The vertical dotted lines indicate odd harmonics while the dashed lines show some selected frequencies of interest. The vertical black lines are placed at Δ_{band}, Δ_{Mott}, and $\Delta_{\text{Mott}} + 2\Delta_{\text{band}}$, respectively (see text). (a) The HHG spectrum calculated using the fully quantum-mechanical theory [Eq. (24)] (blue). We see a transition between intraband harmonics and interband harmonics at $\omega/\omega_L \approx 21$. For comparison the spectrum based on a semiclassical calculation [Eq. (25)] is shown (orange) which does not differ notably from the quantum optical spectrum. The classical spectrum is normalized to lie on top of the spectrum obtained by the fully quantum-mechanical theory. (b) The Mandel Q parameter [Eq. (26)]. We see a clear increase in Q for interband harmonics showing clear non-Poissonian photon statistics for the emitted Harmonics. (c) The squeezing parameter [Eq. (27)]. Note that the scaling is in units of 10^{-10} dB. We note an increased squeezing for higher harmonics showing that the light is slightly squeezed, i.e., nonclassical.

is the central frequency. We see in both Figs. 4(b) and 4(c) that the values drastically increase around and above the Mott gap (middle vertical solid black line). That is, the nonvanishing values of Q and η show that the harmonics created by the Hubbard-interband current have non-Poissonian photon statistics as well as nonzero squeezing. In this sense, the results show that correlation between electrons affects the HHG generation process and the photon statistics of the emitted light. This is a key result of the present paper. In this sense, the present findings open the door to the study of correlation-induced nonclassicality of light in the context of strong-field processes.

IV. DISCUSSION

In the results presented we use a coupling strength of $g_0 = 4 \times 10^{-8}$ a.u. which corresponds to a quantization volume with a side length of few wavelengths and is similar to the value of $g_0 = 10^{-8}$ a.u. used in Ref. [28] (in length gauge) for a single electron.

The value of g_0 does not affect spectra in the $U = 0$ case. This is because the g_0 dependency in Eq. (35) cancels the g_0 dependency in Eq. (24) leading to the expression in Eq. (25). The value of g_0 in relation to the classical field is discussed in Appendix A. In contrast to the uncorrelated case, the value g_0 explicitly enters in the expression for the spectrum in Eq. (24) for $U \neq 0$ and quantitatively affects the results shown in Fig. 4. Specifically, we find much smaller values of both Q and η than the ones presented for similar work in atoms in Ref. [17]. However, we emphasize that the present results are based on a single Fermi-Hubbard chain with $L = 8$ electrons. In Ref. [28] the number of atoms participating in the HHG process is estimated to be on the order of $N_p \approx 10^{13}$, while in Ref. [17] results are presented with up to $N_p = 5 \times 10^4$ phase-matched atoms which in both cases drastically increases the effective coupling. In our work we find that both Q and η increase significantly when increasing g_0. However, we do not pursue phase matching of multiple Fermi-Hubbard models since a clear assessment would require a consideration of propagation effects of the light, which is beyond the scope of this paper. Still, we can conclude that the emitted light from HHG in a correlated material is nonclassical at certain wavelengths and only show weak squeezing for a small system size.

We also note that in Ref. [17] sub-Poissonian statistics was found at lower harmonics and particular at transition resonances within a single atom. However, for many atoms only super-Poissonian statistics was found. In the present paper only super-Poissonian statistics was found across all frequencies. We note that only the harmonics related to the interband current are nonclassical. At a qualitative level, one

can assume this is because the intraband current is simply a classical oscillating charge distribution whereas the intersubband transitions are decidedly more quantum mechanical in nature.

Another point worth discussing is how well Eq. (22) approximates Eq. (21), i.e., how good of an approximation it is to decouple the different harmonics. This is at present unclear. It is in general not feasible to solve Eq. (21) and hence approximations are needed. Instead of neglecting couplings between different harmonics as done here and in Ref. [17], one could also consider making approximations on $\boldsymbol{j}_{n,m}(t)$. In Ref. [24], e.g., this approach is followed by neglecting dipole transitions from continuum states to continuum states. In the Fermi-Hubbard model this would amount to only including contributions from $\boldsymbol{j}_{m,i}(t) \neq 0$ with i referring to the ground state. This approximation can be justified on grounds of small matrix elements or, as in our case, that population transfer from $\boldsymbol{j}_{n,m}(t)$ with both $n, m \neq i$ is second order in g_0 and hence negligible. Following this approach, Ref. [24] finds that in the case of atoms, all harmonics are indeed squeezed by including the dipole-dipole coupling. However, in doing so a Markov-type approximation has to be made on the photonic quantum state, the implications of which also call for further investigation.

V. SUMMARY AND CONCLUSION

In this paper, we studied how electron-electron correlations affect the quantum state of the emitted HHG light using the prototypical Fermi-Hubbard model. We simulated this within a fully quantum-mechanical setting where both the driving and emitted electromagnetic fields are quantized, different from usual semiclassical HHG calculations where only the electronic system is described quantum mechanically. We studied the two limiting cases of an uncorrelated phase ($U = 0$) and a Mott-insulating phase ($U = 10t_0$), the latter of which may be rationalized in a quasiparticle picture of doublons and holons.

We set out to investigate how the HHG spectrum differs when using a quantized field description, how correlations affect the photons statistics of the emitted light as well as its squeezing, investigating if the emitted light is nonclassical. With respect to the spectrum, we find that in general it does not differ notably when performing a fully quantum-mechanical calculation compared to a conventional semiclassical approach. This clearly shows that the spectrum is largely dominated by the classical current, set up by the oscillating electrons starting out in the field-free ground state. Furthermore, we find that in the uncorrelated phase, the analytical formula for the spectrum matches that of a semiclassical calculation, proving that no quantum optical considerations are needed in this case, and that the generated light is coherent, i.e., no quantum features were found in the uncorrelated phase. In contrast to this situation, we find, using the fully quantum-mechanical approach, that in the Mott-insulating phase nonclassical states of light are generated. Specifically, we find that the Hubbard interband current yields nonclassical light while the doublon-holon intraband current does not show clear nonclassical features, highlighting the importance of accounting for electron-electron interactions for predicting the quantum properties of HHG radiation.

Our paper reports the generation of nonclassical light in a generic condensed-matter model without any subsequent condition measurements, that is, a correlated material is shown to generate nonclassical light. This opens the door to study other types of interactions in other kinds of systems as a source for obtaining different nonclassical states of light. To this end one can benefit from the generality of this quantum optical approach. It requires one to calculate the time-dependent transition currents (or dipoles) between all quantum states of the system. In order to obtain the transition currents, one can benefit from conventional TDSE solvers. Once the transition currents are obtained, one can directly study the quantum nature of the emitted light. The formalism also allows for the possibility of a nonclassical driving field and it would be worth investigating the interplay between nonclassical driving and correlations with regard to generation of nonclassical light with this approach. Such studies would further bridge the gap between strong-field physics and quantum information science by considering strong-field processes as a reliable source for nonclassical light, which is central in quantum information and quantum technology [36,72,81].

ACKNOWLEDGMENTS

This work was supported by the Independent Research Fund Denmark (Grant No. 1026-00040B) and by the Danish National Research Foundation through the Center of Excellence for Complex Quantum Systems (Grant No. DNRF156).

APPENDIX A: INTERACTION WITH A QUANTIZED FIELD

Here we derive the Hamiltonian [Eq. (7)] of the main text for the full system of electronic and photonic degrees of freedom when considering a fully quantized field. The presentation builds on the supplementary material in Ref. [17], and is included here for completeness and reference. In vacuum the free electromagnetic field is given as

$$\hat{\boldsymbol{A}} = \sum_{\boldsymbol{k},\sigma} \frac{g_0}{\sqrt{\omega_k}} (\hat{\boldsymbol{e}}_\sigma \hat{a}_{\boldsymbol{k},\sigma} e^{i\boldsymbol{k}\cdot\boldsymbol{r}} + \hat{\boldsymbol{e}}^*_\sigma \hat{a}^\dagger_{\boldsymbol{k},\sigma} e^{-i\boldsymbol{k}\cdot\boldsymbol{r}}), \tag{A1}$$

where $\boldsymbol{k}$ is the wave vector with related frequency ω_k, σ denotes the polarization, $\hat{\boldsymbol{e}}_\sigma$ is a unit vector, $\hat{a}_{\boldsymbol{k},\sigma}$ ($\hat{a}^\dagger_{\boldsymbol{k},\sigma}$) is the annihilation (creation) operator, and $g_0 = \sqrt{2\pi/V}$ is the coupling constant with quantization volume V. In this paper we use $g_0 = 4 \times 10^{-8}$ a.u. which corresponds to a quantization volume with a side length of a few wavelengths, and which is similar to the value used in Ref. [28].

A general many-body Hamiltonian of N identical electrons for the system of interest reads

$$\hat{H} = \frac{1}{2} \sum_{j=1}^{N} (\hat{\boldsymbol{p}}_j + \hat{\boldsymbol{A}})^2 + \hat{U} + \hat{H}_F, \tag{A2}$$

where $\hat{\boldsymbol{p}}_j$ is the momentum operator for particle j, $\hat{U}$ is an interaction (Coulomb) within the system, and $\hat{H}_F$ is the Hamiltonian of the electromagnetic field.

Before any interaction between system and laser ($t < t_0$), the state of the combined electronic and photonic system is simply

$$|\Psi_i(t)\rangle = |\phi_i(t)\rangle\,|\psi_{\text{laser}}(t)\rangle \quad \text{for } t < t_0, \tag{A3}$$

where $|\phi_i(t)\rangle = e^{-iE_i t}\,|\phi_i\rangle$ is the initial electronic state with trivial time evolution and

$$|\psi_{\text{laser}}(t)\rangle = \otimes_{k,\sigma}\,|\alpha_{\boldsymbol{k},\sigma}e^{-i\omega_k t}\rangle \tag{A4}$$

is the state of the laser which has a frequency broadening around the laser frequency, ω_L. Note that $\alpha_{\boldsymbol{k},\sigma}$ determines the coherent-state amplitude for the given frequency component. For frequencies far away from ω_L there is no amplitude, i.e., $\alpha_{\boldsymbol{k},\sigma} = 0$ for $\omega_k \gg \omega_L$.

We now define the displacement operator

$$\hat{D}(t) = \otimes_{\boldsymbol{k},\sigma}\hat{\mathcal{D}}[\alpha_{\boldsymbol{k}\sigma}(t)] \tag{A5}$$

with

$$\hat{\mathcal{D}}[\alpha_{\boldsymbol{k},\sigma}(t)] = \exp[\alpha_{\boldsymbol{k}\sigma}(t)\hat{a}^\dagger_{\boldsymbol{k},\sigma} - \alpha^*_{\boldsymbol{k}\sigma}(t)\hat{a}_{\boldsymbol{k},\sigma}], \tag{A6}$$

where we take the coherent-state parameters to be those of the laser, i.e., $\alpha_{\boldsymbol{k},\sigma}(t) = \alpha_{\boldsymbol{k},\sigma}e^{-i\omega_k t}$. The displacement operator satisfies the following relations:

$$\hat{D}(t)\,|0\rangle = \otimes_{k,\sigma}\,|\alpha_{\boldsymbol{k},\sigma}e^{-i\omega_k t}\rangle\,, \tag{A7a}$$

$$\hat{D}(t)\hat{D}^\dagger(t) = \mathbb{1}, \tag{A7b}$$

$$\hat{D}^\dagger(t)\hat{a}_{\boldsymbol{k},\sigma}\hat{D}(t) = \hat{a}_{\boldsymbol{k},\sigma} + \alpha_{\boldsymbol{k},\sigma}e^{-i\omega_k t}, \tag{A7c}$$

$$\hat{D}(t)\hat{a}_{\boldsymbol{k},\sigma}\hat{D}^\dagger(t) = \hat{a}_{\boldsymbol{k},\sigma} - \alpha_{\boldsymbol{k},\sigma}e^{-i\omega_k t}, \tag{A7d}$$

where it has been used that $[\hat{a}_{\boldsymbol{k},\sigma}, \hat{a}^\dagger_{\boldsymbol{k}',\sigma'}] = \delta_{\boldsymbol{k},\boldsymbol{k}'}\delta_{\sigma,\sigma'}$ and $[\hat{a}_{\boldsymbol{k},\sigma}, \hat{a}_{\boldsymbol{k}',\sigma'}] = [\hat{a}^\dagger_{\boldsymbol{k},\sigma}, \hat{a}^\dagger_{\boldsymbol{k}',\sigma'}] = 0$.

We now displace the photonic state by

$$\hat{D}^\dagger(t)\,|\psi_{\text{laser}}(t)\rangle = |0\rangle \quad \text{for } t < t_0, \tag{A8}$$

such that the photonic state prior to any interaction is simply vacuum.

Using the displacement operator on the combined electronic and photonic state in Eq. (A3) we hence obtain

$$|\tilde{\Psi}_i(t)\rangle = \hat{D}^\dagger(t)\,|\Psi_i(t)\rangle = |\phi_i(t)\rangle\,|0\rangle \quad \text{for } t < t_0, \tag{A9}$$

which is the initial state for the transformed system. When interactions are turned on for $t \geqslant t_0$, $|\Psi_i(t)\rangle$ satisfies the time-dependent Schrödinger equation, $i\frac{\partial}{\partial t}\,|\Psi_i(t)\rangle = \hat{H}(t)\,|\Psi_i(t)\rangle$. It then follows that the transformed state, $|\tilde{\Psi}_i(t)\rangle$, with interactions, satisfies

$$i\frac{\partial\,|\tilde{\Psi}_i(t)\rangle}{\partial t} = \hat{\tilde{H}}(t)\,|\tilde{\Psi}_i(t)\rangle \tag{A10}$$

with

$$\hat{\tilde{H}}(t) = \hat{D}^\dagger(t)\hat{H}(t)\hat{D}(t) - i\hat{D}^\dagger(t)\frac{\partial\hat{D}(t)}{\partial t}. \tag{A11}$$

It is the coupling between the electronic and photonic degrees of freedom in $\hat{\tilde{H}}(t)$ [explicitly given in Eq. (A20) below] that generates population in photonic modes other than the laser mode.

Using the properties of $\hat{D}(t)$ from Eq. (A7) one can find that

$$i\hat{D}^\dagger(t)\,\frac{\partial\hat{D}(t)}{\partial t} = \sum_{\boldsymbol{k},\sigma}\omega_k(\alpha_{\boldsymbol{k},\sigma}e^{-i\omega_k t}\hat{a}^\dagger_{\boldsymbol{k},\sigma} + \alpha^*_{\boldsymbol{k},\sigma}e^{i\omega_k t}\hat{a}_{\boldsymbol{k},\sigma} + |\alpha_{\boldsymbol{k},\sigma}|^2), \tag{A12}$$

$$\begin{aligned}\hat{D}^\dagger(t)\hat{H}\hat{D}(t) - i\hat{D}^\dagger(t)\,\frac{\partial\hat{D}(t)}{\partial t} &= \sum_{j=1}^{N}\frac{\hat{\boldsymbol{p}}_j^2}{2} + \hat{U} + \sum_{j=1}^{N}\frac{1}{2}[\hat{D}^\dagger(t)\hat{\boldsymbol{A}}\hat{D}(t)]^2 \\ &+ \sum_{j=1}^{N}\frac{1}{2}[\hat{\boldsymbol{p}}_j\cdot\hat{D}^\dagger(t)\hat{\boldsymbol{A}}\hat{D}(t) + \hat{D}^\dagger(t)\hat{\boldsymbol{A}}\hat{D}(t)\cdot\hat{\boldsymbol{p}}_j] + \left(\hat{D}^\dagger(t)\hat{H}_F\hat{D}(t) - i\hat{D}^\dagger(t)\,\frac{\partial\hat{D}(t)}{\partial t}\right),\end{aligned} \tag{A13}$$

$$\hat{D}^\dagger(t)\hat{H}_F\hat{D}(t) - i\hat{D}^\dagger(t)\,\frac{\partial\hat{D}(t)}{\partial t} = \hat{H}_F = \sum_{\boldsymbol{k},\sigma}\omega_k\hat{a}^\dagger_{\boldsymbol{k},\sigma}\hat{a}_{\boldsymbol{k},\sigma}. \tag{A14}$$

The action of the displacement operator on the quantized electromagnetic field is the following:

$$\hat{D}^\dagger(t)\hat{\boldsymbol{A}}\hat{D}(t) = \boldsymbol{A}_{\text{cl}}(t) + \hat{\boldsymbol{A}}_Q, \tag{A15}$$

where

$$\begin{aligned}\boldsymbol{A}_{\text{cl}}(t) &= \langle\psi_{\text{laser}}(t)|\hat{\boldsymbol{A}}\,|\psi_{\text{laser}}(t)\rangle \\ &= \sum_{\boldsymbol{k},\sigma}\frac{g_0}{\sqrt{\omega_k}}(\hat{\boldsymbol{e}}_\sigma\alpha_{\boldsymbol{k},\sigma}e^{i\boldsymbol{k}\cdot\boldsymbol{r}-i\omega_k t} + \text{H.c.}), \\ \hat{\boldsymbol{A}}_Q &= \sum_{\boldsymbol{k},\sigma}\frac{g_0}{\sqrt{\omega_k}}(\hat{\boldsymbol{e}}_\sigma\hat{a}_{\boldsymbol{k},\sigma}e^{i\boldsymbol{k}\cdot\boldsymbol{r}} + \text{H.c.})\end{aligned} \tag{A16}$$

is a classical and a quantized field, respectively. Note that the interval of $\boldsymbol{k}$ and σ in the first equation is only over the populated coherent states in the laser. It then follows that the Hamiltonian of Eq. (A11) transforms as

$$\begin{aligned}\hat{\tilde{H}}(t) &= \sum_{j=1}^{N}\frac{1}{2}[\hat{\boldsymbol{p}}_j + \boldsymbol{A}_{\text{cl}}(t)]^2 + \hat{U} \\ &+ \sum_{j=1}^{N}\hat{\boldsymbol{A}}_Q\cdot[\hat{\boldsymbol{p}}_j + \boldsymbol{A}_{\text{cl}}(t)] + \hat{H}_F\end{aligned} \tag{A17}$$

where we work in the Coulomb gauge and also discard the term $\hat{\boldsymbol{A}}_Q^2/2$ as it is assumed to be of much smaller magnitude.

We can order the terms in the Hamiltonian as

$$\hat{\tilde{H}}(t) = \hat{H}_{\mathrm{TDSE}}(t) + \hat{H}_F + \hat{V}(t), \tag{A18}$$

with

$$\hat{H}_{\mathrm{TDSE}}(t) = \sum_{j=1}^{N} \frac{1}{2}[\hat{\boldsymbol{p}}_j + \boldsymbol{A}_{\mathrm{cl}}(t)]^2 + \hat{U}, \tag{A19}$$

$$\hat{V}(t) = \sum_{j=1}^{N} \hat{\boldsymbol{A}}_Q \cdot [\hat{\boldsymbol{p}}_j + \boldsymbol{A}_{\mathrm{cl}}(t)]. \tag{A20}$$

The net result of this transformation is that the laser driving on the electronic system only needs to be accounted for on a classical level as seen in $\hat{H}_{\mathrm{TDSE}}(t)$. However, the electronic system then interacts with a quantized field via $\hat{V}(t)$ which then affects the photon emission. Equation (A18) corresponds to Eq. (7) of the main text.

We note that the classical electromagnetic field is described both in Eq. (23) and in a quantum optical version in Eq. (A16). Most notably is the fact that g_0 only enters explicitly in the latter expression. We drive the system with a given vector potential amplitude of A_0. By comparing Eqs. (23) and (A16) we see that A_0 is proportional to $g_0 \cdot \alpha_{\boldsymbol{k},\sigma}$. Thus for a fixed A_0, changing g_0 should be followed by a change in the numerical value of $\alpha_{\boldsymbol{k},\sigma}$ to keep the product constant. The value of $\alpha_{\boldsymbol{k},\sigma}$ does not affect the results presented as it does not enter the equations of motion.

APPENDIX B: ADAPTATION TO THE FERMI-HUBBARD MODEL

In this Appendix we show how we go from the general TDSE Hamiltonian in Eq. (A19) to the Hamiltonian of the Fermi-Hubbard model. For notational convenience, we define the operator $\hat{\boldsymbol{P}}(t)$:

$$\hat{\boldsymbol{P}}(t) = \sum_{l=1}^{N} [\hat{\boldsymbol{p}}_l + \boldsymbol{A}_{\mathrm{cl}}(t)], \tag{B1}$$

which is the quantity that interacts with the quantum field in Eq. (A20).

We calculate the commutator $[\hat{H}_{\mathrm{TDSE}}(t), \sum_{n=1}^{N} \boldsymbol{r}_n]$ and obtain

$$\left[\hat{H}_{\mathrm{TDSE}}(t), \sum_{n=1}^{N} \boldsymbol{r}_n\right] = -i\hat{\boldsymbol{P}}(t). \tag{B2}$$

We now specify that $\hat{H}_{\mathrm{TDSE}}(t) \to \hat{H}_{\mathrm{FH}}(t)$ with the $H_{\mathrm{FH}}(t)$ given in Eq. (16). Likewise, the dipole operator will be adapted to the discrete Fermi-Hubbard model:

$$\sum_{n=1}^{N} \boldsymbol{r}_n \to \hat{\boldsymbol{R}} = \sum_{l=1}^{L} \boldsymbol{R}_l (\hat{c}_{l,\uparrow}^{\dagger}\hat{c}_{l,\uparrow} + \hat{c}_{l,\downarrow}^{\dagger}\hat{c}_{l,\downarrow}) \tag{B3}$$

where N is the number of electrons and L is the number of sites in the system. Inserting $\hat{H}_{\mathrm{FH}}$ and Eq. (B3) into Eq. (B2) gives

$$\hat{\boldsymbol{P}}(t) = i[\hat{H}_{\mathrm{FH}}, \hat{\boldsymbol{R}}]. \tag{B4}$$

Since the right-hand side of Eq. (B4) is the current operator [82]

$$i[\hat{H}_{\mathrm{FH}}, \hat{\boldsymbol{R}}] = \frac{\partial}{\partial t}\hat{\boldsymbol{R}} \equiv \hat{\boldsymbol{j}}(t), \tag{B5}$$

we obtain

$$\hat{\boldsymbol{P}}(t) = \hat{\boldsymbol{j}}(t). \tag{B6}$$

The explicit expression of the current operator, $\hat{\boldsymbol{j}}(t)$, is found by calculating the commutator on the left-hand side of Eq. (B5) and we obtain

$$\hat{\boldsymbol{j}}(t) = -iat_0 \sum_{j,\mu} (e^{iaA_{\mathrm{cl}}(t)}\hat{c}_{j,\mu}^{\dagger}\hat{c}_{j+1,\mu} - \mathrm{H.c.})\hat{\boldsymbol{x}}, \tag{B7}$$

which is the same as Eq. (19) of the main text. Here we have used that the jth position in the Fermi-Hubbard chain is $R_j = ja$ and taken the direction of the chain to be along the x axis (polarization direction) without loss of generality.

APPENDIX C: EXPLICIT CALCULATION OF EXPECTATION VALUES

This Appendix is dedicated to the calculation of expectation values from the state in Eq. (20) which we restate here:

$$|\tilde{\Psi}(t)\rangle_I = \sum_{m=1}^{M} |\tilde{\chi}^{(m)}(t)\rangle\, |\phi_m\rangle\,. \tag{C1}$$

By assuming that all modes can be treated independently, i.e., neglecting correlations between different modes [going from Eq. (21) to Eq. (22)] we can expand the photonic state as a product state where each product state is further expanded in terms of Fock states:

$$|\tilde{\chi}^{(m)}\rangle = \otimes_{\boldsymbol{k},\sigma} \left|\tilde{\chi}_{\boldsymbol{k},\sigma}^{(m)}\right\rangle \quad \text{with} \quad \left|\tilde{\chi}_{\boldsymbol{k},\sigma}^{(m)}\right\rangle = \sum_{n_{\boldsymbol{k},\sigma}} c_{n_{\boldsymbol{k},\sigma}}^{(m)}\, |n_{\boldsymbol{k},\sigma}\rangle\,. \tag{C2}$$

In our calculations, the Hilbert space was truncated to contain at most 100 photons, though we did not find any population for Fock states with more than $n_{\boldsymbol{k},\sigma} \leqslant 15$. This cutoff depends on the choice of g_0 as a larger value would give a larger population when applying the photon operators in Eq. (21), meaning that higher photon numbers can be reached.

We are particularly interested in calculating moments of the number operator $\langle(\hat{n}_{\boldsymbol{k},\sigma})^l\rangle$ used for photon statistics and will use this as an example for a general expectation value. As the full state in Eq. (C1) is in the interaction picture we have to transform accordingly. To this end it is useful to use the following relations [with $\hat{\mathcal{U}}_0(t) = \hat{\mathcal{U}}_{\mathrm{TDSE}}(t) \cdot \hat{\mathcal{U}}_F(t)$]:

$$\begin{aligned} \hat{\mathcal{U}}_0^{\dagger}(t)\hat{a}_{\boldsymbol{k},\sigma}\hat{\mathcal{U}}_0(t) &= \hat{a}_{\boldsymbol{k},\sigma}\, e^{-i\omega_k t}, \\ \hat{\mathcal{U}}_0^{\dagger}(t)\hat{a}_{\boldsymbol{k},\sigma}^{\dagger}\hat{\mathcal{U}}_0(t) &= \hat{a}_{\boldsymbol{k},\sigma}^{\dagger}\, e^{i\omega_k t}. \end{aligned} \tag{C3}$$

We now calculate the expectation value of the number operator to the power of l. We find that

$$\begin{aligned} \langle(\hat{n}_{\boldsymbol{k}',\sigma'})^l\rangle &= {}_I\langle\tilde{\Psi}(t)|\, \hat{\mathcal{U}}_0^{\dagger}(t)\, (\hat{n}_{\boldsymbol{k}',\sigma'})^l \hat{\mathcal{U}}_0(t)\, |\tilde{\Psi}(t)\rangle_I \\ &= \sum_{m,m'} \langle\phi_{m'}|\,\phi_m\rangle\, \langle\tilde{\chi}^{(m')}|\, (\hat{n}'^{l}_{\boldsymbol{k}',\sigma})\, |\tilde{\chi}^{(m)}\rangle \\ &= \sum_{m} \langle\tilde{\chi}^{(m)}|\, (\hat{n}_{\boldsymbol{k}',\sigma'})\, |\tilde{\chi}^{(m)}\rangle\,, \end{aligned} \tag{C4}$$

where the orthogonality of the electronic states has been exploited. Now expanding into product states via Eq. (C2) we find

$$\langle(\hat{n}_{\boldsymbol{k}',\sigma'})^l\rangle = \sum_m \left\langle \chi^{(m)}_{\boldsymbol{k}',\sigma'}\right| (\hat{n}_{\boldsymbol{k}',\sigma'})^l \left|\chi^{(m)}_{\boldsymbol{k}',\sigma'}\right\rangle \prod_{\substack{\boldsymbol{k},\sigma\\ \neq \boldsymbol{k}',\sigma'}} \left\langle \tilde{\chi}^{(m)}_{\boldsymbol{k},\sigma}\right| \left.\tilde{\chi}^{(m)}_{\boldsymbol{k},\sigma}\right\rangle. \tag{C5}$$

Expanding further in terms of Fock states via Eq. (C2), the two factors can readily be calculated:

$$\begin{aligned}&\left\langle \chi^{(m)}_{\boldsymbol{k}',\sigma'}\right| (\hat{n}_{\boldsymbol{k}',\sigma'})^l \left|\chi^{(m)}_{\boldsymbol{k}',\sigma'}\right\rangle\\ &= \sum_{n'_{\boldsymbol{k}',\sigma'}} \sum_{n''_{\boldsymbol{k}',\sigma'}} \left(c^{(m)}_{n'_{\boldsymbol{k}',\sigma'}}\right)^* c^{(m)}_{n''_{\boldsymbol{k}',\sigma'}} \langle n'_{\boldsymbol{k}',\sigma'}| (\hat{n}_{\boldsymbol{k}',\sigma'})^l |\hat{n}''_{\boldsymbol{k}',\sigma'}\rangle\\ &= \sum_{n_{\boldsymbol{k}',\sigma'}} \left|c^{(m)}_{n_{\boldsymbol{k}',\sigma'}}\right|^2 (n_{\boldsymbol{k}',\sigma'})^l,\end{aligned} \tag{C6}$$

and

$$\left\langle \tilde{\chi}^{(m)}_{\boldsymbol{k},\sigma}\right| \left.\tilde{\chi}^{(m)}_{\boldsymbol{k},\sigma}\right\rangle = \sum_{n_{\boldsymbol{k},\sigma}} \left|c^{(m)}_{n_{\boldsymbol{k},\sigma}}\right|^2, \tag{C7}$$

and hence the expectation value is given by

$$\begin{aligned}\langle(\hat{n}_{\boldsymbol{k}',\sigma'})^l\rangle = \sum_m \Bigg\{ &\left[\sum_{n_{\boldsymbol{k}',\sigma'}} \left|c^{(m)}_{n_{\boldsymbol{k}',\sigma'}}\right|^2 (n_{\boldsymbol{k}',\sigma'})^l\right]\\ &\times \prod_{\substack{\boldsymbol{k},\sigma\\ \neq \boldsymbol{k}',\sigma'}} \left(\sum_{n_{\boldsymbol{k},\sigma}} \left|c^{(m)}_{n_{\boldsymbol{k},\sigma}}\right|^2\right)\Bigg\},\end{aligned} \tag{C8}$$

which allows all moments of the number operator to be calculated. A similar calculation is done for expectation values of other operators, e.g., $\hat{a}_{\boldsymbol{k},\sigma}$ and $\hat{a}^\dagger_{\boldsymbol{k},\sigma}$.

APPENDIX D: PERTURBATIVE CALCULATION

Here we derive the state of the system in the perturbative limit of small coupling to the quantum field and show that this yields the exact spectrum in the uncorrelated ($U = 0$) phase despite the fact that the perturbative calculation gives a wrong description of the generated light statistics (see below). A perturbative calculation is also found in Supplementary Note 2 in Ref. [17].

Starting from Eq. (9) in the main text, we have

$$i\frac{\partial}{\partial t} |\tilde{\Psi}(t)\rangle_I = \hat{V}_I(t) |\tilde{\Psi}(t)\rangle_I, \tag{D1}$$

with

$$\hat{V}_I(t) = \hat{\boldsymbol{A}}_{Q,I}(t) \cdot \hat{\mathcal{U}}^\dagger_{\rm FH}(t,t_0)\hat{\boldsymbol{j}}(t)\hat{\mathcal{U}}_{\rm FH}(t,t_0), \tag{D2}$$

with $\hat{\boldsymbol{A}}_{Q,I}(t)$ given in Eq. (11) of the main text. The general solution to Eq. (D1) is given by

$$|\tilde{\Psi}(t)\rangle_I = \hat{T} \exp\left[-i\int_{t_0}^t \hat{V}_I(t')\,dt'\right] |\tilde{\Psi}(t_0)\rangle_I, \tag{D3}$$

where $\hat{T}$ is the time ordering operator and t_0 is the initial time prior to any interaction between the laser and the electronic system. We now investigate the case of a weak interaction with

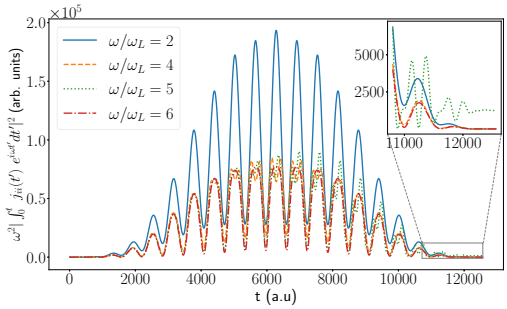

FIG. 5. The occupation of the lowest even harmonics during the dynamics of the pulse. We see a clear nonzero occupation at most times except at the end where all even harmonics have a vanishing occupation and hence a vanishing contribution to the signal. For comparison the fifth harmonic (green line) does not vanish after the interaction with the pulse as seen in the inset.

the quantized field and expand Eq. (D3) to first order in $\hat{V}_I(t)$:

$$|\tilde{\Psi}(t)\rangle_I = \left[1 - i\int_{t_0}^t \hat{V}_I(t')\,dt'\right] |\tilde{\Psi}(t_0)\rangle_I. \tag{D4}$$

We now take the electronic state to initially be its ground state prior to interaction with the laser. Due to the coherent displacement done in Eq. (A8), the photonic state is initially in the vacuum state for all modes. That is, we take $|\tilde{\Psi}(t_0)\rangle_I = |0\rangle\,|\phi_i\rangle$. Now writing out $\hat{V}_I(t)$ and letting the photonic operators act on $|\tilde{\Psi}(t_0)\rangle_I$ yields

$$\begin{aligned}|\tilde{\Psi}(t)\rangle_I &= |0\rangle\,|\phi_i\rangle - i\sum_{\boldsymbol{k},\sigma} \frac{g_0}{\sqrt{\omega_k}}\\ &\quad\times \left[\int_{t_0}^t e^{i\omega_k t'} \hat{\mathcal{U}}^\dagger_{\rm FH}(t')\hat{\boldsymbol{j}}(t')\cdot \boldsymbol{e}^*_\sigma \hat{\mathcal{U}}_{\rm FH}(t')dt'\right] |\boldsymbol{k},\sigma\rangle\,|\phi_i\rangle\\ &= |0\rangle\,|\phi_i\rangle - i\sum_m |\phi_m\rangle \sum_{\boldsymbol{k},\sigma} \frac{g_0}{\sqrt{\omega_k}}\\ &\quad\times \left[\int_{t_0}^t e^{i\omega_k t'} \boldsymbol{j}_{m,i}(t')\cdot \boldsymbol{e}^*_\sigma dt\right] |\boldsymbol{k},\sigma\rangle,\end{aligned} \tag{D5}$$

where we in the second line have inserted $\mathbb{1} = \Sigma_m |\phi_m\rangle\langle\phi_m|$ and defined $\boldsymbol{j}_{m,i}(t) = \langle\phi_m(t_0)|\hat{\mathcal{U}}^\dagger_{\rm FH}(t,t_0)\hat{\boldsymbol{j}}(t)\hat{\mathcal{U}}_{\rm FH}(t,t_0)\,|\phi_i(t_0)\rangle$. In the weak-coupling limit Eq. (D5) is valid for all choices of U within the electronic system.

We now investigate the uncorrelated phase of $U = 0$. In this case the transition current is diagonal, i.e., $\boldsymbol{j}_{m,i}(t) = \boldsymbol{j}_{i,i}(t)\delta_{m,i}$. Inserting this into Eq. (D5) we obtain

$$|\tilde{\Psi}(t)\rangle_I = \left[|0\rangle + \sum_{\boldsymbol{k},\sigma} \beta^{(i)}_{\boldsymbol{k},\sigma}(t)\,|\boldsymbol{k},\sigma\rangle\right] |\phi_i\rangle, \tag{D6}$$

where we have used the definition of $\beta^{(i)}_{\boldsymbol{k},\sigma}$ in Eq. (35) in the main text. Calculating the expectation value of the number operator yields $\langle\hat{n}_{\boldsymbol{k},\sigma}\rangle = |\beta_{\boldsymbol{k},\sigma}|^2$, which yields the exact spectrum in Eq. (36) when inserted into Eq. (24) for $t \to \infty$. However, higher moments such as $\langle(\hat{n}_{\boldsymbol{k},\sigma})^2\rangle$ are not exact in this perturbative approach as the state in Eq. (D6) is truncated

to contain at most one photon and is hence not a coherent state. We have found that this perturbative approach in general does not match the nonperturbative results for a finite value of $U \neq 0$, which is why the perturbative approach is not pursued further.

APPENDIX E: NONZERO SIGNAL FOR EVEN HARMONICS

Here we briefly show that even harmonics have a nonzero signal during the dynamics though they vanish in the spectrum after the end of the pulse. We will use the case of $U = 0$ as an example, as we have an exact analytical solution, namely, $\langle \hat{n}_{\boldsymbol{k},\sigma} \rangle = |\beta^{(i)}_{\boldsymbol{k},\sigma}(t)|^2$ with the coherent-state amplitude given in Eq. (35). In Fig. 5 we show the quantity

$$\omega^2 \left| \int_0^t j_{ii}(t) e^{i\omega t} \right|^2 = \frac{\omega^3}{g_0^2} \left| \beta^{(i)}_{\boldsymbol{k},\sigma}(t) \right|^2, \tag{E1}$$

which is directly related to the classical spectrum as seen from Eqs. (25) and (36). We see from Fig. 5 that there is a nonzero occupation for all harmonics during most of the interaction with the laser pulse but only the odd harmonics (here the fifth harmonic as an example) are visible in the final spectrum as seen in the inset. If one could very rapidly stop the dynamics during the pulse, even harmonics would be observed since such a rapid change of the system breaks the inversion symmetry that usually permits only odd harmonics.

[1] F. Krausz and M. Ivanov, Attosecond physics, Rev. Mod. Phys. **81**, 163 (2009).

[2] M. Ferray, A. L'Huillier, X. F. Li, L. A. Lompre, G. Mainfray, and C. Manus, Multiple-harmonic conversion of 1064 nm radiation in rare gases, J. Phys. B **21**, L31 (1988).

[3] P. M. Paul, E. S. Toma, P. Breger, G. Mullot, F. Augé, P. Balcou, H. G. Muller, and P. Agostini, Observation of a train of attosecond pulses from high harmonic generation, Science **292**, 1689 (2001).

[4] M. Hentschel, R. Kienberger, C. Spielmann, G. A. Reider, N. Milosevic, T. Brabec, P. Corkum, U. Heinzmann, M. Drescher, and F. Krausz, Attosecond metrology, Nature (London) **414**, 509 (2001).

[5] K. J. Schafer, B. Yang, L. F. DiMauro, and K. C. Kulander, Above threshold ionization beyond the high harmonic cutoff, Phys. Rev. Lett. **70**, 1599 (1993).

[6] P. B. Corkum, Plasma perspective on strong field multiphoton ionization, Phys. Rev. Lett. **71**, 1994 (1993).

[7] M. Lewenstein, P. Balcou, M. Y. Ivanov, A. L'Huillier, and P. B. Corkum, Theory of high-harmonic generation by low-frequency laser fields, Phys. Rev. A **49**, 2117 (1994).

[8] S. Ghimire, A. D. DiChiara, E. Sistrunk, P. Agostini, L. F. DiMauro, and D. A. Reis, Observation of high-order harmonic generation in a bulk crystal, Nat. Phys. **7**, 138 (2011).

[9] S. Ghimire and D. A. Reis, High-harmonic generation from solids, Nat. Phys. **15**, 10 (2019).

[10] E. Goulielmakis and T. Brabec, High harmonic generation in condensed matter, Nat. Photon. **16**, 411 (2022).

[11] D. Golde, T. Meier, and S. W. Koch, High harmonics generated in semiconductor nanostructures by the coupled dynamics of optical inter- and intraband excitations, Phys. Rev. B **77**, 075330 (2008).

[12] G. Vampa, C. R. McDonald, G. Orlando, D. D. Klug, P. B. Corkum, and T. Brabec, Theoretical analysis of high-harmonic generation in solids, Phys. Rev. Lett. **113**, 073901 (2014).

[13] G. Vampa, C. R. McDonald, G. Orlando, P. B. Corkum, and T. Brabec, Semiclassical analysis of high harmonic generation in bulk crystals, Phys. Rev. B **91**, 064302 (2015).

[14] G. Vampa and T. Brabec, Merge of high harmonic generation from gases and solids and its implications for attosecond science, J. Phys. B **50**, 083001 (2017).

[15] A. V. Bogatskaya, E. A. Volkova, and A. M. Popov, Spontaneous emission of atoms in a strong laser field, J. Exp. Theor. Phys. **125**, 587 (2017).

[16] A. Gombkötő, P. Földi, and S. Varró, Quantum-optical description of photon statistics and cross correlations in high-order harmonic generation, Phys. Rev. A **104**, 033703 (2021).

[17] A. Gorlach, O. Neufeld, N. Rivera, O. Cohen, and I. Kaminer, The quantum-optical nature of high harmonic generation, Nat. Commun. **11**, 4598 (2020).

[18] A. Pizzi, A. Gorlach, N. Rivera, A. Nunnenkamp, and I. Kaminer, Light emission from strongly driven many-body systems, Nat. Phys. **19**, 551 (2023).

[19] P. Stammer, J. Rivera-Dean, A. Maxwell, T. Lamprou, A. Ordóñez, M. F. Ciappina, P. Tzallas, and M. Lewenstein, Quantum electrodynamics of intense laser-matter interactions: A tool for quantum state engineering, PRX Quantum **4**, 010201 (2023).

[20] J. Rivera-Dean, P. Stammer, A. S. Maxwell, T. Lamprou, A. F. Ordóñez, E. Pisanty, P. Tzallas, M. Lewenstein, and M. F. Ciappina, Entanglement and non-classical states of light in a strong-laser driven solid-state system, arXiv:2211.00033.

[21] I. Gonoskov, R. Sondenheimer, C. Hünecke, D. Kartashov, U. Peschel, and S. Gräfe, Nonclassical light generation and control from laser-driven semiconductor intraband excitations, arXiv:2211.06177.

[22] M. Even Tzur, M. Birk, A. Gorlach, M. Krüger, I. Kaminer, and O. Cohen, Photon-statistics force in ultrafast electron dynamics, Nat. Photon. **17**, 501 (2023).

[23] A. Gorlach, M. E. Tzur, M. Birk, M. Krüger, N. Rivera, O. Cohen, and I. Kaminer, High-harmonic generation driven by quantum light, Nat. Phys. **19**, 1689 (2023).

[24] P. Stammer, J. Rivera-Dean, A. S. Maxwell, T. Lamprou, J. Argüello-Luengo, P. Tzallas, M. F. Ciappina, and M. Lewenstein, Entanglement and squeezing of the optical field modes in high harmonic generation, arXiv:2310.15030.

[25] D. N. Yangaliev, V. P. Krainov, and O. I. Tolstikhin, Quantum theory of radiation by nonstationary systems with application to high-order harmonic generation, Phys. Rev. A **101**, 013410 (2020).

[26] P. Stammer, Theory of entanglement and measurement in high-order harmonic generation, Phys. Rev. A **106**, L050402 (2022).

[27] M. E. Tzur, M. Birk, A. Gorlach, I. Kaminer, M. Krueger, and O. Cohen, Generation of squeezed high-order harmonics, arXiv:2311.11257.

[28] M. Lewenstein, M. F. Ciappina, E. Pisanty, J. Rivera-Dean, P. Stammer, T. Lamprou, and P. Tzallas, Generation of optical Schrödinger cat states in intense laser–matter interactions, Nat. Phys. **17**, 1104 (2021).

[29] J. Rivera-Dean, P. Stammer, A. S. Maxwell, T. Lamprou, A. F. Ordóñez, E. Pisanty, P. Tzallas, M. Lewenstein, and M. F. Ciappina, Nonclassical states of light after high-harmonic generation in semiconductors: A Bloch-based perspective, Phys. Rev. B **109**, 035203 (2024).

[30] N. Tsatrafyllis, I. K. Kominis, I. A. Gonoskov, and P. Tzallas, High-order harmonics measured by the photon statistics of the infrared driving-field exiting the atomic medium, Nat. Commun. **8**, 15170 (2017).

[31] N. Tsatrafyllis, S. Kühn, M. Dumergue, P. Foldi, S. Kahaly, E. Cormier, I. A. Gonoskov, B. Kiss, K. Varju, S. Varro, and P. Tzallas, Quantum optical signatures in a strong laser pulse after interaction with semiconductors, Phys. Rev. Lett. **122**, 193602 (2019).

[32] J. Rivera-Dean, T. Lamprou, E. Pisanty, P. Stammer, A. F. Ordóñez, A. S. Maxwell, M. F. Ciappina, M. Lewenstein, and P. Tzallas, Strong laser fields and their power to generate controllable high-photon-number coherent-state superpositions, Phys. Rev. A **105**, 033714 (2022).

[33] A. Ourjoumtsev, R. Tualle-Brouri, J. Laurat, and P. Grangier, Generating optical Schrödinger kittens for quantum information processing, Science **312**, 83 (2006).

[34] A. Ourjoumtsev, H. Jeong, R. Tualle-Brouri, and P. Grangier, Generation of optical "Schrödinger cats" from photon number states, Nature (London) **448**, 784 (2007).

[35] A. Zavatta, S. Viciani, and M. Bellini, Quantum-to-classical transition with single-photon-added coherent states of light, Science **306**, 660 (2004).

[36] A. Acín, I. Bloch, H. Buhrman, T. Calarco, C. Eichler, J. Eisert, D. Esteve, N. Gisin, S. J. Glaser, F. Jelezko, S. Kuhr, M. Lewenstein, M. F. Riedel, P. O. Schmidt, R. Thew, A. Wallraff, I. Walmsley, and F. K. Wilhelm, The quantum technologies roadmap: A european community view, New J. Phys. **20**, 080201 (2018).

[37] I. H. Deutsch, Harnessing the power of the second quantum revolution, PRX Quantum **1**, 020101 (2020).

[38] E. Polino, M. Valeri, N. Spagnolo, and F. Sciarrino, Photonic quantum metrology, AVS Quantum Sci. **2**, 024703 (2020).

[39] M. Barbieri, Optical quantum metrology, PRX Quantum **3**, 010202 (2022).

[40] R. E. F. Silva, I. V. Blinov, A. N. Rubtsov, O. Smirnova, and M. Ivanov, High-harmonic spectroscopy of ultrafast many-body dynamics in strongly correlated systems, Nat. Photon. **12**, 266 (2018).

[41] Y. Murakami, M. Eckstein, and P. Werner, High-harmonic generation in Mott insulators, Phys. Rev. Lett. **121**, 057405 (2018).

[42] Y. Murakami and P. Werner, Nonequilibrium steady states of electric field driven Mott insulators, Phys. Rev. B **98**, 075102 (2018).

[43] T. Hansen, S. V. B. Jensen, and L. B. Madsen, Correlation effects in high-order harmonic generation from finite systems, Phys. Rev. A **105**, 053118 (2022).

[44] T. Hansen and L. B. Madsen, Doping effects in high-harmonic generation from correlated systems, Phys. Rev. B **106**, 235142 (2022).

[45] Y. Murakami, S. Takayoshi, A. Koga, and P. Werner, High-harmonic generation in one-dimensional Mott insulators, Phys. Rev. B **103**, 035110 (2021).

[46] M. Lysne, Y. Murakami, and P. Werner, Signatures of bosonic excitations in high-harmonic spectra of Mott insulators, Phys. Rev. B **101**, 195139 (2020).

[47] N. Tancogne-Dejean, M. A. Sentef, and A. Rubio, Ultrafast modification of hubbard U in a strongly correlated material: Ab initio high-harmonic generation in NiO, Phys. Rev. Lett. **121**, 097402 (2018).

[48] S. Imai, A. Ono, and S. Ishihara, High harmonic generation in a correlated electron system, Phys. Rev. Lett. **124**, 157404 (2020).

[49] K. Chinzei and T. N. Ikeda, Disorder effects on the origin of high-order harmonic generation in solids, Phys. Rev. Res. **2**, 013033 (2020).

[50] C. Orthodoxou, A. Zaïr, and G. H. Booth, High harmonic generation in two-dimensional Mott insulators, npj Quantum Mater. **6**, 76 (2021).

[51] C. Shao, H. Lu, X. Zhang, C. Yu, T. Tohyama, and R. Lu, High-harmonic generation approaching the quantum critical point of strongly correlated systems, Phys. Rev. Lett. **128**, 047401 (2022).

[52] J. Masur, D. I. Bondar, and G. McCaul, Optical distinguishability of Mott insulators in the time versus frequency domain, Phys. Rev. A **106**, 013110 (2022).

[53] M. Udono, K. Sugimoto, T. Kaneko, and Y. Ohta, Excitonic effects on high-harmonic generation in Mott insulators, Phys. Rev. B **105**, L241108 (2022).

[54] Y. Murakami, K. Uchida, A. Koga, K. Tanaka, and P. Werner, Anomalous temperature dependence of high-harmonic generation in Mott insulators, Phys. Rev. Lett. **129**, 157401 (2022).

[55] K. Uchida, G. Mattoni, S. Yonezawa, F. Nakamura, Y. Maeno, and K. Tanaka, High-order harmonic generation and its unconventional scaling law in the Mott-insulating Ca_2RuO_4, Phys. Rev. Lett. **128**, 127401 (2022).

[56] O. Grånäs, I. Vaskivsky, X. Wang, P. Thunström, S. Ghimire, R. Knut, J. Söderström, L. Kjellsson, D. Turenne, R. Y. Engel, M. Beye, J. Lu, A. H. Reid, W. Schlotter, G. Coslovich, M. Hoffmann, G. Kolesov, C. Schüßler-Langeheine, A. Styervoyedov, N. Tancogne-Dejean *et al.*, Ultrafast modification of the electronic structure of a correlated insulator, arXiv:2008.11115.

[57] M. R. Bionta, E. Haddad, A. Leblanc, V. Gruson, P. Lassonde, H. Ibrahim, J. Chaillou, N. Émond, M. R. Otto, A. Jiménez-Galán, R. E. F. Silva, M. Ivanov, B. J. Siwick, M. Chaker, and F. Légaré, Tracking ultrafast solid-state dynamics using high harmonic spectroscopy, Phys. Rev. Res. **3**, 023250 (2021).

[58] J. Sloan, A. Gorlach, M. E. Tzur, N. Rivera, O. Cohen, I. Kaminer, and M. Soljačić, Entangling extreme ultraviolet photons through strong field pair generation, arXiv:2309.16466.

[59] F. H. L. Essler, H. Frahm, F. Göhmann, A. Klümper, and V. E. Korepin, *The One-Dimensional Hubbard Model* (Cambridge University, Cambridge, England, 2005).

[60] P. A. Lee, N. Nagaosa, and X.-G. Wen, Doping a Mott insulator: Physics of high-temperature superconductivity, Rev. Mod. Phys. **78**, 17 (2006).

[61] M. Imada, A. Fujimori, and Y. Tokura, Metal-insulator transitions, Rev. Mod. Phys. **70**, 1039 (1998).

[62] B. R. Mollow, Pure-state analysis of resonant light scattering: Radiative damping, saturation, and multiphoton effects, Phys. Rev. A **12**, 1919 (1975).

[63] C. Cohen-Tannoudji, G. Grynberg, and J. Dupont-Roc, *Atom-Photon Interactions: Basic Processes and Applications* (Wiley, New York, 1998).

[64] N. Tomita and K. Nasu, Quantum fluctuation effects on light absorption spectra of the one-dimensional extended Hubbard model, Phys. Rev. B **63**, 085107 (2001).

[65] T. J. Park and J. C. Light, Unitary quantum time evolution by iterative Lanczos reduction, J. Chem. Phys. **85**, 5870 (1986).

[66] E. S. Smyth, J. S. Parker, and K. Taylor, Numerical integration of the time-dependent Schrödinger equation for laser-driven helium, Comput. Phys. Commun. **114**, 1 (1998).

[67] X. Guan, O. Zatsarinny, K. Bartschat, B. I. Schneider, J. Feist, and C. J. Noble, General approach to few-cycle intense laser interactions with complex atoms, Phys. Rev. A **76**, 053411 (2007).

[68] A. L. Frapiccini, A. Hamido, S. Schröter, D. Pyke, F. Mota-Furtado, P. F. O'Mahony, J. Madroñero, J. Eiglsperger, and B. Piraux, Explicit schemes for time propagating many-body wave functions, Phys. Rev. A **89**, 023418 (2014).

[69] J. C. Baggesen and L. B. Madsen, On the dipole, velocity and acceleration forms in high-order harmonic generation from a single atom or molecule, J. Phys. B **44**, 115601 (2011).

[70] C. Gerry and P. Knight, *Introductory Quantum Optics* (Cambridge University Press, New York, 2004).

[71] M. O. Scully and M. S. Zubairy, *Quantum Optics* (Cambridge University, New York, 1997).

[72] S. L. Braunstein and P. van Loock, Quantum information with continuous variables, Rev. Mod. Phys. **77**, 513 (2005).

[73] R. E. Slusher, L. W. Hollberg, B. Yurke, J. C. Mertz, and J. F. Valley, Observation of squeezed states generated by four-wave mixing in an optical cavity, Phys. Rev. Lett. **55**, 2409 (1985).

[74] G. Breitenbach, S. Schiller, and J. Mlynek, Measurement of the quantum states of squeezed light, Nature (London) **387**, 471 (1997).

[75] R. Short and L. Mandel, Observation of sub-poissonian photon statistics, Phys. Rev. Lett. **51**, 384 (1983).

[76] T. J. Bartley, G. Donati, X.-M. Jin, A. Datta, M. Barbieri, and I. A. Walmsley, Direct observation of sub-binomial light, Phys. Rev. Lett. **110**, 173602 (2013).

[77] F. Gebhard, *The Mott Metal-Insulator Transition: Models and Methods* Vol. 137 (Springer-Verlag, Berlin, 1997).

[78] S. Maekawa, *Physics of Transition Metal Oxides*, 1st ed., Springer Series in Solid-State Sciences (Springer-Verlag, Berlin, 2004).

[79] T. Oka, Nonlinear doublon production in a Mott insulator: Landau-Dykhne method applied to an integrable model, Phys. Rev. B **86**, 075148 (2012).

[80] T. Hansen and L. B. Madsen, Effects of lattice imperfections on high-harmonic generation from correlated systems, arXiv:2306.08379.

[81] I. A. Walmsley, Quantum optics: Science and technology in a new light, Science **348**, 525 (2015).

[82] G. D. Mahan, *Many-Particle Physics* (Springer, New York, 2000).

Phys. Rev. Lett. 135, 043603 (2025)

Paper information

By the terms and conditions of the American Physical Society's Reuse and Permissions License, the paper Digital Object Identifier (DOI) is provided: 10.1103/wyk5-k8tk. Reprinted with permission from C. S. Lange, Thomas Hansen, and L. B. Madsen, *Excitonic Enhancement of Squeezed Light in Quantum-Optical High-Harmonic Generation from a Mott Insulator*, Phys. Rev. Lett. **135**, 043603 (2025).

Author contributions

I conducted the numerical simulations and contributed to the analysis and interpretation of the research findings. Additionally, I was involved in preparing the manuscript, including the creation of figures.

PHYSICAL REVIEW LETTERS **135,** 043603 (2025)

Excitonic Enhancement of Squeezed Light in Quantum-Optical High-Harmonic Generation from a Mott Insulator

Christian Saugbjerg Lange, Thomas Hansen, and Lars Bojer Madsen
Department of Physics and Astronomy, Aarhus University, Ny Munkegade 120, DK-8000 Aarhus C, Denmark

(Received 20 March 2025; revised 26 May 2025; accepted 8 July 2025; published 24 July 2025)

The strong-field induced generation of nonclassical states of light is not only a subject of fundamental research but also has potential usage in quantum information science and technology. The emerging field of strong-field quantum optics has developed ways of generating nonclassical states of light from the process of high-harmonic generation (HHG) at much wider frequency ranges and intensities than is typical for quantum optics. Here, we study the response from an exciton in a Mott-insulating system, using the extended Hubbard model. We find that the exciton plays a key role in the nonclassical response and generates squeezing at the exciton energy, showing a clear mapping between the quantum nature of the electronic system and the quantum nature of emitted radiation. We relate this nonclassical response to the nonvanishing time correlations of the current operator in the system. Our work defines a direction for experimental work to search for squeezed light from HHG in a spectrally confined region defined by the exciton energy.

DOI: 10.1103/wyk5-k8tk

For decades, a semiclassical description of strong-field processes with quantized electrons and classical electromagnetic fields has been successful. In recent years, a shift toward a fully quantized description including the quantized electromagnetic field has begun in an effort to merge the fields of strong-field physics and quantum optics. This emerging field of strong-field quantum optics enables the study of strong-field processes at a fundamental level, as it enables inquiries at the quantum level regarding, e.g., light-matter and photonic-mode entanglement. Such investigations bring new insights and can lead to potential applications in quantum information at ultrafast timescales [1].

In quantum optics, one typically considers only a few photons and a few electronic states. In strong-field physics, the case is quite the opposite because a macroscopic number of photons is involved and the electronic Hilbert space involves many electronic states including the continuum. Consequently, new theoretical approaches to a quantum optical description of a macroscopic number of photons are needed. In recent years, various strong-field phenomena have been considered from a quantum optical perspective. For example, free electrons coupled to a quantized electromagnetic field can probe the photon statistics of the driving field [2], transfer optical coherence [3], generate quantum light [4,5], have the quantum statistics of photons imprinted onto the electronic spectrum [6], can be used for photonic state tomography [7], and even have applications in quantum information science [8]. Additionally, other strong-field processes such as strong-field ionization have been considered with nonclassical driving fields for both single [9] and double ionization [10] of atoms, revealing how the nonclassical nature of the driver significantly influences the ionization process. A key process in strong-field physics is high-order harmonic generation (HHG). Many works have surfaced studying HHG from a quantum optical perspective, revealing that the emitted light is indeed nonclassical from atoms [11–13], correlated solids [14,15], and entangled systems [16], and can be engineered by subsequent measurements to generate an optical cat state [17,18]. Experimental works are confirming the nonclassical nature of light generated by HHG [18–22]. Works have considered HHG with nonclassical driving fields, in particular bright-squeezed vacuum [23,24], showing that the photon statistics of the driver drastically change the emitted harmonic spectrum [25–28]. Recently, experiments with nonclassical driving fields [29–33] have revealed how the nonclassical driver generates nonclassical states of light in HHG.

So far, when driven by a coherent state, all electronic systems considered have shown weak squeezing in the emitted light from HHG at seemingly arbitrary frequencies with no clear, strong squeezing at a distinct and clearly identifiable wavelength [11,14,15]. The lack of such a clear unambiguous signal at a well-defined frequency has hindered a clear identification of the relation between the electronic system and its nonclassical response, and it also poses a challenge to future experimental work, as the broad frequency range with weak squeezing signal puts high demands on the experimental equipment. From semiclassical HHG studies, it has recently been found that excitons play a prominent role in the nonlinear response of the

system [34–36]. Here, we study the excitonic effects on the nonclassical response in HHG from Mott insulators. We find a relatively large degree of squeezing centered around the exciton energy. This response is drastically different from that reported earlier from an exciton-free Mott insulator both semiclassically [34] and quantum optically [14,15] and shows a clear mapping between the presence of the exciton and the nonclassical response. Mott excitons have been observed in, e.g., nickel compounds [37,38] as well as Sr_2IrO_4 and $Sr_3Ir_2O_7$ [39].

We study the excitonic effects on the nonclassical response in HHG from a Mott insulator using the extended Hubbard model (atomic units used throughout)

$$\hat{H}_{\mathrm{sc}}(t) = \hat{H}_{\mathrm{hop}}(t) + \hat{H}_{e-e} \tag{1}$$

with kinetic energy from nearest-neighbor hopping modified by the driving field

$$\hat{H}_{\mathrm{hop}}(t) = -t_0 \sum_{j,\mu} \left(e^{iaA_{\mathrm{cl}}(t)} \hat{c}^{\dagger}_{j,\mu} \hat{c}_{j+1,\mu} + \mathrm{H.c.} \right) \tag{2a}$$

and potential energy from electron-electron repulsion

$$\hat{H}_{e-e} = U \sum_{j} \hat{n}_{j,\uparrow} \hat{n}_{j,\downarrow} + V \sum_{j} \hat{n}_{j} \hat{n}_{j+1}, \tag{2b}$$

where $\hat{c}_{j,\mu}$ ($\hat{c}^{\dagger}_{j,\mu}$) is the electronic annihilation (creation) operator on site j with spin $\mu = (\uparrow, \downarrow)$, $\hat{n}_{j,\mu} = \hat{c}^{\dagger}_{j,\mu} \hat{c}_{j,\mu}$ is the electronic counting operator, and $\hat{n}_j = \hat{n}_{j,\uparrow} + \hat{n}_{j,\downarrow}$. Following similar works, we set the nearest-neighbor hopping amplitude $t_0 = 0.0191$ a.u. and the lattice spacing $a = 7.5589$ a.u. [14,15,40–43]. $A_{\mathrm{cl}}(t)$ is the classical driving field entering Perierl's phase, and U and V are the parameters for the on-site and nearest-neighbor electron-electron repulsion, respectively. We consider a 1D cut along the linear polarization of A_{cl}, employ periodic boundary conditions, and assume half filling with an equal number of both spin orientations. Note that for $U = V = 0$, the system is a simple tight-binding model for uncorrelated electrons which can be diagonalized in crystal-momentum space, i.e., in a Bloch basis. For $U, V \neq 0$, the electrons are correlated meaning the electrons interact through U and V and are all treated simultaneously: the dynamics of one electron depends on all the others. We limit ourselves to $L = 8$ electrons, $U = 12t_0$, and $V = 4t_0$ which supports a spin-density-wave phase and the presence of excitons in the Mott insulator. For details on U and V and the related phases of the system, see Ref. [44]. The V binds the empty sites (holons) to doubly occupied sites (doublons) giving rise to the Mott exciton. When $V = 0$, there are no excitons in the system. The effect of $V \neq 0$ is illustrated in Fig. 1(a), where three different electron configurations are shown with their respective potential energies [Eq. (2b)] on the right (periodic boundary conditions). An electron hopping

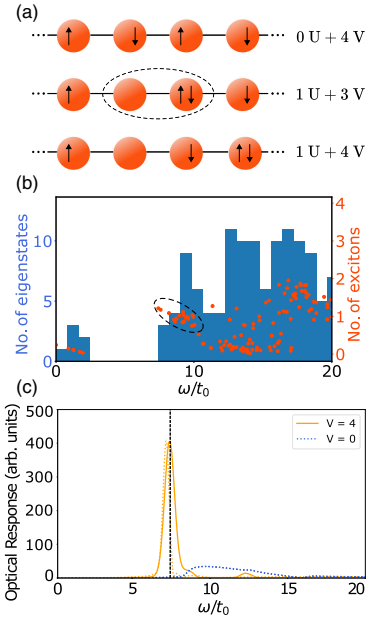

FIG. 1. (a) Schematic of electron configurations and their potential energy obtained from Eq. (2b) assuming periodic boundary conditions. V effectively binds the doublon and holon giving rise to the exciton (dashed ellipse). (b) Energy histogram of the field-free eigenstates (blue) obtained from exact diagonalization for the low-energy regime of the system. The red dots show the expectation value of the number of excitons. (c) Linear optical response. A clear and distinct peak for the exciton system (orange) is seen, while the blue curve shows the system without the presence of excitons ($V = 0$). The vertical dashed line indicates the exciton energy, while the dotted curves show the linear response from an infinite system (see text) normalized to the linear response from the finite system (solid orange).

from the antiferromagnetic state which is present in the ground state of the system (top row) creates a doublon and a holon (middle row) next to each other. An additional electron hop separating the holon and doublon (bottom row) comes with an increase in potential energy from evaluating Eq. (2b). In this sense, V effectively binds the doublon and holon giving rise to the exciton. To further characterize the system, we obtain the field-free eigenstates of Eq. (1) from exact diagonalization and show the corresponding energies in Fig. 1(b). Here, the lowest-lying states, including the ground state, are energetically separated by an energy gap making the system insulating. Further, we calculate the expectation value of the number of excitons in the field-free eigenstates, indicated by red dots in Fig. 1(b). The lowest-lying states contain virtually no excitons, while the lowest energy states above the energy gap (marked by a dashed eclipse) contain approximately

one exciton, which means that the energy gap from the ground state to the lowest-lying states across the gap is equal to the exciton energy. This is in line with the fact that the ground state is dominated by configurations with single-site occupations from which all first-order transitions result in the creation of an exciton and hence a substantial energy increase. The effect of the exciton is also clearly seen from the linear optical response obtained by applying a single-cycle, perturbative high-frequency pulse ($\omega \approx 10t_0$). In fact, it is the transition energy between the ground state and exciton states that dominates the optical linear response as seen in Fig. 1(c), where the single dominating peak for $V = 4t_0$ corresponds exactly to the above-mentioned transition congruent with previous studies [34,44,45]. The solid orange curve is obtained from exact diagonalization, while the dotted curves are obtained from infinite time-evolving block decimation calculations (iTEBD) [46,47] for an infinite system, showing that the strong exciton response (dashed orange) is still present in a large system and is not a finite-size effect. We note that without excitons in the system, $V = 0$ (dashed blue), the linear optical response is a weaker continuum above the band gap without any clear peaks, showing that the response from free doublon-holon dynamics is drastically different from the exciton dynamics. A more detailed semiclassical analysis of the system in relation to HHG can be found in Ref. [34].

We now turn to a fully quantum optical description of the HHG process. After transforming away the coherent driving field, the Hamiltonian of the system is given as [11,14,15]

$$\hat{H}(t) = \hat{H}_{\mathrm{sc}}(t) + \hat{\boldsymbol{A}} \cdot \hat{\boldsymbol{j}}(t) + \hat{H}_F, \tag{3}$$

where $\hat{H}_{\mathrm{sc}}(t)$ is the semiclassical Hamiltonian given in Eq. (1), and $\hat{\boldsymbol{A}} = \sum_{\boldsymbol{k},\sigma}(g_0/\sqrt{\omega_k})(\hat{a}_{\boldsymbol{k},\sigma} + \mathrm{H.c.})$ is the quantized vector potential in the dipole approximation with g_0 the coupling constant. The operator $\hat{a}_{\boldsymbol{k},\sigma}$ annihilates a photon with momentum $\boldsymbol{k}$ and polarization σ with $\hat{a}^\dagger_{\boldsymbol{k},\sigma}$ being the corresponding creation operator, $\hat{\boldsymbol{j}}(t) = -iat_0 \sum_{j,\mu}\left(e^{iaA_{\mathrm{cl}}(t)}\hat{c}^\dagger_{j,\mu}\hat{c}_{j+1,\mu} - \mathrm{H.c.}\right)\hat{\boldsymbol{x}}$ is the current operator taken along the direction of the chain, and $\hat{H}_F = \sum_{\boldsymbol{k},\sigma}\omega_k \hat{a}^\dagger_{\boldsymbol{k},\sigma}\hat{a}_{\boldsymbol{k},\sigma}$ is the Hamiltonian of the free electromagnetic field. Inserting Eq. (3) into the time-dependent Schrödinger equation (TDSE), $i\partial_t|\Psi(t)\rangle = \hat{H}(t)|\Psi(t)\rangle$, and going to a rotating frame with respect to $\hat{H}_{\mathrm{sc}}(t)$ and $\hat{H}_F$, we obtain the equation of motion

$$i\partial_t|\chi^{(m)}_{\boldsymbol{k},\sigma}(t)\rangle = \hat{\boldsymbol{A}}^{(\boldsymbol{k},\sigma)}_Q(t) \cdot \sum_n \boldsymbol{j}_{m,n}(t)|\chi^{(n)}_{\boldsymbol{k},\sigma}(t)\rangle, \tag{4}$$

where $|\chi^{(m)}_{\boldsymbol{k},\sigma}(t)\rangle = \langle\phi_m|\Psi(t)\rangle$ is the photonic state correlated to the mth electronic eigenstate, $|\phi_m\rangle$, and $\boldsymbol{j}_{m,n}(t) = \langle\phi_m|\hat{\boldsymbol{j}}_H(t)|\phi_n\rangle$ are current matrix elements with $\hat{\boldsymbol{j}}_H(t) = \mathcal{U}^\dagger_{\mathrm{sc}}(t)\hat{\boldsymbol{j}}(t)\mathcal{U}_{\mathrm{sc}}(t)$ a Heisenberg-type operator of the current operator with $\mathcal{U}_{\mathrm{sc}}(t)$ the time-evolution operator for $\hat{H}_{\mathrm{sc}}(t)$ of Eq. (1). In Eq. (4), $\hat{\boldsymbol{A}}^{(\boldsymbol{k},\sigma)}_Q(t) = (g_0/\sqrt{\omega_k})\times(\hat{a}_{\boldsymbol{k},\sigma}e^{-i\omega_k t} + \mathrm{H.c.})$ is the time-dependent operator for the vector potential acting on mode $(\boldsymbol{k},\sigma)$, and the photonic modes are decoupled as in Refs. [11,14,15] in order to be able to solve the dynamics numerically. We use a coherent driving pulse $A_{\mathrm{cl}}(t) = (F_0/\omega_L)e^{-(t-t_c)^2/2\sigma_L^2}\sin[\omega_L(t-t_c)]$ with $F_0 = 0.0025$ a.u. corresponding to peak intensity of 2.2×10^{11} W/cm^2 and $\omega_L = t_0/2 = 0.00955$ a.u. = 396 THz the carrier angular frequency of the pulse such that the exciton energy in Fig. 1(c) is $\omega \approx 15\omega_L$. The parameter $t_c = 15T_L$ is the central peak time of the pulse, $\sigma_L = 3T_L$ is the pulse width where $T_L = 2\pi/\omega_L$, and we set $g_0 = 4 \times 10^{-8}$ a.u. [11,14,15,17]. We obtain $\boldsymbol{j}_{m,n}(t)$ from a semiclassical TDSE integration using the Arnoldi-Lancoz algorithm [48–51] with the dimension of the Krylov subspace set to 6 [14,15]. Once all currents are obtained, Eq. (4) is solved by fourth-order Runge-Kutta integration by expanding the photonic state in a Fock basis truncated at maximum 50 photons. All numerical results have been checked for convergence.

Before discussing the results, we consider a newly derived approximative expression for the photonic state, the so-called Markov-state approximation (MSA), first presented in Ref. [12] and numerically verified in Ref. [15]. It is obtained by considering only current matrix elements involving the initial state, then performing a Markov approximation, and finally neglecting higher-order terms in g_0. The photonic state in the MSA is given as

$$|\chi^{(i)}_{\boldsymbol{k},\sigma}(t)\rangle = \hat{D}[\beta_{\boldsymbol{k},\sigma}(t)]e^{-\langle\hat{W}^2_{\boldsymbol{k},\sigma}(t)\rangle_{\mathrm{el}}}|0\rangle, \tag{5}$$

where $\hat{D}[\beta_{\boldsymbol{k},\sigma}(t)] = \exp[\beta_{\boldsymbol{k},\sigma}(t)\hat{a}^\dagger_{\boldsymbol{k},\sigma} - \beta^*_{\boldsymbol{k},\sigma}(t)\hat{a}_{\boldsymbol{k},\sigma}]$ is the displacement operator with $\beta_{\boldsymbol{k},\sigma}(t) = -i(g_0/\sqrt{\omega_k})\int^t dt'\langle\hat{\boldsymbol{j}}(t')\rangle\cdot\hat{\boldsymbol{e}}^*_\sigma e^{i\omega_k t'}$ and

$$\langle\hat{W}^2_{\boldsymbol{k},\sigma}(t)\rangle_{\mathrm{el}} = \int^t dt' \int^t dt'' \hat{A}^{(\boldsymbol{k},\sigma)}_Q(t')\hat{A}^{(\boldsymbol{k},\sigma)}_Q(t'')C(t',t''), \tag{6}$$

with $C(t',t'') = \langle\hat{\boldsymbol{j}}_H(t')\hat{\boldsymbol{j}}_H(t'')\rangle - \langle\hat{\boldsymbol{j}}_H(t)\rangle\langle\hat{\boldsymbol{j}}_H(t'')\rangle$ the time-correlation function of the current operator, $\hat{\boldsymbol{j}}_H(t)$. The variables t' and t'' appear as integration variables in Eq. (6) originating from an iterative expansion of the time evolution to obtain the MSA [15]. The subscript on the left-hand side of Eq. (6) denotes an expectation value only over the electronic degrees of freedom such that $\langle\hat{W}^2_{\boldsymbol{k},\sigma}(t)\rangle_{\mathrm{el}}$ is an operator in the photonic Hilbert space. Equation (5) shows that if $C(t',t'') = 0$, i.e., if the currents are completely uncorrelated in time, the photonic state is a coherent state with no squeezing. On the other hand, if $C(t',t'') \neq 0$, Eq. (6) shows that the MSA contains quadratic photonic

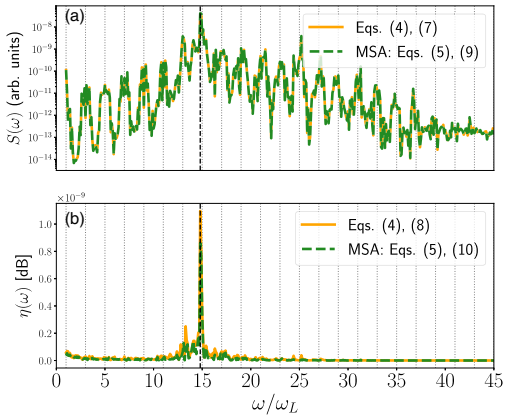

FIG. 2. (a) Spectra obtained from Eqs. (4) and (7) (orange) and the MSA expressions in Eqs. (5) and (9) (dashed green). The spectra peak at the exciton energy (vertical dashed line at $\omega \approx 15\omega_L$) showing that the exciton plays a significant role in the nonlinear response. (b) Squeezing from Eqs. (4) and (8) (orange) and the MSA expressions from Eqs. (5) and (10) (dashed green). A clear peak in the signal is present at the exciton energy showing that the exciton is prominent in the nonclassical response of the system. The MSA captures the spectrum in (a) exactly and the squeezing to a good degree in (b). The vertical dotted lines at odd harmonics are added to guide the eye.

operators which generate squeezing [52–54]. The MSA description thus shows that the nonclassical response of the system is due to the time correlations of the induced current, which is similar to considering depletion of the ground state; see the End Matter.

We consider two observables in the HHG simulation: the spectrum and the squeezing. In the quantum optical formulation, the spectrum is given as [11,14]

$$S(\omega) = \frac{\omega^3}{g_0^2(2\pi)^2 c^3} \sum_{\sigma} \langle \hat{a}^{\dagger}_{\boldsymbol{k},\sigma} \hat{a}_{\boldsymbol{k},\sigma} \rangle, \tag{7}$$

where ω is the frequency of the mode $(\boldsymbol{k}, \sigma)$ and c is the speed of light in vacuum. The degree of squeezing is given by the expression [54,55]

$$\eta_{\boldsymbol{k},\sigma} = -10\log_{10}\left\{ 4 \min_{\theta \in [0,\pi)} [\Delta \hat{X}_{\boldsymbol{k},\sigma}(\theta)]^2 \right\}, \tag{8}$$

where the minimization is of the variance of the quadrature operator $\hat{X}_{\boldsymbol{k},\sigma}(\theta) = (\hat{a}_{\boldsymbol{k},\sigma} e^{-i\theta} + \text{H.c.})/2$. A nonvanishing squeezing, $\eta_{\boldsymbol{k},\sigma} > 0$, shows the presence of nonclassical states of light [52].

Figure 2 shows the results obtained from numerical integration of Eq. (4) (solid orange) and from the MSA [Eq. (5)] (dashed green). Figure 2(a) shows that the spectrum [Eq. (7)] peaks at the exciton energy ($\omega \approx 15\omega_L$), indicated by the vertical dashed line, showing that the exciton is highly involved in the nonlinear response [34]. We note that clear harmonic peaks are present in Fig. 2(a). The presence of such peaks is sensitive to the pulse duration (see, e.g., Ref. [43]). The spectrum in the MSA is given as [15]

$$S^{(\mathrm{MSA})}(\omega) = \frac{\omega^2}{(2\pi)^2 c^3} \sum_{\sigma} |\hat{\boldsymbol{e}}^*_{\sigma} \cdot \langle \hat{\boldsymbol{j}}(\omega) \rangle|^2, \tag{9}$$

which is proportional to the square of the Fourier transform of the current and is hence similar to the semiclassical expression for the spectrum. In other words, the quantum optical description of HHG does not, to leading order in the coupling constant, g_0, predict deviations from the classical spectrum [14,15].

The degree of squeezing calculated from Eq. (8) and shown in Fig. 2(b) (orange line), shows a distinct peak at the exciton energy highlighting that the exciton dominates the nonclassical response of the system. To analyze the origin of this squeezing, we use the expression from the MSA also illustrated in Fig. 2(b) (green dashed line), which shows good agreement with the more exact calculation. In the MSA, the expression for the degree of squeezing is given as [15]

$$\eta^{(\mathrm{MSA})}_{\boldsymbol{k},\sigma} = -10\log_{10}\left\{ \min_{\theta \in [0,\pi)} [1 - 2B_{\boldsymbol{k},\sigma} \cos(2\theta - \phi)] \right\}, \tag{10}$$

where ϕ is a phase related to $B_{\boldsymbol{k},\sigma} = (g_0^2/\omega_k)| \int_{-\infty}^{\infty} dt' \times \int_{-\infty}^{\infty} dt'' \exp[i\omega_k(t' + t'')] C(t', t'')|$. Equation (10) shows that the degree of squeezing is determined by $B_{\boldsymbol{k},\sigma}$ which is related to the time-correlation function $C(t', t'')$. Interestingly, a similar time-correlation function was considered in the Heisenberg picture in early work on HHG but not in the context of the nonclassical observables [56]. For $U \neq 0$ and $V \neq 0$, the electrons are correlated, and Eq. (10) shows that this correlation generates the squeezing, in accordance with the results presented in Fig. 2(b) where it is clearly seen that the presence of an exciton is central to the nonclassical response of the system. The reported degree of squeezing is low compared to studies assuming coherent participation of thousands of atoms [11]. However, the present results are obtained with $L = 8$ electrons and hence qualitatively show that the exciton is principal to the nonclassical response of the system. As the current operator encompasses more sites with increasing system size, the fluctuations likewise increase with system size for constant electron filling. We hence believe the squeezing will be much larger for a macroscopic system or with an enhanced coupling strength, g_0. Our findings also encourage experimental work: if the linear response of such an excitonic system is measured, we predict that the light emitted from HHG at the exciton energy will have a relatively large degree of squeezing. This puts fewer demands on the

experimental equipment as only a small frequency window has to be considered. The spectral width of the excitonic peak in Fig. 2 is ∼396 THz (angular frequencies) centered at 5940 THz. In contrast, if one considers the squeezing in, e.g., Ref. [14], the range of squeezing is ∼3110 THz centered at 6740 THz. Clearly, the frequencies in this work put fewer demands on the optical equipment in terms of the frequency range required to capture squeezing at all the frequencies of the generated radiation.

When simulating HHG from solids, it is relevant to discuss the role of dephasing. Electron dephasing is typically added phenomenologically in a formulation using semiconductor Bloch equations (SBE) for independent electrons. Notably, to match experimental results, the required dephasing times are a few femtoseconds [57] which in real space strongly suppresses long electron trajectories [58]. The sources of electron dephasing are, e.g., lattice imperfections, electron-phonon scattering, and, most importantly in the strong-field regime, electron-electron scattering [59]. In fact, it is the latter that requires the very short dephasing time mentioned above. In contrast to the modeling using SBEs with additional dephasing terms, the electron-electron interaction is already accounted for in the dynamics of strongly correlated materials making additional phenomenological dephasing redundant. In the electronic system considered here, the correlation length is 1.15 lattice sites (calculated using iTEBD; see, e.g., Refs. [46,47]). This correlation length on the order of a lattice spacing, which is due to electron-electron correlations, clearly shows that long electron trajectories are strongly suppressed, consistent with the analysis of both Refs. [58] and [59]. Further, as clear harmonic peaks are generated in the spectrum in Fig. 2(a) consistent with experimental results [60,61], the motivation for the inclusion of additional decoherence effects in excess to that already accounted for in the electronic degrees of freedom is lacking.

In summary, we have considered the nonclassical response of an exciton in a Mott-insulating system. This response has previously been studied semiclassically showing that the exciton plays a central role in the HHG spectrum [34]. Here, we have gone beyond the semiclassical analysis and considered the full quantum optical description of the HHG process, and found that the exciton is also central in the nonclassical response as a relatively large degree of squeezing was found at the exciton energy. We interpreted this finding in the MSA and found that this nonclassical response is due to a nonvanishing time correlation of the current, which shows that the exciton is a key ingredient in the degree of correlation in the system. Previous studies have not shown a clear nonclassical response at a distinct and unambiguous energy, and as such, our findings motivate further work to investigate the squeezing of the light emitted from HHG in Mott insulators at the exciton energy. This also opens the avenue to consider how the degree of squeezing is sensitive to, e.g., different carrier-envelope phases, pulse durations, and laser intensities which are topics beyond the scope of this work.

Acknowledgments—This work was supported by the Independent Research Fund Denmark (Grant No. 1026-00040B).

Data availability—The data that support the findings of this Letter are not publicly available upon publication because it is not technically feasible and/or the cost of preparing, depositing, and hosting the data would be prohibitive within the terms of this research project. The data are available from the authors upon reasonable request.

[1] M. Lewenstein, N. Baldelli, U. Bhattacharya, J. Biegert, M. F. Ciappina, T. Grass, P. T. Grochowski, A. S. Johnson, T. Lamprou, A. S. Maxwell, A. Ordóñez, E. Pisanty, J. Rivera-Dean, P. Stammer, and P. Tzallas, Attosecond physics and quantum information science, in *Proceedings of the 8th International Conference on Attosecond Science and Technology*, edited by L. Argenti, M. Chini, and L. Fang (Springer International Publishing, Cham, 2024), pp. 27–44, 10.1007/978-3-031-47938-0_4.

[2] V. D. Giulio, M. Kociak, and F. J. G. de Abajo, Probing quantum optical excitations with fast electrons, Optica **6**, 1524 (2019).

[3] O. Kfir, V. D. Giulio, F. J. G. de Abajo, and C. Ropers, Optical coherence transfer mediated by free electrons, Sci. Adv. **7**, eabf6380 (2021).

[4] A. B. Hayun, O. Reinhardt, J. Nemirovsky, A. Karnieli, N. Rivera, and I. Kaminer, Shaping quantum photonic states using free electrons, Sci. Adv. **7**, eabe4270 (2021).

[5] R. Dahan, G. Baranes, A. Gorlach, R. Ruimy, N. Rivera, and I. Kaminer, Creation of optical cat and GKP states using shaped free electrons, Phys. Rev. X **13**, 031001 (2023).

[6] R. Dahan, A. Gorlach, U. Haeusler, A. Karnieli, O. Eyal, P. Yousefi, M. Segev, A. Arie, G. Eisenstein, P. Hommelhoff, and I. Kaminer, Imprinting the quantum statistics of photons on free electrons, Science **373**, eabj7128 (2021).

[7] A. Gorlach, S. Malka, A. Karnieli, R. Dahan, E. Cohen, A. Pe'er, and I. Kaminer, Photonic quantum state tomography using free electrons, Phys. Rev. Lett. **133**, 250801 (2024).

[8] R. Ruimy, A. Karnieli, and I. Kaminer, Free-electron quantum optics, Nat. Phys. **21**, 193 (2025).

[9] Y. Fang, F.-X. Sun, Q. He, and Y. Liu, Strong-field ionization of hydrogen atoms with quantum light, Phys. Rev. Lett. **130**, 253201 (2023).

[10] H. Liu, H. Zhang, X. Wang, and J. Yuan, Atomic double ionization with quantum light, Phys. Rev. Lett. **134**, 123202 (2025).

[11] A. Gorlach, O. Neufeld, N. Rivera, O. Cohen, and I. Kaminer, The quantum-optical nature of high harmonic generation, Nat. Commun. **11**, 4598 (2020).

[12] P. Stammer, J. Rivera-Dean, A. S. Maxwell, T. Lamprou, J. Argüello-Luengo, P. Tzallas, M. F. Ciappina, and M. Lewenstein, Entanglement and squeezing of the optical

field modes in high harmonic generation, Phys. Rev. Lett. **132**, 143603 (2024).

[13] S. Yi, N. D. Klimkin, G. G. Brown, O. Smirnova, S. Patchkovskii, I. Babushkin, and M. Ivanov, Generation of massively entangled bright states of light during harmonic generation in resonant media, Phys. Rev. X **15**, 011023 (2025).

[14] C. S. Lange, T. Hansen, and L. B. Madsen, Electron-correlation-induced nonclassicality of light from high-order harmonic generation, Phys. Rev. A **109**, 033110 (2024).

[15] C. S. Lange and L. B. Madsen, Hierarchy of approximations for describing quantum light from high-harmonic generation: A Fermi-Hubbard-model study, Phys. Rev. A **111**, 013113 (2025).

[16] A. Pizzi, A. Gorlach, N. Rivera, A. Nunnenkamp, and I. Kaminer, Light emission from strongly driven many-body systems, Nat. Phys. **19**, 551 (2023).

[17] M. Lewenstein, M. F. Ciappina, E. Pisanty, J. Rivera-Dean, P. Stammer, T. Lamprou, and P. Tzallas, Generation of optical Schrödinger cat states in intense laser–matter interactions, Nat. Phys. **17**, 1104 (2021).

[18] T. Lamprou, P. Stammer, J. Rivera-Dean, N. Tsatrafyllis, M. F. Ciappina, M. Lewenstein, and P. Tzallas, Recent developments in the generation of non-classical and entangled light states using intense laser-matter interactions, arXiv:2410.17452.

[19] I. A. Gonoskov, N. Tsatrafyllis, I. K. Kominis, and P. Tzallas, Quantum optical signatures in strong-field laser physics: Infrared photon counting in high-order-harmonic generation, Sci. Rep. **6**, 32821 (2016).

[20] N. Tsatrafyllis, I. K. Kominis, I. A. Gonoskov, and P. Tzallas, High-order harmonics measured by the photon statistics of the infrared driving-field exiting the atomic medium, Nat. Commun. **8**, 15170 (2017).

[21] N. Tsatrafyllis, S. Kühn, M. Dumergue, P. Foldi, S. Kahaly, E. Cormier, I. A. Gonoskov, B. Kiss, K. Varju, S. Varro, and P. Tzallas, Quantum optical signatures in a strong laser pulse after interaction with semiconductors, Phys. Rev. Lett. **122**, 193602 (2019).

[22] D. Theidel, V. Cotte, R. Sondenheimer, V. Shiriaeva, M. Froidevaux, V. Severin, A. Merdji-Larue, P. Mosel, S. Fröhlich, K.-A. Weber, U. Morgner, M. Kovacev, J. Biegert, and H. Merdji, Evidence of the quantum optical nature of high-harmonic generation, PRX Quantum **5**, 040319 (2024).

[23] M. Manceau, K. Y. Spasibko, G. Leuchs, R. Filip, and M. V. Chekhova, Indefinite-mean pareto photon distribution from amplified quantum noise, Phys. Rev. Lett. **123**, 123606 (2019).

[24] P. R. Sharapova, G. Frascella, M. Riabinin, A. M. Pérez, O. V. Tikhonova, S. Lemieux, R. W. Boyd, G. Leuchs, and M. V. Chekhova, Properties of bright squeezed vacuum at increasing brightness, Phys. Rev. Res. **2**, 013371 (2020).

[25] M. Even Tzur, M. Birk, A. Gorlach, M. Krüger, I. Kaminer, and O. Cohen, Photon-statistics force in ultrafast electron dynamics, Nat. Photonics **17**, 501 (2023).

[26] A. Gorlach, M. E. Tzur, M. Birk, M. Krüger, N. Rivera, O. Cohen, and I. Kaminer, High-harmonic generation driven by quantum light, Nat. Phys. **19**, 1689 (2023).

[27] M. E. Tzur, M. Birk, A. Gorlach, I. Kaminer, M. Krüger, and O. Cohen, Generation of squeezed high-order harmonics, Phys. Rev. Res. **6**, 033079 (2024).

[28] R. V. Gothelf, C. S. Lange, and L. B. Madsen, High-harmonic generation in a crystal driven by quantum light, Phys. Rev. A **111**, 063105 (2025).

[29] K. Y. Spasibko, D. A. Kopylov, V. L. Krutyanskiy, T. V. Murzina, G. Leuchs, and M. V. Chekhova, Multiphoton effects enhanced due to ultrafast photon-number fluctuations, Phys. Rev. Lett. **119**, 223603 (2017).

[30] A. Rasputnyi, Z. Chen, M. Birk, O. Cohen, I. Kaminer, M. Krüger, D. Seletskiy, M. Chekhova, and F. Tani, High-harmonic generation by a bright squeezed vacuum, Nat. Phys. **20**, 1960 (2024).

[31] S. Lemieux, S. A. Jalil, D. N. Purschke, N. Boroumand, T. J. Hammond, D. Villeneuve, A. Naumov, T. Brabec, and G. Vampa, Photon bunching in high-harmonic emission controlled by quantum light, Nat. Photonics **19**, 767 (2025).

[32] M. E. Tzur, C. Mor, N. Yaffe, M. Birk, A. Rasputnyi, O. Kneller, I. Nisim, I. Kaminer, M. Krüger, N. Dudovich, and O. Cohen, Measuring and controlling the birth of quantum attosecond pulses, arXiv:2502.09427.

[33] T. Lamprou, J. Rivera-Dean, P. Stammer, M. Lewenstein, and P. Tzallas, Nonlinear optics using intense optical coherent state superpositions, Phys. Rev. Lett. **134**, 013601 (2025).

[34] M. Udono, K. Sugimoto, T. Kaneko, and Y. Ohta, Excitonic effects on high-harmonic generation in Mott insulators, Phys. Rev. B **105**, L241108 (2022).

[35] E. B. Molinero, B. Amorim, M. Malakhov, G. Cistaro, Álvaro Jiménez-Galán, A. Picón, P. San-José, M. Ivanov, and R. E. F. Silva, Subcycle dynamics of excitons under strong laser fields, Sci. Adv. **10**, eadn6985 (2024).

[36] S. V. B. Jensen, L. B. Madsen, A. Rubio, and N. Tancogne-Dejean, High-harmonic spectroscopy of strongly bound excitons in solids, Phys. Rev. A **109**, 063104 (2024).

[37] M. Ono, K. Miura, A. Maeda, H. Matsuzaki, H. Kishida, Y. Taguchi, Y. Tokura, M. Yamashita, and H. Okamoto, Linear and nonlinear optical properties of one-dimensional Mott insulators consisting of Ni-halogen chain and CuO-chain compounds, Phys. Rev. B **70**, 085101 (2004).

[38] M. Ono, H. Kishida, and H. Okamoto, Direct observation of excitons and a continuum of one-dimensional Mott insulators: A reflection-type third-harmonic-generation study of ni-halogen chain compounds, Phys. Rev. Lett. **95**, 087401 (2005).

[39] O. Mehio, Y. Han, X. Li, H. Ning, Z. Porter, S. D. Wilson, and D. Hsieh, Observation of excitons bound by antiferromagnetic correlations, Phys. Rev. Res. **7**, 013114 (2025).

[40] R. E. F. Silva, I. V. Blinov, A. N. Rubtsov, O. Smirnova, and M. Ivanov, High-harmonic spectroscopy of ultrafast many-body dynamics in strongly correlated systems, Nat. Photonics **12**, 266 (2018).

[41] T. Hansen, S. V. B. Jensen, and L. B. Madsen, Correlation effects in high-order harmonic generation from finite systems, Phys. Rev. A **105**, 053118 (2022).

[42] T. Hansen and L. B. Madsen, Doping effects in high-harmonic generation from correlated systems, Phys. Rev. B **106**, 235142 (2022).

[43] C. S. Lange, T. Hansen, and L. B. Madsen, Noninteger high-order harmonic generation from extended correlated systems, Phys. Rev. A **109**, 063103 (2024).
[44] E. Jeckelmann, Optical excitations in a one-dimensional Mott insulator, Phys. Rev. B **67**, 075106 (2003).
[45] F. H. L. Essler, F. Gebhard, and E. Jeckelmann, Excitons in one-dimensional Mott insulators, Phys. Rev. B **64**, 125119 (2001).
[46] G. Vidal, Classical simulation of infinite-size quantum lattice systems in one spatial dimension, Phys. Rev. Lett. **98**, 070201 (2007).
[47] J. A. Kjäll, M. P. Zaletel, R. S. K. Mong, J. H. Bardarson, and F. Pollmann, Phase diagram of the anisotropic spin-2 XXZ model: Infinite-system density matrix renormalization group study, Phys. Rev. B **87**, 235106 (2013).
[48] T. J. Park and J. C. Light, Unitary quantum time evolution by iterative Lanczos reduction, J. Chem. Phys. **85**, 5870 (1986).
[49] E. S. Smyth, J. S. Parker, and K. Taylor, Numerical integration of the time-dependent Schrödinger equation for laser-driven helium, Comput. Phys. Commun. **114**, 1 (1998).
[50] X. Guan, O. Zatsarinny, K. Bartschat, B. I. Schneider, J. Feist, and C. J. Noble, General approach to few-cycle intense laser interactions with complex atoms, Phys. Rev. A **76**, 053411 (2007).
[51] A. L. Frapiccini, A. Hamido, S. Schröter, D. Pyke, F. Mota-Furtado, P. F. O'Mahony, J. Madroñero, J. Eiglsperger, and B. Piraux, Explicit schemes for time propagating many-body wave functions, Phys. Rev. A **89**, 023418 (2014).
[52] C. Gerry and P. Knight, *Introductory Quantum Optics* (Cambridge University Press, Cambridge, England, 2004).
[53] C. Cohen-Tannoudji, G. Grynberg, and J. Dupont-Roc, *Atom-Photon Interactions: Basic Processes and Applications* (Wiley, New York, 1998).
[54] M. O. Scully and M. S. Zubairy, *Quantum Optics* (Cambridge University Press, Cambridge, England, 1997).
[55] S. L. Braunstein and P. van Loock, Quantum information with continuous variables, Rev. Mod. Phys. **77**, 513 (2005).
[56] B. Sundaram and P. W. Milonni, High-order harmonic generation: Simplified model and relevance of single-atom theories to experiment, Phys. Rev. A **41**, 6571 (1990).
[57] G. Vampa, C. R. McDonald, G. Orlando, D. D. Klug, P. B. Corkum, and T. Brabec, Theoretical analysis of high-harmonic generation in solids, Phys. Rev. Lett. **113**, 073901 (2014).
[58] G. G. Brown, A. Jiménez-Galán, R. E. F. Silva, and M. Ivanov, Real-space perspective on dephasing in solid-state high harmonic generation, Phys. Rev. Res. **6**, 043005 (2024).
[59] U. Huttner, M. Kira, and S. W. Koch, Ultrahigh off-resonant field effects in semiconductors, Laser Photonics Rev. **11**, 1700049 (2017).
[60] M. R. Bionta, E. Haddad, A. Leblanc, V. Gruson, P. Lassonde, H. Ibrahim, J. Chaillou, N. Émond, M. R. Otto, A. Jiménez-Galán, R. E. F. Silva, M. Ivanov, B. J. Siwick, M. Chaker, and F. m. c. Légaré, Tracking ultrafast solid-state dynamics using high harmonic spectroscopy, Phys. Rev. Res. **3**, 023250 (2021).
[61] K. Uchida, G. Mattoni, S. Yonezawa, F. Nakamura, Y. Maeno, and K. Tanaka, High-order harmonic generation and its unconventional scaling law in the Mott-insulating Ca_2RuO_4, Phys. Rev. Lett. **128**, 127401 (2022).

End Matter

Appendix: Current fluctuations and the relation to depletion of the ground state—From Eq. (10), we see that squeezing occurs due to time correlations of the current. This is similar to considering depletion of the ground state as discussed in Ref. [12] as we will now show. The fluctuations can equivalently be described by the current matrix elements $\boldsymbol{j}_{m,n}(t) = \langle\phi_m|\hat{\boldsymbol{j}}_H(t)|\phi_n\rangle = \langle\phi_m(t)|\hat{\boldsymbol{j}}(t)|\phi_n(t)\rangle$. The relation is then

$$\begin{aligned} C(t',t'') &= \sum_m \boldsymbol{j}_{i,m}(t')\boldsymbol{j}_{m,i}(t'') - \boldsymbol{j}_{i,i}(t')\boldsymbol{j}_{i,i}(t'') \\ &= \sum_{m\neq i} \boldsymbol{j}_{i,m}(t')\boldsymbol{j}_{m,i}(t''), \end{aligned} \tag{A1}$$

where it has been used that $\langle\hat{\boldsymbol{j}}_H(t)\rangle = \boldsymbol{j}_{i,i}(t)$. To consider the fluctuations is thus the same as including these nondiagonal current matrix elements. In Ref. [12], this is referred to as "depletion of the ground state," since this makes one consider population in the state $|\phi_m(t)\rangle$ where $m \neq i$. If one did not consider the depletion of the ground state, one would have $C(t',t'') = 0$ which is the same as neglecting the fluctuations. Consequently, if the ground state has negligible depletion, then the fluctuations will also be negligible. On the other hand, if the ground state has non-negligible depletion, that means that the current operator has a non-negligible fluctuation which is the root origin of the squeezing. In this sense the two concepts are equivalent regardless of the nature of the electronic system.

PAPER IV

Phys. Rev. A 111, 013113 (2025)

Paper information

Author contributions

I conducted the numerical simulations and contributed to the analysis and interpretation of the research findings. Additionally, I was involved in preparing the manuscript, including the creation of figures.

PHYSICAL REVIEW A **111**, 013113 (2025)

Hierarchy of approximations for describing quantum light from high-harmonic generation: A Fermi-Hubbard-model study

Christian Saugbjerg Lange and Lars Bojer Madsen
Department of Physics and Astronomy, Aarhus University, Ny Munkegade 120, DK-8000 Aarhus C, Denmark

(Received 28 October 2024; accepted 6 January 2025; published 22 January 2025)

The quantum optical description of high-order harmonic generation where both the electrons of the generating medium and the driving and generated light fields are described quantum mechanically has been of significant interest in the past years. The quantum optical formulation leads to equations of motion for the generated light field in which the quantum optical field couples to the time-dependent current of the electronic medium irrespectively of the specifics of the electronic system being an atom, molecule, or solid. These equations of motion are not solvable for any realistic system and accurate and verified approximations are hence needed. In this paper, we present a hierarchy of approximations for the equations of motion for the photonic state. At each level in this hierarchy, we compare it to the previous level justifying the validity using the Fermi-Hubbard model as an example of an electronic system with correlations. This model allows us to perform an accurate simulation of the electron motion of all the required states. We find that for the typical experimental situation of weak quantized-light-matter-coupling constant and at intensities well below the damage threshold, an explicit expression for the generated quantum light, referred to as the Markov-state approximation, captures the high-harmonic spectrum quantitatively and describes the single-mode quantum properties of the generated light as characterized by the Mandel-Q parameter and the degree of squeezing qualitatively.

DOI: 10.1103/PhysRevA.111.013113

I. INTRODUCTION

High-harmonic generation (HHG) is a highly nonlinear process where an intense laser field interacts with a quantum system (atoms, molecules, solids) and an up-conversion of the laser frequency occurs, resulting in the emission of light consisting of higher harmonics of the driving field. For decades, a semiclassical description of HHG has proven successful in its predictability and description of strong-field phenomena and attosecond physics [1]. This semiclassical description of HHG, where the electronic system is described quantum mechanically and the involved light fields are described classically, has successfully predicted observables such as the harmonic cutoff, selection rules for the presence of even and odd harmonics, and their polarization [2].

Though the semiclassical description of HHG has proven useful for a wide range of applications, it cannot account for the quantum optical nature of either the driving field or the emitted light. In recent years, there has been a growing interest in describing HHG from a fully quantum perspective, i.e., with both a quantized electronic system and a quantum optical description of the involved light fields. Theoretical work using a coherent driving field has studied atomic gases [3–9], molecules [10], semiconductors [11–13], and correlated systems [14,15]. Further, using intense nonclassical states of light as driving fields has been considered [16–19], highlighting the various ways of engineering nonclassical states of light from high-harmonic generation.

A seminal experimental report of nonclassical light from HHG was on the so-called cat state, a macroscopic superposition between two different coherent states, which was created with a postselection measurement scheme of the emitted light [5]. Recent experimental work has reported that HHG can indeed be nonclassical [20] without any postselection and also considered nonclassical driving fields [21,22] showing how the nonclassicality of the driving field is transferred to some of the emitted harmonics.

Central to the understanding of all of the above approaches is the quantum optical description of an electronic system driven by a coherent-state laser. Interestingly, there are many open questions in this direction. One such open question is the validity of typical approximations used. As the exact equations of motion for the quantum optical state of the emitted light are not solvable in the general case, valid approximations are called for, potentially improving the analytical understanding. In this paper, we introduce a hierarchy of approximations to the equations of motion for the emitted photonic state similar to those considered in Ref. [9] where each step builds on top of the previous approximations. Here, each step is numerically verified using the Fermi-Hubbard model, a generic many-electron model including electron correlations, which allows for an accurate solution of the electronic problem as all electronic states can be included for a suitable size chain. This model, hence, allows for a quantitative assessment of all levels of approximations and qualifies a systematic discussion of these. Working within these justified approximations, we show how the nonclassical features (photon statistics, photon squeezing) of the emitted light relate to the transition current elements of the classically driven system or, equivalently, to the time correlations of the classical current. As these transition currents do not, in general, have the same spectral features as the HHG spectrum [15], this explains why the

nonclassical features peak in signal at other frequencies than the peaks in the spectrum as found in Refs. [3,15]. Employing these validated approximations simplifies and reduces the equations to be solved, possibly allowing simulation of larger systems in the future. In particular, we show that an explicit closed expression for the emitted quantum light, obtained within what we call the Markov-state approximation (MSA) (see also Ref. [9]), captures qualitatively both the shape of HHG spectra and quantum observables such as the Mandel-Q parameter and the squeezing of the emitted light.

This paper is organized as follows. First, an introduction to quantum optical HHG is given in Sec. II. Then, a hierarchy of approximations is introduced in Sec. III followed by a specification of the electronic system in Sec. IV. In Sec. V, a presentation of numerical results is given followed by a discussion of the validity of the approximations. Finally, a conclusion and an outlook is given in Sec. VI.

II. THEORY

A. Quantum optical description of high-harmonic generation

In this section, we briefly present the key equations of high-harmonic generation from a quantum optical perspective. For related detailed derivations see, e.g., Refs. [3,15,23]. We consider the time-dependent Schrödinger equation (TDSE) (atomic units are used throughout)

$$i\frac{\partial}{\partial t}|\Psi(t)\rangle = \hat{H}|\Psi(t)\rangle, \tag{1}$$

where $|\Psi(t)\rangle$ is the combined state of both the electronic and photonic system and where

$$\hat{H} = \frac{1}{2}\sum_{j=1}^{N}(\hat{\boldsymbol{p}}_j + \hat{\boldsymbol{A}})^2 + \hat{U} + \hat{H}_F \tag{2}$$

is the general many-electron Hamiltonian consisting of N electrons. Here, $\hat{\boldsymbol{p}}_j$ is the momentum for the electron with the index j, $\hat{U}$ is accounting for the electron-electron and electron-nuclear interaction,

$$\hat{\boldsymbol{A}} = \sum_{\boldsymbol{k},\sigma}\frac{g_0}{\sqrt{\omega_k}}(\hat{\boldsymbol{e}}_\sigma \hat{a}_{\boldsymbol{k},\sigma} + \hat{\boldsymbol{e}}^*_\sigma \hat{a}^\dagger_{\boldsymbol{k},\sigma}) \tag{3}$$

is the quantized vector potential in the dipole approximation, and $\hat{H}_F = \Sigma_{\boldsymbol{k},\sigma}\omega_k \hat{a}^\dagger_{\boldsymbol{k},\sigma}\hat{a}_{\boldsymbol{k},\sigma}$ is the Hamiltonian of the free electromagnetic field. In Eqs. (2) and (3) the sum $\Sigma_{\boldsymbol{k},\sigma}$ is over all photonic wave numbers $\boldsymbol{k}$ and polarizations σ with unit vector $\hat{\boldsymbol{e}}_\sigma$, and $g_0 = \sqrt{2\pi/V}$ is the effective coupling for the quantization volume V. The operator $\hat{a}_{\boldsymbol{k},\sigma}$ ($\hat{a}^\dagger_{\boldsymbol{k},\sigma}$) annihilates (creates) a photon with the frequency $\omega_k = |\boldsymbol{k}|c$. The initial state of the system prior to any interaction between the laser and electrons is $|\Psi(t)\rangle = |\phi_i\rangle|\psi_{\text{laser}}(t)\rangle$, where $|\phi_i\rangle$ is the initial field-free electronic eigenstate (which we take to be the ground state) and

$$|\psi_{\text{laser}}(t)\rangle = \bigotimes_{\boldsymbol{k}_L,\sigma_L}\hat{\mathcal{D}}\big[\alpha_{\boldsymbol{k}_L,\sigma_L}(t)\big]|0\rangle \tag{4}$$

is a multimode coherent state involving the laser modes $(\boldsymbol{k}_L, \sigma_L)$ and where

$$\hat{\mathcal{D}}[\alpha_{\boldsymbol{k},\sigma}(t)] = e^{\alpha_{\boldsymbol{k},\sigma}(t)\hat{a}^\dagger_{\boldsymbol{k},\sigma} - \alpha^*_{\boldsymbol{k},\sigma}(t)\hat{a}_{\boldsymbol{k},\sigma}} \tag{5}$$

is the displacement operator with coherent state amplitude $\alpha_{\boldsymbol{k},\sigma}(t) = \alpha_{\boldsymbol{k},\sigma}\exp(-i\omega_k t)$.

To avoid dealing with a macroscopic number of photons, we transform away the driving field of the laser and the Hamiltonian in Eq. (2) separates into $\hat{\tilde{H}}(t) = \hat{H}_{\text{SC}}(t) + \hat{V} + \hat{H}_F$, where the tilde denotes a displaced frame, $\hat{V}$ is the coupling between the electrons and the quantized field, and $\hat{H}_{\text{SC}}(t)$ is the semiclassical Hamiltonian similar to Eq. (2) but where $\hat{\boldsymbol{A}} \to \boldsymbol{A}_{\text{cl}}(t)$, i.e., the quantized vector potential has been replaced by a classical driving potential. Going into a rotating frame with respect to both $\hat{H}_{\text{SC}}(t)$ and $\hat{H}_F$, we obtain the equation

$$i\frac{\partial}{\partial t}|\tilde{\Psi}(t)\rangle_I = \hat{V}_I(t)|\tilde{\Psi}(t)\rangle_I, \tag{6}$$

where the subscript I indicates that the state is in the rotating frame. The interaction between the quantized vector potential and the electrons is given by the coupling

$$\hat{V}_I(t) = \hat{\boldsymbol{A}}_Q(t)\cdot\sum_{m,n}\boldsymbol{j}_{m,n}(t)|\phi_m\rangle\langle\phi_n|, \tag{7}$$

with $|\phi_m\rangle$ and $|\phi_n\rangle$ denoting time-independent eigenstates of the field-free Hamiltonian for the electronic system, and with the time-dependent quantized vector potential

$$\hat{\boldsymbol{A}}_Q(t) = \sum_{\boldsymbol{k},\sigma}\frac{g_0}{\sqrt{\omega_k}}\big(\hat{\boldsymbol{e}}_\sigma \hat{a}_{\boldsymbol{k},\sigma}e^{-i\omega_k t} + \hat{\boldsymbol{e}}^*_\sigma \hat{a}^\dagger_{\boldsymbol{k},\sigma}e^{i\omega_k t}\big), \tag{8}$$

and the transition current matrix elements

$$\boldsymbol{j}_{m,n}(t) = \langle\phi_m(t)|\hat{\boldsymbol{j}}(t)|\phi_n(t)\rangle, \tag{9}$$

where $\hat{\boldsymbol{j}}(t) = \Sigma_{j=1}^{N}[\hat{\boldsymbol{p}}_j + \boldsymbol{A}_{\text{cl}}(t)]$ is the electronic current operator. In Eq. (9), $|\phi_m(t)\rangle$ is the time-evolved mth field-free eigenstate satisfying the TDSE with the semiclassical Hamiltonian

$$i\frac{\partial}{\partial t}|\phi_m(t)\rangle = \hat{H}_{\text{SC}}(t)|\phi_m(t)\rangle. \tag{10}$$

By expanding the full state of the combined electronic and photonic system in terms of field-free electronic eigenstates

$$|\tilde{\Psi}(t)\rangle_I = \sum_m |\phi_m\rangle|\chi^{(m)}(t)\rangle, \tag{11}$$

and projecting onto the electronic state $\langle\phi_m|$ we obtain the equation of motion for the corresponding photonic state:

$$i\frac{\partial}{\partial t}|\chi^{(m)}(t)\rangle = \hat{\boldsymbol{A}}_Q(t)\cdot\sum_n \boldsymbol{j}_{m,n}(t)|\chi^{(n)}(t)\rangle. \tag{12}$$

Equation (12) is the central equation describing the evolution of the quantized photonic state and is describing the coupling between the quantized vector potential and the transition current elements between different dressed electronic states. As such, we emphasize that Eq. (12) is completely general and does not depend on the electronic medium (atom, molecule, solid). Equation (12) is also found in, e.g., Refs. [3,15] and in a length gauge formulation in Refs. [7–10]. Unfortunately, the size of the combined Hilbert space of both photons and electrons generally impedes any direct numerical solution of Eq. (12) without further approximations. These will be introduced and discussed in Sec. III. First, we turn to a presentation of the observables of interest in the present paper.

B. Observables

In the quantum optical formalism, the HHG spectrum is given by [15]

$$S(\omega_k) = \frac{\omega_k^3}{g_0^2(2\pi)^2c^3}\sum_\sigma \langle \hat{n}_{\boldsymbol{k},\sigma}\rangle, \tag{13}$$

where $\hat{n}_{\boldsymbol{k},\sigma} = \hat{a}^\dagger_{\boldsymbol{k},\sigma}\hat{a}_{\boldsymbol{k},\sigma}$ is the photonic counting operator. This is different from the usual semiclassical spectrum given by [24]

$$S_{\rm cl}(\omega) = \omega^2|\tilde{\boldsymbol{j}}_{i,i}(\omega)|^2, \tag{14}$$

where $\tilde{\boldsymbol{j}}_{i,i}(\omega)$ is the Fourier transform of the classical current.

In the quantum optical description of HHG, however, more than just the spectrum can be measured. In particular, the photon statistics and squeezing properties of the generated light are of great interest with regard to nonclassical features. The photon statistics can be quantified by the Mandel-Q parameter defined by [25]

$$Q_{\boldsymbol{k},\sigma} = \frac{\langle \hat{n}^2_{\boldsymbol{k},\sigma}\rangle - \langle \hat{n}_{\boldsymbol{k},\sigma}\rangle^2}{\langle \hat{n}_{\boldsymbol{k},\sigma}\rangle} - 1, \tag{15}$$

for a given mode. A classical coherent state will have Poissonian statistics and hence $Q_{\boldsymbol{k},\sigma} = 0$. If $Q_{\boldsymbol{k},\sigma} > 0$ the photon emission follows super-Poissonian statistics while $Q_{\boldsymbol{k},\sigma} < 0$ yields sub-Poissonian statistics, corresponding to a photon number distribution wider or narrower than a Poissonian distribution, respectively. While both a classical and nonclassical state can yield super-Poissonian statistics, sub-Poissonian statistics is a clear telltale sign of a nonclassical state [25]. Another telltale sign of nonclassicality is a nonvanishing squeezing [26,27]. The degree of squeezing can be quantified by the squeezing parameter $\eta_{\boldsymbol{k},\sigma}$. In the unit of dB, $\eta_{\boldsymbol{k},\sigma}$ is given as

$$\eta_{\boldsymbol{k},\sigma} = -10\log_{10}\left\{4\min_{\theta\in[0,\pi)}[\Delta\hat{X}_{\boldsymbol{k},\sigma}(\theta)]^2\right\}, \tag{16}$$

where $\hat{X}_{\boldsymbol{k},\sigma}(\theta) = (\hat{a}_{\boldsymbol{k},\sigma}e^{-i\theta} + \hat{a}^\dagger_{\boldsymbol{k},\sigma}e^{i\theta})/2$ is the quadrature operator. The angle, θ, that minimizes the variance of the quadrature operator in Eq. (16) gives the direction in phase space where the uncertainty in the corresponding quadrature is decreased below that of a coherent state at the expense of increasing the uncertainty in the conjugate quadrature. For a coherent state $\eta_{\boldsymbol{k},\sigma} = 0$ for all polarizations and modes. In Sec. V, we consider results for the spectra [Eq. (13)], the Mandel-Q parameter [Eq. (15)], and the squeezing parameter [Eq. (16)].

III. HIERARCHY OF APPROXIMATIONS

The exact equation of motion for the photonic state [Eq. (12)] is not solvable for any realistic system, as the number of photonic states required would be too large when expanded in, e.g., a Fock basis

$$|\chi^{(m)}(t)\rangle = \sum_{\{n\}} c^{(m)}_{\{n\}}(t)\left|n_{\boldsymbol{k}_1,\sigma_1}, n_{\boldsymbol{k}_2,\sigma_2}, \ldots\right\rangle, \tag{17}$$

where the sum is over all $\{n\}$ possible combinations of photon numbers in all the considered modes. The number of basis states required in Eq. (17) is $p^{k_{\rm max}}$, where p is the maximum number of photons allowed in a given mode, and $\boldsymbol{k}_{\rm max}$ is the highest mode considered. For an extended HHG spectrum, this basis is too large even when allowing for only a few photons per mode and even for a few-level electronic system, and hence further approximations on the photonic state are necessary. Thus far, two different approaches have been taken in the literature, as we now summarize.

One approach is to neglect all transition currents generated by $|\phi_m(t)\rangle$ for $m \neq i$ in Eq. (12) and only keep $\boldsymbol{j}_{i,i}(t) = \langle\phi_i(t)|\hat{\boldsymbol{j}}(t)|\phi_i(t)\rangle$, i.e., the current generated by the solution to the semiclassical TDSE, when the electronic system starts in the ground state $|\phi(t=0)\rangle = |\phi_i\rangle$. This limit yields an analytical solution for the photonic state as a product of coherent states [5,7,12,23], i.e., the most classical state possible. From these states, one can perform a conditioning measurement to generate cat states [5,7,23]. Other works have included both the ground state and an excited state (possibly resonantly coupled by the laser) in Eq. (12), and under certain approximations an expression for the photonic quantum state associated with the two bound states can be obtained [8,10,28]. This approach neglects the contribution from many bound and continuum states which will affect the quantum properties of the emitted light as detailed below. In contrast to the case where only the ground state is considered, this inclusion of more than a single photonic state, however, allows for nondiagonal transition currents in Eq. (12) which is, as we stress below, a key ingredient towards generating nonclassical light in the HHG process itself. We further note that the required transition current elements in Eq. (12), e.g., $\boldsymbol{j}_{i,i}(t)$, typically are obtained with the inclusion of more electronic states, either from an exact integration of the TDSE or via the strong-field approximation (SFA) ansatz for the wave function.

Another approach to simplify Eq. (12) is to decouple the photonic modes such that each mode is solved independently [3,15]. Different from the first essential state approach, this allows one to keep all photonic states in Eq. (12) thus keeping contributions from all transition currents. In terms of the ansatz for the state in mode $(\boldsymbol{k},\sigma)$, Eq. (17) reduces, in the decoupled case, to

$$\left|\chi^{(m)}_{\boldsymbol{k},\sigma}(t)\right\rangle = \sum_n c^{(m)}_n(t)|n_{\boldsymbol{k},\sigma}\rangle, \tag{18}$$

which requires only $p \times \boldsymbol{k}_{\rm max}$ basis states for a given state with index m, drastically reducing the computational requirements. On the other hand, this approximation to decouple the photonic modes neglects some quantum features such as two-mode squeezing and entanglement between different harmonics. For the rest of this paper, we follow this latter decoupled approach as the two-mode photonic coupling is insignificant for most pairs of harmonic modes as indicated in Ref. [28]. In the remainder of this section we will derive a hierarchy of approximations where each new approximation assumes the previous approximations. These approximations are made to both ease the numerical cost required to simulate the system while also, at the same time, providing a better analytical understanding of the underlying physics. The hierarchy of the approximations made in this section and their related

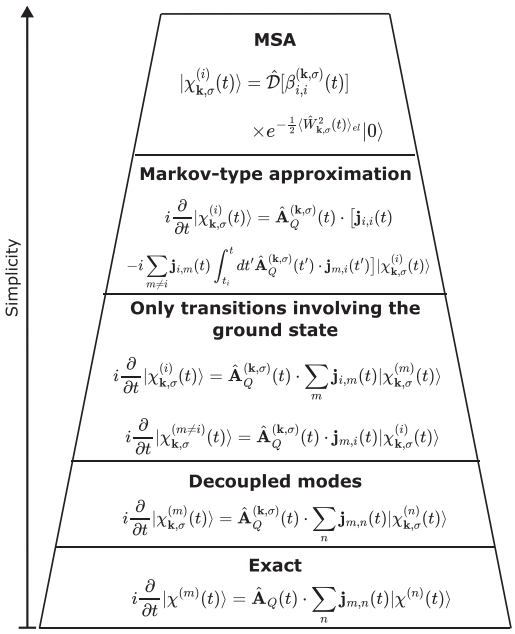

FIG. 1. Hierarchy of approximations with related equations for the photonic states as discussed in detail in the text. With increasing simplicity, each approximation assumes all the previous approximations made.

equations are summarized in Fig. 1 and will be evaluated and discussed further in Sec. V.

A. Decoupled modes

To proceed from Eq. (12), we neglect all couplings between different modes and solve the decoupled system of equations as done in Refs. [3,15]. The state $|\chi^{(m)}(t)\rangle$ in Eq. (12) is then approximated as a product state

$$|\chi^{(m)}(t)\rangle = \otimes_{\boldsymbol{k},\sigma}\big|\chi^{(m)}_{\boldsymbol{k},\sigma}(t)\big\rangle, \tag{19}$$

and each state on the right-hand side of Eq. (19) evolves according to

$$i\frac{\partial}{\partial t}\big|\chi^{(m)}_{\boldsymbol{k},\sigma}(t)\big\rangle = \hat{\boldsymbol{A}}^{(\boldsymbol{k},\sigma)}_Q(t)\cdot\sum_n \boldsymbol{j}_{m,n}(t)\big|\chi^{(n)}_{\boldsymbol{k},\sigma}(t)\big\rangle, \tag{20}$$

where the quantized field operator $\hat{\boldsymbol{A}}^{(\boldsymbol{k},\sigma)}_Q(t)$ only acts on mode $(\boldsymbol{k},\sigma)$:

$$\hat{\boldsymbol{A}}^{(\boldsymbol{k},\sigma)}_Q(t) = \frac{g_0}{\sqrt{\omega_k}}\big(\hat{\boldsymbol{e}}_\sigma\hat{a}_{\boldsymbol{k},\sigma}e^{-i\omega_k t} + \hat{\boldsymbol{e}}^*_\sigma\hat{a}^\dagger_{\boldsymbol{k},\sigma}e^{i\omega_k t}\big). \tag{21}$$

Note that solving Eq. (20) will yield the most exact practically obtainable results within this framework.

B. Keeping only transitions involving the electronic ground state

As a next approximation, we include only couplings that involve the electronic ground state, i.e., we only include transition current elements $\boldsymbol{j}_{i,m}(t)$ and $\boldsymbol{j}_{m,i}(t)$ [see Eq. (9)], where the subscript i denotes the ground state, and neglect all other terms in Eq. (20). As the initial photonic state is the vacuum state associated with the field-free electronic ground state, $c^{(m)}_n(t_i) = \delta_{m,i}\,\delta_{n,0}$ [see Eq. (19)], the coupling to a state $|\chi^{(m)}(t)\rangle$ is via $\hat{\boldsymbol{A}}^{(\boldsymbol{k},\sigma)}_Q\cdot\boldsymbol{j}_{i,m}(t)$, as seen in Eq. (20), which is first order in the coupling constant g_0. As we take $g_0 = 4\times10^{-8}$ a.u. (similar to Refs. [5,15,18], see also Ref. [29]), this coupling is weak and we neglect all higher-order couplings which are those that do not involve the initial state. From Eq. (20), we hence obtain the approximate set of equations

$$i\frac{\partial}{\partial t}\big|\chi^{(i)}_{\boldsymbol{k},\sigma}(t)\big\rangle = \hat{\boldsymbol{A}}^{(\boldsymbol{k},\sigma)}_Q(t)\cdot\sum_m \boldsymbol{j}_{i,m}(t)\big|\chi^{(m)}_{\boldsymbol{k},\sigma}(t)\big\rangle, \tag{22a}$$

$$i\frac{\partial}{\partial t}\big|\chi^{(m\neq i)}_{\boldsymbol{k},\sigma}(t)\big\rangle = \hat{\boldsymbol{A}}^{(\boldsymbol{k},\sigma)}_Q(t)\cdot\boldsymbol{j}_{m,i}(t)\big|\chi^{(i)}_{\boldsymbol{k},\sigma}(t)\big\rangle. \tag{22b}$$

We note that Eq. (22) only requires M transition current elements $\{\boldsymbol{j}_{i,m}(t)\}$, while the full system of equations in Eq. (20) requires M^2 transition current elements $\{\boldsymbol{j}_{m,n}(t)\}$, with M being the total number of field-free electronic eigenstates in the simulation. As such the memory requirement is less demanding and larger systems might be considered.

C. Markov-type approximation

To go further, we seek to bring Eq. (22) into a simpler form. We first formally integrate Eq. (22b):

$$\big|\chi^{(m\neq i)}_{\boldsymbol{k},\sigma}(t)\big\rangle = -i\int_{t_i}^{t}dt'\hat{\boldsymbol{A}}^{(\boldsymbol{k},\sigma)}_Q(t')\cdot\boldsymbol{j}_{m,i}(t')\big|\chi^{(i)}_{\boldsymbol{k},\sigma}(t')\big\rangle, \tag{23}$$

where t_i denotes the initial time of the interaction. Equation (23) is then inserted into the right-hand side of Eq. (22a) resulting in the expression

$$i\frac{\partial}{\partial t}\big|\chi^{(i)}_{\boldsymbol{k},\sigma}(t)\big\rangle = \hat{\boldsymbol{A}}^{(\boldsymbol{k},\sigma)}_Q(t)\cdot\Bigg[\boldsymbol{j}_{i,i}(t)\big|\chi^{(i)}_{\boldsymbol{k},\sigma}(t)\big\rangle - i\sum_{m\neq i}\boldsymbol{j}_{i,m}(t) \times\int_{t_i}^{t}dt'\hat{\boldsymbol{A}}^{(\boldsymbol{k},\sigma)}_Q(t')\cdot\boldsymbol{j}_{m,i}(t')\big|\chi^{(i)}_{\boldsymbol{k},\sigma}(t')\big\rangle\Bigg]. \tag{24}$$

Following Ref. [9], we now employ a Markov-type approximation [30] by expanding the state $|\chi^{(i)}_{\boldsymbol{k},\sigma}(t')\rangle$ around $t' = t$ as

$$\big|\chi^{(i)}_{\boldsymbol{k},\sigma}(t')\big\rangle \simeq \big|\chi^{(i)}_{\boldsymbol{k},\sigma}(t)\big\rangle + (t'-t)\frac{\partial}{\partial t'}\big|\chi^{(i)}_{\boldsymbol{k},\sigma}(t')\big\rangle\Big|_{t'=t} + \frac{(t'-t)^2}{2!}\frac{\partial^2}{\partial t'^2}\big|\chi^{(i)}_{\boldsymbol{k},\sigma}(t')\big\rangle\Big|_{t'=t} + \cdots \tag{25}$$

and only keeping the first term, i.e., letting the state become local in time and thus without memory. With this approximation, we bring Eq. (24) into the expression

$$i\frac{\partial}{\partial t}\big|\chi^{(i)}_{\boldsymbol{k},\sigma}(t)\big\rangle = \hat{\boldsymbol{A}}^{(\boldsymbol{k},\sigma)}_Q(t)\cdot\Bigg[\boldsymbol{j}_{i,i}(t) - i\sum_{m\neq i}\boldsymbol{j}_{i,m}(t) \times\int_{t_i}^{t}dt'\hat{\boldsymbol{A}}^{(\boldsymbol{k},\sigma)}_Q(t')\cdot\boldsymbol{j}_{m,i}(t')\Bigg]\big|\chi^{(i)}_{\boldsymbol{k},\sigma}(t)\big\rangle. \tag{26}$$

In contrast to Eqs. (20) and (22) which require the integration of M photonic states, $\{|\chi^{(m)}_{\boldsymbol{k},\sigma}(t)\rangle\}$, Eq. (26) only requires the

integration of a single state, as we only keep the state with the index $m = i$, which eases the numerical effort.

This Markov-type approximation is quantified by considering higher-order terms in the expansion in Eq. (25). Including the first-order term in $(t' - t)$ yields terms of the form

$$\hat{a}_{\boldsymbol{k},\sigma} \sum_{m\neq i} \boldsymbol{j}_{i,m}(t) \int_{t_i}^{t} dt' e^{-i\omega_k t'} \boldsymbol{j}_{m,i}(t')(t' - t) \times \partial_t \left|\chi^{(i)}_{\boldsymbol{k},\sigma}(t)\right\rangle, \tag{27}$$

with similar expressions proportional to $\hat{a}^{\dagger}_{\boldsymbol{k},\sigma}$. Though the integral in Eq. (27) in general yields a larger value than the integral in the second line of Eq. (26), the fact that Eq. (27) is proportional to $\partial_t |\chi^{(i)}_{\boldsymbol{k},\sigma}(t)\rangle \propto g_0$ [see Eq. (22a)] means that the first term in Eq. (25) dominates all higher-order terms for reasonable pulse lengths. However, for sufficiently long pulses the integrals related to the higher-order terms will be on the order of $1/g_0$ such that the approximation is no longer valid. In the present paper, we do not consider such long pulses.

One could consider including the higher-order terms in the expansion in Eq. (25) for improved accuracy. It turns out, however, that all higher-order terms contribute to the same order in g_0 and the expression cannot be truncated at a given order of g_0 as an infinite number of terms would have to be included. See Appendix A for more details on going beyond the first term in Eq. (25).

D. Neglecting higher-order commutators: MSA

As we are interested in the origin of the nonclassical features in HHG, we manipulate Eq. (26) further for better analytical insights. Following Ref. [9], we first use that $\sum_{m\neq i} |\phi_m\rangle\langle\phi_m| = \mathbb{1} - |\phi_i\rangle\langle\phi_i|$ and define

$$\hat{W}_{k,\sigma}(t) = \int_{t_i}^{t} dt' \hat{\boldsymbol{A}}^{(\boldsymbol{k},\sigma)}_{Q}(t')[\hat{\boldsymbol{j}}_H(t') - \langle\hat{\boldsymbol{j}}_H(t')\rangle], \tag{28}$$

where $\hat{\boldsymbol{j}}_H(t) = \hat{\mathcal{U}}^{\dagger}_{\mathrm{SC}}(t)\hat{\boldsymbol{j}}(t)\hat{\mathcal{U}}_{\mathrm{SC}}(t)$ is a Heisenberg-type formulation of the time-dependent current operator with $\hat{\mathcal{U}}_{\mathrm{SC}}(t)$ being the time-evolution operator associated with the semiclassical Hamiltonian. Note that $\langle\hat{\boldsymbol{j}}_H(t)\rangle = \langle\phi_i|\hat{\mathcal{U}}^{\dagger}_{\mathrm{SC}}(t)\hat{\boldsymbol{j}}(t)\hat{\mathcal{U}}_{\mathrm{SC}}(t)|\phi_i\rangle = \boldsymbol{j}_{i,i}(t)$. Equation (26) is then rewritten as

$$\begin{aligned} i\frac{\partial}{\partial t}\left|\chi^{(i)}_{\boldsymbol{k},\sigma}(t)\right\rangle \\ = \left[\hat{\boldsymbol{A}}^{(\boldsymbol{k},\sigma)}_{Q}(t)\cdot\boldsymbol{j}_{i,i}(t) - i\langle\hat{W}_{\boldsymbol{k},\sigma}(t)\hat{W}_{\boldsymbol{k},\sigma}(t)\rangle_{\mathrm{el}}\right]\left|\chi^{(i)}_{\boldsymbol{k},\sigma}(t)\right\rangle, \end{aligned} \tag{29}$$

where $\langle\cdot\rangle_{\mathrm{el}}$ denotes the expectation value of only the electronic operators. Equation (29) yields the solution

$$\left|\chi^{(i)}_{\boldsymbol{k},\sigma}(t)\right\rangle = \hat{\mathcal{D}}\left[\beta^{(\boldsymbol{k},\sigma)}_{i,i}(t)\right]e^{-\frac{1}{2}\langle\hat{W}^2_{\boldsymbol{k},\sigma}(t)\rangle_{\mathrm{el}}}|0\rangle, \tag{30}$$

where the time-dependent displacement amplitude in the $\boldsymbol{k}$th mode is given by

$$\beta^{(\boldsymbol{k},\sigma)}_{m,n}(t) = -i\frac{g_0}{\sqrt{\omega_k}}\int_{t_i}^{t} dt'\, \boldsymbol{j}_{m,n}(t')\cdot\hat{\boldsymbol{e}}^{*}_{\sigma}e^{i\omega_k t'}. \tag{31}$$

We will refer to Eq. (30) as the MSA as it is achieved from the Markov-type approximation in Eq. (26). In obtaining Eq. (30), we neglected the commutator $[\hat{W}_{\boldsymbol{k},\sigma}(t), \hat{W}_{\boldsymbol{k},\sigma}(t)]$ which expresses the fluctuations of the fluctuations of the current operator. Further, only terms up to second order in g_0 are kept. A full derivation of Eq. (30) can be found in Appendix B and a derivation without decoupling but with an SFA approach can be found in Ref. [9].

We now investigate $\langle\hat{W}^2_{\boldsymbol{k},\sigma}(t)\rangle_{\mathrm{el}}$. It is seen from Eq. (30) that for $\langle\hat{W}^2_{\boldsymbol{k},\sigma}(t)\rangle_{\mathrm{el}} = 0$ the photonic state would be a coherent state and hence have $Q_{\boldsymbol{k},\sigma} = \eta_{\boldsymbol{k},\sigma} = 0$. This implies that $\langle\hat{W}^2_{\boldsymbol{k},\sigma}(t)\rangle_{\mathrm{el}}$ is the cause of the quantum properties of the emitted HHG in the present MSA limit. We thus write out $\langle\hat{W}^2_{\boldsymbol{k},\sigma}(t)\rangle_{\mathrm{el}}$ explicitly:

$$\begin{aligned} \left\langle\hat{W}^2_{\boldsymbol{k},\sigma}(t)\right\rangle_{\mathrm{el}} = \int_{t_i}^{t} dt' \int_{t_i}^{t} dt'' \hat{\boldsymbol{A}}^{(\boldsymbol{k},\sigma)}_{Q}(t')\hat{\boldsymbol{A}}^{(\boldsymbol{k},\sigma)}_{Q}(t'') \\ \times [\langle\hat{\boldsymbol{j}}_H(t')\hat{\boldsymbol{j}}_H(t'')\rangle - \langle\hat{\boldsymbol{j}}_H(t')\rangle\langle\hat{\boldsymbol{j}}_H(t'')\rangle]. \end{aligned} \tag{32}$$

Interestingly, similar expressions with the time correlation of the current are obtained when using Heisenberg equations of motion for the photonic operators [31]. The time-correlation function in Eq. (32) is numerically complicated to calculate. Rewriting, we instead express the correlations of the current in terms of the transition current matrix elements, which is equally exact. To this end, we use $\mathbb{1} = \Sigma_m|\phi_m\rangle\langle\phi_m|$ and obtain the relation

$$\langle\hat{\boldsymbol{j}}_H(t')\hat{\boldsymbol{j}}_H(t'')\rangle - \langle\hat{\boldsymbol{j}}_H(t')\rangle\langle\hat{\boldsymbol{j}}_H(t'')\rangle = \sum_{m\neq i}\boldsymbol{j}_{i,m}(t')\boldsymbol{j}_{m,i}(t''). \tag{33}$$

Equation (33) highlights an interesting equivalence between the time correlations of the (Heisenberg type) current and the transitions current matrix elements. This equation shows that the role of the transition current elements can be reformulated as time correlations of the current within the presented scheme of approximations. Inserting Eq. (33) into Eq. (32), we find

$$\begin{aligned} \left\langle\hat{W}^2_{\boldsymbol{k},\sigma}(t)\right\rangle_{\mathrm{el}} = \sum_{m\neq i}\left[\int_{t_i}^{t} dt' \hat{\boldsymbol{A}}^{(\boldsymbol{k},\sigma)}_{Q}(t')\boldsymbol{j}_{i,m}(t')\right] \\ \times\left[\int_{t_i}^{t} dt'' \hat{\boldsymbol{A}}^{(\boldsymbol{k},\sigma)}_{Q}(t'')\boldsymbol{j}_{m,i}(t'')\right]. \end{aligned} \tag{34}$$

As we are interested in the final photon state after the end of the driving pulse, we let $t \to \infty$. Writing out Eq. (34) then yields

$$\begin{aligned} \left\langle\hat{W}^2_{\boldsymbol{k},\sigma}\right\rangle_{\mathrm{el}} = B_{\boldsymbol{k},\sigma}\left[\hat{a}^2_{\boldsymbol{k},\sigma}e^{-i\varphi_k} + (\hat{a}^{\dagger}_{\boldsymbol{k},\sigma})^2 e^{i\varphi_k}\right] \\ + C_{\boldsymbol{k},\sigma}\,\hat{a}^{\dagger}_{\boldsymbol{k},\sigma}\hat{a}_{\boldsymbol{k},\sigma} + D_{\boldsymbol{k},\sigma}\,\hat{a}_{\boldsymbol{k},\sigma}\hat{a}^{\dagger}_{\boldsymbol{k},\sigma}, \end{aligned} \tag{35}$$

where we have defined

$$B_{\boldsymbol{k},\sigma} = \left|\sum_{m\neq i} J^{(\boldsymbol{k},\sigma,+)}_{i,m} J^{(\boldsymbol{k},\sigma,+)}_{m,i}\right|, \tag{36a}$$

$$\varphi_{\boldsymbol{k},\sigma} = \arg\left[\sum_{m\neq i} J^{(\boldsymbol{k},\sigma,+)}_{i,m} J^{(\boldsymbol{k},\sigma,+)}_{m,i}\right], \tag{36b}$$

$$C_{\boldsymbol{k},\sigma} = \sum_{m\neq i}\left|J^{(\boldsymbol{k},\sigma,+)}_{i,m}\right|^2, \tag{36c}$$

$$D_{\boldsymbol{k},\sigma} = \sum_{m\neq i}\left|J^{(\boldsymbol{k},\sigma,-)}_{i,m}\right|^2, \tag{36d}$$

with the integrated transition current elements

$$J_{m,n}^{(\boldsymbol{k},\sigma,\pm)} = \frac{g_0}{\sqrt{\omega_k}} \int_{t_i}^{\infty} dt' e^{\pm i\omega_k t'} \boldsymbol{j}_{m,n}(t') \cdot \hat{\boldsymbol{e}}_\sigma^{(*)}, \tag{37}$$

where the polarization unit vector is complex conjugated for the positive phase. Note that $[J_{m,n}^{(\boldsymbol{k},\sigma,-)}(t)]^* = J_{n,m}^{(\boldsymbol{k},\sigma,+)}(t)$. However, different from the case presented in Ref. [9], we do not make further assumptions on the elements in Eq. (36).

We now calculate expectation values for the state in Eq. (30) by expanding the exponential function in Eq. (30) to second order in g_0, i.e., $e^{-\frac{1}{2}\langle \hat{W}^2 \rangle_{\rm el}} \simeq 1 - \frac{1}{2}\langle \hat{W}^2 \rangle_{\rm el}$, which yields the approximate state for a given mode:

$$|\chi_{\boldsymbol{k},\sigma}^{(i)}\rangle \simeq \hat{\mathcal{D}}\big[\beta_{i,i}^{(\boldsymbol{k},\sigma)}(t)\big]\left[\left(1 - \frac{1}{2}D_{\boldsymbol{k},\sigma}\right)|0\rangle - \frac{1}{\sqrt{2}}B_{\boldsymbol{k},\sigma}e^{i\varphi_{\boldsymbol{k},\sigma}}|2\rangle\right]. \tag{38}$$

The spectrum [Eq. (13)] is then to lowest order in g_0 given as

$$\begin{aligned} S(\omega_k) &= \frac{\omega_k^3}{g_0^2(2\pi)^2c^3} \sum_\sigma \left|\beta_{i,i}^{(\boldsymbol{k},\sigma)}\right|^2 \\ &= \frac{\omega_k^2}{(2\pi)^2c^3} \sum_\sigma |\hat{\boldsymbol{e}}_\sigma^* \cdot \tilde{\boldsymbol{j}}_{i,i}(\omega_k)|^2, \end{aligned} \tag{39}$$

where the definition of $\beta_{i,i}^{(\boldsymbol{k},\sigma)}$ in Eq. (31) was used. We note that Eq. (39) up to constants is identical to the semiclassical spectrum in Eq. (14). This shows that in the limit of a weak coupling (here $g_0 = 4 \times 10^{-8}$ a.u.) the spectrum itself is dominated by the classical current, highlighting that the HHG spectrum is not a suitable observable for inferring nonclassical properties of the generated light. To investigate the nonclassical properties of light, we calculate the Mandel-Q and the squeezing parameters. Within the MSA, the Mandel-Q parameter [Eq. (15)] is given by

$$\begin{aligned} Q_{\boldsymbol{k},\sigma} = &\frac{B_{\boldsymbol{k},\sigma}^2 + \left|\beta_{i,i}^{(\boldsymbol{k},\sigma)}\right|^4 - 2B_{\boldsymbol{k},\sigma}\mathrm{Re}\left[\left(\beta_{i,i}^{(\boldsymbol{k},\sigma)}\right)^2 e^{i\varphi_{\boldsymbol{k},\sigma}}\right]}{\left|\beta_{i,i}^{(\boldsymbol{k},\sigma)}\right|^2(1 - D_{\boldsymbol{k},\sigma}) + B_{\boldsymbol{k},\sigma}^2} \\ &- \left|\beta_{i,i}^{(\boldsymbol{k},\sigma)}\right|^2, \end{aligned} \tag{40}$$

where terms of order $O(g_0^4)$ have been included for the necessary numerical stability. The quadrature variance minimized to calculate the squeezing [Eq. (16)] is within the MSA given by

$$[\Delta\hat{X}_{\boldsymbol{k},\sigma}(\theta)]^2 = \tfrac{1}{4}[1 - 2B_{\boldsymbol{k},\sigma}\cos(2\theta - \varphi_{\boldsymbol{k},\sigma})]. \tag{41}$$

We note that the quantum features calculated by Eqs. (40) and (41) are dependent on the transition currents [or equivalently the current correlations, see Eq. (33)] that in general have different spectral features than the classical current. This means that the quantum features do not follow the spectral structure, e.g., with peaks placed at odd harmonics, and consequently will not have the same selection rules.

We further emphasize that Eqs. (39)–(41) only require solving the TDSE of the electronic system driven by a classical field [Eq. (10)] and do not require the integration of any additional equations of motion for the photonic state as is necessary for the previous levels of approximations [Eqs. (20), (22), and (26)], easing the numerical effort significantly, which is the main advantage of the MSA.

Finally, we note that if one uses the MSA without the decoupling of modes, one would end up with the same expressions for the examined observables as in Eqs. (39)–(41). This shows that the single-mode observables as considered here are not affected by the decoupling of photonic modes in the present MSA. Consequently, the errors introduced when deriving the MSA are larger than the errors introduced by decoupling the photonic modes. Unfortunately, it is not possible to test the case of coupled photonic modes in the lower levels of approximations (see Fig. 1) due to numerical constraints, and as such it is challenging to quantify the validity of the photonic decoupling. Studying these levels of approximations in a simpler electronic system in an appropriate limit where coupled photonic modes can be considered and by extension also considering multimode observables would deserve an entire paper on its own.

IV. ELECTRONIC SYSTEM

The derivations in Secs. II and III are completely general for any electronic system one might consider. In the present paper, we use the driven Fermi-Hubbard model as the electronic system. This model was recently shown to yield nonclassical harmonics in the so-called Mott-insulating limit [15]. That is, we take the semiclassical Hamiltonian to be that of the field-driven Fermi-Hubbard model, i.e., $\hat{H}_{\rm SC}(t) \to \hat{H}_{\rm FH}(t)$. The Fermi-Hubbard model is a generic many-body model that captures beyond-mean-field electronic interaction with the Hubbard U. This choice of model allows us to simulate the semiclassical TDSE without any further approximations as all states can be included in the numerical modeling for a small enough chain. We specifically consider a model with periodic boundary conditions at half filling with an equal number of spin-up and spin-down electrons. Within the dipole approximation, the system driven by a classical laser pulse is described by the time-dependent Hamiltonian [32]

$$\hat{H}_{\rm SC}(t) = \hat{H}_{\rm FH}(t) = \hat{H}_{\rm hop}(t) + \hat{H}_U, \tag{42}$$

with

$$\begin{aligned} \hat{H}_{\rm hop}(t) &= -t_0 \sum_{j,\mu} (e^{iaA_{\rm cl}(t)}\hat{c}_{j,\mu}^\dagger \hat{c}_{j+1,\mu} + \text{H.c.}), \\ \hat{H}_U &= U \sum_j (\hat{c}_{j,\uparrow}^\dagger \hat{c}_{j,\uparrow})(\hat{c}_{j,\downarrow}^\dagger \hat{c}_{j,\downarrow}), \end{aligned} \tag{43}$$

where t_0 is the hopping matrix element for an electron to hop from site j to site $j \pm 1$, the operator $\hat{c}_{j,\mu}^\dagger$ ($\hat{c}_{j,\mu}$) creates (annihilates) an electron with spin $\mu \in \{\uparrow, \downarrow\}$ on site j, a is the lattice constant, and U describes the degree of beyond-mean-field onsite electron-electron repulsion. We only include nearest-neighbor hopping which is the common limit of this model [15,33–36]. A schematic overview of the model is given in Fig. 2. In this model, the time-dependent current

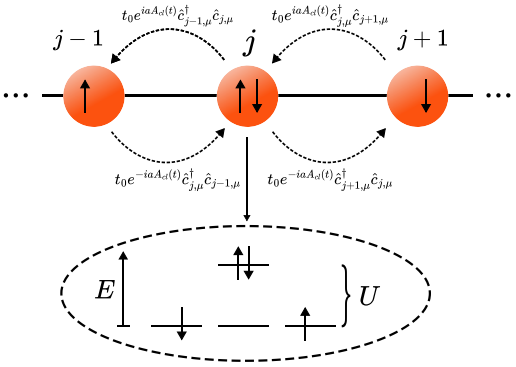

FIG. 2. Illustration of the Fermi-Hubbard model. The top figure shows the nearest-neighbor hopping while the bottom diagram shows the energy cost of U associated with a single doubly occupied site, a doublon.

operator is given as [15,32]

$$\hat{\boldsymbol{j}}(t) = -iat_0 \sum_{j,\mu} (e^{iaA_{\rm cl}(t)} \hat{c}^\dagger_{j,\mu} \hat{c}_{j+1,\mu} - \text{H.c.}) \hat{\boldsymbol{x}}, \qquad (44)$$

which is in the direction of the Fermi-Hubbard chain, taken to be in the $\hat{\boldsymbol{x}}$ direction. For details on the model see, e.g., Refs. [15,32].

In this paper, we use a chain of $L = 8$ sites (with periodic boundary conditions), a lattice spacing of $a = 7.5589$ a.u., and $t_0 = 0.0191$ a.u. picked specifically to match those of the cuprate Sr_2CuO_3 [37] as done previously in Refs. [15,33,34,36,38,39]. We investigate the Mott-insulating phase with $U = 10t_0$ which highly favors antiferromagnetic ordering in the field-free ground state of the system. For the driving field, we use a $\sin^2$ envelope function for a pulse polarized along the lattice dimension with N_c cycles:

$$A_{\rm cl}(t) = A_0 \sin(\omega_L t + \pi/2) \sin^2\left(\frac{\omega_L t}{2N_c}\right), \qquad (45)$$

where the vector potential is chosen to be $A_0 = F_0/\omega_L = 0.194$ a.u. This corresponds to a peak intensity of 3.3×10^{10} W/cm^2, well below the expected damage threshold. The laser frequency is $\omega_L = 0.005$ a.u. $= 33$ THz, which is not the typical wavelength used in strong-field physics but is chosen to match the energy scale of the system [15,33,38,40]. In order to obtain the transition current elements $\boldsymbol{j}_{m,n}(t)$, we solve Eq. (10) for all states $\{|\phi_m(t)\rangle\}$ using the Arnoldi-Lanczos algorithm [41–44] with a Krylov subspace of dimension 4. We use a time step of $\Delta t = 1/\sqrt{10}$ a.u. and all results have been checked for convergence. To limit the dimensionality of the required Hilbert space, we start from a spin-symmetric ground state with vanishing total crystal momentum. As the Hamiltonian Eq. (42) is invariant under spin flip and conserves total crystal momentum only states within that subspace are needed.

V. RESULTS AND DISCUSSION

We calculate both the HHG spectrum, photon statistics, and squeezing for all levels of approximations. When solving the photonic equations of motion for a given level of approximation [Eqs. (20), (22), and (26)], the photonic states are expanded in a Fock basis truncated at 50 photons per mode and have been tested for convergence by truncating at 100 photons. After the end of the driving pulse, we rarely find population in a Fock state with more than two photons. Details on the calculation of expectation values can be found in Ref. [15].

The results for a simulation with a laser pulse of $N_c = 10$ cycles are shown in Fig. 3. Looking at the spectrum [Fig. 3(a)], we note two different regimes. At lower harmonics ($\omega/\omega_L \leqslant 19$), we see regular peaks in the signal at odd harmonics. This part of the spectrum is due to the so-called intrasubband current. At higher harmonics ($\omega/\omega_L > 19$), the spectrum is generated by the so-called intersubband current. We note that the signal in this part of the spectrum is more irregular with peaks at noninteger harmonics. The origin of the presence of this signal at noninteger harmonics is due to a population of several Floquet states. A more detailed discussion of the spectrum can be found in Refs. [15,39]. Comparing the different levels of approximation in Fig. 3(a), we find that all levels of approximation produce the same spectrum with no noticeable difference. This highlights that in the regime of weak coupling ($g_0 = 4 \times 10^{-8}$ a.u.), the quantum optical nature of HHG does not appear in the spectrum. Looking at the photon statistics calculated via the Mandel-Q parameter [Fig. 3(b)], we first note that finite values are only seen at distinct typically nonodd harmonic frequencies, clearly showing that the Mandel-Q parameter does not peak at the same frequencies as the spectrum in Fig. 3(a). This can be understood from the MSA [Eq. (30)] where it is seen that all the transition currents, $\boldsymbol{j}_{i,m}(t)$, are included to calculate the Mandel-Q parameter [see Eqs. (36) and (40)]. These transition current elements have different spectral features than the diagonal current, $\boldsymbol{j}_{i,i}(t)$, used to generate the spectrum [15], which is why the Mandel-Q parameter peaks at other frequencies. Looking at Fig. 3(b), we see that all levels of approximations qualitatively show the same features. The MSA [Eq. (38), dotted green], however, shows some relatively minor deviations at certain harmonics. For the squeezing [Fig. 3(c)] we see two spectral regions with nonvanishing squeezing. At the lowest harmonics ($\omega/\omega_L \leqslant 5$) we see a small degree of squeezing. Most squeezing is, however, seen in the intersubband region ($\omega/\omega_L > 19$). As for the Mandel-Q parameter, we note that the degree of squeezing does not peak at the same harmonics as the spectrum in Fig. 3(a). This can again be understood from the MSA, where we see that the quantities involved in calculating the degree of squeezing [Eq. (41)] contain contributions from the transition current elements with different spectral features than those in the classical current. Comparing the different levels of approximations, we also find good agreement between the produced results for the degree of squeezing. Note that the MSA does not capture the squeezing at the lower harmonics as shown in the inset in Fig. 3(c). This squeezing results from higher-order terms not included in the derivation of Eq. (38).

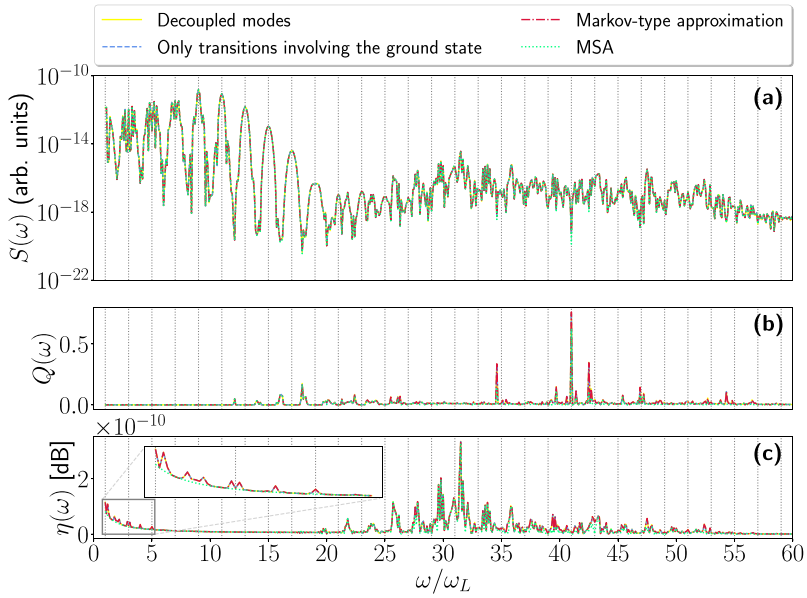

FIG. 3. Results for the various degrees of approximation (see Fig. 1) for an $N_c = 10$ cycle pulse; see text for additional parameters. (a) The spectrum [Eq. (13)]. We note that no level of approximation shows any significant difference. (b) The Mandel-Q parameter [Eq. (15)]. (c) The squeezing [Eq. (16)]. We note that the calculation in the decoupled limit [Eq. (20), orange full line], only including transitions involving the electronic ground state [Eq. (22), blue dashed line], and the Markov-type approximation [Eq. (26), red dash-dotted line] match very well for all frequencies. The MSA [Eq. (38), green dotted line] also shows good agreement with all results but has some deviations at various harmonics in both the Mandel-Q parameter and squeezing. We also note that the MSA does not capture the squeezing at the lower harmonics as seen in the inset in (c).

We also consider a longer pulse of $N_c = 18$ cycles shown in Fig. 4 to see how the different levels of approximations match in that case. Recall that the Markov-type approximation and the MSA rely on a local-time approximation [Eqs. (25) and (26)] which is expected to be less accurate for a longer pulse duration. Again for this case of $N_c = 18$ cycles, we see in Fig. 4, that the spectrum consists of a regular intrasubband region and a more irregular intersubband region as in Fig. 3(a). Also for the longer pulse duration of $N_c = 18$ cycles in Fig. 4(a), all levels of approximations produce the same spectrum, though the MSA shows some minor deviations on lower even harmonics. The photon statistics characterized by the Mandel-Q parameter is significantly different for the longer pulse of $N_c = 18$ cycles in Fig. 4(b) than for the shorter pulse of $N_c = 10$ cycles in Fig. 3(b). We see two different regions in Fig. 4(b): one region at lower harmonics ($\omega_L/\omega \leqslant 25$) with sharp peaks in the signal and a region at higher harmonics ($\omega/\omega_L > 25$) with smaller and less distinct peaks. This difference can partially be explained by the MSA. By investigating the expression for the Mandel-Q parameter for the MSA [Eq. (40)], we see that the denominator is dominated by $|\beta_{i,i}^{(\boldsymbol{k},\sigma)}|^2$ which is proportional to the spectrum [see Eq. (39)]. Now, as the pulse duration is increased much less signal is found at even harmonics, i.e, $|\beta_{i,i}^{(\boldsymbol{k},\sigma)}|^2$ is significantly smaller at even harmonics for the longer pulse, which can be seen by comparing Figs. 4(a) and 3(a). From Eq. (40), we see that this drop in signal at even harmonics yields a larger value for the Mandel-Q parameter. Experimentally, this means that if any signal at these lower even harmonics is measured, the photon distribution will be highly non-Poissonian. Comparing the different levels of approximations, we see that they yield close to identical results for the Mandel-Q parameter. The MSA, however, does deviate for certain harmonics and is generally less accurate for higher harmonics. The squeezing parameter for the longer pulse of $N_c = 18$ cycles is shown in Fig. 4(c). Opposite to the situation for the $N_c = 10$ cycle pulse in Fig. 3(c), we now see that the degree of squeezing is largest for the lower harmonic ($\omega/\omega_L \leqslant 5$) which is almost an order of magnitude larger than the largest value for the squeezing parameter for the $N_c = 10$ cycle pulse. This difference in magnitude is due to a different response of the electronic system, and we do not believe this to be a general feature for all electronic systems. For the $N_c = 18$ cycle pulse we still see a finite degree of squeezing at higher harmonics ($\omega/\omega_L > 25$) comparable to the values seen in Fig. 3(c). Comparing the different levels of approximations for the squeezing in Fig. 4(c), we see a good agreement between all produced results. Notably, however, the MSA does again not capture the degree of squeezing at lower harmonics.

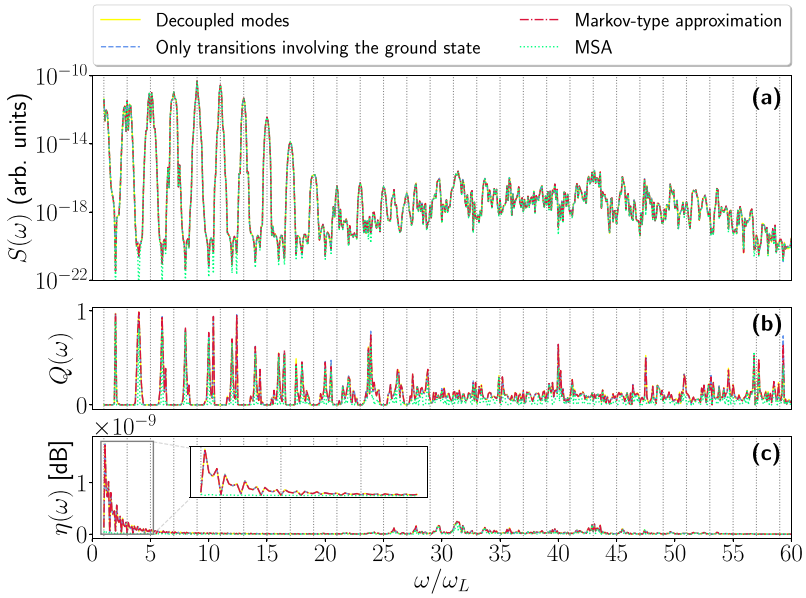

FIG. 4. Results for the various degrees of approximation (see Fig. 1) for an $N_c = 18$ cycle pulse; see text for additional parameters. (a) The spectrum [Eq. (13)]. We note that no level of approximation shows any significant deviation from the others. (b) The Mandel-Q parameter [Eq. (15)]. We note that the calculation in the decoupled limit [Eq. (20), solid orange], the limit that only includes transitions involving the electronic ground state [Eq. (22), dashed blue], as well as the Markov-type approximation [Eq. (26), dash-dotted red] match well for all frequencies. The MSA [Eq. (38), dotted green] matches the more exact results well, but deviates more for higher harmonics. (c) The squeezing [Eq. (16)]. Here all levels of approximations match well, except for the MSA, which does not capture the squeezing at lower harmonics captured by the other methods as seen in the inset.

The deviation of the MSA in both the Mandel-Q parameter and squeezing from the most exact obtainable solution [Eq. (20)] is shown in Fig. 5. We compute the mean of this deviation over the considered harmonics ($\omega/\omega_L \leqslant 60$) as $\overline{|Q - Q_{\rm dec}|}$ for different pulse lengths with similar expressions for the squeezing, η. Here, the bar denotes the average over the considered harmonics, and the subscript "dec" refers to the solution obtained with decoupling of the harmonic modes as the only approximation [Eq. (20)]. We note that averaging the deviation across all considered harmonics only partially yields a truthful measure of the validity of the approximation as it does not capture if the deviation is a general trend or related to specific harmonics. We first note that the accuracy of the Mandel-Q parameter deviates with an increasing pulse length. Further, we see that the MSA does not exactly capture the degree of squeezing. The offset in the deviation is due to the lower harmonics not being captured. These large deviations at lower harmonics are due to higher-order commutators that are neglected in the derivation of the MSA in Eq. (30). For the present system, the degree of squeezing at lower harmonics is less for $N_c = 10$ and 20 cycles than for, e.g., $N_c = 18$ cycles as seen in Figs. 3 and 4 and inferred from Fig. 5. We believe that this low degree of squeezing at certain pulse durations is specific to the Fermi-Hubbard model and not a general trend. The main point of Fig. 5 is to show that the accuracy of the MSA decreases with increasing pulse duration as expected.

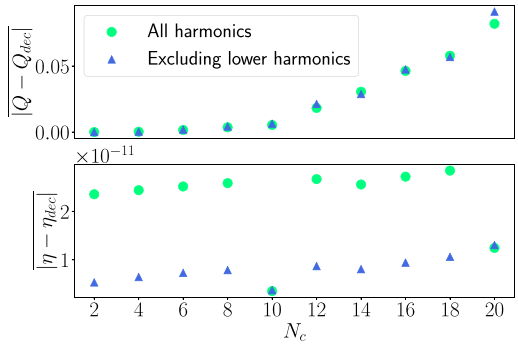

FIG. 5. The absolute difference of the Mandel-Q parameter (upper panel) and squeezing parameter (lower panel) between the exact solution [Eq. (20)] and the MSA averaged over all considered harmonics ($1 \leqslant \omega/\omega_L \leqslant 60$, green circles) and all higher harmonics ($10 \leqslant \omega/\omega_L \leqslant 60$, blue triangles) for various number of pulse lengths determined by the number of cycles, N_c. For the Mandel-Q parameter, we see that the deviation grows with increasing pulse length. Similarly, the squeezing deviates slightly more for increasing pulse length. We note that, for $N_c = 10, 20$, the system has less squeezing in the lower harmonics, which improves the MSA as it does not capture the degree of squeezing in the lower harmonics.

VI. CONCLUSION AND OUTLOOK

In this paper, we derived and verified a hierarchy of approximations on the equations of motion for the quantum state of light emitted from HHG. Each step in the hierarchy of approximations, which are general for all types of electronic systems, was tested numerically using the Fermi-Hubbard model in the Mott-insulating phase. This model allowed us to solve all semiclassical TDSEs required without any further approximations. We found that including only couplings that involve the ground state is a good approximation to the full system for all considered pulse lengths. Going further, a Markov-type approximation and an even further related approximated state, the MSA, show good agreement with the more exact results. Notably, the spectrum calculated based on these approximations matched more exact results for all pulse lengths considered. The MSA does, however, deviate from more exact results for the Mandel-Q parameter and the squeezing with increased pulse lengths. Especially, it does not capture the squeezing of the lower harmonics. The main advantage of the MSA is the low numerical cost as it only requires the integration of the electronic states and not a subsequent integration of the photonic state in all modes, easing the numerical effort significantly.

The analytical insights based on the Markov-type approximation leading to the MSA highlight that the nonclassical features of the light are due to time correlations of the current (or dipole for atomic systems). Further, the time correlations of the current are related to the transition current elements, which is an important connection highlighting the physical relevance of the latter. By investigating the expressions for the nonclassical features of the emitted light in the MSA, we found that these have different spectral features than the HHG spectrum, as these are calculated from the transition current elements the spectral features of which are different from those of the classical current generating the HHG spectrum. We also emphasize that the approximations in this paper assume a small coupling, g_0, to the quantized electromagnetic field as is the typical experimental situation. Hence, the presented equations and results would become less accurate for a larger value of g_0. Indeed it would be worth pursuing experimental setups that would enhance the coupling to the quantized field, e.g., a cavity, as this would increase the nonclassical properties of the emitted HHG radiation [8]. In this connection, we note that alternative approaches addressing this problem begin to appear: very recent work considers in reduced dimension a single-active electron coupled to a single quantized photon mode in a cavity by both an exact quantum electrodynamical approach and a semiclassical multitrajectory simulation [45].

As an outlook, the validated approximations may be an aid when considering the quantum backaction from the electronic system to the radiation field with a nonclassical driving field. In the theory for nonclassical driving [16–18], the TDSE needs to be integrated for many different classical driving fields. Without any approximations or limiting cases for which the photonic state can be analytically derived, a subsequent integration of the equations of motion for the photonic field is required, making it numerically demanding and tedious to consider a general electronic system with potential backaction onto the quantum field. However, with the explicit expression of the MSA, it might be feasible to ease the numerical effort such that the quantum backaction onto the quantized field can be studied with a nonclassical driving field, and as such the MSA can aid in the generation of nonclassical states of light in the XUV region with applications in quantum information, sensing, and technology.

ACKNOWLEDGMENTS

We thank Thomas Hansen for numerical simulations of the classically driven Fermi-Hubbard model and Philipp Stammer and Rasmus Vesterager Gothelf for discussions. This work was supported by the Danish National Research Foundation through the Center of Excellence for Complex Quantum Systems (Grant No. DNRF152).

APPENDIX A: HIGHER-ORDER TERMS IN THE MARKOV-TYPE APPROXIMATION

In this Appendix, we show how going beyond the Markov-type approximation presented in Eq. (26) by including higher-order terms in the expansion in Eq. (25) leads to an expression that cannot be truncated consistently in orders of g_0. Inserting the higher-order expansion [Eq. (25)] into Eq. (24) yields

$$i\frac{\partial}{\partial t}\left|\chi^{(i)}_{\boldsymbol{k},\sigma}(t)\right\rangle = \hat{\boldsymbol{A}}^{(\boldsymbol{k},\sigma)}_{Q}(t)\cdot\boldsymbol{j}_{i,i}(t)\left|\chi^{(i)}_{\boldsymbol{k},\sigma}(t)\right\rangle - i\hat{\boldsymbol{A}}^{(\boldsymbol{k},\sigma)}_{Q}(t)\cdot\sum_{m\neq i}\boldsymbol{j}_{i,m}(t)\int_{t_i}^{t}dt'\hat{\boldsymbol{A}}^{(\boldsymbol{k},\sigma)}_{Q}(t')\cdot\boldsymbol{j}_{m,i}(t')$$
$$\times\left[\left|\chi^{(i)}_{\boldsymbol{k},\sigma}(t)\right\rangle + (t'-t)\frac{\partial}{\partial t'}\left|\chi^{(i)}_{\boldsymbol{k},\sigma}(t')\right\rangle\Big|_{t'=t} + \frac{(t'-t)^2}{2!}\frac{\partial^2}{\partial t'^2}\left|\chi^{(i)}_{\boldsymbol{k},\sigma}(t')\right\rangle\Big|_{t'=t} + \cdots\right]. \tag{A1}$$

Calculating the first and second derivative to lowest order in g_0 we find

$$\frac{\partial}{\partial t'}\left|\chi^{(i)}_{\boldsymbol{k},\sigma}(t')\right\rangle\Big|_{t'=t} \simeq -i\hat{\boldsymbol{A}}^{(\boldsymbol{k},\sigma)}_{Q}(t)\cdot\boldsymbol{j}_{i,i}(t)\left|\chi^{(i)}_{\boldsymbol{k},\sigma}(t)\right\rangle, \tag{A2}$$

$$\frac{\partial^2}{\partial t'^2}\left|\chi^{(i)}_{\boldsymbol{k},\sigma}(t')\right\rangle\Big|_{t'=t} \simeq -i\left\{\left[\frac{\partial}{\partial t}\hat{\boldsymbol{A}}^{(\boldsymbol{k},\sigma)}_{Q}(t)\right]\cdot\boldsymbol{j}_{i,i}(t) + \hat{\boldsymbol{A}}^{(\boldsymbol{k},\sigma)}_{Q}(t)\frac{\partial}{\partial t}\boldsymbol{j}_{i,i}(t)\right\}\left|\chi^{(i)}_{\boldsymbol{k},\sigma}(t)\right\rangle. \tag{A3}$$

All higher-order terms would then also yield terms that are linear in $\hat{\boldsymbol{A}}^{(\boldsymbol{k},\sigma)}_{Q}(t)$ and hence g_0. However, we numerically find that the two terms in Eq. (A3) are comparable in magnitude, which prevents us from consistently truncating the expansion of the

state in Eq. (25) to a given order in g_0. Consequently, one cannot go beyond the leading order in the Markov-type approximation consistently with a finite number of terms and hence we consider only the Markov-type approximation in Eq. (26) in the present paper. Of course, one could truncate the higher-order terms when the numerical value of the related integrals reaches a certain threshold. However, this procedure would rely on the specifics of the electronic system and laser parameters.

APPENDIX B: DERIVATION OF THE QUANTUM STATE IN EQ. (30)

Here we derive the quantum state in Eq. (30) as the solution to Eq. (29). We do this by multiplying Eq. (30) with a time-dependent phase, $e^{-ib(t)}$, and insert it into Eq. (29):

$$i\frac{\partial}{\partial t}e^{-ib(t)}\big|\chi^{(i)}_{\boldsymbol{k},\sigma}(t)\big\rangle = i\frac{\partial}{\partial t}e^{-ib(t)}\hat{\mathcal{D}}\big[\beta^{(\boldsymbol{k},\sigma)}_{i,i}(t)\big]e^{-\frac{1}{2}\langle\hat{W}^2(t)\rangle_{\rm el}}|0\rangle = b(t)e^{-ib(t)}\big|\chi^{(i)}_{\boldsymbol{k},\sigma}(t)\big\rangle + ie^{-ib(t)}\left[\frac{\partial}{\partial t}\hat{\mathcal{D}}\big[\beta^{(\boldsymbol{k},\sigma)}_{i,i}(t)\big]\right]e^{-\frac{1}{2}\langle\hat{W}^2_{\rm el}(t)\rangle}|0\rangle$$
$$+ ie^{-ib(t)}\hat{\mathcal{D}}\big[\beta^{(\boldsymbol{k},\sigma)}_{i,i}(t)\big]\frac{\partial}{\partial t}e^{-\frac{1}{2}\langle\hat{W}^2_{\rm el}(t)\rangle}|0\rangle. \tag{B1}$$

We now calculate the time derivative of the displacement operator in the second line in Eq. (B1):

$$\frac{\partial}{\partial t}\hat{\mathcal{D}}\big[\beta^{(\boldsymbol{k},\sigma)}_{i,i}(t)\big] = \left\{\frac{1}{2}\big[\dot{\beta}^{(\boldsymbol{k},\sigma)*}_{i,i}(t)\beta^{(\boldsymbol{k},\sigma)}_{i,i}(t) - \beta^{(\boldsymbol{k},\sigma)*}_{i,i}(t)\dot{\beta}^{(\boldsymbol{k},\sigma)}_{i,i}(t)\big] + \dot{\beta}^{(\boldsymbol{k},\sigma)}_{i,i}(t)\hat{a}^\dagger_{\boldsymbol{k},\sigma} - \dot{\beta}^{(\boldsymbol{k},\sigma)*}_{i,i}(t)\hat{a}_{\boldsymbol{k},\sigma}\right\}\hat{\mathcal{D}}\big[\beta^{(\boldsymbol{k},\sigma)}_{i,i}(t)\big]. \tag{B2}$$

We can, upon comparison with Eq. (29), deduce that the time-dependent amplitude, $\beta^{(\boldsymbol{k},\sigma)}_{i,i}(t)$, has to be the expression given in Eq. (31). The first and second line in Eq. (B1) thus correspond to the first term on the right-hand side of Eq. (29) by absorbing the constant terms into $b(t)$. This means that the third line in Eq. (B1) must yield the second term on the right-hand side of Eq. (29).

We now calculate the time derivative of the exponential operator in the third line in Eq. (B1). A derivative of an exponential of a general operator, $\hat{F}(t)$, is given by [46]

$$\frac{d}{dt}e^{\hat{F}(t)} = \left[\dot{\hat{F}}(t) + \frac{1}{2!}[\hat{F}(t),\dot{\hat{F}}(t)] + \frac{1}{3!}[\hat{F}(t),[\hat{F}(t),\dot{\hat{F}}(t)]] + \cdots\right]e^{\hat{F}(t)}. \tag{B3}$$

In the present case, we have to calculate

$$\frac{d}{dt}e^{-\frac{1}{2}\langle\hat{W}^2_{\boldsymbol{k},\sigma}(t)\rangle_{\rm el}} = -\langle\dot{\hat{W}}_{\boldsymbol{k},\sigma}(t)\hat{W}_{\boldsymbol{k},\sigma}(t)\rangle_{\rm el}\, e^{-\frac{1}{2}\langle\hat{W}^2_{\boldsymbol{k},\sigma}(t)\rangle_{\rm el}} + O\big(g_0^3\big), \tag{B4}$$

where we have neglected the commutator $[\dot{\hat{W}}_{\boldsymbol{k},\sigma},\hat{W}_{\boldsymbol{k},\sigma}(t)]$ and only included terms up to second order in g_0. Inserting Eq. (B4) into Eq. (B1) yields a term of the form

$$\hat{\mathcal{D}}\big[\beta^{(\boldsymbol{k},\sigma)}_{i,i}(t)\big]\langle\dot{\hat{W}}_{\boldsymbol{k},\sigma}(t)\hat{W}_{\boldsymbol{k},\sigma}(t)\rangle_{\rm el}\, e^{-\frac{1}{2}\langle\hat{W}^2_{\boldsymbol{k},\sigma}(t)\rangle_{\rm el}} \overset{!}{=} \langle\langle\dot{\hat{W}}_{\boldsymbol{k},\sigma}(t)\hat{W}_{\boldsymbol{k},\sigma}(t)\rangle_{\rm el}\hat{\mathcal{D}}\big[\beta^{(\boldsymbol{k},\sigma)}_{i,i}(t)\big]\, e^{-\frac{1}{2}\langle\hat{W}^2_{\boldsymbol{k},\sigma}(t)\rangle_{\rm el}}, \tag{B5}$$

where the equality should be fulfilled by comparing with Eq. (29).

We note that the equality in Eq. (B5) holds if $\hat{\mathcal{D}}[\beta^{(\boldsymbol{k},\sigma)}_{i,i}(t)]$ commutes with $\langle\dot{\hat{W}}_{\boldsymbol{k},\sigma}(t)\hat{W}_{\boldsymbol{k},\sigma}(t)\rangle_{\rm el}$. A tedious but straightforward calculation shows that $[\hat{\mathcal{D}}[\beta^{(\boldsymbol{k},\sigma)}_{i,i}(t)],\langle\dot{\hat{W}}_{\boldsymbol{k},\sigma}(t)\hat{W}_{\boldsymbol{k},\sigma}(t)\rangle_{\rm el}] = O(g_0^3)$ which we disregard due to $g_0 \ll 1$ and the two operators hence commute up to second order in g_0. We can thus conclude that the state in Eq. (30) is a solution to Eq. (26) up to g_0^2. As $e^{-ib(t)}$ is just a phase, it has no physical consequence and is thus ignored.

[1] F. Krausz and M. Ivanov, Attosecond physics, Rev. Mod. Phys. **81**, 163 (2009).

[2] O. Neufeld, D. Podolsky, and O. Cohen, Floquet group theory and its application to selection rules in harmonic generation, Nat. Commun. **10**, 405 (2019).

[3] A. Gorlach, O. Neufeld, N. Rivera, O. Cohen, and I. Kaminer, The quantum-optical nature of high harmonic generation, Nat. Commun. **11**, 4598 (2020).

[4] D. N. Yangaliev, V. P. Krainov, and O. I. Tolstikhin, Quantum theory of radiation by nonstationary systems with application to high-order harmonic generation, Phys. Rev. A **101**, 013410 (2020).

[5] M. Lewenstein, M. F. Ciappina, E. Pisanty, J. Rivera-Dean, P. Stammer, T. Lamprou, and P. Tzallas, Generation of optical Schrödinger cat states in intense laser–matter interactions, Nat. Phys. **17**, 1104 (2021).

[6] Á. Gombkötő, P. Földi, and S. Varró, Quantum-optical description of photon statistics and cross correlations in high-order harmonic generation, Phys. Rev. A **104**, 033703 (2021).

[7] J. Rivera-Dean, T. Lamprou, E. Pisanty, P. Stammer, A. F. Ordóñez, A. S. Maxwell, M. F. Ciappina, M. Lewenstein, and P. Tzallas, Strong laser fields and their power to generate controllable high-photon-number coherent-state superpositions, Phys. Rev. A **105**, 033714 (2022).

[8] S. Yi, I. Babushkin, O. Smirnova, and M. Ivanov, Generation of massively entangled bright states of light during harmonic generation in resonant media, arXiv:2401.02817.

[9] P. Stammer, J. Rivera-Dean, A. S. Maxwell, T. Lamprou, J. Argüello-Luengo, P. Tzallas, M. F. Ciappina, and M. Lewenstein, Entanglement and squeezing of the optical field modes in high harmonic generation, Phys. Rev. Lett. **132**, 143603 (2024).

[10] J. Rivera-Dean, P. Stammer, A. S. Maxwell, T. Lamprou, E. Pisanty, P. Tzallas, M. Lewenstein, and M. F. Ciappina, Quantum-optical analysis of high-order harmonic generation in H_2^+ molecules, Phys. Rev. A **109**, 033706 (2024).

[11] J. Rivera-Dean, P. Stammer, A. S. Maxwell, T. Lamprou, A. F. Ordóñez, E. Pisanty, P. Tzallas, M. Lewenstein, and M. F. Ciappina, Entanglement and non-classical states of light in a strong-laser driven solid-state system, arXiv:2211.00033.

[12] J. Rivera-Dean, P. Stammer, A. S. Maxwell, T. Lamprou, A. F. Ordóñez, E. Pisanty, P. Tzallas, M. Lewenstein, and M. F. Ciappina, Nonclassical states of light after high-harmonic generation in semiconductors: A Bloch-based perspective, Phys. Rev. B **109**, 035203 (2024).

[13] I. Gonoskov, R. Sondenheimer, C. Hünecke, D. Kartashov, U. Peschel, and S. Gräfe, Nonclassical light generation and control from laser-driven semiconductor intraband excitations, Phys. Rev. B **109**, 125110 (2024).

[14] A. Pizzi, A. Gorlach, N. Rivera, A. Nunnenkamp, and I. Kaminer, Light emission from strongly driven many-body systems, Nat. Phys. **19**, 551 (2023).

[15] C. S. Lange, T. Hansen, and L. B. Madsen, Electron-correlation-induced nonclassicality of light from high-order harmonic generation, Phys. Rev. A **109**, 033110 (2024).

[16] M. Even Tzur, M. Birk, A. Gorlach, M. Krüger, I. Kaminer, and O. Cohen, Photon-statistics force in ultrafast electron dynamics, Nat. Photon. **17**, 501 (2023).

[17] A. Gorlach, M. E. Tzur, M. Birk, M. Krüger, N. Rivera, O. Cohen, and I. Kaminer, High-harmonic generation driven by quantum light, Nat. Phys. **19**, 1689 (2023).

[18] M. E. Tzur, M. Birk, A. Gorlach, I. Kaminer, M. Krüger, and O. Cohen, Generation of squeezed high-order harmonics, Phys. Rev. Res. **6**, 033079 (2024).

[19] P. Stammer, Absence of quantum optical coherence in high harmonic generation, Phys. Rev. Res. **6**, L032033 (2024).

[20] D. Theidel, V. Cotte, R. Sondenheimer, V. Shiriaeva, M. Froidevaux, V. Severin, P. Mosel, A. Merdji-Larue, S. Fröhlich, K.-A. Weber, U. Morgner, M. Kovacev, J. Biegert, and H. Merdji, Evidence of the quantum-optical nature of high-harmonic generation, PRX Quantum **5**, 040319 (2024).

[21] A. Rasputnyi, Z. Chen, M. Birk, O. Cohen, I. Kaminer, M. Krüger, D. Seletskiy, M. Chekhova, and F. Tani, High harmonic generation by bright squeezed vacuum, Nat. Phys. **20**, 1960 (2024).

[22] S. Lemieux, S. A. Jalil, D. Purschke, N. Boroumand, D. Villeneuve, A. Naumov, T. Brabec, and G. Vampa, Photon bunching in high-harmonic emission controlled by quantum light, arXiv:2404.05474.

[23] P. Stammer, J. Rivera-Dean, A. Maxwell, T. Lamprou, A. Ordóñez, M. F. Ciappina, P. Tzallas, and M. Lewenstein, Quantum electrodynamics of intense laser-matter interactions: A tool for quantum state engineering, PRX Quantum **4**, 010201 (2023).

[24] J. C. Baggesen and L. B. Madsen, On the dipole, velocity and acceleration forms in high-order harmonic generation from a single atom or molecule, J. Phys. B **44**, 115601 (2011).

[25] C. Gerry and P. Knight, *Introductory Quantum Optics* (Cambridge University, Cambridge, England, 2004).

[26] M. O. Scully and M. S. Zubairy, *Quantum Optics* (Cambridge University, Cambridge, England, 1997).

[27] S. L. Braunstein and P. van Loock, Quantum information with continuous variables, Rev. Mod. Phys. **77**, 513 (2005).

[28] J. Rivera-Dean, H. B. Crispin, P. Stammer, T. Lamprou, E. Pisanty, M. Krüger, P. Tzallas, M. Lewenstein, and M. F. Ciappina, Squeezed states of light after high-harmonic generation in excited atomic systems, Phys. Rev. A **110**, 063118 (2024).

[29] C. Riek, D. V. Seletskiy, A. S. Moskalenko, J. F. Schmidt, P. Krauspe, S. Eckart, S. Eggert, G. Burkard, and A. Leitenstorfer, Direct sampling of electric-field vacuum fluctuations, Science **350**, 420 (2015).

[30] L. Mandel and E. Wolf, *Optical Coherence and Quantum Optics* (Cambridge University, New York, 1995).

[31] B. Sundaram and P. W. Milonni, High-order harmonic generation: Simplified model and relevance of single-atom theories to experiment, Phys. Rev. A **41**, 6571 (1990).

[32] F. H. L. Essler, H. Frahm, F. Göhmann, A. Klümper, and V. E. Korepin, *The One-Dimensional Hubbard Model* (Cambridge University, Cambridge, England, 2005).

[33] T. Hansen, S. V. B. Jensen, and L. B. Madsen, Correlation effects in high-order harmonic generation from finite systems, Phys. Rev. A **105**, 053118 (2022).

[34] T. Hansen and L. B. Madsen, Doping effects in high-harmonic generation from correlated systems, Phys. Rev. B **106**, 235142 (2022).

[35] Y. Murakami, S. Takayoshi, A. Koga, and P. Werner, High-harmonic generation in one-dimensional Mott insulators, Phys. Rev. B **103**, 035110 (2021).

[36] T. Hansen and L. B. Madsen, Lattice imperfections and high-harmonic generation in correlated systems, New J. Phys. **26**, 063023 (2024).

[37] N. Tomita and K. Nasu, Quantum fluctuation effects on light absorption spectra of the one-dimensional extended Hubbard model, Phys. Rev. B **63**, 085107 (2001).

[38] R. E. F. Silva, I. V. Blinov, A. N. Rubtsov, O. Smirnova, and M. Ivanov, High-harmonic spectroscopy of ultrafast many-body dynamics in strongly correlated systems, Nat. Photon. **12**, 266 (2018).

[39] C. S. Lange, T. Hansen, and L. B. Madsen, Noninteger high-order harmonic generation from extended correlated systems, Phys. Rev. A **109**, 063103 (2024).

[40] S. Ghimire, A. D. DiChiara, E. Sistrunk, P. Agostini, L. F. DiMauro, and D. A. Reis, Observation of high-order harmonic generation in a bulk crystal, Nat. Phys. **7**, 138 (2011).

[41] T. J. Park and J. C. Light, Unitary quantum time evolution by iterative Lanczos reduction, J. Chem. Phys. **85**, 5870 (1986).

[42] E. S. Smyth, J. S. Parker, and K. Taylor, Numerical integration of the time-dependent Schrödinger equation for laser-driven helium, Comput. Phys. Commun. **114**, 1 (1998).

[43] X. Guan, O. Zatsarinny, K. Bartschat, B. I. Schneider, J. Feist, and C. J. Noble, General approach to few-cycle intense laser

interactions with complex atoms, Phys. Rev. A **76**, 053411 (2007).

[44] A. L. Frapiccini, A. Hamido, S. Schröter, D. Pyke, F. Mota-Furtado, P. F. O'Mahony, J. Madroñero, J. Eiglsperger, and B. Piraux, Explicit schemes for time propagating many-body wave functions, Phys. Rev. A **89**, 023418 (2014).

[45] S. de-la Peña, O. Neufeld, M. E. Tzur, O. Cohen, H. Appel, and A. Rubio, Quantum electrodynamics in high harmonic generation: Multi-trajectory Ehrenfest and exact quantum analysis, J. Chem. Theory Comput. **21**, 283 (2014).

[46] E. Merzbacher, *Quantum Mechanics*, 3rd ed. (Wiley, New York, 1998).

PAPER V

Phys. Rev. A 111, 063105 (2025)

Paper information

Author contributions

I took part in the analytical theoretical analysis, interpretation, and discussion of the research results. I contributed to the preparation of the manuscript.

PHYSICAL REVIEW A **111**, 063105 (2025)

High-order harmonic generation in a crystal driven by quantum light

Rasmus Vesterager Gothelf, Christian Saugbjerg Lange, and Lars Bojer Madsen
Department of Physics and Astronomy, Aarhus University, Ny Munkegade 120, DK-8000 Aarhus C, Denmark

(Received 24 February 2025; accepted 22 May 2025; published 6 June 2025)

We study intraband high-harmonic generation (HHG) in a crystal driven by quantum light. Previous theoretical studies have developed a framework based on coherent state expansions in terms of P distributions to consider nonclassical driving fields for HHG in atoms. Here we adapt this framework to the context of solids and consider an intraband model of ZnO. We investigate the effect of the quantum optical nature of the driving field on the harmonic spectra including the cutoff and the intensity scaling of the harmonics with driving field intensity. Based on analytical calculations in the Floquet limit, we explain why driving with thermal light or bright-squeezed vacuum (BSV) produces a much higher cutoff than when driving with fields described by coherent or Fock states. Further, we derive an expression for the generated time-dependent electric field and its fluctuations and find that it inherits characteristics of the driving field. Finally, we discuss the limitations of an approximative positive P representation, which is introduced to be able to reduce the numerical complexity for Fock and BSV driving fields.

DOI: 10.1103/PhysRevA.111.063105

I. INTRODUCTION

High-harmonic generation (HHG), the nonlinear upconversion of a low-frequency intense laser field via an electronic medium, has through the years proven to be a subject of much interest. After the phenomenon was observed [1] and analyzed theoretically [2,3] it was used to produce subfemtosecond laser pulses [4,5], which brought with them the research area of attosecond physics [6–8].

The original studies of HHG considered atomic gasses as the generating medium. However, a new avenue for exploration opened when HHG with near-infrared fields was observed from a bulk crystal [9]. HHG from solids proved to have many unique characteristics, such as the harmonic cutoff scaling linearly with field strength [9], as opposed to the quadratic scaling in gasses, as well as, e.g., topological features that affect the spectra [10–14]. Understanding of HHG in this context is reached through the three-step model [8,15–17]. First, electrons are promoted from the valence band to a conduction band. In the conduction band, the electrons propagate driven by the external electric field. Last, the electrons recombine with their holes in the valence band, and the excess energy is released as light. Because of the nonparabolic shape of the conduction band, high harmonics are also generated in the propagation step. As such, it has been useful to divide theoretical considerations of HHG in solids into generation from intraband and interband currents. Not only was this development a subject of scientific curiosity, it also pointed towards applications, such as using optical methods to reconstruct the conduction bands [18].

In these investigations, the electromagnetic field used to drive HHG as well as the generated field were modeled by classical fields, while the electronic degrees of freedom were typically treated quantum mechanically. This approach has produced many successful results, as the quantum properties of intense pulses of coherent light are typically negligible when considering intense-field-induced processes.

Recently, a shift towards a fully quantum description of HHG is developing. This is motivated by the wish to combine attoscience and quantum optics, involving the investigation of the quantum nature of the emitted light. These quantum degrees of freedom of the emitted light can be used as spectroscopic measures to study the HHG medium and potentially create attosecond pulses of nonclassical light in the XUV regime. Overall, this field of study can be categorized into two areas: (1) fully quantum descriptions of HHG when driven by coherent light [19–27] and (2) HHG driven by quantum light [28–31], such as squeezed light or Fock states. In both cases, the accurate treatment of the quantum degrees of freedom of both electrons *and* photons presents a challenge to theory.

In the first category, the theoretical framework for considering quantum fields in the context of HHG is described in detail in, e.g., Refs. [19,21]. This methodology has been used to show that the harmonic modes are entangled [19,20,23,27], that electron correlations in many-body systems can cause nonclassicality in the produced light [23,32], that HHG can be used to generate optical cat states [33], and that a so-called Markov-state approximation, where the photonic degrees of freedom are accounted for in a closed analytical form can be accurate [26]. Recently the quantum optical nature of HHG was verified experimentally in crystals [24,25].

In the second category, models of HHG in atomic gasses driven with quantum light have been presented, which use coherent-state expansions in terms of generalized P distributions to describe the photonic degrees of freedom [28,29]. This coherent-state expansion is attractive, as it allows for theory and methods developed for a semiclassical description to be applied. The theoretical results show that quantum properties of the driving field can affect characteristics of the harmonic spectrum such as the cutoff [28]. Furthermore, it has been shown that driving HHG with squeezed coherent light produces squeezed harmonics [30], indicating that quantum properties of the driving field are mapped onto the

properties of the generated field. To this end, we note that new experimental methods allow for the production of nonclassical bright-squeezed vacuum (BSV) fields, which are becoming sufficiently intense to drive HHG [34,35]. Such a BSV field can also be used to perturb a stronger coherent driving field resulting in the emission of bunched sidebands from HHG [36].

As a whole, the quantum-optical consideration of HHG has multiple prospects. Besides the ability to optimize the cutoff, the study bridges the gap between strong-field physics and quantum optics. HHG has the potential to produce and control high-intensity quantum states of light, which points towards applications in the field of quantum information [20,22,37,38].

As stated, most theoretical models of HHG driven by quantum light have so far considered the medium of atomic gasses [28,29]. This paper aims to extend this development to HHG in crystals driven by quantum light. To do so, we adapt the newly developed models for nonclassical driving of HHG [28,29] to the established model for intraband HHG in crystals. The intraband HHG description is sufficiently simple to lend itself to analytic considerations, which we use to determine and interpret the characteristics of the generated spectrum. Intraband contributions typically dominate the HHG spectrum for harmonics below the band gap in classically driven solids (see, e.g., Ref. [39]), and the results of the present work are expected to be valid in this spectral regime. Hereby, we show that these recent developments can also be applied to solids, and we identify some of the immediate differences between HHG in gasses and crystals.

The paper is organized as follows. In Sec. II we present the derivation of the generated photonic state for intraband HHG driven by quantum light, and we discuss the different choices of coherent state expansions of the driving fields, i.e., the P representations that are considered. In Sec. III we discuss the HHG spectrum. We consider the Floquet limit of a time-periodic driving field and relate these results to simulations of the generated field using a 16-cycle pulse. From this, we study the dependence of the harmonic cutoff of the spectra on the quantum optical nature of the driving field and the scaling of the harmonic intensity in terms of the driving field intensity. In Sec. IV we derive an expression for and compute the time-resolved electric field generated from the HHG spectrum. In Sec. V we discuss the accuracy of an introduced approximative positive P representation that is considered in the case of Fock and BSV driving fields. Last, in Sec. VI we give a conclusion and an outlook. The Appendixes A, B, C, and D give details on the validity of an approximative positive P representation based on an exact expansion of the Bessel functions, the accuracy of an approximate positive P representation with respect to different observables, the accuracy of the lowest-order expansion of the Bessel function involved in the analysis of the perturbative regime, and the derivation of the generated time-dependent electric field, respectively.

Atomic units ($\hbar = m_e = 4\pi\epsilon_0 = e = 1$) are used throughout the paper unless stated otherwise.

II. THEORY

The theory of HHG in solids driven by quantum light is based on the models of Refs. [28,29] developed for atoms. For completeness, we present an overview of the derivation of the generated field. Readers familiar with these matters may therefore skip this section. We will be utilizing the velocity gauge as in Refs. [23,26] and as opposed to Refs. [28,29], since this is a more convenient gauge for considering solids, as the interaction is independent of electron spatial coordinate in the dipole approximation, and Bloch's theorem therefore still applies. We will be deriving the model using a general P representation to describe the photonic degrees of freedom. As there are multiple choices of such representations, we keep the notation general for the derivation of the generated field and specify the choice of representation later (Sec. II B).

A. Derivation of the photonic state

Consider the minimally coupled, fully quantized Hamiltonian in the velocity gauge

$$\hat{H} = \frac{1}{2}\sum_j (\hat{\boldsymbol{p}}_j + \hat{\boldsymbol{A}})^2 + \hat{V}_e + \hat{H}_F, \tag{1}$$

where $\hat{\boldsymbol{p}}_j$ is the momentum of the jth electron, $\hat{V}_e$ is the electronic potential, $\hat{H}_F = \sum_{\boldsymbol{k},\sigma} \omega_{\boldsymbol{k}} \hat{a}^\dagger_{\boldsymbol{k},\sigma} \hat{a}_{\boldsymbol{k},\sigma}$ is the free-field Hamiltonian with $\hat{a}_{\boldsymbol{k},\sigma}$ ($\hat{a}^\dagger_{\boldsymbol{k},\sigma}$) being the annihilation (creation) operator of the field mode of wave vector $\boldsymbol{k}$ and polarization σ and $\omega_{\boldsymbol{k}}$ being the frequency of the corresponding mode, and, last, $\hat{\boldsymbol{A}} = \sum_{\boldsymbol{k},\sigma} \frac{g_0}{\sqrt{\omega_{\boldsymbol{k}}}} (\boldsymbol{e}_\sigma \hat{a}_{\boldsymbol{k},\sigma} + \text{H.c.})$ is the quantized vector potential in the dipole approximation with $\boldsymbol{e}_\sigma$ being the unit vector of the polarization, $g_0 = \sqrt{2\pi/V}$ the coupling constant, and V the quantization volume.

Similarly to Refs. [28,29], the state of the combined electronic and photonic system at the initial time t_i is assumed to be described by the total density operator,

$$\hat{\rho}(t_i) = |\phi_i\rangle\langle\phi_i| \bigotimes_{(\mathbf{k},\sigma)\neq(\mathbf{k}_0,\sigma_0)} |0_{\mathbf{k},\sigma}\rangle\langle 0_{\mathbf{k},\sigma}| \otimes \int d\mu P(\alpha,\beta) \frac{|\alpha\rangle\langle\beta^*|}{\langle\beta^*|\alpha\rangle}, \tag{2}$$

where $|\phi_i\rangle$ is the electronic ground state and $|0_{\boldsymbol{k},\sigma}\rangle$ is the vacuum state in the photonic mode of wave vector $\boldsymbol{k}$ and polarization σ. The driving field is assumed to be described by a single mode $(\boldsymbol{k}_0, \sigma_0)$ and is expressed in terms of a generalized P representation [40,41] over the coherent states of that mode. In this way, the theory is built in a general representation, and a specific representation can be chosen by specifying the measure $d\mu$ in Eq. (2) over the coherent phase space (Sec. II B).

To determine the time evolution of Eq. (2) through the Hamiltonian [Eq. (1)], the ansatz is made that the time-dependent density matrix can be written as

$$\hat{\rho}(t) = \int d\mu \frac{P(\alpha,\beta)}{\langle\beta^*|\alpha\rangle} \hat{\rho}_{\alpha\beta^*}(t), \tag{3}$$

where integration is still over the coherent phase space of the driving mode with the measure $d\mu$ and where $\hat{\rho}_{\alpha\beta^*}(t)$ is the time evolution of the state $|\phi_i\rangle\langle\phi_i| \otimes$

$|\alpha\rangle\langle\beta^*|\bigotimes_{(\boldsymbol{k},\sigma)\neq(\boldsymbol{k}_0,\sigma_0)}|0_{\boldsymbol{k},\sigma}\rangle\langle 0_{\boldsymbol{k},\sigma}|$. By the linearity of the integral in Eq. (3), it is then apparent that such a solution would also determine the time evolution of Eq. (2).

To find $\hat{\rho}_{\alpha\beta^*}(t)$, the interaction picture with respect to $\hat{H}_F$ is employed. This picture introduces the time-dependent phases $e^{\pm i\omega_k t}$ to the vector potential

$$\hat{\boldsymbol{A}}(t)=\sum_{\boldsymbol{k},\sigma}\frac{g_0}{\sqrt{\omega_{\boldsymbol{k}}}}(\boldsymbol{e}_\sigma\hat{a}_{\boldsymbol{k},\sigma}e^{-i\omega_k t}+\text{H.c.}). \tag{4}$$

Next, another unitary transformation is applied, using displacement operators with the coherent state amplitudes α and β^*, such that the driving mode of $\hat{\rho}_{\alpha\beta^*}(t)$ is shifted to a vacuum state at time t_i, that is, we let $\hat{\tilde{\rho}}_{\alpha\beta^*}(t)=\hat{D}^\dagger(\alpha)\hat{\rho}_{\alpha\beta^*}(t)\hat{D}(\beta^*)$, and it follows that $\hat{\tilde{\rho}}_{\alpha\beta^*}(t_i)=|\phi_i\rangle\langle\phi_i|\bigotimes_{(\boldsymbol{k},\sigma)}|0_{\boldsymbol{k},\sigma}\rangle\langle 0_{\boldsymbol{k},\sigma}|$. Applying this transform to the Hamiltonian in Eq. (1), the vector potential transforms as $\hat{\boldsymbol{A}}(t)\mapsto\hat{\boldsymbol{A}}_Q(t)+\boldsymbol{A}^\alpha_{\rm cl}(t)$ [42], where $\hat{\boldsymbol{A}}_Q(t)$ is the same quantum vector potential as $\hat{\boldsymbol{A}}(t)$ in Eq. (4) but now given a subscript for the sake of distinction, and where

$$\boldsymbol{A}^\alpha_{\rm cl}(t)=\langle\alpha|\hat{\boldsymbol{A}}(t)|\alpha\rangle=\frac{g_0}{\sqrt{\omega_0}}\left(\boldsymbol{e}_{\sigma_0}\alpha e^{-i\omega_0 t}+\text{H.c.}\right) \tag{5}$$

is the classical vector potential of the driving field corresponding to the coherent state $|\alpha\rangle$. It then follows that

$$i\frac{\partial\hat{\tilde{\rho}}_{\alpha\beta^*}(t)}{\partial t}=\hat{H}_\alpha(t)\hat{\tilde{\rho}}_{\alpha\beta^*}(t)-\hat{\tilde{\rho}}_{\alpha\beta^*}(t)\hat{H}_\beta(t), \tag{6}$$

where $\hat{H}_\xi(t)=\frac{1}{2}\sum_j(\hat{\boldsymbol{p}}_j+\hat{\boldsymbol{A}}_Q(t)+\boldsymbol{A}^\xi_{\rm cl}(t))^2+\hat{V}_e$ for $\xi=\{\alpha,\beta\}$. We neglect $\hat{\boldsymbol{A}}^2_Q(t)$ as done in Refs. [19,23]. Hence,

$$\hat{H}_\xi(t)=\hat{H}_{\rm SC}(t;\xi)+\hat{\boldsymbol{A}}_Q(t)\cdot\sum_j\left[\hat{\boldsymbol{p}}_j+\boldsymbol{A}^\xi_{\rm cl}(t)\right], \tag{7}$$

where

$$\hat{H}_{\rm SC}(t;\xi)=\frac{1}{2}\sum_j\left[\hat{\boldsymbol{p}}_j+\boldsymbol{A}^\xi_{\rm cl}(t)\right]^2+\hat{V}_e, \tag{8}$$

is the semiclassical (SC) Hamiltonian of the single-mode coherent field with amplitude ξ.

Letting $|\Psi_\xi(t)\rangle$ be the solution to the time-dependent Schrödinger equation

$$i\frac{\partial}{\partial t}|\Psi_\xi(t)\rangle=\hat{H}_\xi(t)|\Psi_\xi(t)\rangle \tag{9}$$

with $|\Psi_\xi(t_i)\rangle=|\phi_i\rangle\bigotimes_{\boldsymbol{k},\sigma}|0_{\boldsymbol{k},\sigma}\rangle$, it is apparent that $|\Psi_\alpha(t)\rangle\langle\Psi_{\beta^*}(t)|$ is a solution to Eq. (6). By the choice of boundary condition on $|\Psi_\xi(t)\rangle$ at $t=t_i$ it is apparent that $|\Psi_\alpha(t)\rangle\langle\Psi_{\beta^*}(t)|$ has the same boundary condition as $\hat{\tilde{\rho}}_{\alpha\beta^*}(t)$, that is, $|\Psi_\alpha(t_i)\rangle\langle\Psi_{\beta^*}(t_i)|=\hat{\tilde{\rho}}_{\alpha\beta^*}(t_i)$. Therefore, we have that $\hat{\tilde{\rho}}_{\alpha\beta^*}(t)=|\Psi_\alpha(t)\rangle\langle\Psi_{\beta^*}(t)|$.

To determine $|\Psi_\xi(t)\rangle$, an interaction picture is employed via the time-evolution operator $\hat{\mathcal{U}}_{\rm SC}(t;\xi)$ associated with $\hat{H}_{\rm SC}(t;\xi)$. In this picture, Eq. (9) becomes

$$i\frac{\partial}{\partial t}|\Psi_\xi(t)\rangle=\hat{\boldsymbol{A}}_Q(t)\cdot[\hat{\mathcal{U}}^\dagger_{\rm SC}(t;\xi)\hat{\boldsymbol{j}}^\xi(t)\hat{\mathcal{U}}_{\rm SC}(t;\xi)]|\Psi_\xi(t)\rangle, \tag{10}$$

where $\hat{\boldsymbol{j}}^\xi(t)=\sum_j[\hat{\boldsymbol{p}}_j+\boldsymbol{A}^\xi_{\rm cl}(t)]$ is the current operator.

Equation (10) may be solved by expanding in the electronic basis $\{|\phi_m\rangle\}$ of solutions to the field-free time-independent Schrödinger equation. Letting $\{|\chi^\xi_m(t)\rangle\}$ denote the corresponding photonic states, the complete state of the combined system can then be expressed as $|\Psi_\xi(t)\rangle=\sum_m|\phi_m\rangle\otimes|\chi^\xi_m(t)\rangle$. Projecting onto the mth electronic state, $\langle\phi_m|$, the equation of motion for the corresponding photonic state $|\chi^\xi_m(t)\rangle$ becomes

$$i\frac{\partial}{\partial t}\left|\chi^\xi_m(t)\right\rangle=\hat{\boldsymbol{A}}_Q(t)\cdot\sum_n\boldsymbol{j}^\xi_{m,n}(t)\left|\chi^\xi_n(t)\right\rangle, \tag{11}$$

where

$$\boldsymbol{j}^\xi_{m,n}(t)=\left\langle\phi^\xi_m(t)\right|\hat{\boldsymbol{j}}^\xi(t)\left|\phi^\xi_n(t)\right\rangle \tag{12}$$

is the current matrix elements between different semiclassically propagated electronic states, $|\phi^\xi_n(t)\rangle=\hat{\mathcal{U}}_{\rm SC}(t;\xi)|\phi_n\rangle$. We note that in the SC theory of HHG, the spectrum is related to the norm square of the Fourier transform of the current matrix element $\boldsymbol{j}^\xi_{i,i}(t)=\langle\phi^\xi_i(t)|\hat{\boldsymbol{j}}^\xi(t)|\phi^\xi_i(t)\rangle$ for i denoting the initial state of the electronic problem. It is the presence of the nondiagonal transition current matrix elements in Eq. (11) that induce quantum light in the HHG process [19,23,26,27].

Before we specify our solid-state model, a few remarks regarding the characteristics of the above developments are in place. First, we note that the expansion in coherent states in terms of the P function allows the usage of SC theory and associated numerical techniques to solve the time-dependent Schrödinger equation. Second, the additional use of displacement operators to transform the initial state to be in the vacuum state allows one to handle the large number of photons considered in this problem, i.e., one only needs to numerically handle the photons generated from the HHG process which are much fewer than the ones in the driving field. These two ingredients are essential for the making the problem tractable numerically.

We now specify the electronic system considered in this work. We use an intraband model which corresponds to considering a one-dimensional cut of the solid along the polarization direction of $\boldsymbol{A}^\xi_{\rm cl}(t)$. We consider a lattice constant a and beyond-nearest-neighbor terms, which in the crystal-momentum basis is expressed as

$$\hat{H}_{\rm SC}(t;\xi)=\sum_{q,\mu}\mathcal{E}\left[q+A^\xi_{\rm cl}(t)\right]\hat{c}^\dagger_{q,\mu}\hat{c}_{q,\mu}, \tag{13}$$

where $\hat{c}_{q,\mu}$ ($\hat{c}^\dagger_{q,\mu}$) is the annihilation (creation) operator of the crystal momentum state q with spin μ, and where

$$\mathcal{E}(q)=\sum_{l=0}b_l\cos(alq) \tag{14}$$

is the dispersion relation of the material, where b_l is the lth Fourier coefficient of the band structure. The current operator in this model is

$$\hat{\boldsymbol{j}}^\xi(t)=\boldsymbol{e}_\sigma\sum_{q,\mu}\frac{\partial\mathcal{E}\left[q+A^\xi_{\rm cl}(t)\right]}{\partial q}\hat{c}^\dagger_{q,\mu}\hat{c}_{q,\mu}, \tag{15}$$

which is a vector along the polarization direction.

From Eqs. (13) and (15) it is apparent that both $\hat{H}_{\rm SC}(t;\xi)$ and $\hat{\boldsymbol{j}}^\xi(t)$ are diagonal in the basis of crystal-momentum states, meaning that the off-diagonal terms in Eq. (12) vanish.

Hereby Eq. (10) reduces to

$$i\frac{\partial}{\partial t}\left|\chi_m^{\xi}(t)\right\rangle = \hat{\boldsymbol{A}}_Q(t)\cdot \boldsymbol{j}_{m,m}^{\xi}(t)\left|\chi_m^{\xi}(t)\right\rangle. \tag{16}$$

We consider the case where the system is initially in its ground state, i.e., $|\chi_m^{\xi}(t_i)\rangle = \delta_{i,m}|0\rangle$, so we only need to consider the state with $m = i$. Equation (16) thus reduces to

$$i\frac{\partial}{\partial t}\left|\chi_i^{\xi}(t)\right\rangle = \hat{\boldsymbol{A}}_Q(t)\cdot \boldsymbol{j}_{i,i}^{\xi}(t)\left|\chi_i^{\xi}(t)\right\rangle, \tag{17}$$

which is linear in creation and annihilation operators and can therefore be solved. The solution to Eq. (17) is a direct product of coherent states [43,44]

$$\left|\chi_i^{\xi}(t)\right\rangle = \bigotimes_{\boldsymbol{k},\sigma}\hat{D}\left[\gamma_{\boldsymbol{k},\sigma}^{\xi}(t)\right]|0_{\boldsymbol{k},\sigma}\rangle, \tag{18}$$

over all considered photonic modes $(\boldsymbol{k},\sigma)$ including the laser mode, and where

$$\gamma_{\boldsymbol{k},\sigma}^{\xi}(t) = -i\frac{g_0}{\sqrt{\omega_{\boldsymbol{k}}}}\int_{t_i}^{t}\boldsymbol{j}_{i,i}^{\xi}(t')\cdot\boldsymbol{e}_{\sigma}e^{i\omega_{\boldsymbol{k}}t'}dt', \tag{19}$$

is the coherent state amplitude which is the Fourier transform of the current matrix element in the Floquet limit of $t\to\infty$ and $t_i\to-\infty$. As such, the time dependence in the model is carried by these integral limits. The photonic state in Eq. (18) was also discussed in Ref. [23] and the result shows that only coherent light can be generated when driving a one-band model with coherent light.

The solution [Eq. (18)] to Eq. (11) is substituted into Eq. (3) by writing $\hat{\tilde{\rho}}_{\alpha\beta^*}(t) = |\phi_i^{\alpha}(t)\rangle\langle\phi_i^{\beta^*}(t)|\otimes|\chi_i^{\alpha}(t)\rangle\langle\chi_i^{\beta^*}(t)|$. Hereby it is found that

$$\begin{aligned}\hat{\rho}(t) = \int d\mu\frac{P(\alpha,\beta)}{\langle\beta^*|\alpha\rangle}&\left|\phi_i^{\alpha}(t)\right\rangle\left\langle\phi_i^{\beta^*}(t)\right|\\ &\bigotimes\hat{D}(\alpha)\left|\gamma_{\mathbf{k}_0,\sigma_0}^{\alpha}(t)\right\rangle\left\langle\gamma_{\mathbf{k}_0,\sigma_0}^{\beta^*}(t)\right|\hat{D}^{\dagger}(\beta^*)\\ &\bigotimes_{(\mathbf{k},\sigma)\neq(\mathbf{k}_0,\sigma_0)}\left|\gamma_{\mathbf{k},\sigma}^{\alpha}(t)\right\rangle\left\langle\gamma_{\mathbf{k},\sigma}^{\beta^*}(t)\right|.\end{aligned} \tag{20}$$

The SC evolution of the field-free eigenstates is simply given as $|\phi_i^{\xi}(t)\rangle = \exp[-iE_{\xi}(t)]|\phi_i(t_i)\rangle$, where $E_{\xi}(t) = \int_{t_i}^{t}dt'\sum_{q,\mu}\mathcal{E}[q+A_{\mathrm{cl}}^{\xi}(t')]\langle\hat{c}_{q,\mu}^{\dagger}\hat{c}_{q,\mu}\rangle$ [45]. The electronic states are then traced out, leaving their phases, and the state of the field at time t is given as

$$\begin{aligned}\hat{\rho}_F(t) = \int d\mu\frac{P(\alpha,\beta)}{\langle\beta^*|\alpha\rangle}&e^{i[E_{\beta^*}(t)-E_{\alpha}(t)]}\\ &\bigotimes\hat{D}(\alpha)\left|\gamma_{\mathbf{k}_0,\sigma_0}^{\alpha}(t)\right\rangle\left\langle\gamma_{\mathbf{k}_0,\sigma_0}^{\beta^*}(t)\right|\hat{D}^{\dagger}(\beta^*)\\ &\bigotimes_{(\mathbf{k},\sigma)\neq(\mathbf{k}_0,\sigma_0)}\left|\gamma_{\mathbf{k},\sigma}^{\alpha}(t)\right\rangle\left\langle\gamma_{\mathbf{k},\sigma}^{\beta^*}(t)\right|.\end{aligned} \tag{21}$$

Equation (21) shows that the emitted field state is a weighted average of many coherent states driven with a SC driving field, all weighted by the distribution function $P(\alpha,\beta)$. We note that the right-hand side of Eq. (21) is completely specified, once the current element $\boldsymbol{j}_{i,i}^{\xi}(t)$ [and hence $\gamma_{\mathbf{k},\sigma}^{\xi}(t)$] is obtained and P is specified. The phase factors with the time-dependent electronic energies will disappear under the choice of representation considered in Sec. II B.

B. Representation of the driving fields

We consider different types of driving fields. Specifically, we drive our model with coherent, Fock, thermal, and BSV light. As the generated photonic state [Eq. (21)] was derived in a general representation, the choice of representation can be made freely which we will now specify for each of the driving fields. For Coherent and thermal light we use the Glauber-Sudarshan (GS) representation which takes $d\mu = d^2\alpha d^2\beta\delta^{(2)}(\alpha-\beta^*)$ [40] with corresponding distributions [43],

$$P_{\mathrm{Coherent}}^{(\alpha_L)}(\alpha) = \delta^{(2)}(\alpha-\alpha_L), \tag{22}$$

$$P_{\mathrm{Thermal}}^{(\langle N\rangle)}(\alpha) = \frac{1}{\pi\langle N\rangle}\exp\left(-\frac{|\alpha|^2}{\langle N\rangle}\right), \tag{23}$$

where α_L is the coherent state amplitude of the driving field and $\langle N\rangle$ is the mean photon number for thermal light. The Glauber-Sudarshan representations for Fock and BSV light are highly singular [41,43] and therefore not computationally useful. Instead, we use the positive P representation for these types of quantum light [43]. In the positive P representation $d\mu = d^2\alpha d^2\beta$, with the corresponding positive P distribution given by

$$P(\alpha,\beta) = (4\pi)^{-1}\exp(-|\alpha-\beta^*|^2/4)Q[(\alpha+\beta^*)/2], \tag{24}$$

with

$$Q(\alpha) = \frac{1}{\pi}\langle\alpha|\hat{\rho}|\alpha\rangle \tag{25}$$

the Husimi-Q function [46]. By carefully investigating the function $P(\alpha,\beta)$ in Eq. (24) for both a Fock and BSV state, we find that it has narrow peaks only when $\alpha=\beta^*$ and is vanishing otherwise. To simplify the expression, we approximate these narrow peaks as a δ function and rewrite Eq. (24) as

$$P(\alpha,\beta)\approx\delta^{(2)}(\alpha-\beta^*)Q\left(\frac{\alpha+\beta^*}{2}\right), \tag{26}$$

where the proportionality factor is the Husimi-Q function which follows from the definition of $P(\alpha,\beta)$. In Sec. V and Appendixes A and B we consider the accuracy of this approximation for computing different observables. We shall refer to Eq. (26) as the approximative positive P (APP) representation. Within the APP we thus describe Fock and BSV light as [46]

$$P_{\mathrm{Fock}}^{(N)}(\alpha,\beta)\approx\delta^{(2)}(\alpha-\beta^*)P_{\mathrm{Fock}}^{(N)}(\alpha), \tag{27}$$

where

$$P_{\mathrm{Fock}}^{(N)}(\alpha) = Q_{\mathrm{Fock}}^{(N)}(\alpha) = \frac{1}{\pi}e^{-|\alpha|^2}\frac{|\alpha|^{2N}}{N!}, \tag{28}$$

and similarly

$$P_{\mathrm{BSV}}^{(r)}(\alpha,\beta)\approx\delta^{(2)}(\alpha-\beta^*)P_{\mathrm{BSV}}^{(r)}(\alpha), \tag{29}$$

where

$$P^{(r)}_{\mathrm{BSV}}(\alpha) = Q^{(r)}_{\mathrm{BSV}}(\alpha) = \frac{1}{\pi\cosh r}\exp\left(-\frac{2[\mathrm{Re}(\alpha)]^2}{1+e^{-2r}} - \frac{2[\mathrm{Im}(\alpha)]^2}{1+e^{2r}}\right) \quad (30)$$

for a Fock state $|N\rangle$ and for a squeezed vacuum state $\hat{S}(r)|0\rangle$, respectively, with $\hat{S}$ being the squeezing operator [43] and where r is chosen to be real for simplicity. In both Eqs. (28) and (30), we have defined the P function within the APP representation to be the appropriate Husimi-Q function.

As the four representations of light in Eqs. (22), (23), (28), and (30) along with the corresponding expression for $d\mu$ are diagonal in phase space [Eqs. (28) and (30) only diagonal within the APP], we can rewrite the field state in Eq. (21) for the cases considered as

$$\hat{\rho}_F(t) = \int d^2\alpha P(\alpha)\left|\gamma^{\alpha}_{\mathbf{k}_0,\sigma_0}(t)+\alpha\right\rangle\left\langle\gamma^{\alpha}_{\mathbf{k}_0,\sigma_0}(t)+\alpha\right| \bigotimes_{(\mathbf{k},\sigma)\neq(\mathbf{k}_0,\sigma_0)} \left|\gamma^{\alpha}_{\mathbf{k},\sigma}(t)\right\rangle\left\langle\gamma^{\alpha}_{\mathbf{k},\sigma}(t)\right|, \quad (31)$$

where the P distribution, $P(\alpha)$, for the driving field can describe either of the four types of driving fields in Eqs. (22), (23), (28), and (30). From Eq. (31), expectation values of interest can be calculated. These expectation values are exact for coherent and thermal light driving fields, while they are approximate for Fock light and BSV driving fields, due to the APP representation. A discussion of the accuracy of the APP representation in relation to different observables is given in Sec. V and Appendixes A and B.

III. THE HARMONIC SPECTRUM

Using Eq. (31), the harmonic spectrum can be found by considering the energy in the photonic degrees of freedom $\mathcal{E} = \sum_{\boldsymbol{k},\sigma}\omega_k\langle\hat{a}^{\dagger}_{\boldsymbol{k},\sigma}\hat{a}_{\boldsymbol{k},\sigma}\rangle$ as in Refs. [19,23,28]. Letting $\sum_{\boldsymbol{k}} \mapsto V/(2\pi c)^3\int d\omega\,\omega^2\int d\Omega$, we can write out the sum over polarizations σ and express the spectrum as the emitted energy per frequency. Furthermore, we disregard the driving field in the laser mode, i.e., we take $|\gamma^{\alpha}_{\mathbf{k}_0,\sigma_0}(t)+\alpha\rangle \to \hat{D}^{\dagger}(\alpha)|\gamma^{\alpha}_{\mathbf{k}_0,\sigma_0}(t)+\alpha\rangle = |\gamma^{\alpha}_{\mathbf{k}_0,\sigma_0}(t)\rangle$ in Eq. (31) since we are only interested in the generated field. The spectrum can then be expressed as

$$S(\omega) \propto \int d^2\alpha P(\alpha) S_{\mathrm{SC}}(\omega;\alpha) \quad (32)$$

with

$$S_{\mathrm{SC}}(\omega;\alpha) = \left|\int_{-\infty}^{\infty} dt'\, j^{\alpha}_{i,i}(t')e^{i\omega t'}\right|^2 \quad (33)$$

being the expression for the SC spectrum. Looking at Eq. (32), this leads to the same interpretation as in Ref. [28]: The spectrum is a weighted average of SC spectra [Eq. (33)] each driven with a classical field characterized by the coherent-state parameter α and weighted by a $P(\alpha)$ distribution.

A. The Floquet limit

To analyze the harmonic spectrum [Eq. (32)] further, we assume a time-periodic vector potential, i.e., a vector potential with no envelope. The vector potential is written as $A^{\alpha}_{\mathrm{cl}}(t) = 2g_0\omega_0^{-1/2}|\alpha|\sin(\omega_0 t-\phi)$ where ϕ is the phase of α. We assume that the conduction band is filled symmetrically around $q=0$ with an equal number of electrons with both spin orientations.

The current matrix element $j^{\alpha}_{i,i}(t)$ from Eq. (12), with the operator $\hat{j}^{\alpha}(t)$ from Eq. (15), is written as $j^{\alpha}_{i,i}(t) = -a\sum_{l,q,\mu} l b_l \sin[alq + alA^{\alpha}_{\mathrm{cl}}(t)]$, along the direction of the chain. The sum over crystal momenta q is now only over the occupied crystal momenta in the electronic initial state. Since each of these crystal momenta is occupied by both a spin up and a spin down electron, a factor of 2 accounts for the summation over electron spins μ. Furthermore, we expand the sine function using the addition formula $\sin[alq + alA^{\alpha}_{\mathrm{cl}}(t)] = \sin(alq)\cos[alA^{\alpha}_{\mathrm{cl}}(t)] + \cos(alq)\sin[alA^{\alpha}_{\mathrm{cl}}(t)]$. As $\sin(alq)$ is an odd function of q, and since the electrons in the initial state are assumed to be distributed symmetrically around $q=0$, this term disappears when summing over q. This leaves us with the expression for the current matrix element

$$j^{\alpha}_{i,i}(t) = -2a\sum_l b_l l\left[\sum_q \cos(alq)\right]\sin\left[alA^{\alpha}_{\mathrm{cl}}(t)\right], \quad (34)$$

Looking at the expression for the spectrum [Eqs. (32) and (33)], we note that it is proportional to the square of Fourier transformed current. To proceed analytically, we use the Jacobi-Anger expansion $\sin[alA^{\alpha}_{\mathrm{cl}}(t)] = 2\sum_{n=1,3,5,\ldots} J_n(l\tilde{g}_0|\alpha|)\sin[n(\omega_0 t-\phi)]$, where J_n is the nth-order Bessel function of the first kind and $\tilde{g}_0 = 2ag_0/\sqrt{\omega_0}$ is a lattice-modified coupling constant. From this expansion the Fourier transform can be computed as done in Ref. [45],

$$\int_{-\infty}^{\infty} dt'\sin\left[alA^{\alpha}_{\mathrm{cl}}(t')\right]e^{i\omega t'} = -2\pi i\sum_{n=1,3,5,\ldots}^{\infty} J_n(l\tilde{g}_0|\alpha|) \times\left[e^{-in\phi}\delta(\omega+n\omega_0) - e^{in\phi}\delta(\omega-n\omega_0)\right], \quad (35)$$

where δ denotes the delta function. Taking the square norm, the products of delta functions for different n's must vanish. Hence, any phase on the delta functions vanishes. Furthermore, as we restrict ourselves to positive frequencies, the terms $\delta[\omega+(2n-1)\omega_0]$ may be discarded. Therefore, by inserting Eqs. (34) and (35) into Eqs. (32) and (33), the generated HHG spectrum in the Floquet limit is given as

$$S(\omega) \propto \sum_{n=1,3,5,\ldots}^{\infty}\omega^2\delta(\omega-n\omega_0)\int d^2\alpha P(\alpha)\left[\sum_l C_l J_n(l\tilde{g}_0|\alpha|)\right]^2, \quad (36)$$

where we collect crystal specific properties in the coefficient $C_l = lb_l\sum_q\cos(alq)$. In Eq. (36), the selection rule for the odd harmonics is clearly seen. We also see that the size of the nth harmonic peak is determined by the integral of the product between the P distribution function and a weighted sum of Bessel functions of order n. As we now show, analysis of these integrals can be used to gain insights into the characteristics of the spectrum.

B. Simulated spectra

From Eqs. (32) and (36) the HHG spectra can be computed for a quantum state of driving light, given the appropriate P functions. To simplify the computation, we note that for the HHG spectrum in the Floquet limit [Eq. (36)] the only dependence on the phase of α in the integrand is contained in the P function. Assuming an adiabatic evolution of the envelope of the driving field [which is already a necessary assumption to apply an envelope to Eq. (5)], we can assume that the norm square of the Fourier transform of the current matrix element is independent of the phase of α. Therefore, we may write the harmonic spectrum of Eq. (32) using polar coordinates for integration as

$$S(\omega) \propto \omega^2 \int_0^\infty d|\alpha| \left| \int_{-\infty}^{\infty} dt' j^{\alpha}_{i,i}(t') e^{i\omega t'} \right|^2 P(|\alpha|), \tag{37}$$

where we have defined the radial distribution as

$$P(|\alpha|) = |\alpha| \int_0^{2\pi} d\phi P(\alpha), \tag{38}$$

and where ϕ again denotes the phase of α. As such, the angular integral can be performed without relation to frequency ω, which lowers the dimensionality of computation. This approximation is valid if the width of the individual harmonic peaks overlap minimally, which is the case for the ∼16 laser cycles pulse that we use for simulations. Using Eq. (37), we calculate the spectra where the electrons are driven by a flat top pulse with 10 cycles of constant amplitude with an additional 3 cycle $\sin^2$ turn-on and turn-off as in Ref. [45]. We use the P functions for coherent [Eq. (22)], thermal [Eq. (23)], Fock [Eq. (28)], and BSV [Eq. (30)] driving fields, at the same mean photons numbers $\langle \hat{a}^\dagger_{\boldsymbol{k}_0,\sigma_0} \hat{a}_{\boldsymbol{k}_0,\sigma_0} \rangle$. This means that the following quantities are equal to the mean photon number: $|\alpha_L|^2$ for the coherent state, $\langle N \rangle$ for the thermal state, N for the Fock state and $\sinh^2(r)$ for the BSV state.

In the simulations, we use $g_0 = 4 \times 10^{-8}$ a.u. and $\omega_0 = 0.005$ a.u. as in Ref. [23], a mean photon number of the driving fields $\langle \hat{a}^\dagger_{\boldsymbol{k}_0,\sigma_0} \hat{a}_{\boldsymbol{k}_0,\sigma_0} \rangle = 7.35 \times 10^{11}$ (a coherent field with this photon number has the intensity $I = 8.26 \times 10^{11}$ W/cm^2). We use the parameters for the first conduction band in a ZnO crystal along the Γ-M direction [47] populated by $L = 10$ electrons. Clearly, the characteristics of the results are independent of the number of electrons. In this model, the lattice constant is $a = 5.32$ a.u. and the Fourier coefficients are $b_1 = -0.0814$ a.u., $b_2 = -0.0024$ a.u., $b_3 = -0.0048$ a.u., $b_4 = -0.0003$ a.u., and $b_5 = -0.0009$ a.u. The periodicity is chosen such that $\Delta q = \frac{2\pi}{10a}$ and $q_{\max} = 2\Delta q$. For the BSV light, the squeezing parameter is obtained from the relation $\langle \hat{a}^\dagger_{\boldsymbol{k}_0,\sigma_0} \hat{a}_{\boldsymbol{k}_0,\sigma_0} \rangle = \sinh^2(r)$, yielding $r = 14.35$ in our simulations. In Ref. [35] the production of BSV fields reaching $r = 15.3 \pm 0.5$ was reported, and the BSV field considered in this work is therefore experimentally realizable.

The spectra in Fig. 1 show the overall same behavior as the spectra in Ref. [28] for atomic gasses. The spectrum generated from a Fock-state driving field is visually identical to the coherently driven spectrum, both with a clear cutoff. On the other hand, the spectra for thermal and BSV driving fields are much broader with less clearly defined cutoffs but with the generation of much higher harmonics. Coherent and Fock fields produce the same spectrum because the radial part of the P function for coherent light is a delta function and similarly the radial part of the P function for a Fock state is approximately a delta function for large photon numbers [28]. This is further discussed in Secs. III C, V and Appendix A.

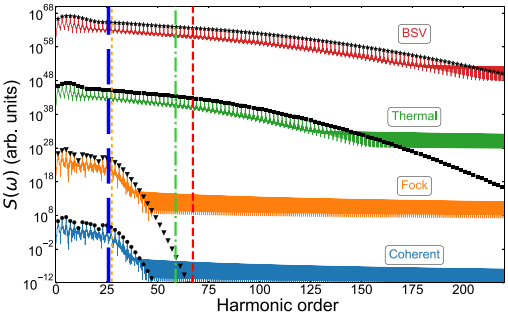

FIG. 1. Simulated HHG spectra using the parameters specified in Sec. III B. Graphs [coherent (blue), Fock (orange), thermal (green), and BSV (red)] are simulated from Eq. (37) with a 10 cycle flat-top pulse with additional three-cycle turn-on and turn-off. For visual clarity, the spectrum for HHG driven by Fock light is multiplied by 10^{20}, for Thermal light 10^{40}, and for BSV 10^{60}. Black markers [coherent (dots), Fock (triangles), thermal (squares), and BSV (stars)] are simulated in the Floquet limit using Eq. (36). Vertical lines [coherent (blue, long dashed), Fock (orange, dotted), thermal (green, dash-dotted), and BSV (red, short dashed)] denote the predicted cutoff calculated with Eq. (39).

Earlier works [28,31] have also used the approximation of Eq. (26), but have, contrary to the present work, based this approximation on the limit of a large interaction volume by changing variables from coherent state amplitude to the electric field amplitude, $\mathcal{E}_\alpha$, via $\mathcal{E}_\alpha = 2g_0\alpha$ and then taking the limit of $g_0 \to 0$ for constant $\mathcal{E}_\alpha$. Critically, as pointed out in Ref. [31], consistently applying this limit also to the Husimi-Q function would imply that neither a Fock nor a BSV driver would generate any harmonic spectrum as opposed to the results presented in the present work. However, we prove in Appendix A without using any further approximations, that both Fock and BSV driving fields indeed generate HHG spectra, validating the results presented in Fig. 1. We believe, that the limiting procedure considered in Refs. [28,31], when also applied to the Husimi-Q function neglects information of the physical state contained in the distribution, leading to a nonphysical result.

In Fig. 1, the finite pulse [Eq. (32)] and Floquet limits [Eq. (36)] are also compared, where the harmonic peaks obtained from the Floquet calculation are given by the black markers. The heights of the harmonic peaks are identical in the two calculations up to a global constant. Longer pulse durations just create sharper peaks. This is congruent with studies of inter- and intracycle aspects of HHG [48].

C. Cutoff

Figure 1 shows that the characteristics of the spectra pertaining to the harmonic peaks can be interpreted in the Floquet

limit. Via Eq. (36), the magnitude of the nth harmonic is proportional to the integral of the product between the distribution function of the driving field, $P(\alpha)$ and the square sum of Bessel functions of order n. The Bessel function $J_n(x)$ quickly vanishes for $x < n$ [48]. Hence, if the P function is only nonzero within the region where the arguments of the Bessel function are smaller than its order, then the overlap between these functions will vanish and there will be no harmonic peak.

The argument of the Bessel function is $l\tilde{g}_0|\alpha|$, which means that the $|\alpha|$ interval where all the Bessel functions of order n vanish is $|\alpha| < n/(l_{\max}\tilde{g}_0)$, where $l_{\max}$ denotes the highest significant order in the Fourier expansion of the conduction band, which in the simulations of Fig. 1 is $l_{\max} = 5$ (see Ref. [48] for a discussion of the relation between the Bessel functions and cutoff in intraband HHG). The distributions for coherent and Fock states are narrow on the axis of $|\alpha|$. In fact, the P function for a coherent state is a delta function on $|\alpha|$, and the APP function for a Fock state can be approximated as a delta function on $|\alpha|$ [28]. Therefore, for ascending harmonic orders, the regime of no overlap is quickly reached for coherent and Fock driving fields in comparison with thermal and BSV driving fields. This is depicted in Fig. 2, where the square of the Bessel function $J_n^2(\tilde{g}_0|\alpha|)$ and the P function is plotted as a function of the argument $|\alpha|\tilde{g}_0$ for harmonics $n = 11$ and 33.

The quickly vanishing overlap for Fock and coherent driving fields explains why these two spectra are very similar in Fig. 1. The heights of the peaks and also the cutoff are determined only from the radial distributions $P(|\alpha|)$ [see Eq. (38)], which for coherent and Fock states are approximately equal. Furthermore, for coherent driving fields this cutoff is the same as found in Ref. [48]. For thermal and BSV fields, the distributions are broad and extend much further than their mean value (see Fig. 2). Hence, even though the mean photon number might be the same, the broad distributions of these reach far larger values of $|\alpha|$ and the overlap between $P(|\alpha|)$ and the Bessel functions is nonvanishing for higher harmonics yielding a higher cutoff. The gradual decrease of the tails also explains why the cutoff is less clearly defined (see Fig. 1).

If we were to define the cutoff (γ_{cutoff}) in the units of harmonic order for such a state, then it makes sense from these considerations to write it as

$$\gamma_{\text{cutoff}} = l_{\max}\tilde{g}_0(\mu_P + 3\sigma_P), \tag{39}$$

where μ_P and σ_P are the mean and standard deviation, respectively, of the variable $|\alpha|$ given the distribution $P(\alpha)$, which are equivalent to the mean and standard deviation of the radial distribution $P(|\alpha|)$ [see Eqs. (C13) and (C14) for explicit expressions]. These quantities are therefore unitless and entirely determined by the choice of P. The cutoffs are calculated numerically and plotted alongside the harmonic spectra in Fig. 1 as vertical lines. This choice of cutoff is sensible, as most of the P function will be contained within the domain of $\mu_P - 3\sigma_P \leqslant |\alpha| \leqslant \mu_P + 3\sigma_P$, and it yields the correct cutoff for the coherent and Fock driving fields as seen in Fig. 1. However, as is also apparent from Fig. 1, the cutoff is not clearly defined for the thermal and BSV fields due to the more gradually vanishing overlap.

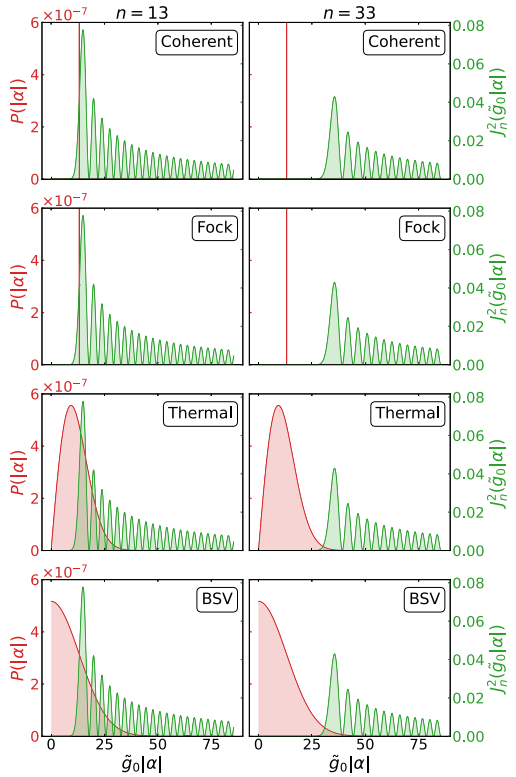

FIG. 2. Illustration of the radial distribution functions, $P(|\alpha|)$ of Eq. (38) for a coherent, Fock, thermal, and BSV driving field at the same mean photon number as used in Fig. 1 plotted against a Bessel function of order 13 (left) and 33 (right). The APP representation is used for the thermal and BSV fields. The behavior of $J_n(x) \approx 0$ for $x < n$ can be seen. For coherent and Fock states, there is no overlap for $n = 33$. However, for the thermal field and even more so for the BSV field, a nonvanishing overlap is seen. Note that the $P(|\alpha|)$ distributions for the coherent and Fock states extend beyond the range of the ordinate.

D. Power-scaling regime

In relation to experimental results like those presented in, e.g., Ref. [34], we can, from Eq. (36), determine that the signal in the nth odd harmonic is

$$S(n\omega_0) \propto \int d^2\alpha P(\alpha)\left[\sum_l C_l J_n(l\tilde{g}_0|\alpha|)\right]^2. \tag{40}$$

Taylor expanding the Bessel functions to the lowest nonvanishing order gives $J_n(x) \approx x^n/(n!2^n)$. From this, it follows that

$$\left[\sum_l C_l J_n(l\tilde{g}_0|\alpha|)\right]^2 \approx \frac{\tilde{g}_0^{2n}K_n}{(n!)^2 2^{2n}}|\alpha|^{2n}, \tag{41}$$

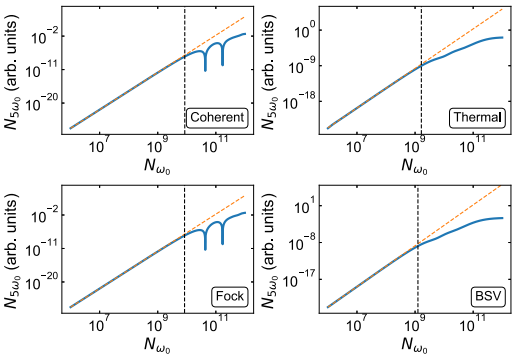

FIG. 3. Solid, blue curves show the mean photon count ($N_{n\omega_0} = \langle \hat{a}^\dagger_{n\boldsymbol{k}_0,\sigma_0} \hat{a}_{n\boldsymbol{k}_0,\sigma_0} \rangle$) in the fifth harmonic as a function of the mean photon count of the driving field as computed from Eq. (40) using the P representation of the different driving fields. The dashed, yellow line shows the perturbative power-scaling approximation computed from Eq. (42), and the black-dashed vertical line denotes the predicted range of applicability of the perturbative treatment.

where $K_n = \sum_{l_1,l_2} l_1^n l_2^n C_{l_1} C_{l_2}$ is a geometric constant of the material, which is determined by the dispersion relation and the filling of the conduction band. Equation (41) is substituted into Eq. (40) to give (to lowest order)

$$\begin{aligned} S(n\omega_0) &\propto K_n \frac{\tilde{g}_0^{2n}}{(n!)^2 2^{2n}} \int d^2\alpha P(\alpha) |\alpha|^{2n} \\ &= K_n \frac{\tilde{g}_0^{2n}}{(n!)^2 2^{2n}} \langle : \left(\hat{a}^\dagger_{\boldsymbol{k}_0,\sigma_0} \hat{a}_{\boldsymbol{k}_0,\sigma_0} \right)^n : \rangle \\ &= K_n \frac{\tilde{g}_0^{2n}}{(n!)^2 2^{2n}} g^{(n)}(0) \langle \hat{a}^\dagger_{\boldsymbol{k}_0,\sigma_0} \hat{a}_{\boldsymbol{k}_0,\sigma_0} \rangle^n, \end{aligned} \tag{42}$$

where $: \hat{O} :$ denotes the normal ordering of the operator $\hat{O}$ and $g^{(n)}(0)$ is the nth-order single-mode normalized correlation function. Thus, we have recovered the power-scaling law $\langle \hat{a}^\dagger_{n\boldsymbol{k}_0,\sigma_0} \hat{a}_{n\boldsymbol{k}_0,\sigma_0} \rangle \propto \langle \hat{a}^\dagger_{\boldsymbol{k}_0,\sigma_0} \hat{a}_{\boldsymbol{k}_0,\sigma_0} \rangle^n$ of the perturbative regime [34]. Interestingly, we note that in this particular model, the nth-order correlation function of the driving field, $g^{(n)}(0)$, enters as a proportionality factor and dictates the height of the signal in the nth harmonic. This is another way of showing how the quantum optical nature of the driving field affects the generated HHG spectrum. In other words, this means that if one could precisely control the mean photon number of the driving field, then the height of the nth harmonic is determined by the quantum nature of the driving field via $g^{(n)}(0)$. We note for clarity that this scaling law only holds when the lowest-order approximation of the Bessel function is a valid approximation, see Appendix C.

In Fig. 3, the peak intensity of the fifth harmonic is plotted as a function of the mean photon count in the driving field using Eq. (40) for the nonperturbative result and using Eq. (42) for the power-scaling approximation. To determine when the lowest-order approximation of $J_m(x)$ is valid, we apply the Taylor remainder theorem, see details in Appendix C. At the photon count, where the perturbative treatment is expected to break down based on the analysis in Appendix C, we mark the cutoff for this expected range of applicability with a vertical dotted line in Fig. 3.

As clearly seen in Fig. 3, this analysis yields a good estimation of the range of applicability of a perturbative treatment. It is clear that this range is smaller for BSV and thermal driving fields. Our predictions can explain this behavior: Since BSV and thermal states have much broader P distributions, their standard deviation will be large. Therefore, these distributions will reach into the range where the lowest-order Taylor expansion is not valid at a lower mean photon count than for states with narrow distributions such as coherent and Fock states. In other words, due to the broad P distributions of thermal and BSV states, these driving fields probe nonperturbative processes at lower intensities than coherent and Fock driving fields.

These findings are not immediately in line with Ref. [34], in which it is reported that HHG driven by BSV has a broader intensity range of the perturbative regime than HHG driven by coherent light. However, multiple factors make the comparison difficult. First, only one of the harmonics reported in Ref. [34] is an odd harmonic below the band gap and can be compared directly with our studies. For this harmonic, the threshold of optical damage for the coherent driving field is around the intensity cutoff of the perturbative regime for the BSV driving field. Below the optical damage threshold for the coherent driving field, a clear deviation from the power-scaling law is not apparent. That coherent driving should become nonperturbative at lower intensities is reported instead for the fourth harmonic, which does not appear in this work, as we consider spatially symmetric crystals. Finally, the results presented in Ref. [34] may be affected by electrons being promoted across the band gap even for the harmonics below the band gap which is an effect not taken into account in this work.

IV. TIME-RESOLVED ELECTRIC FIELD

As is apparent in Eq. (31), the derived density operator of the fields is time dependent. This allows for the evaluation of time-dependent observables such as the electric field, which bears relevance in relation to experimental work [39,49–52], where the temporal characteristics of the generated field may be observed. We therefore determine the electric field in the time domain within the considered model.

The quantized electric field operator in the dipole approximation is given as

$$\hat{\boldsymbol{E}}(t) = i \sum_{\boldsymbol{k},\sigma} g_0 \sqrt{\omega_{\boldsymbol{k}}} \left(\boldsymbol{e}_\sigma \hat{a}_{\boldsymbol{k},\sigma} e^{-i\omega_k t} - \text{H.c.} \right). \tag{43}$$

As the APP for Fock and BSV fields is an approximate description of the density matrix [Eq. (31)], we verify in Appendix D that this approximation produces the correct electrical field for the different types of driving fields considered. We now investigate the generated electric field. Using that the coherent states are eigenstates of the annihilation operator, we use Eqs. (31) and (43) to determine the expectation value of

the generated electric field as

$$\langle \hat{\boldsymbol{E}}(t)\rangle_{\mathrm{HHG}} = \mathrm{Tr}[\hat{\rho}(t)\hat{\boldsymbol{E}}(t)] = -\sum_{\mathbf{k},\sigma} g_0\sqrt{\omega_{\mathbf{k}}}\int d^2\alpha P(\alpha) 2\,\mathrm{Im}\big[\hat{\boldsymbol{e}}_{\mathbf{k},\sigma}\gamma^{\alpha}_{\mathbf{k},\sigma}(t)e^{-i\omega_{\mathbf{k}}t}\big], \tag{44}$$

where we, as in connection with Eq. (32), have neglected the $+\alpha$ from the laser in the driving mode as we are only interested in the generated field.

Inserting Eq. (19) and executing the sum over the polarizations and the solid angle integral, it is found that

$$\langle \hat{\boldsymbol{E}}(t)\rangle_{\mathrm{HHG}} = -\frac{2Vg_0}{3\pi^2c^3}\int d^2\alpha P(\alpha) \times \mathrm{Im}\left[-i\int_{t_i}^{t} dt' \boldsymbol{j}^{\alpha}_{i,i}(t')\int_0^{\infty} d\omega\,\omega^2 e^{i\omega(t'-t)}\right], \tag{45}$$

where the innermost integral can be recognized as the distribution $-\pi\frac{d^2}{dt^2}\delta(t'-t)$, when the imaginary part is taken. As $t\in[t_i,t]$ and by writing out g_0, we obtain

$$\langle \hat{\boldsymbol{E}}(t)\rangle_{\mathrm{HHG}} = -\frac{4}{3c^3}\int d^2\alpha P(\alpha)\frac{d^2}{dt^2}\boldsymbol{j}^{\alpha}_{i,i}(t). \tag{46}$$

Likewise, the variance of the generated field can be derived. Taking $\boldsymbol{j}_{i,i}$ along the one-dimensional chain of the model to be in the z direction, we compute $\langle E_z^2\rangle$. Generally, this will yield four terms: The square of the generated fields, the square of the driving field, an interference term between the driving and generated field, and the zero-point fluctuations. As the generated field at frequencies different from ω_0 is of interest, the other terms are neglected. For details, see Appendix D. We then find that

$$\langle \hat{E}_z^2\rangle_{\mathrm{HHG}} = \frac{16}{9c^6}\int d^2\alpha P(\alpha)\left[\frac{d^2}{dt^2}j^{\alpha}_{ii}(t)\right]^2, \tag{47}$$

which is used to determine the variance

$$\langle \Delta\hat{E}_z^2\rangle_{\mathrm{HHG}} = \frac{16}{9c^6}\left\{\int d^2\alpha P(\alpha)\left[\frac{d^2}{dt^2}j^{\alpha}_{ii}(t)\right]^2 - \left[\int d^2\alpha P(\alpha)\frac{d^2}{dt^2}j^{\alpha}_{ii}(t)\right]^2\right\}. \tag{48}$$

Note that the distribution function of the driving field, $P(\alpha)$, also enters into the expressions of the characteristics of the generated fields in Eqs. (46) and (48), indicating that the quantum nature of the driving field is mapped onto the generated field. This mapping of field characteristics is in accordance with the simulations of the generated electric fields shown in Fig. 4 where both the electric field, $\langle\hat{\boldsymbol{E}}(t)\rangle_{\mathrm{HHG}}$ [Eq. (46)], along with its uncertainty, $\sqrt{\langle\Delta\hat{E}_z^2\rangle_{\mathrm{HHG}}}$ [Eq. (48)], for different driving fields is shown. In Fig. 4, it is apparent that the field generated from coherent light has the characteristics of coherent light. This is in accordance with the result of Ref. [23], in which it is found that the harmonics of HHG are coherent when the driving field is coherent and the electrons of the medium are uncorrelated. For the BSV driving field, the generated field also has the characteristics of BSV fields,

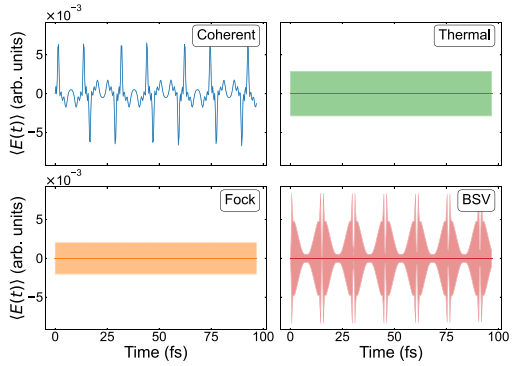

FIG. 4. Time-resolved electric field generated by HHG for coherent, Fock, thermal, and BSV driving fields. Solid lines represent the expectation value of the electric field and the shaded area represents the uncertainty in the electric field neglecting the zero-point vacuum fluctuations. Simulated from Eqs. (46) and (48). The same parameters are used as in Sec. III B.

where the expectation value of the electric field is vanishing but it still has a large time-dependent uncertainty. Likewise, the generated fields from the Fock and thermal driving fields have vanishing expectations values of the fields with constant uncertainty, which are the same characteristics as their corresponding driving fields.

Estimating the width of the peaks in Fig. 4, they are all at least 0.8 fs corresponding to a maximum frequency of around 1 PHz. This spectral resolution is within reach for experimental settings using, e.g., TIPTOE [39,52]. As such, it should be feasible to measure such time-dependent fields, from which we can uncover information on how the quantum state of the driving field maps onto the quantum state of the emitted field via the process of HHG.

V. ACCURACY OF THE APPROXIMATIVE POSITIVE *P* REPRESENTATION

Figures 1 and 3 were computed using the APP representation for BSV and Fock light. The accuracy of these results therefore depends on the accuracy of the APP representation as introduced in Sec. II B. To illustrate why this is an important point, consider a Fock state $|N\rangle$, which is described by the density operator $\hat{\rho} = \int d^2\alpha P(\alpha)|\alpha\rangle\langle\alpha|$ in the Glauber-Sudarshan representation where the P function is [43]

$$P^{(N)}_{\mathrm{Fock,\,GS}}(\alpha) = \frac{e^{|\alpha|^2}}{N!}\frac{\partial^{2N}}{\partial\alpha^N\partial\alpha^{*N}}\delta^{(2)}(\alpha). \tag{49}$$

Here derivatives of the delta function are understood in the distributional sense. On the other hand, the APP representation for the Fock state is given by Eq. (28). From Eqs. (28) and (49) it is not trivial that $\hat{\rho} = \int d^2\alpha P^{(N)}_{\mathrm{GS}}(\alpha)|\alpha\rangle\langle\alpha| \approx \int d^2\alpha Q^{(N)}_{\mathrm{Fock}}(\alpha)|\alpha\rangle\langle\alpha|$ for large N. Indeed, it would be difficult to make the arguments of Secs. III C and III D using the highly singular P function of Eq. (49), as one cannot make statements on the value of P at a given α. Hence, it is important to study

if the APP is accurate for the observables that we consider and verify the APP on a case-by-case basis.

In order to verify that the APP representation indeed yields reliable results (for BSV and Fock light), we test it on the incoming driving field. We find that it yields the correct photon number $\langle \hat{a}^\dagger_{\boldsymbol{k},\sigma} \hat{a}_{\boldsymbol{k},\sigma} \rangle$ in the limit of a large mean photon number for both BSV and Fock light. Further, it reproduces the correct mean and variance of the time-dependent electric field as discussed in Appendix D. However, the APP representation does not reproduce the correct photon statistics or degree of squeezing for the driving field. This is due to the fact that the APP representation neglects the coherence of α and β in the positive P distribution [Eq. (24), see also Eq. (26)]. This shows a limitation of the APP and we do therefore not consider the photon statistics or squeezing of the emitted field. Further calculations and discussion on the validity of the APP representation is given in Appendix B.

VI. CONCLUSION

In this work, we presented a derivation of the quantum optical state of light emitted from intraband HHG driven by quantum light. Using this quantum optical state for the emitted field, we calculated the harmonic spectrum for different types of driving fields: coherent, Fock, thermal, and BSV light. These results were compared to the Floquet limit which produced identical spectra. Using the analytical Floquet limit, we studied the harmonic spectrum and predicted the harmonic cutoff for a given type of driving field. In this limit, the spectrum is expressed analytically in terms of Bessel functions $J_n(l\tilde{g}_0|\alpha|)$, with arguments that depend on the dispersion relation of the generating crystal as well as the strength of the driving field. We found that the harmonic cutoff is dictated by the overlap between these Bessel functions and the P distributions used to describe the driving field. This enabled us to explain why the cutoff is less clearly defined when driving with a thermal or BSV field than for a coherent or Fock field. Furthermore, we estimated the intensity range of the driving field for which the harmonic peaks can be treated perturbatively. From this analysis, we found that fields with broad coherent phase-space distributions can probe nonperturbative processes with a lower intensity than fields with narrow distributions such as coherent and Fock fields.

Utilizing that the derived field state is time dependent, we also derived expressions for the expectation value of the generated electric field and its variance. In the single-band model of a solid considered in this paper, we found that the temporal characteristics of the driving field are mapped to the generated field. Since these generated time-dependent fields vary on a timescale that can be observed experimentally, this presents potential for experimental studies on how the HHG process maps the quantum state of the driving field onto the generated field, as temporal characteristics depend on the quantum state of the field. To relate this study of the generated electric field to possible experiments it is prudent to study the propagation of such quantum fields through the crystal. The inclusion of propagation effects is presently unresolved in strong-field quantum optics [53] and is beyond the scope of this work. For this reason, the results in this paper are experimentally relevant in the limit of thin films.

We also discussed the accuracy of approximating the nondiagonal positive $P(\alpha, \beta)$ representation of a quantum state by an approximate positive P description for the Fock and BSV driving fields. We confirmed that this approximation yields the correct harmonic spectra (in the limit of large photon numbers) and time-dependent electric fields for the driving fields before calculating these observables for the emitted field. However, this approximation does not yield the correct photon statistics or degree of squeezing for the driving field and we did therefore not consider these observables for the emitted field. Going beyond the APP and using the full positive $P(\alpha, \beta)$ is to be considered in future work, such that the nonclassical observables of the emitted light can be investigated in more detail.

The model of solids considered in this work is a simple one-dimensional single-band model. It is therefore relevant for future work to extend the description of the electronic system to include, e.g., multiple bands, topological effects and electron correlation. Specifically, it is a natural continuation of this work to consider a model with multiple bands, which would allow the inclusion of interband currents. Driving with a classical field, intraband processes dominate for harmonics below the band gap while it has been seen that interband currents dominate the spectrum above the band gap [39]. As seen in the present work, using, e.g., a BSV driving field, intraband harmonics with energies far above a typical band gap energy are generated and it is a subject for future research to investigate how the inclusion of interband currents would interplay with the intraband currents with respect to the above-band-gap-generated harmonics. The interplay between harmonics originating from intraband and interband currents would hence be interesting to study, including their respective nonclassical properties such as squeezing and photon statistics. However, in such extensions it would not generally be possible to make the same analytical considerations regarding the induced current as in this work without further approximations. More specifically, the current operator would not generally commute with the Hamiltonian as it does in the model of this work and hence all cross current matrix elements would need to be considered which greatly increases the complexity of the problem. Approaches to get around this could be considered, such as using a Markov state approximation (see Refs. [26,54]), which can accurately capture features such as the generated spectrum, including squeezing and photon statistics.

DATA AVAILABILITY

The data that support the findings of this article are not publicly available upon publication because it is not technically feasible and/or the cost of preparing, depositing, and hosting the data would be prohibitive within the terms of this research project. The data are available from the authors upon reasonable request.

APPENDIX A: ANALYTICAL EXPRESSION FOR HHG SPECTRUM

In this Appendix, we show, based on analytical considerations using the GS representation, that both a Fock and BSV

driving field indeed do generate a harmonic spectrum, contrary to the comments in Ref. [31], as discussed in Sec. III B. We derive a general expression for the generated HHG spectrum as a function of the mth-order coherence function, $g^{(m)}(0)$, which shows that the harmonic spectrum depends on the photon statistics of the driving field. We use this to show that spectra for the coherent and Fock drivers are identical and then show why the HHG spectra produced by a thermal or a BSV driving field are qualitatively much different. Note that these considerations do *not* rely on the APP used in Eq. (26) but verify the results for the generated spectra within the APP presented in the present work as seen, e.g., in Fig. 1.

We cannot evaluate Eq. (40) directly in the GS representation, but we can make further analytical considerations by expanding the Bessel functions in power series

$$J_n(x) = \sum_k \frac{(-1)^k}{k!(n+k)!}\left(\frac{x}{2}\right)^{n+2k}. \tag{A1}$$

Inserting Eq. (A1) into Eq. (40) gives

$$S(n\omega_0) \propto \sum_{k_1,k_2} \frac{(-1)^{k_1+k_2} K_{n,k_1,k_2}}{k_1!k_2!(n+k_1)!(n+k_2)!}\left(\frac{\tilde{g}_0}{2}\right)^{2(n+k_1+k_2)} \times \int d^2\alpha\, P(\alpha)|\alpha|^{2(n+k_1+k_2)}. \tag{A2}$$

Letting $\hat{N}_{\omega_0} = \hat{a}^\dagger_{\boldsymbol{k}_0,\sigma_0}\hat{a}_{\boldsymbol{k}_0,\sigma_0}$ denote the number operator of the driving mode, its normal-ordered expectation value in the driving field is given by

$$\left\langle :\hat{N}_{\omega_0}^{n+k_1+k_2}: \right\rangle = \int d^2\alpha\, P(\alpha)|\alpha|^{2(n+k_1+k_2)}. \tag{A3}$$

Using the definition of the normalized coherence functions $g^{(m)}(0) = \langle :\hat{N}^m_{\omega_0}:\rangle / \langle \hat{N}_{\omega_0}\rangle^m$ [43], we re-express Eq. (A2) as

$$S(n\omega_0) \propto \sum_{k_1,k_2} \frac{(-1)^{k_1+k_2} K_{n,k_1,k_2}}{k_1!k_2!(n+k_1)!(n+k_2)!}\left(\frac{\tilde{g}_0}{2}\right)^{2(n+k_1+k_2)} \times g^{(n+k_1+k_2)}(0)\left\langle \hat{N}_{\omega_0}\right\rangle^{n+k_1+k_2}, \tag{A4}$$

which shows that the photon statistics enter the spectrum only through the coherence functions. Equation (A4) is not practical for numerical consideration. It is, however, revealing regarding the similarity between the coherent spectrum and the Fock spectrum. For a coherent field it is known that $g^{(m)}_{\text{Coherent}}(0) = 1$ while for a Fock state $|N\rangle$ we find that

$$\begin{aligned} g^{(m)}_{\text{Fock}}(0) &= \frac{1}{N^m}\frac{N!}{(N-m)!} \\ &= 1 - \frac{1}{N}\sum_{k=1}^{m} k + O\left(\frac{1}{N^2}\right) \\ &= 1 - \frac{1}{N}\frac{m(m+1)}{2} + O\left(\frac{1}{N^2}\right), \end{aligned} \tag{A5}$$

where the factorial term is written out in the last two lines, and the higher-order terms of $1/N$ are collected in $O(1/N^2)$. This result was found by direct calculation using that $\hat{a}_{\boldsymbol{k}_0,\sigma_0}|N\rangle = \sqrt{N}|N-1\rangle$. The coherence function is thereby $g^{(m)}_{\text{Fock}}(0) \approx 1$ at large photon numbers. We have used a mean photon number of $N = \langle \hat{N}_{\omega_0}\rangle = 7.35 \times 10^{11}$ in our simulations. This means that even for very large m, multiple orders of magnitude greater than the relevant harmonic orders of the coherent spectrum, we have that $g^{(m)}_{\text{Fock}}(0) \approx g^{(m)}_{\text{Coherent}}(0)$. Hereby, in the limit of large photon numbers, we find that the spectra of coherent and Fock driving fields are approximately equal

$$S_{\text{Fock}}(n\omega_0) \approx S_{\text{Coherent}}(n\omega_0). \tag{A6}$$

The above calculation only relies on the large photon number $N \gg 1$ of the driving field. It shows that the result for the Fock spectrum using the APP representation is consistent with the GS representation, and the results for the Fock driving field in Sec. III B, and by extension Ref. [28], are therefore verified. This also shows that the large-volume-based limiting procedure considered in both Refs. [28,31] is troublesome when also applied to the Husimi-Q function as that procedure would predict a vanishing spectrum when driving with a Fock state.

For completeness, using the exact formulation in Eq. (A4), we note that

$$g^{(m)}_{\text{Thermal}}(0) = m! \tag{A7}$$

and

$$g^{(m)}_{\text{BSV}}(0) = (2m-1)!! + O(1/\langle \hat{N}_{\omega_0}\rangle), \tag{A8}$$

which clearly shows that the spectra generated by a thermal or a BSV driving field are vastly different from those generated by a coherent or a Fock state driver.

The thermal mth-order coherence function was found using the GS P function from Eq. (23) along with the optical equivalence theorem.

For BSV, the mth-order coherence function can be computed as follows: First, we rewrite

$$\begin{aligned} &\langle \xi|\hat{a}^{\dagger m}_{\boldsymbol{k}_0,\sigma_0}\hat{a}^m_{\boldsymbol{k}_0,\sigma_0}|\xi\rangle \\ &\quad = \langle 0|[S^\dagger(\xi)\hat{a}^\dagger_{\boldsymbol{k}_0,\sigma_0}S(\xi)]^m[S^\dagger(\xi)\hat{a}_{\boldsymbol{k}_0,\sigma_0}S(\xi)]^m|0\rangle. \end{aligned} \tag{A9}$$

Next, we use the identities

$$\begin{aligned} S^\dagger(\xi)\hat{a}_{\boldsymbol{k}_0,\sigma_0}S(\xi) &= \hat{a}_{\boldsymbol{k}_0,\sigma_0}\cosh(r) - \hat{a}^\dagger_{\boldsymbol{k}_0,\sigma_0}\sinh(r) \\ S^\dagger(\xi)\hat{a}^\dagger_{\boldsymbol{k}_0,\sigma_0}S(\xi) &= -\hat{a}_{\boldsymbol{k}_0,\sigma_0}\sinh(r) + \hat{a}^\dagger_{\boldsymbol{k}_0,\sigma_0}\cosh(r), \end{aligned} \tag{A10}$$

where $r = |\xi|$ and where we have assumed without loss of generality that $\arg\xi = 0$. We insert Eq. (A10) into Eq. (A9) and use that $\cosh^2(r) = \sinh^2(r) + 1$ to find that

$$\begin{aligned} &\langle \xi|\hat{a}^{\dagger m}_{\boldsymbol{k}_0,\sigma_0}\hat{a}^m_{\boldsymbol{k}_0,\sigma_0}|\xi\rangle \\ &\quad = \sinh^{2m}(r)\,\langle 0|\left(-\hat{a}_{\boldsymbol{k}_0,\sigma_0} + \hat{a}^\dagger_{\boldsymbol{k}_0,\sigma_0}\right)^m\left(\hat{a}_{\boldsymbol{k}_0,\sigma_0} - \hat{a}^\dagger_{\boldsymbol{k}_0,\sigma_0}\right)^m|0\rangle \\ &\qquad + O[\sinh^{2m-2}(r)]. \end{aligned} \tag{A11}$$

Using that $\langle \xi|\hat{N}_{\omega_0}|\xi\rangle = \sinh^2(r)$ we divide Eq. (A11) by $\sinh^{2m}(r)$ and obtain the coherence function

$$\begin{aligned} g^{(m)}_{\text{BSV}}(0) &= \langle 0|\left(-\hat{a}_{\boldsymbol{k}_0,\sigma_0} + \hat{a}^\dagger_{\boldsymbol{k}_0,\sigma_0}\right)^m\left(\hat{a}_{\boldsymbol{k}_0,\sigma_0} - \hat{a}^\dagger_{\boldsymbol{k}_0,\sigma_0}\right)^m|0\rangle \\ &\quad + O\left(1/\left\langle \hat{N}_{\omega_0}\right\rangle\right). \end{aligned} \tag{A12}$$

We can then use the second quadrature operator $\hat{X}_2 = (\hat{a} - \hat{a}^\dagger)/2i$ to rewrite the matrix element

$$\begin{aligned}\langle 0|\big(-\hat{a}_{\boldsymbol{k}_0,\sigma_0} + \hat{a}^\dagger_{\boldsymbol{k}_0,\sigma_0}\big)^m \big(\hat{a}_{\boldsymbol{k}_0,\sigma_0} - \hat{a}^\dagger_{\boldsymbol{k}_0,\sigma_0}\big)^m |0\rangle \\ = \langle 0|(-2i\hat{X}_2)^m (2i\hat{X}_2)^m|0\rangle \\ = 2^{2m}\langle 0|\hat{X}_2^{2m}|0\rangle. \end{aligned} \tag{A13}$$

This matrix element can be computed using the momentum space wave functions of the harmonic oscillator ground state, which yields

$$\begin{aligned}2^{2m}\langle 0|\hat{X}_2^{2m}|0\rangle &= \frac{(2m)!}{2^m m!} \\ &= (2m-1)!! \end{aligned} \tag{A14}$$

Inserting Eqs. (A14) and (A13) into Eq. (A12) yields exactly Eq. (A8).

In conclusion, this approach based on an exact expansion of the Bessel functions verifies the presented results and in particular the APP introduced in Eq. (26).

APPENDIX B: OBSERVABLES USING THE APPROXIMATIVE POSITIVE *P* REPRESENTATION

In this Appendix, we discuss which observables of the driving field are reproduced by using the APP representation for the Fock and BSV driving fields in Eqs. (28) and (30). The approximative APP for the density matrix for the driving field is then

$$\hat{\rho}^{(\mathrm{APP})} = \int d^2\alpha\, Q(\alpha)|\alpha\rangle\langle\alpha|, \tag{B1}$$

where $Q(\alpha)$ represents either Fock or BSV driving fields.

First, we calculate the mean photon number. The spectrum for a Fock state is determined by

$$\begin{aligned}\langle \hat{a}^\dagger\hat{a}\rangle^{(\mathrm{APP})}_{\mathrm{Fock}} &= \mathrm{Tr}[\hat{a}^\dagger\hat{a}\hat{\rho}^{(\mathrm{APP})}] \\ &= \int d^2\alpha\, Q^{(N)}_{\mathrm{Fock}}(\alpha)|\alpha|^2 \\ &= \int_0^{2\pi} d\phi \int_0^\infty d|\alpha|\, \frac{1}{\pi} e^{-|\alpha|^2}\frac{|\alpha|^{2N}}{N!}|\alpha|^3, \\ &= N+1 \\ &\neq \langle \hat{a}^\dagger\hat{a}\rangle^{\mathrm{Exact}}_{\mathrm{Fock}}, \end{aligned} \tag{B2}$$

which shows that in the limit of $N \gg 1$ where $N+1 \approx N$ the APP approximately gives the correct result for the spectrum. Similarly, we find for a BSV state

$$\begin{aligned}\langle \hat{a}^\dagger\hat{a}\rangle^{(\mathrm{APP})}_{\mathrm{BSV}} &= \mathrm{Tr}[\hat{a}^\dagger\hat{a}\hat{\rho}^{(\mathrm{APP})}] \\ &= \int_{-\infty}^\infty dx \int_{-\infty}^\infty dy\, Q^{(r)}_{\mathrm{BSV}}(x^2+y^2) \\ &= \cosh^2(r) \\ &\neq \langle \hat{a}^\dagger\hat{a}\rangle^{\mathrm{Exact}}_{\mathrm{BSV}}, \end{aligned} \tag{B3}$$

where we have used $\alpha = x + iy$. Equation (B3) differs from the exact result for a squeezed vacuum state which is $\langle \hat{a}^\dagger\hat{a}\rangle^{\mathrm{Exact}}_{\mathrm{BSV}} = \sinh^2(r)$ [43]. However, in the limit of a large photon number, we see that $\sinh^2(r) = \cosh^2(r) - 1 \approx \cosh^2(r)$ approximately yielding the correct result. Thus, as the spectrum is proportional to the mean photon number, we conclude that the spectra for the driving fields are correctly reproduced by the APP representation and we extend the analysis to the emitted HHG spectrum with this representation in Sec. III in the main text. Further justification in the case of a Fock driving field can be found in Appendix A.

We now consider the photon statistics for the Fock driving field. Here we consider the Mandel-$\mathcal{Q}$ parameter (not to be confused with the Husimi-Q function) given by

$$\begin{aligned}\mathcal{Q} &= \frac{\langle(\hat{a}^\dagger\hat{a})^2\rangle - \langle\hat{a}^\dagger\hat{a}\rangle^2}{\langle\hat{a}^\dagger\hat{a}\rangle} - 1 \\ &= \frac{\langle\hat{a}^\dagger\hat{a}^\dagger\hat{a}\hat{a}\rangle - \langle\hat{a}^\dagger\hat{a}\rangle^2}{\langle\hat{a}^\dagger\hat{a}\rangle}. \end{aligned} \tag{B4}$$

Calculating the second moment in the APP representation, we find

$$\langle \hat{a}^\dagger\hat{a}^\dagger\hat{a}\hat{a}\rangle^{(\mathrm{APP})}_{\mathrm{Fock}} = N^2 + 3N + 2, \tag{B5}$$

yielding a Mandel-$\mathcal{Q}$ parameter of $\mathcal{Q}^{(\mathrm{APP})}_{\mathrm{Fock}} = 3 + 2/N$, which does not match the exact result of $\mathcal{Q}^{\mathrm{Exact}}_{\mathrm{Fock}} = -1$. This is a significant error, as the APP result predicts super-Poissonian statistics for a state with sub-Poissonian statistics.

Similarly, we consider the degree of squeezing for the BSV driving field. This is done through minimizing the variance of the quadrature operator $\hat{X}(\theta) = \frac{1}{2}(\hat{a}e^{-i\theta} + \hat{a}^\dagger e^{i\theta})$ for $\theta \in [0, \pi)$. The variance of this operator is

$$\begin{aligned}\langle \Delta\hat{X}^2(\theta)\rangle = \tfrac{1}{4}[e^{-2i\theta}(\langle\hat{a}^2\rangle - \langle\hat{a}\rangle^2) + e^{2i\theta}(\langle\hat{a}^{\dagger 2}\rangle - \langle\hat{a}^\dagger\rangle^2) \\ + 2(\langle\hat{a}^\dagger\hat{a}\rangle - \langle\hat{a}\rangle\langle\hat{a}^\dagger\rangle) + 1]. \end{aligned} \tag{B6}$$

Calculating the moments of the photonic operators, we find that in

$$\langle\hat{a}\rangle^{(\mathrm{APP})}_{\mathrm{BSV}} = \langle\hat{a}^\dagger\rangle^{(\mathrm{APP})}_{\mathrm{BSV}} = 0, \tag{B7}$$

$$\langle\hat{a}^2\rangle^{(\mathrm{APP})}_{\mathrm{BSV}} = \langle(\hat{a}^\dagger)^2\rangle^{(\mathrm{APP})}_{\mathrm{BSV}} = -\tanh(r)\cosh^2(r). \tag{B8}$$

Inserting Eqs. (B7) and (B8) into Eq. (B6), we find that

$$\langle \Delta\hat{X}^2(\theta)\rangle = \tfrac{1}{2}\cosh^2 r[1 - \cos(2\theta)\tanh r] + \tfrac{1}{4}. \tag{B9}$$

To minimize this, we can take the derivative with respect to θ, which vanishes for $\theta = 0, \pi/2$. Obviously, of these two, $\theta = 0$ minimizes the expression, and hence

$$\vartheta^{(\mathrm{APP})}_{\mathrm{BSV}} = \min_{\theta\in[0,\pi)} \langle \Delta\hat{X}^2(\theta)\rangle = \tfrac{1}{2}\cosh^2 r(1 - \tanh r) + \tfrac{1}{4}. \tag{B10}$$

Notice especially that $|\tanh x| \leqslant 1$ for all $x \in \mathbb{R}$, so $1 - \tanh r \geqslant 0$, which means that in the APP representation

$$\vartheta^{(\mathrm{APP})}_{\mathrm{BSV}} = \min_{\theta\in[0,\pi)} \langle \Delta\hat{X}^2(\theta)\rangle \geqslant \tfrac{1}{4}, \tag{B11}$$

which does clearly does not match exact results where $\vartheta^{\mathrm{Exact}}_{\mathrm{BSV}} = \frac{1}{4}e^{-2r}$ [43].

Hence, the APP representation does not capture the correct photon statistics for Fock states or correct squeezing BSV fields and hence we abstain from considering these observables for the emitted field.

APPENDIX C: DETAILS ON THE LOWEST-ORDER EXPANSION OF THE BESSEL FUNCTIONS

For the discussion of the range of the perturbative regime of HHG in Sec. III D, we are interested in determining the error in approximating the Bessel functions $J_n(x)$ to the lowest order. To this end, we employ Taylor's remainder theorem to obtain an upper bound on the error for some interval of x.

Specifically, we use the theorem that states that for an analytic function $f : [a, b] \in \mathbb{R} \to \mathbb{R}$ the remainder $R_n(x)$ of the nth-order Taylor expansion of f can be estimated as for $x \in [a, b]$ as

$$|R_n(x)| \leqslant M \frac{x^{n+1}}{(n+1)!}, \tag{C1}$$

where M is a positive real number that fulfills

$$M \geqslant \left| \frac{d^{n+1}}{dx^{n+1}} f(x) \right|, \quad \forall x \in [a, b]. \tag{C2}$$

Writing the Bessel function as a Taylor expansion we have

$$J_n(x) = \sum_{k=0}^{\infty} \frac{(-1)^k}{k!(n+k)!} \left(\frac{x}{2}\right)^{n+2k}, \tag{C3}$$

which means that the lowest nonvanishing order in the expansion is n. Since we know that Bessel functions vanish when the argument is smaller than the order, we are motivated to consider the interval $[0, n/r]$, where r is some positive real number that we will tune to give an acceptably low remainder. We fix this tolerance for the remainder to be $|R_n(x)| \leqslant 1/100$, as we deem a 1% error acceptable.

We can then determine the M parameter for a given r as

$$M \geqslant \left| \frac{d^{n+1}}{dx^{n+1}} J_n(x) \right|, \quad \forall x \in \left[0, \frac{n}{r}\right]. \tag{C4}$$

Using the identities for differentiating a Bessel function we may write

$$\frac{d^{n+1}}{dx^{n+1}} J_n(x) = \frac{1}{2^{n+1}} \sum_{k=0}^{n+1} \binom{n+1}{k} J_{2k-1}(x), \tag{C5}$$

and utilizing that $|J_n(x)| \leqslant 1/\sqrt{2}$ for all x and for $n \geqslant 1$, we conclude that

$$\left| \frac{d^{n+1}}{dx^{n+1}} J_n(x) \right| \leqslant \frac{1}{2^{n+1}} \sum_{k=0}^{n+1} \binom{n+1}{k} \frac{1}{\sqrt{2}} = \frac{1}{\sqrt{2}}. \tag{C6}$$

Hence, we choose $M = 1/\sqrt{2}$ to obtain that

$$\begin{aligned} |R_n(x)| &\leqslant \frac{1}{\sqrt{2}} \frac{x^{n+1}}{(n+1)!} \\ &\leqslant \frac{1}{\sqrt{2}} \frac{n^{n+1}}{r^{n+1}(n+1)!}, \end{aligned} \tag{C7}$$

which is independent of x. Last, we want a universal estimate for all n. For this, we can use that $n! \geqslant \sqrt{2\pi} e (n/e)^n$, where e is Euler's number. Hereby we can estimate that

$$\begin{aligned} |R_n(x)| &\leqslant \frac{1}{2\sqrt{\pi} e} \left(\frac{n}{n+1}\right)^{n+1} \left(\frac{e}{r}\right)^{n+1} \\ &\leqslant \frac{1}{2\sqrt{\pi} e} \left(\frac{e}{r}\right)^{n+1}, \end{aligned} \tag{C8}$$

which is a decreasing function of n when $r \geqslant e$. We therefore find that

$$|R_n(x)| \leqslant \frac{1}{2\sqrt{\pi} e} \left(\frac{e}{r}\right)^2, \tag{C9}$$

for all $n \geqslant 1$. We can then solve the equation for r given the tolerance

$$\begin{aligned} &\frac{1}{2\sqrt{\pi} e} \left(\frac{e}{r}\right)^2 \leqslant \frac{1}{100} \\ &\Rightarrow r \geqslant 10 \frac{\sqrt{e}}{2\sqrt[4]{\pi}} \approx 9. \end{aligned} \tag{C10}$$

As such we have found an estimate of an interval $[0, n/9]$, where the error of the Bessel functions is within the set tolerance.

We note that this is a rough estimate since we have made an estimation that is valid for all n. For more precise results, which could yield lower r values, one could consider each order separately and obtain an order dependent r_n. This could be done from Eq. (C7), and could also be improved by making a less rough estimation of the bounds of $J_n(x)$, which become smaller with the harmonic orders. The point is that we now know that the lowest-order approximation of $J_n(x)$ is valid within the tolerance $1/100$ on at least the interval $[0, n/9]$.

Hereby, in relation to Sec. III D, we can say that the lowest-order approximation is valid for the Bessel function $J_n(l\tilde{g}_0|\alpha|)$ when

$$|\alpha| \leqslant \frac{n}{9l\tilde{g}_0}. \tag{C11}$$

We can then argue similarly to Sec. III C, that we can use this approximation when the P distribution is contained within this region. Again, we estimate the region where $P(\alpha)$ is not negligible as $\mu_P - 3\sigma_P \leqslant |\alpha| \leqslant \mu_P + 3\sigma_P$. Hence, we can use the power-scaling law [Eq. (42)] for the nth harmonic when

$$\mu_P + 3\sigma_P \leqslant n/(9l_{\max}\tilde{g}_0). \tag{C12}$$

The parameters μ_P and σ_P are the mean and standard deviation of the distribution $P(|\alpha|)$, respectively, which depends on the mean photon count of the driving field. Explicitly, they are given as

$$\mu_P = \int d^2\alpha P(\alpha)|\alpha|, \tag{C13}$$

$$\begin{aligned} \sigma_P^2 &= \int d^2\alpha P(\alpha)|\alpha|^2 - \left[\int d^2\alpha P(\alpha)|\alpha|\right]^2 \\ &= \langle \hat{a}^\dagger_{\boldsymbol{k}_0,\sigma_0} \hat{a}_{\boldsymbol{k}_0,\sigma_0} \rangle - \mu_P^2. \end{aligned} \tag{C14}$$

For a coherent state [Eq. (22)], the mean photon number is $\langle \hat{a}^\dagger_{\boldsymbol{k},\sigma} \hat{a}_{\boldsymbol{k},\sigma} \rangle = |\alpha_{\boldsymbol{k},\sigma}|^2$ while for BSV fields [Eq. (30)] it is $\langle \hat{a}^\dagger_{\boldsymbol{k},\sigma} \hat{a}_{\boldsymbol{k},\sigma} \rangle = \sinh^2(r)$. For Fock and thermal fields, the mean photon number enters the respective distributions explicitly [see Eqs. (28) and (23)]. The parameters μ_P and σ_P are calculated numerically using Eqs. (C13) and (C14) for each value of mean photon number in the driving field. Thus, the inequality of Eq. (C12) is checked for each of these values, and the cutoff is set at the lowest mean photon number for which the inequality is broken. These cutoffs are plotted in Fig. 3.

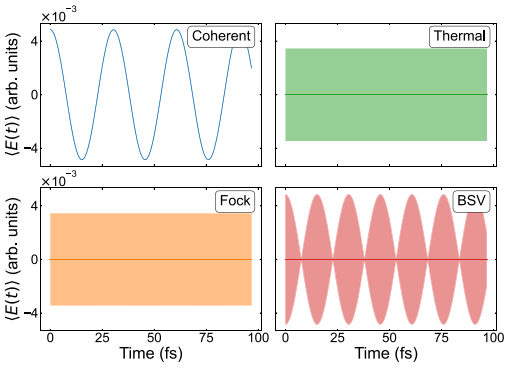

FIG. 5. Time-resolved electric driving fields for coherent, Fock, thermal, and BSV fields. Solid lines represent the expectation value of the electric field and the shaded area represent the uncertainty in the electric field neglecting the zero-point vacuum fluctuations.

APPENDIX D: DERIVATION OF THE TIME-RESOLVED ELECTRIC FIELD

In this Appendix, we investigate the electric fields emitted from the HHG process. Before deriving the expressions for the emitted electric field, we first verify that the electric field of the driving laser is correctly reproduced in the APP. To this end, we compute $\langle \hat{\boldsymbol{E}}(t)\rangle$ with $\hat{\boldsymbol{E}}(t)$ given in Eq. (43) for the driving fields using the P functions in Eqs. (22), (23), (28), and (30). Likewise, we can compute the variance of the driving field and hereby the uncertainty in the field (neglecting zero-point fluctuations). These results are shown in Fig. 5. It is seen that the fields are as expected: The coherent field has a well-defined frequency and amplitude with vanishing fluctuations. Thermal and Fock fields have vanishing mean fields, but their uncertainties are on the scale of the coherent state amplitude and are constant in time. The BSV field also has a vanishing mean field but the uncertainty oscillates in time with the same amplitude and twice the frequency of the coherent oscillations. As the APP representation reproduces the correct time-dependent driving fields for Fock and BSV, we trust its validity to produce the correct time-dependent generated fields.

We now derive the equation for the mean and variance for the generated electric field. We consider the derived state of the field [Eq. (31)]

$$\hat{\rho}_F(t) = \int d^2\alpha P(\alpha) \left|\gamma^{\alpha}_{\mathbf{k}_0,\sigma_0}(t)+\alpha\right\rangle\!\left\langle\gamma^{\alpha}_{\mathbf{k}_0,\sigma_0}(t)+\alpha\right| \bigotimes_{(\mathbf{k},\sigma)\neq(\mathbf{k}_0,\sigma_0)} \left|\gamma^{\alpha}_{\mathbf{k},\sigma}(t)\right\rangle\!\left\langle\gamma^{\alpha}_{\mathbf{k},\sigma}(t)\right|, \tag{D1}$$

where

$$\gamma^{\alpha}_{\mathbf{k},\sigma}(t) = -i\frac{g_0}{\sqrt{\omega_{\mathbf{k}}}}\int_{t_i}^{t} j^{\alpha}_{ii}(t')\cdot\boldsymbol{e}_{\sigma}e^{i\omega_{\mathbf{k}}t'}dt'. \tag{D2}$$

The electric field operator in the dipole approximation is given again for clarity,

$$\hat{\boldsymbol{E}}(t) = i\sum_{\boldsymbol{k}\sigma} g_0\sqrt{\omega_k}(\boldsymbol{e}_{\sigma}\hat{a}_{\boldsymbol{k}\sigma}e^{-i\omega_k t} - \text{H.c.}). \tag{D3}$$

Computing the expectation value of the electric field operator yields

$$\begin{aligned}\langle\hat{\boldsymbol{E}}(t)\rangle &= \int d^2\alpha P(\alpha)\Big[ig_0\sqrt{\omega_0}\big(\boldsymbol{e}_{\sigma_0}\big(\gamma^{\alpha}_{\mathbf{k}_0,\sigma_0}(t)+\alpha\big)e^{-i\omega_0 t} - \text{c.c.}\big) \\ &\quad + i\sum_{\mathbf{k},\sigma\neq\mathbf{k}_0,\sigma_0} g_0\sqrt{\omega_{\mathbf{k}}}\big(\boldsymbol{e}_{\sigma}\gamma^{\alpha}_{\mathbf{k},\sigma}(t)e^{-i\omega_{\mathbf{k}}t} - \text{c.c.}\big)\Big] \\ &= ig_0\int d^2\alpha P(\alpha)\sum_{\mathbf{k},\sigma}\sqrt{\omega_{\mathbf{k}}}\big(\boldsymbol{e}_{\sigma}\gamma^{\alpha}_{\mathbf{k},\sigma}(t)e^{-i\omega_{\mathbf{k}}t} - \text{c.c.}\big) \\ &\quad + ig_0\sqrt{\omega_0}\int d^2\alpha P(\alpha)\big(\boldsymbol{e}_{\sigma_0}\alpha e^{-i\omega_0 t} - \text{c.c.}\big).\end{aligned} \tag{D4}$$

The last term in this equation is just the expectation value of the driving field, which we shall henceforth neglect, since we are interested in the generated field. With this, we let $\sum_{\boldsymbol{k}} \mapsto V/(2\pi c)^3\int d\omega\omega^2\int d\Omega$, where V is the quantization volume, c the speed of light in vacuum and $d\Omega$ the solid angle infinitesimal,

$$\begin{aligned}\langle\hat{\boldsymbol{E}}_{\text{HHG}}(t)\rangle &= i\frac{g_0 V}{(2\pi c)^3}\int d^2\alpha P(\alpha)\int_0^{\infty} d\omega\,\omega^2\sqrt{\omega} \\ &\quad\times\int d\Omega\sum_{\sigma} 2i\text{Im}\big(\boldsymbol{e}_{\sigma}\gamma^{\alpha}_{k\sigma}(t)e^{-i\omega t}\big) \\ &= \frac{2g_0^2 V}{(2\pi c)^3}\int d^2\alpha P(\alpha)\text{Im}\Big[i\int_{t_i}^{t} dt' \\ &\quad\times\int d\Omega\sum_{\sigma}\boldsymbol{e}_{\sigma}\big(\boldsymbol{j}^{\alpha}_{ii}(t')\cdot\boldsymbol{e}_{\sigma}\big)\int_0^{\infty} d\omega\,\omega^2 e^{i\omega(t'-t)}\Big].\end{aligned} \tag{D5}$$

We now seek to simplify this. Consider first the term

$$\int d\Omega\sum_{\sigma}\boldsymbol{e}_{\sigma}\big(\boldsymbol{j}^{\alpha}_{ii}(t')\cdot\boldsymbol{e}_{\sigma}\big). \tag{D6}$$

As a one-dimensional model of a solid is applied, we can let this direction be $\hat{\boldsymbol{z}}$ and take the polarization vectors be $\boldsymbol{e}_1 = \hat{\boldsymbol{\theta}}$ and $\boldsymbol{e}_2 = \hat{\boldsymbol{\phi}}$, which are the spherical coordinate unit vectors, that form an orthonormal basis of the orthogonal complement to the k vector. Hereby $\boldsymbol{j}^{\alpha}_{ii}(t')\cdot\boldsymbol{e}_1 = -j^{\alpha}_{ii}(t')\sin\theta$ and $\boldsymbol{j}^{\alpha}_{ii}(t')\cdot\boldsymbol{e}_2 = 0$. Hereby it is found that $\sum_{\sigma}\boldsymbol{e}_{\sigma}(\boldsymbol{j}^{\alpha}_{ii}(t')\cdot\boldsymbol{e}_{\sigma}) = -\hat{\boldsymbol{\theta}}j^{\alpha}_{ii}(t')\sin\theta$, and utilizing the spherical symmetry of the problem around the $\hat{\boldsymbol{z}}$ axis, it is found that

$$\begin{aligned}\int d\Omega\sum_{\sigma}\boldsymbol{e}_{\sigma}\big(\boldsymbol{j}^{\alpha}_{ii}(t')\cdot\boldsymbol{e}_{\sigma}\big) &= -j^{\alpha}_{ii}(t')\hat{\boldsymbol{z}}\int_0^{2\pi} d\phi\int_0^{\pi} d\theta\sin^3\theta \\ &= -\frac{8\pi}{3}\boldsymbol{j}^{\alpha}_{ii}(t'),\end{aligned} \tag{D7}$$

and we thereby get

$$\langle \hat{\boldsymbol{E}}_{\mathrm{HHG}}(t)\rangle = \frac{2g_0^2 V}{3\pi^2 c^3}\int d^2\alpha P(\alpha) \times \mathrm{Im}\left[i\int_{t_i}^{t} dt' \boldsymbol{j}_{ii}^{\alpha}(t')\int_0^{\infty} d\omega\, \omega^2 e^{i\omega(t'-t)}\right]. \tag{D8}$$

Next, we rewrite the term

$$\begin{aligned}
&\mathrm{Im}\left[-i\int_{t_0}^{t} dt' \boldsymbol{j}_{ii}^{\alpha}(t')\int_0^{\infty} d\omega\, \omega^2 e^{i\omega(t'-t)}\right]\\
&= \mathrm{Im}\left[i\int_{t_0}^{t} dt' \boldsymbol{j}_{ii}^{\alpha}(t')\frac{d^2}{dt'^2}\int_0^{\infty} d\omega e^{i\omega(t'-t)}\right]\\
&= \mathrm{Im}\Big(i\int_{t_0}^{t} dt' \boldsymbol{j}_{ii}^{\alpha}(t')\frac{d^2}{dt'^2}\int_0^{\infty} d\omega\{\cos[\omega(t'-t)]\\
&\quad + i\sin[\omega(t'-t)]\}\Big)\\
&= \int_{t_0}^{t} dt' \boldsymbol{j}_{ii}^{\alpha}(t')\frac{d^2}{dt'^2}\int_0^{\infty} d\omega\cos[\omega(t'-t)]\\
&= \frac{1}{2}\int_{t_0}^{t} dt' \boldsymbol{j}_{ii}^{\alpha}(t')\frac{d^2}{dt'^2}\int_{-\infty}^{\infty} d\omega\cos[\omega(t'-t)]\\
&= \frac{1}{2}\int_{t_0}^{t} dt' \boldsymbol{j}_{ii}^{\alpha}(t')\frac{d^2}{dt'^2}[2\pi\delta(t'-t)]\\
&= \pi\int_{t_0}^{t} dt' \boldsymbol{j}_{ii}^{\alpha}(t')\frac{d^2}{dt'^2}\delta(t'-t)\\
&= \pi\frac{d^2}{dt^2}\boldsymbol{j}_{ii}^{\alpha}(t),
\end{aligned} \tag{D9}$$

where we have utilized that $\boldsymbol{j}_{ii}^{\alpha}(t)$ is real, from being a diagonal matrix element, derivatives of distributions, and that $t \in [t_i, t]$.

By writing out $g_0 = \sqrt{2\pi/V}$, the front factor is then $\frac{4}{3c^3}$ and we achieve that the generated electric field is then given as

$$\langle \hat{\boldsymbol{E}}_{\mathrm{HHG}}(t)\rangle = -\frac{4}{3c^3}\int d^2\alpha P(\alpha)\frac{d^2}{dt^2}\boldsymbol{j}_{ii}^{\alpha}(t). \tag{D10}$$

The variance of the electric field can be derived in a similar way.

[1] M. Ferray, A. L'Huillier, X. F. Li, L. A. Lompre, G. Mainfray, and C. Manus, Multiple-harmonic conversion of 1064 nm radiation in rare gases, J. Phys. B: At. Mol. Opt. Phys. **21**, L31 (1988).

[2] P. B. Corkum, Plasma perspective on strong field multiphoton ionization, Phys. Rev. Lett. **71**, 1994 (1993).

[3] M. Lewenstein, Ph. Balcou, M. Yu. Ivanov, A. L'Huillier, and P. B. Corkum, Theory of high-harmonic generation by low-frequency laser fields, Phys. Rev. A **49**, 2117 (1994).

[4] P. M. Paul, E. S. Toma, P. Breger, G. Mullot, F. Augé, Ph. Balcou, H. G. Muller, and P. Agostini, Observation of a train of attosecond pulses from high harmonic generation, science **292**, 1689 (2001).

[5] M. Hentschel, R. Kienberger, C. Spielmann, G. A. Reider, N. Milosevic, T. Brabec, P. Corkum, U. Heinzmann, M. Drescher, and F. Krausz, Attosecond metrology, Nature (London) **414**, 509 (2001).

[6] F. Krausz and M. Ivanov, Attosecond physics, Rev. Mod. Phys. **81**, 163 (2009).

[7] D. M. Villeneuve, Attosecond science, Contemp. Phys. **59**, 47 (2018).

[8] G. Vampa and T. Brabec, Merge of high harmonic generation from gases and solids and its implications for attosecond science, J. Phys. B: At., Mol. Opt. Phys. **50**, 083001 (2017).

[9] S. Ghimire, A. D. DiChiara, E. Sistrunk, P. Agostini, L. F. DiMauro, and D. A. Reis, Observation of high-order harmonic generation in a bulk crystal, Nat. Phys. **7**, 138 (2011).

[10] D. Bauer and K. K. Hansen, High-harmonic generation in solids with and without topological edge states, Phys. Rev. Lett. **120**, 177401 (2018).

[11] Y. Bai, F. Fei, S. Wang, N. Li, X. Li, F. Song, R. Li, Z. Xu, and P. Liu, High-harmonic generation from topological surface states, Nat. Phys. **17**, 311 (2021).

[12] T. Morimoto and N. Nagaosa, Topological nature of nonlinear optical effects in solids, Sci. Adv. **2**, e1501524 (2016).

[13] A. Chacón, D. Kim, W. Zhu, S. P. Kelly, A. Dauphin, E. Pisanty, A. S. Maxwell, A. Picón, M. F. Ciappina, D. E. Kim, C. Ticknor, A. Saxena, and M. Lewenstein, Circular dichroism in higher-order harmonic generation: Heralding topological phases and transitions in Chern insulators, Phys. Rev. B **102**, 134115 (2020).

[14] R. E. F. Silva, Á. Jiménez-Galán, B. Amorim, O. Smirnova, and M. Ivanov, Topological strong-field physics on sub-laser-cycle timescale, Nat. Photon. **13**, 849 (2019).

[15] S. Ghimire, A. D. DiChiara, E. Sistrunk, G. Ndabashimiye, U. B. Szafruga, A. Mohammad, P. Agostini, L. F. DiMauro, and D. A. Reis, Generation and propagation of high-order harmonics in crystals, Phys. Rev. A **85**, 043836 (2012).

[16] G. Vampa, C. R. McDonald, G. Orlando, D. D. Klug, P. B. Corkum, and T. Brabec, Theoretical analysis of high-harmonic generation in solids, Phys. Rev. Lett. **113**, 073901 (2014).

[17] L. Yue and M. B. Gaarde, Introduction to theory of high-harmonic generation in solids: Tutorial, J. Opt. Soc. Am. B **39**, 535 (2022).

[18] G. Vampa, T. J. Hammond, N. Thiré, B. E. Schmidt, F. Légaré, C. R. McDonald, T. Brabec, D. D. Klug, and P. B. Corkum, All-optical reconstruction of crystal band structure, Phys. Rev. Lett. **115**, 193603 (2015).

[19] A. Gorlach, O. Neufeld, N. Rivera, O. Cohen, and I. Kaminer, The quantum-optical nature of high harmonic generation, Nat. Commun. **11**, 4598 (2020).

[20] P. Stammer, J. Rivera-Dean, T. Lamprou, E. Pisanty, M. F. Ciappina, P. Tzallas, and M. Lewenstein, High photon number entangled states and coherent state superposition from the extreme ultraviolet to the far infrared, Phys. Rev. Lett. **128**, 123603 (2022).

[21] P. Stammer, J. Rivera-Dean, A. Maxwell, T. Lamprou, A. Ordóñez, M. F. Ciappina, P. Tzallas, and M. Lewenstein, Quantum electrodynamics of intense laser-matter interactions: A

tool for quantum state engineering, PRX Quantum **4**, 010201 (2023).

[22] U. Bhattacharya, T. Lamprou, A. S. Maxwell, A. Ordóñez, E. Pisanty, J. Rivera-Dean, P. Stammer, M. F. Ciappina, M. Lewenstein, and P. Tzallas, Strong–laser–field physics, non–classical light states and quantum information science, Rep. Prog. Phys. **86**, 094401 (2023).

[23] C. S. Lange, T. Hansen, and L. B. Madsen, Electron-correlation-induced nonclassicality of light from high-order harmonic generation, Phys. Rev. A **109**, 033110 (2024).

[24] D. Theidel, V. Cotte, R. Sondenheimer, V. Shiriaeva, M. Froidevaux, V. Severin, A. Merdji-Larue, P. Mosel, S. Fröhlich, K.-A. Weber, U. Morgner, M. Kovacev, J. Biegert, and H. Merdji, Evidence of the quantum optical nature of high-harmonic generation, PRX Quantum **5**, 040319 (2024).

[25] D. Theidel, V. Cotte, P. Heinzel, H. Griguer, M. Weis, R. Sondenheimer, and H. Merdji, Observation of a multi-mode displaced squeezed state inhigh-harmonic generation, arXiv:2411.02311

[26] C. S. Lange and L. B. Madsen, Hierarchy of approximations for describing quantum light from high-harmonic generation: A Fermi-Hubbard-model study, Phys. Rev. A **111**, 013113 (2025).

[27] S. Yi, N. D. Klimkin, G. G. Brown, O. Smirnova, S. Patchkovskii, I. Babushkin, and M. Ivanov, Generation of massively entangled bright states of light during harmonic generation in resonant media, Phys. Rev. X **15**, 011023 (2025).

[28] A. Gorlach, M. E. Tzur, M. Birk, M. Krüger, N. Rivera, O. Cohen, and I. Kaminer, High-harmonic generation driven by quantum light, Nat. Phys. **19**, 1689 (2023).

[29] M. Even Tzur, M. Birk, A. Gorlach, M. Krüger, I. Kaminer, and O. Cohen, Photon-statistics force in ultrafast electron dynamics, Nat. Photon. **17**, 501 (2023).

[30] M. E. Tzur, M. Birk, A. Gorlach, I. Kaminer, M. Krüger, and O. Cohen, Generation of squeezed high-order harmonics, Phys. Rev. Res. **6**, 033079 (2024).

[31] P. Stammer, Absence of quantum optical coherence in high harmonic generation, Phys. Rev. Res. **6**, L032033 (2024).

[32] A. Pizzi, A. Gorlach, N. Rivera, A. Nunnenkamp, and I. Kaminer, Light emission from strongly driven many-body systems, Nat. Phys. **19**, 551 (2023).

[33] M. Lewenstein, M. F. Ciappina, E. Pisanty, J. Rivera-Dean, P. Stammer, T. Lamprou, and P. Tzallas, Generation of optical Schrödinger cat states in intense laser–matter interactions, Nat. Phys. **17**, 1104 (2021).

[34] A. Rasputnyi, Z. Chen, M. Birk, O. Cohen, I. Kaminer, M. Krüger, D. Seletskiy, M. Chekhova, and F. Tani, High-harmonic generation by a bright squeezed vacuum, Nat. Phys. **20**, 1960 (2024).

[35] M. Manceau, K. Y. Spasibko, G. Leuchs, R. Filip, and M. V. Chekhova, Indefinite-mean Pareto photon distribution from amplified quantum noise, Phys. Rev. Lett. **123**, 123606 (2019).

[36] S. Lemieux, S. A. Jalil, D. N. Purschke, N. Boroumand, T. J. Hammond, D. Villeneuve, A. Naumov, T. Brabec, and G. Vampa, Photon bunching inhigh-harmonic emission controlled by quantum light, Nat. Photon. (2025), doi:10.1038/s41566-025-01673-6.

[37] J. Rivera-Dean, in *Non-classical States of Light: Generation via Strong-Field Processes and Applications in Quantum Key Distribution* (Springer Nature Switzerland, Cham, 2024).

[38] S. L. Braunstein and P. van Loock, Quantum information with continuous variables, Rev. Mod. Phys. **77**, 513 (2005).

[39] P. D. Keathley, S. V. B. Jensen, M. Yeung, M. R. Bionta, and L. B. Madsen, Uncovering extreme nonlinear dynamics in solids through time-domain field analysis, Phys. Rev. B **107**, 054302 (2023).

[40] P. D. Drummond and C. W. Gardiner, Generalised P-representations in quantum optics, J. Phys. A: Math. Gen. **13**, 2353 (1980).

[41] D. Walls and G. J. Milburn, *Quantum Optics* (Springer, Berlin, 2008).

[42] C. Cohen-Tannoudji, G. Grynberg, and J. Dupont-Roc, *Atom-Photon Interactions: Basic Processes and Applications* (Wiley, New York, 1998).

[43] C. Gerry and P. Knight, *Introductory Quantum Optics* (Cambridge University Press, Cambridge, UK, 2004).

[44] M. O. Scully and M. S. Zubairy, *Quantum Optics* (Cambridge University Press, Cambridge, UK, 1997).

[45] C. S. Lange, T. Hansen, and L. B. Madsen, Noninteger high-order harmonic generation from extended correlated systems, Phys. Rev. A **109**, 063103 (2024).

[46] M. S. Kim, F. A. M. de Oliveira, and P. L. Knight, Properties of squeezed number states and squeezed thermal states, Phys. Rev. A **40**, 2494 (1989).

[47] G. Vampa, C. R. McDonald, G. Orlando, P. B. Corkum, and T. Brabec, Semiclassical analysis of high harmonic generation in bulk crystals, Phys. Rev. B **91**, 064302 (2015).

[48] A. T. Andersen, Simon Vendelbo Bylling Jensen, and L. B. Madsen, Intra- and intercycle analysis of intraband high-order harmonic generation, Phys. Rev. A **109**, 063109 (2024).

[49] S. Sederberg, D. Zimin, S. Keiber, F. Siegrist, M. S. Wismer, V. S. Yakovlev, I. Floss, C. Lemell, J. Burgdörfer, M. Schultze, F. Krausz, and N. Karpowicz, Attosecond optoelectronic field measurement in solids, Nat. Commun. **11**, 430 (2020).

[50] D. A. Zimin, V. S. Yakovlev, and N. Karpowicz, Ultra-broadband all-optical sampling of optical waveforms, Sci. Adv. **8**, eade1029 (2022).

[51] A. Husakou, N. Karpowicz, V. S. Yakovlev, M. Ivanov, and D. A. Zimin, Towards multi-petahertz all-optical electric field sampling, arXiv:2410.19196.

[52] M. R. Bionta, F. Ritzkowsky, M. Turchetti, Y. Yang, D. Cattozzo Mor, W. P. Putnam, F. X. Kärtner, K. K. Berggren, and P. D. Keathley, On-chip sampling of optical fields with attosecond resolution, Nat. Photon. **15**, 456 (2021).

[53] T. Lamprou, P. Stammer, J. Rivera-Dean, N. Tsatrafyllis, M. F. Ciappina, M. Lewenstein, and P. Tzallas, Recent developments in the generation of non-classical and entangled light states using intense laser-matter interactions, J. Phys. B: At., Mol. Opt. Phys. (2025), doi:10.1088/1361-6455/add9fe.

[54] C. S. Lange, T. Hansen, and L. B. Madsen, Excitonic enhancement of squeezed light in quantum-optical high-harmonic generation from a Mott insulator, arXiv:2503.15932.